Structure and Mechanics
of Neuronal Model Systems
– Insights from Atomic Force Microscopy
and Micropipette Aspiration

Dissertation

for the award of the degree
"Doctor rerum naturalium"
of the Georg-August-Universität Göttingen

within the doctoral program *Physics of Biological and Complex Systems*
of the Georg-August University School of Science (GAUSS)

submitted by

Marian Vache

born in Gronau (Leine)

Göttingen 2019

Thesis Committee

Prof. Dr. Andreas Janshoff
Institute of Physical Chemistry
Georg-August-University Göttingen

Dr. Franziska Thomas
Institute of Organic and Biomolecular Chemistry
Georg-August-University Göttingen

Dr. Florian Rehfeldt
Third Institute of Physics – Biophysics
Georg-August-University Göttingen

Members of the Examination Board

Referee: Prof. Dr. Andreas Janshoff
Institute of Physical Chemistry
Georg-August-University Göttingen

2nd Referee: Dr. Franziska Thomas
Institute of Organic and Biomolecular Chemistry
Georg-August-University Göttingen

Further members of the Examination Board

Dr. Florian Rehfeldt
Third Institute of Physics – Biophysics
Georg-August-University Göttingen

Prof. Dr. Silvio O. Rizzoli
Department of Neuro- and Sensory Physiology
University Medical Center Göttingen

Prof. Dr. Carolin Wichmann
Institute for Auditory Neurosciences and InnerEarLab
University Medical Center Göttingen

Prof. Bert L. de Groot, PhD
Computational Biomolecular Dynamics
Max Planck Institute for Biophysical Chemistry

Date of oral examination: 09.04.2019

Declaration

- I -

I, Marian Vache, hereby certify that my doctoral thesis entitled "Structure and Mechanics of Neuronal Model Systems – Insights from Atomic Force Microscopy and Micropipette Aspiration" has been written independently and with no other sources and aids than quoted.

Göttingen, 13.11.2019

_____

Marian Vache

Meiner Familie

"We choose to go to the moon in this decade and do the other things, not because they are easy, but because they are hard, because that goal will serve to organize and measure the best of our energies and skills, because that challenge is one that we are willing to accept, one we are unwilling to postpone, and one we intend to win, and the others, too."

John F. Kennedy

Table of Contents

Table of Contents

Abstract

Neurons of advanced animals need fast and efficient mechanisms to enable the functionality of a complex nervous system. In the life cycle of synaptic vesicles this is reflected in the endocytosis which generates new vesicles, the uptake of neurotransmitters and the fusion reaction which finally releases the neurotransmitters into the synaptic cleft to propagate the signal to the next cell. Despite considerable effort, many processes and functions in this cycle still need to be unravelled. As a contribution to that aim, this thesis describes the investigation of neuronal model systems.

In the first project, plasma membrane sheets derived from PC12 cells were investigated by atomic force microscopy to obtain topographic images for stating generally on the heterogeneity of their surface. Furthermore, it was attempted to infer the distribution of syntaxin-1 inside the membrane sheets by molecular recognition imaging employing conventional antibodies and nanobodies coupled to the tip of atomic force microscopy cantilevers. A heterogeneous structure of the membrane sheets was observed in atomic force microscopy height images. The molecular recognition imaging experiments did not yield specific interactions which could be discriminated from the vast amount of unspecific interactions and the latter were also found in control experiments. The unspecific interaction events were revealed to be distributed non-homogeneously on the membrane sheets.

In the second project the influence of the synaptic vesicle protein synaptophysin on the mechanical moduli of giant unilamellar vesicles (GUVs) and on their general behaviour was investigated by micropipette aspiration. To this end, a micropipette aspiration device was successfully implemented and the software necessary for the analysis was developed. The area compressibility moduli, the bending modulus, the maximum apparent area strain and the maximum membrane tension did not show significant differences between GUVs containing synaptophysin and those containing synaptobrevin or pure lipid vesicles. This might be attributed to the low amount of reliable data. However, GUVs containing synaptophysin are more prone to fission during aspiration. GUVs containing proteins and especially those containing synaptophysin were found to lose volume while maintaining their surface area additionally to the fission events possibly indicating the formation of a channel.

Zusammenfassung (German Abstract)

Um die Funktionalität eines komplexen Nervensystems zu ermöglichen müssen Neuronen höherer Tiere über schnelle und effiziente Mechanismen verfügen. Im Lebenszyklus synaptischer Vesikel spiegelt sich dies in der Endozytose, welche neue Vesikel generiert, der Aufnahme von Neurotransmittern und der Fusionsreaktion, die schließlich Neurotransmitter in den synaptischen Spalt freisetzt um Signale an die nächste Zelle zu übermitteln, wider. Trotz beträchtlicher Fortschritte müssen noch viele Prozesse und Funktionen in diesem Zyklus aufgeklärt werden. Als Beitrag zu diesem Ziel beschreibt diese Arbeit die Untersuchung neuronaler Modellsysteme.

Im ersten Projekt wurden aus PC12 Zellen generierte Plasmamembranfragmente mittels Rasterkraftmikroskopie untersucht um topographische Bilder zu erhalten und daraus allgemeine Aussagen über die heterogene Organisation von deren Oberflächen zu treffen. Darüber hinaus wurde versucht die Verteilung von Syntaxin-1 innerhalb der Membranfragmente mittels molekularer Erkennungsbildgebung durch konventionelle Anti- oder Nanokörper welche an die Spitze des Federbalkens eines Rasterkraftmikroskops gebunden wurden zu ermitteln. In rasterkraftmikroskopischen Höhenbildern wurde eine heterogene Struktur der Membranfragmente beobachtet. Durch die Experimente zur molekularen Erkennungsbildgebung wurden keine spezifischen Bindungen identifiziert welche von der großen Anzahl unspezifischer Wechselwirkungen unterschieden werden konnten. Letztere waren auch in Kontrollversuchen vorhanden. Es wurde aufgeklärt, dass die unspezifischen Wechselwirkungen nicht homogen in den Membranfragmenten verteilt sind.

Im zweiten Projekt wurde der Einfluss des in synaptischen Vesikeln vorkommenden Proteins Synaptophysin auf die mechanischen Moduln großer unilamellarer Vesikel (GUV) und auf deren generelle Verhaltensweise mittels Mikropipettenaspiration untersucht. Zu diesem Zweck wurde eine Mikropipettenaspirationseinheit erfolgreich implementiert und ein zur Analyse der Experimente notwendiges Computerprogramm entwickelt. Es konnten keine signifikanten Unterschiede in den Flächenkompressibilitätsmoduln, dem Biegemodul, der maximalen ersichtlichen Flächendehnung und der maximalen Membranspannung zwischen synaptophysin- und synaptobrevinhaltigen GUV oder reinen Lipidvesikeln festgestellt werden. Dies könnte in der geringen Anzahl verlässlicher Daten begründet sein. Allerdings neigen synaptophysinhaltige GUV während der Aspiration eher zu Fission. Es wurde herausgefunden, dass protein- und insbesondere synaptophysinhaltige GUV zusätzlichen zu den Fissionsereignissen auch unter Erhaltung ihrer Oberfläche Volumen verlieren was möglicherweise auf die Ausbildung eines Kanals hindeutet.

1   Introduction

The evolution of highly advanced and intelligent animals required the development of a complex and efficient nervous system. The human brain comprises about 86 billion neurons[1] and an average neocortical neuron forms approximately 7000 synapses.[2] Signals can progress with a speed of about 60 m·s^{-1} through human sensory nerve fibres.[3] Such a huge speed of transfer also needs fast processes on the cellular level. When a presynaptic action potential reaches the presynaptic membrane it takes only 1.3 ms to transfer this signal into a postsynaptic action potential.[4] This efficiency requires a sophisticated organisation of the processes within the presynaptic cell. An interplay of about 100 proteins enables the fast fusion of synaptic vesicles upon arrival of an electric signal at the presynaptic membrane.[4] Amongst these proteins syntaxin-1 and SNAP-25 residing on the cellular membrane and synaptobrevin present on synaptic vesicles form the synaptic core complex which plays the central role in the completion of the fusion reaction. When fusion is triggered by the presence of calcium ions, it takes less than 1 ms for a subset of vesicles to fuse and release their neurotransmitters.[5] For ongoing transmission the efficient retrieval of new vesicles via endocytosis is indispensable. Different routes of endocytosis are discussed. Obviously, newly endocytosed vesicles have to be refilled with neurotransmitters.[4] The basic principles of neurotransmission are known for decades. However, there are still a lot of details of these mechanisms which remain enigmatic.

Syntaxin-1[6–9] and other synaptic membrane proteins[10–12] are described to be segregated in clusters. Advantages of clustering might be a facilitated uptake of a large number of proteins at once by endocytosis or clusters might serve as a reserve pool of proteins.[13] Furthermore, synaptic plasticity, i.e. dynamic changes in the synapse which influence the amount of transmission, can be influenced by clustering of participating molecules, which is especially described for the postsynaptic cell.[14] For example, a knockout of the scaffolding protein radixin, which clusters neurotransmitter receptors extrasynaptically, in mice leads to an impairment of memory.[15] Since in the presynapse alteration of neurotransmitter release is suggested to be the main contributor to synaptic plasticity,[14] clustering of proteins participating in release is a feasible candidate. On the presynaptic side the involvement of clustering of calcium ion channels in synaptic plasticity is reported.[11] Altered synaptic

plasticity influences learning and memory and in that sense it might also have implications in diseases. As such, impairment of long term potentiation, i.e. an increase of synaptic activity which lasts over long times, is a common pathological characteristic in schizophrenia.[16]

The vesicular protein synaptophysin is also occasionally suggested to alter synaptic plasticity.[17] However, its real function is less known than that of syntaxin-1. Other studies imply, for example, a function in endocytosis.[18] After being endocytosed, the synaptic vesicles are refilled with neurotransmitters as mentioned before. Interestingly, in two independent studies a swelling of synaptic vesicles during the latter process was recognised.[19,20] However, this swelling is accompanied with an increase of the vesicle's surface area which is not compatible with the generally observed maximum possible area dilation of lipid membranes.[21,22]

The described clustering is predominantly investigated by super resolution fluorescence microscopy.[6,9,23,24] However, these techniques are prone to intrinsic errors as for some the detection of physically non-existent pseudoclusters is reported,[25] and the same proteins are described to induce varying amounts of clustering in the cell's plasma membrane when marked with different fluorescent tags.[26] An elegant way to probe the distribution of proteins in a label free approach, and thereby circumventing the concerns about fluorescent staining mentioned before, is molecular recognition atomic force microscopy. During the last two decades this method has been applied to map the distribution of biomolecules on artificial as well as cellular surfaces commonly by an antibody against the protein of interest coupled to the tip of an atomic force microscopy (AFM) cantilever.[27–30] To the best of the author's knowledge there is no report on molecular recognition AFM imaging of protein distributions on the inner leaflet of the cellular plasma membrane. Albeit molecular recognition AFM imaging is described to be a cumbersome technique as Peter Hinterdorfer, the pioneer of molecular recognition AFM imaging, and Yves Dufrêne stated that *"[…] it is fair to say that accurate data collection and interpretation remain often delicate and require strong expertise, especially when dealing with complex specimens […]"*[31], the challenge was taken to apply molecular recognition AFM to the inner leaflet of the plasma membrane of mammalian cells. To this end, in the first project described here the heterogenic organisation of plasma membrane sheets derived from neuroendocrine PC12 cells, which serve as model system for neurons, was investigated by AFM height imaging and especially by molecular recognition AFM imaging. For the latter experiments conventional IgG antibodies and nanobodies raised against syntaxin-1 were coupled to the tips of AFM cantilevers. An observation of specific clusters of syntaxin-1 by this complementary method could dispel doubts that clusters of syntaxin-1 observed by fluorescence based methods are artificially induced.

To shed more light on possible functions of synaptophysin and especially to test whether it could contribute to the large area dilation observed in synaptic vesicles, the protein was reconstituted into membranes of giant unilamellar vesicles. This model system was investigated in the second project of the present thesis, which was a collaboration with Dr. Julia Preobraschenski and Prof. Reinhard Jahn (Max Planck Institute for Biophysical Chemistry, Göttingen). In order to determine mechanical parameters of the protein-bearing membrane, such as the area compressibility modulus, micropipette aspiration of the giant unilamellar vesicles[32] was established. To this end, a micropipette aspiration device was set-up to infer the desired quantities from the fluorescence micrographs recorded during aspiration and the measured aspiration pressure. Afterwards, this device was used to probe the above mentioned giant unilamellar vesicles.

In the next chapter (chapter 2) a deeper insight into the biological background of cells, synapses and synaptophysin and a detailed description of the investigation of protein clusters and of molecular recognition AFM imaging studies is given. Chapter 3 provides an outline of the materials and methods utilised for the experiments. This includes an explanation of the instrumental methods used, important theories necessary for the interpretation of the raw data and for the determination of the desired quantities and a detailed description of the analyses performed with computer software. The results of both projects are presented in chapter 4 and their significance is discussed separately in chapter 5 together with a brief outlook for each project. Finally, in chapter 6 the thesis is summarised.

2 Biological Background and Basic Principles

2.1 The Cell

The cell is frequently called the smallest unit of life. Indeed, single cells can live autonomously and procreate, and most prokaryotes and some phylogenetically old eukaryotes are single cell organisms. Cells from multicellular organisms, even though not persistent on their own, can be sustained in culture.[33]

Cells are utilised for biophysical studies either to probe the behaviour of the native cell[34,35] or in a top-down approach to investigate the function of single compounds by their disruption[36] or knockout of the corresponding genes.[17]
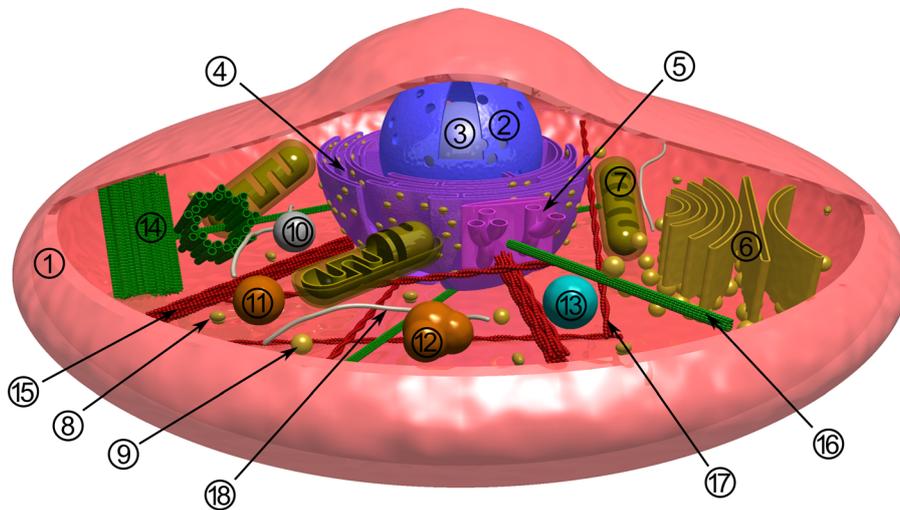
Figure 2.1: Schematic illustration of the cell as a complex and crowded entity. The numbered elements represent: 1: the plasma membrane, 2: the nuclear envelope, 3: the nucleolus, 4: the rough endoplasmic reticulum, 5: the smooth endoplasmic reticulum, 6: the Golgi apparatus, 7: mitochondria, 8: ribosomes, 9: vesicles, 10: peroxisomes, 11: late endosomes, 12: early endosomes, 13: lysosomes, 14: centrioles, 15: stress fibres, 16: microtubules, 17: actin fibres and 18: intermediate filaments.

Cells are surrounded by a plasma membrane which separates the interior of the cell, containing all the organelles and the cytoplasm, from the exterior. The interior of eukaryotic cells is a crowded entity containing numerous organelles like the nucleus, the endoplasmic reticulum, the Golgi apparatus, mitochondria, vesicles and others. A schematic representation of a eukaryotic cell and its content is given in Figure 2.1. To provide mechanical stability and to enable cellular motion, a complex filamentous network, the cytoskeleton, is present in eukaryotic cells. This network is crosslinked and connected to the plasma membrane by a variety of proteins like members of the ezrin-radixin-moesin family, for example by stress fibres, and forms a cortical membrane skeleton underneath the plasma membrane.[33] The plasma membrane consists of a complex lipid matrix with some hundreds of distinct lipid species[33] in which proteins are embedded (see Figure 2.2). These proteins comprise membrane-spanning and peripheral ones, some of which are glycosylated on the extracellular side. In red blood cells one fourth of the area inside the plasma membrane is suggested to be occupied by proteins.[37]
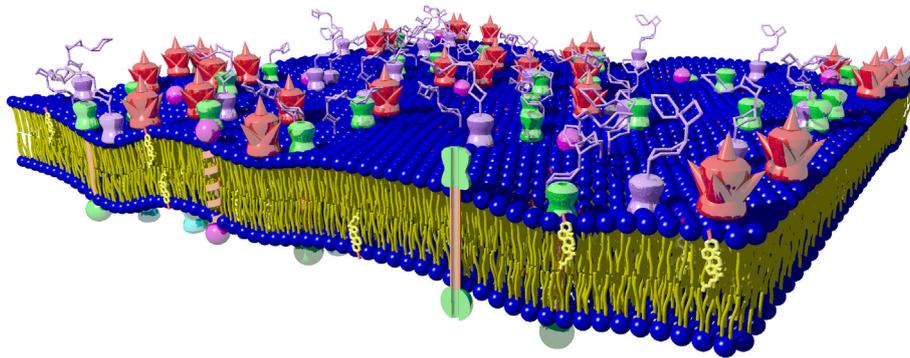
Figure 2.2: Schematic rendering of the plasma membrane. The model shown here is made up of a lipid matrix consisting of phospholipids (brownish yellow and blue), cholesterol (light yellow) and glycolipids (purple). A dense structure of peripheral (red) and integral (green and magenta) membrane proteins with their transmembrane domains (brownish orange) is shown along with glycoproteins (purple).

The possible existence of membrane inhomogeneities and protein clusters will be discussed in section 2.4 in detail.

2.2   Cellular Model Systems

As indicated in section 2.1, cells are the subject of a large number of biophysical studies. [34–36] However, their complexity can render the interpretation of the obtained data cumbersome. For facilitation and to study the influence of specific cellular compounds, cellular model systems have been developed. The most frequently used ones are based on lipid membranes alone. Depending on the spontaneous curvature of the lipids used and on the method of preparation different structures can emerge (Figure 2.3).
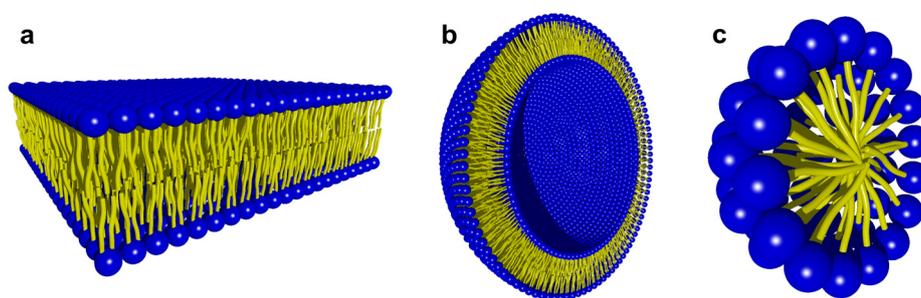
Figure 2.3: Schematic illustration of structures formed by lipid molecules. The renderings show a planar membrane bilayer (**a**), a cross-section of a vesicle (**b**) and a cross-section of a micelle (**c**). The sizes of the structures are not to scale.

Conical lipids with a bulky head-group give rise to the formation of micelles, whereas lipids of cylindrical shape cause planar bilayers. For the formation of vesicles, lipids forming a truncated cone are best suited.[38] Besides these, there are further structures which can be formed by lipids,[38] however, for biophysical model systems vesicles and planar bilayers are most frequently used, especially due to their morphological similarity to cells or at least to cellular membranes. Small unilamellar vesicles are usually produced by sonication of a suspension of lipids. These vesicles will spread on a suitable solid substrate to form a solid-supported membrane.[39,40] Electroformation of a lipid film on platinum or indium-tin-oxide electrodes leads to the generation of giant unilamellar vesicles (GUVs) with a diameter of typically 30 μm,[41,42] however, the actual size distribution depends on the conditions of the electroformation. In a bottom-up approach these lipid aggregates can be equipped with further molecules or structures as steps towards closing the gap to complete cells.[42] Namely, proteins were frequently reconstituted into the membrane[42,43] and actin networks, simulating the cytoskeleton, were polymerised inside vesicles.[43–45] Due to the relative ease of their preparation and the insight into basic principles provided by studying these model

systems, lipid model membranes are not only used to simulate entire cells, but also to investigate physical properties of membranes and their constituents.[46]

2.3   The Synapse and Neurotransmission

A synapse is a junction between a neuron and another cell, like sensory cells, endocrine cells, muscle cells or other neurons. It establishes the transmission of neuronal signals between the involved cells. In the cell which sends the signal, the presynaptic cell, an electric signal, the so-called action potential, propagates until it reaches the axon terminal. Here, voltage dependent calcium channels cause an influx of calcium ions which leads to the fusion of synaptic vesicles with the presynaptic membrane. These vesicles are filled with neurotransmitters, which are released upon fusion into the synaptic cleft, an intercellular space of about 20-50 nm distance[47], and open up ion channels on the signal-receiving, postsynaptic cell. By this means the signal is transferred from one cell to another one.[48] The exact mechanisms of both, the recycling process of synaptic vesicles and especially of the fusion reaction are still under debate but the basic principles of the situation in mammalian synapses can be summarised as described in the following paragraph.

In the axon terminal three pools of vesicles are distinguished, the reserve, the recycling and the readily releasable pool. The latter probably consists of vesicles which are primed and docked at the active zone,[49] an area of the presynaptic membrane which is enriched in some proteins, like Munc13, α-liprin and in vertebrates bassoon and piccolo. Furthermore, they are the main sites of exocytosis.[48] Upon influx of calcium ions, the fusion of the vesicles is initiated (for an illustration see Figure 2.4 (2)-(3)). Despite considerable effort to unravel the details of this mechanism, most assumptions remained the same during the past 20 years.[5,50] According to the current knowledge, it is assumed that the main player for the completion of the fusion reaction is the synaptic core complex which is made up of a coiled-coil complex of the three proteins syntaxin-1, SNAP-25 and synaptobrevin. The former two are bound to the presynaptic membrane and the latter one is incorporated in the membrane of the synaptic vesicle.[5] All three proteins share a common homologous motif, the soluble N-ethylmaleimide sensitive factor attachment protein receptor (SNARE) motif, which drives the formation of the coiled-coil complex.[5,50] Syntaxin-1 and synaptobrevin each contribute with one SNARE domain to the complex, whereas SNAP-25 provides two SNAREs. Upon interaction, the coiled-coil complex is believed to be formed and to exert a force on the

opposing membranes, bending and pulling them into close contact and thereby inducing the fusion of the proximal and the distal bilayer leaflets afterwards.[5] This basic textbook model in questioned in that way that more proteins are likely to be involved in this process, as described briefly in the following. According to a more sophisticated model, Munc18-1 and a closed conformation of syntaxin-1 assemble prior to the formation of the SNARE complex. The latter might than be partially assembled while opening syntaxin-1 by Munc13-1 and Munc18-1, leading to the primed state. Synaptotagmin, a calcium sensor, is suggested to initiate the fusion process, accompanied by the complete assembly of the SNARE complex as soon as the concentration of calcium ions is sufficiently high. In any case, the resulting *cis*-SNARE complex is probably disassembled by the protein N-ethylmaleimide sensitive factor (NSF) and soluble NSF adaptor proteins.[5]
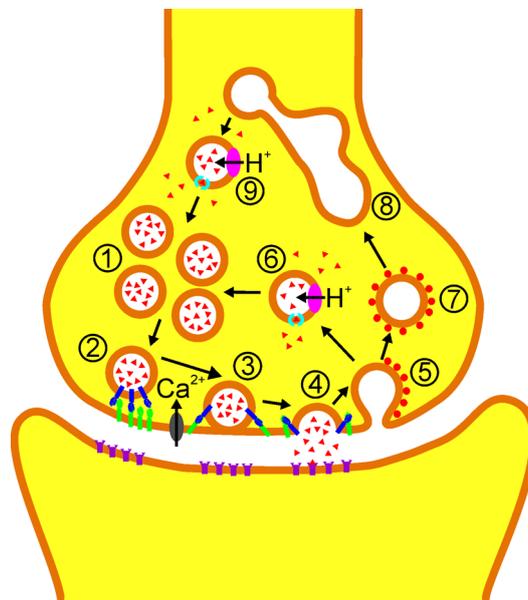
Figure 2.4: Neurotransmission and cycling synaptic vesicles. The upper structure represents the presynaptic axon terminal. Vesicles of the reserve or recycling pool (1) can dock to the membrane (2) to become part of the readily releasable pool. Upon influx of Ca^{2+}-ions through voltage gated channels (grey ellipse) the fusion reaction is initiated (3) and exocytosis (4) is mediated by SNARE-proteins (green and blue) and others. The released neurotransmitters (red triangles) can bind to postsynaptic membrane channels (violet), thereby transmitting the signal to the postsynaptic cell (bottom). Afterwards, endocytosis takes place (5), either by a fast pathway (6) or by a clathrin (red circles) dependent pathway (7), possibly by fusing with the early endosome intermediately (8). Like in the fast pathway (6) reacidification by an ATPase (magenta ellipse) and reloading with neurotransmitters by a transporter (cyan) has to take place (9) before the vesicle can substitute depleted vesicles. For clarity some structures are only shown in the steps in which they contribute considerably.

To sustain repetitive synaptic transmission and to provide the vesicles necessary for the transmission of a future signal, new vesicles have to be created by endocytosis (Figure 2.4

(5)). Afterwards, three different pathways of recycling are distinguished: two fast ways either by local recycling (Figure 2.4 (6)) or by vesicles resting in contact with the presynaptic membrane and a slow way (Figure 2.4 (7)) mediated by clathrin-coated pits and possibly via intermediate fusion with the early endosome (Figure 2.4 (8)). In any case the vesicles are reacidified by an ATPase and reloaded with neurotransmitters (Figure 2.4 (6) and (9)).[4]

The readily releasable pool is believed to be usually refilled by the fast endocytic pathways, the reserve pool is probably refilled by the slow pathway. It is assumed that the reserve pool intermixes with the recycling pool. The latter one might afterwards also replenish the exhausted readily releasable pool.[4,49] In any case the endocytosed vesicles have to be acidified again, because the resulting electrochemical gradient is believed to drive the neurotransmitter uptake (Figure 2.4 (6) and (9)), which is necessary for another round of exocytosis.[4,51]

2.4 Membrane Heterogeneity and Protein Clusters

2.4.1 A short history of the investigation of membrane heterogeneity

When the fluid mosaic model of lipid membranes was introduced by Singer and Nicolson in 1972, biological membranes were predominantly regarded as homogeneous entities, consisting of mostly not interacting lipids and proteins that only form small aggregates based on specific interactions at short distances, but are distributed homogeneously on longer scales.[52] In the following decades, however, membrane heterogeneity was investigated, primarily by the concept of so-called detergent resistant membranes.[53–55] This process resulted in the formulation of the lipid raft hypothesis, which describes lipid rafts as membrane domains that are enriched in cholesterol, glycosphingolipids, sphingomyelin and glycosylphosphatidylinositol-anchored proteins.[56] However, only six year after the formulation of the aforementioned hypothesis the conference report of an international conference focussing on lipid rafts stated that it was doubtful that detergent resistant membranes correspond to pre-existing domains in cellular membranes.[57] The current understanding of the term lipid raft does not include detergent resistant membranes anymore, the corresponding domains are believed to have a much shorter lifetime than originally thought and the suggested size is smaller as well.[58] But even this revised model is not accepted without contradiction. For example, it was shown that an artificially produced

cluster of glycosylphosphatidylinositol anchors in the outer leaflet of a cell was not capable of recruiting other glycosylphosphatidylinositol-anchored proteins to these sites.[59] Since the term lipid raft is still quite controversial it will not be used in the following to describe clusters.

Besides investigating heterogeneities in lipid distributions, in the meantime more publications focused directly on heterogeneous distributions and clustering of proteins.[11,24,60] A hurdle for the investigation of tens of nanometres sized protein clusters is the optical resolution. Early studies circumvented this problem by the use of electron microscopy along with confocal microscopy.[7] However, compared with more recent studies, confocal microscopy overestimated the size of the clusters, due to the lower spatial resolution.[7] With the establishment of super resolution optical microscopy and the development of further techniques of that class of microscopy, a new impulse was set to the investigation of protein clusters, and they became the major techniques for such investigations.[61]

A detailed overview of the investigation of protein clusters in the plasma membrane will be given in the following section, and some exemplary studies will be highlighted.

2.4.2 Protein clusters in the plasma membrane

Protein clusters are described to exist in a variety of organisms of a broad range of phylogenetically distantly related organisms like animals but also plants, fungi and bacteria.[62] By means of fluorescence microscopy many proteins of various types were found to be organised in clusters in animal cell membranes, such as receptor proteins,[63–66] the tyrosine kinase Lck or a truncated derivative,[26,67] scaffolding proteins,[63] adaptor proteins of signalling processes,[67–69] the amyloid precursor protein[70] and numerous synaptic proteins like the Drosophila protein bruchpilot,[9,11,71] the calcium sensor synaptotagmin[10] and SNARE proteins[9,12,24,72,73]. Furthermore, the investigated cells cover a wide range of species and tissues of origin, including human epithelial cells (HeLa cells),[26,66,69] rat spinal cord[63] or hippocampal neurons,[10] *Drosophila* neuro-muscular junctions,[9,11,71,74] bovine chromaffin cells[24], rat neuroendocrine cells[12,24,70,72,74] and human liver cells transfected with a synaptic protein[6].

Regardless of the protein, clusters investigated by super resolution microscopy are usually described to have a mean diameter or full width at half maximum of the intensity profile of the cluster between 50 nm and less than 200 nm. Older reports of clusters, based on studies performed by confocal microscopy, name sizes of 200 nm[7] or even 700 nm[8]. Thus, the size

of the clusters is probably overestimated due to the lower lateral resolution of the applied technique. Exemplary, Lang and Jahn investigated clusters of syntaxin-1 in rat neuroendocrine cells by confocal microscopy in 2001 and reported an upper limit of the cluster size of almost 200 nm.[7] Only six years later by using the super resolution method of stimulated emission depletion (STED) microscopy (for details see section 3.3.3.3), investigating the same molecule and using the same cell line, Lang was able to determine a cluster diameter of 50-60 nm.[75] The number of molecules involved in a single cluster was estimated several times, where by single molecule localisation microscopic techniques like photo-activated localisation microscopy (PALM) and stochastic optical reconstruction microscopy (STORM), which are based on multiple stochastic imaging of a subset of all fluorescent dyes, researchers are able to count the number of molecules.[61] However, these techniques are generally believed to only provide an estimate for the minimal number of participating molecules, but false identification of locations can also lead to an overestimation (*vide infra*).[25][25] For syntaxin-1 clusters minimum values of only ten molecules[74] and an upper limit of 90 molecules per cluster can be found.[75] Clusters of the adaptor protein Lat consist of about 40 molecules in resting T cells.[68] However, clusters can be as large as 600 molecules as reported for the postsynaptic scaffolding protein gephyrin in spinal cord neurons.[63] Besides these larger assemblies, homooligomeric clusters of only a few molecules can be found as well like in HeLa cells for the tumour necrosis factor receptor 1.[66] The existence of small-sized protein clusters is supported by coarse-grained molecular dynamics simulations of polypeptides with a single or seven transmembrane domains in an asymmetric multi compound lipid bilayer.[76]
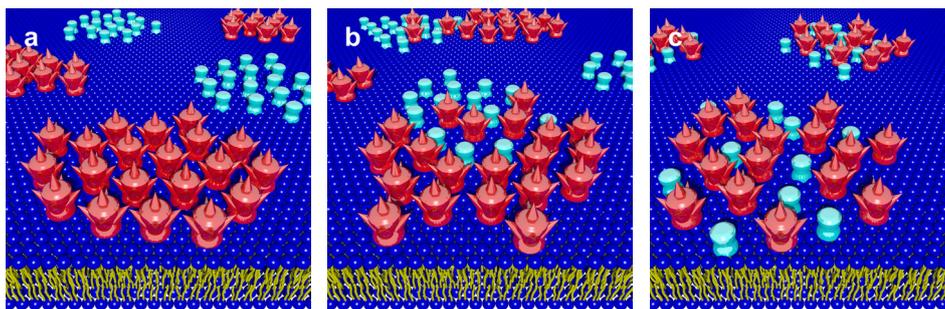
Figure 2.5: Schematic of the possible spatial relationships of two proteins to each other. Distinct proteins are shown in different colours and different shapes. The protein clusters can either be segregated (**a**), form partially overlapping clusters (**b**) or a cocluster (**c**).

A further question in cluster research is to which extend clusters of distinct proteins overlap, or in other words, if they form homotypic clusters or coclusters. Basically, three principle

situations can be differentiated: segregated homotypic clusters (Figure 2.5 a), partial overlap of clusters of different proteins (Figure 2.5 b) and coclusters (Figure 2.5 c).

As an example for overlapping clusters Triller and coworkers reported a huge colocalisation of the glycine receptor and its binding partner gephyrin in fixed spinal cord neurons.[63] STED microscopy revealed that syntaxin-1 and another member of the syntaxin family, syntaxin-4, which enables targeting of a glucose transporter to the plasma membrane,[77] form discrete clusters.[72] On the other hand, syntaxin-1 is assumed to form heterotypic coclusters with other synaptic proteins.[24,73] This clustering behaviour will be discussed in more detail in the next section which deals specifically with clusters of syntaxin-1.

The possible function of clusters might be related to their spatial organisation. It is quite intuitive that a protein which binds to a scaffold proteins, as in the case of the glycine receptor and gephyrin, follows the structural organisation of the latter one. Accordingly, syntaxin-1 needs at least the proximity to its binding partners for its physiological function. Syntaxin-4, however, does not participate in synaptic functions and can therefore operate without syntaxin-1, a contact is not needed or might even be disadvantageous. Along the same lines, clusters are suggested to serve as a supramolecular functional unit which can be taken up as a whole unit by endocytosis.[10,13] Another possible function are clusters acting as pools of inactive reserve molecules and in signalling accumulated molecules might induce a stronger local signal than loosely distributed ones.[13] Furthermore, the induction of cell polarity and tasks in information processing are discussed.[78]

As major mechanisms for cluster formation, which are suggested frequently, four distinct ones can be identified. The first relies on lipid-protein interactions, often under involvement of cholesterol, still frequently referred to as lipid rafts (see section 2.4.1).[53] A schematic of these clusters is shown in Figure 2.6 a. Next, specific protein-protein interactions might induce clustering (Figure 2.6 b). Exemplary studies supporting such a mechanism include the investigation of clustering of the amyloid precursor protein transfected in rat neuroendocrine cells. This homotypic clustering depends on the N-terminal amyloid-β domain.[70] A similar mechanism is reported for the T cell adaptor protein Lat.[68] A study by Gaus and coworkers revealed that the type of fluorescent protein fused to membrane proteins not only influences the amount of clustering itself, but also the extent to which clustering is altered by influencing the membrane order by addition of 7-ketocholesterol.[26] The latter finding indicates that clustering is probably determined by more than one of the mentioned mechanisms in a single cluster. The third one presented here was suggested by Kusumi, who proposed a mechanism by which proteins are confined in a membrane compartment formed by the membrane-skeleton (Figure 2.6 c).[58] Experimental evidence for this model is given by the finding that proteins undergo a so-called hop diffusion characterised by a fast diffusion

constant, probably inside a compartment, and a slower one, because for these steps the protein has to hop across the actin barrier to another compartment.[58] Finally, if the length of the transmembrane domain of proteins does not match the hydrophobic thickness of the lipid bilayer, they will tend to aggregate, since the exposure of hydrophobic regions of molecules to the surrounding water causes an energy penalty.[53] To reduce the resulting line tension, the proteins can aggregate, thereby reducing the overall line tension and thus the entropic cost of clustering can be compensated.[79] This hydrophobic mismatch is illustrated in Figure 2.6 d. Besides the mentioned mechanisms, others might contribute to clustering as well. For example there is evidence that actin pinning points can induce clustering as well.[80]
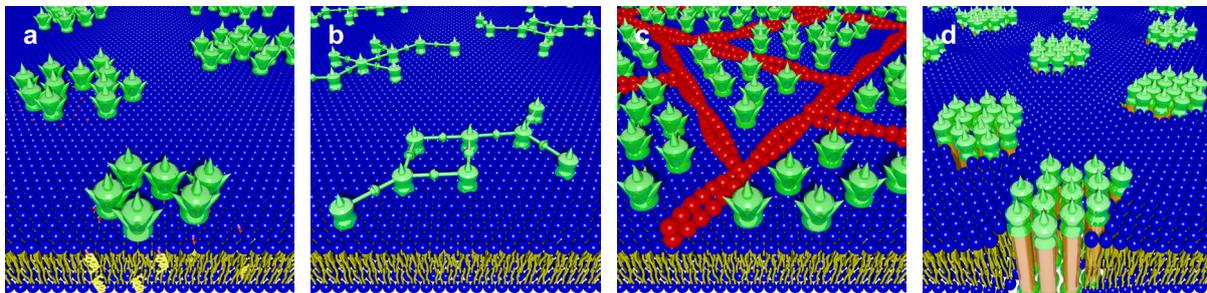
Figure 2.6: Schematic illustration of suggested mechanisms for clustering. In **a** clustering caused by protein lipid interactions is shown, here demonstrated by cholesterol enriched regions which contain the proteins. **b** illustrates a cluster generated by specific protein-protein interactions. In **c** a mechanism by which proteins enrich and thereby form clusters in membrane compartments built by an actin network is shown. In **d** clustering caused by a hydrophobic mismatch between the protein and the surrounding lipids is presented.

Studies illustrate that for some proteins clusters are organised in a super structure. For example Triller and coworkers described that a larger gephyrin cluster is composed of several subdomains.[63] Multiple clusters of the *Drosophila* protein bruchpilot are organised in local arrangements, the so-called active zone cytomatrices. One or even a few of these structures grouped in close proximity make up an active zone. So, the study reveals a multi-stage arrangement of proteins on different length scales.[71] Rizzoli and coworkers showed by STED microscopy that different proteins of a broad range of functions and structures are arranged in common general protein assemblies in membrane sheets derived from neuroendocrine cells. Notable, distinct proteins are localised preferably in a specific region of these assemblies, e.g. syntaxin-1 can be found predominantly towards the edges whereas NSF tends to accumulate at the centres.[81]

A couple of the studies cited before are based on the stochastic fluorescence imaging techniques STORM and PALM. However, these methods are prone to errors, especially caused by stochastic blinking of fluorescent proteins and organic fluorescent dyes, a process

in which fluorophores randomly switch to a dark state and turn back to the fluorescent one later.[82] Schütz and coworkers investigated the influence of blinking on cluster detection.[25] By simulations and microcontact printing they revealed that blinking leads to overcounting of the respective molecules and thereby to the detection of non-existing pseudoclusters in homogeneous distributions of molecules. Furthermore, they proposed a method to correct for this error. By that approach they were able to identify the kinase Lck to be distributed homogeneously, in contrast to other reports.[25] Before, Sauer and coworkers showed the identification of pseudoclusters by using low intensities of the laser which transfers the dyes to the non-fluorescent state in *direct* STORM experiments. This effect was predominantly observed on non-planar structures, where out-of-focus fluorescence intensity was abundant.[83] The same group identified glycoproteins to be distributed homogeneously in neuroblastoma and osteosarcoma cells.[23] Especially the fact that three dimensional structures might lead to a false-detection of clusters is of importance, as for example gephyrin is described to be organised in three dimensional domains at the postsynaptic membrane.[63] These artefacts might explain the report that identified clusters of carbohydrates appear to be larger on the apical cell membrane than on the basal one.[60] As described before, fluorescent proteins can also influence clustering.[26] Next, Zimmerberg and coworkers showed by a multicycle labelling and imaging technique that the images obtained in subsequent cycles do not perfectly overlap, which reveals stochasticity in the labelling process.[84] Protein modifications were in general described to alter the properties of proteins. This was shown by the fact that numerous proteins are sequestered to other cellular compartments when labelled with a fluorescent protein compared to labelling by immunofluorescence. Furthermore, a similar effect was identified, depending on the end of the protein to which the fluorescent protein was fused.[85] Nevertheless, it has to be acknowledged that protein clustering is, in general, a quite accepted phenomenon since other methods also suggest the presence of protein clusters. These methods comprise diffusion analyses like single particle tracking,[74,86] which, in this case, however, also depends on single molecule localisation by super resolution fluorescence microscopy, fluorescence recovery after photobleaching[6,70,75], fluorescence correlation spectroscopy,[79] electron microscopy[7], atomic force microscopy[29,87,88] and simulations[9,89].

2.4.3 Clusters of the synaptic protein syntaxin-1

Since in the present study clustering of syntaxin-1 is investigated, clusters of this protein are described in more detail in this section. Syntaxin-1 is a 288 amino acid long protein, consisting of a C-terminal transmembrane domain, followed by a short linker and the SNARE-domain. Closer to the N-terminus, the regulatory H_{abc}-domain is located, which consists of three helices that can bind reversibly to the SNARE-domain, leading to the aforementioned closed conformation of syntaxin-1. Finally, at the N-terminal end the short N-peptide is located.[5] As already indicated in the previous section, according to super resolution fluorescence microscopy studies, syntaxin-1 clusters have mean sizes of about 50-150 nm, but some are even larger, as found in a variety of cell types like mammalian central neurons, *Drosophila* neuro-muscular junctions and neuroendocrine cells.[6,9,24,73,75,86,90]. Bademosi *et al.* found only about ten molecules per cluster.[74] Other lower estimates of the number of syntaxin-1 molecules in a cluster are as low as 30 copies.[24] Sieber *et al.* discovered a maximum molecule to cluster ratio of 90 but concluded by performing corresponding simulations that a number of 75 molecules in one cluster is more reasonable.[75] By STED microscopy on average 20[75] and by *direct* STORM about 14 clusters per μm^2 were found,[90] both in rat neuroendocrine cells.

The current knowledge of coclustering of syntaxin-1 with other synaptic proteins and a potential overlap with clusters of other proteins can be described as follows. Older publications of experiments based on confocal microscopy already suggested a partial[7] or a huge[8] overlap between clusters of syntaxin-1 and those of its binding partner SNAP-25. Most studies are in agreement with this point of view,[24,73] or describe at least a preference for the same region within the discovered general protein assemblies,[81] however a study by Lang and coworkers by STED microscopy described both clusters to be in proximity to each other but still separated.[7] Notably, this difference does not depend on the cell line used, since the work done by Lang and coworkers as well as one study indicating colocalisation were both performed with rat neuroendocrine cells. Another work, which was performed with cortical neurons, even indicated the existence of a ternary cluster with Munc18-1, where the colocalisation between SNAP-25 and Munc18-1 depends on the presence of syntaxin-1.[73] Taken together, the existence of coclusters of syntaxin-1 with other proteins, especially with SNAP-25, is plausible, however still controversial.

Next, the question might arise which mechanism could be responsible for clustering of syntaxin-1. Many studies describe a protein-protein interaction by the SNARE domain as the main contributor.[72,75,91] This was, for example, indicated by a loss of colocalisation of the fluorescence signals of both proteins upon cleavage of SNAP-25 by treatment with botulinum

toxin E.[8] Milovanovic *et al.* have shown by STED microscopy and fluorescence correlation spectroscopy that the transmembrane domain of syntaxin-1 in a supported lipid membrane is capable of forming clusters on its own, without the necessity of the presence of the SNARE domain, most likely by hydrophobic mismatch.[79] Both of these findings are in agreement with a suggestion by Lang and coworkers that the transmembrane domain enables loose clustering of syntaxin-1, whereas the SNARE domain is necessary for dense clusters.[6] Lipid-protein interactions are presumably also important for the maintenance of syntaxin-1 clusters, since removal of phosphatidylinositol-4,5-bisphosphate from membrane sheets derived from rat neuroendocrine cells results in a lower amount of clustering.[92] This was confirmed by the study of Milovanovic *et al.* who found that syntaxin-1 and phosphatidylinositol-4,5-bisphosphate are colocalised in a single cluster in the same cell line. The authors furthermore revealed a cluster inducing effect of cholesterol. This is not necessarily caused by lipid-protein interactions, but was in this report attributed to the hydrophobic mismatch, since cholesterol increases the thickness of bilayers.[79] Finally, the general protein assemblies observed by Rizzoli and coworkers are also disrupted upon depletion of cholesterol.[81] Furthermore, they have shown that the size of these assemblies increases when the actin cytoskeleton is depolymerised, indicating that the membrane compartmentalisation proposed by Kusumi might also play a role in clustering of syntaxin-1.[58,81] This variety of studies which identify different contributors to syntaxin-1 clustering suggest that more than a single mechanism is responsible for the aggregation of the proteins into clusters.

Syntaxin-1 clusters were suggested to serve as docking and fusion sites for synaptic vesicles.[7] However, as the corresponding experiments were performed by confocal microscopy, the localisation of these events was not quite precise and it might be that they occurred in between clusters. That would be in agreement with other studies which describe SNARE complex formation to occur at the rim of syntaxin-1 clusters by experiments[12] and by simulations[9,90]. In agreement with that, Bademosi *et al.* found that the general anaesthetic propofol increases the cluster radius, the density and the number of syntaxin-1 molecules per cluster. As anaesthesia by propofol is manifested in a decrease in synaptic transmission, the larger clusters can explain this finding, provided that the molecules in the centre of the cluster are indeed docking incompetent.[74] Therefore, syntaxin-1 clusters might serve as a reservoir of inactive proteins.[9,12,75]

2.5 Molecular Recognition Atomic Force Microscopy

Besides fluorescence microscopy, atomic force microscopy[1] can be utilised to determine the distribution of biomolecules in a sample of interest as well. Pioneering work in this field was done by Peter Hinterdorfer, who published a technique by which the localisation of a molecule of interest is detected by a specific binding partner coupled to an AFM tip in 1996.[93] In the present thesis this method is referred to as molecular recognition atomic force microscopy (MR-AFM). For that first publication human serum albumin was adsorbed to mica and recognised in a line scan of force curves by an antibody raised against that protein which was tethered to the AFM tip. MR-AFM was therein already suggested as an imaging technique.[93] The further development of the technique was also performed by Hinterdorfer and until today most studies in that field are published by Peter Hinterdorfer, Daniel Müller and their respective former coworkers and collaborators.[31,94–96] To bind the molecules to the cantilever, a functionalisation strategy based on linker molecules designed and developed by the Gruber lab is most commonly used.[97,98]

The next step was performed in 1999 when the distribution of lysozyme, adsorbed to mica, was detected in two dimensions by antibody recognition in the group of Hinterdorfer.[27] Five years later, the probably most sophisticated technique for MR-AFM was developed: simultaneous topography and recognition (TREC) imaging.[99] In this method, an AFM cantilever oscillates in a magnetic field with an amplitude lower than the length of the linker which couples the probe molecule to the tip and with a frequency significantly lower than the resonance frequency of the cantilever. Thereby, the lowest amplitude value of the oscillating cantilever is reduced upon repulsive interaction with the surface of the sample and the highest amplitude value is reduced when the probe molecule interacts with its binding partner and thereby the cantilever is pulled towards the sample. The lowest values are used to determine the topography and fed into the feedback loop of the AFM and the highest ones provide the recognition image.[99] This mode has become one of the most commonly used.[28,29,100,101] Besides this elaborated technique, spatial information about protein distributions was obtained from recording conventional force curves inside a lateral grid, a so-called force map.[101,102] With progress in AFM technique, modern instruments are capable of recording laterally resolved force curves in high speed modes, known as force distance curve based imaging (FD-AFM), which is frequently utilised for MR-AFM as well.[30,88,103] It provides the advantage that mechanical information can be obtained simultaneously from the

---

[1] In this section a specific technique of atomic force microscopy is described without introducing the general concept of the method. For a detailed description of the physical principles, the setup and experimental methods see section 3.3.4.

recorded force curves, which provided insight into the relation between possible sites of budding of newly formed viruses and the mechanics of cells infected by a virus.[88] Furthermore, the so-called lift scan mode was introduced, where the cantilever is driven at a certain distance from the sample surface, keeping this distance constant by using the topographic information obtained from a previous height scan.[104] Creasey *et al.* revealed that the TREC mode performs best on complex biological samples, as compared with phase imaging and force maps.[101]

Initially, experiments were carried out with the molecule of interest adsorbed to mica (*vide supra*).[27,93] As the method developed, biologically more relevant samples were used, like proteins reconstituted into supported bilayers,[30,100] or even molecules residing on cells[29,87,104] and whole tissues[101] were investigated. Namely, by recognition of antibodies or hormones, the distributions of proteins being predominantly expressed in cancer cells were examined[29,104] and an enzyme which is part of aggregates formed in course of a disease was mapped on human lenses.[101] This indicates a medicinal relevance of the described technique. Recently, MR-AFM was used to map lipid domains in artificial bilayers by toxins tethered to the cantilever tip which recognise certain lipids specifically.[105] Of greater interest for biophysics might be the finding of the formation of force induced adhesion domains in yeast by Alsteens *et al.*.[87] But spatially resolved imaging of protein distributions on live cells remains a challenge.[106] When antibodies are utilised for the recognition of the molecule of interest, generally an interaction force in the range from 40 to 60 pN is observed.[28,101,102] In these cases, furthermore, a suitable control experiment is the competition by addition of free antibodies[27,101,102] or epitope bearing polypeptides[28,100] to the measuring buffer, leading to a disappearance of the binding events. By exchange of the buffer containing the binding partner to fresh buffer, the interactions were shown to reappear.[93,100] These steps confirm that the initially measured events are caused by the desired interaction rather than by nonspecific ones. This is crucial since on complex biological samples frequently appearing nonspecific events are not easily distinguished from the specific ones.[107] Other control experiments comprise the use of deficient mutants of the cell used as specimen[87] or as probe[103] (*vide infra*), other cells which do not express the target protein like healthy cells[88,102,104] and the utilisation of antibodies[87] or similar but mutated peptides[108] as probes which are not capable of binding any protein in the sample.[87]

The studies mentioned so far employed a molecule tethered to the AFM tip to probe the interaction with the molecule of interest inside the biological sample. More recently, by Müller and coworkers a virus was attached to the end of an AFM tip which recognised its binding partners expressed in modified epithelial cells.[109] By Dufrêne and coworkers *Staphylococcus aureus* bacteria were used to probe the interaction with corneocytes from the human skin.

Thereby, they were able to map the distribution of the bacterial binding partners on the corneocytes and to shed more light on the underlying molecular interactions.[103]

Finally, three inspiring publications should be described in more detail. In 2013, Pohl and coworkers published a study which describes the investigation of the mitochondrial uncoupling protein 1 reconstituted into a supported lipid membrane.[100] By TREC mode MR-AFM the proteins were detected by binding adenosine triphosphate or an antibody which was raised against the protein. As the antibody binding site is located at a protein domain facing the matrix of the mitochondrion, it is only accessible for the AFM tip when inserted into the bilayer in an orientation exposing the natively matrix oriented side to the solution, but is inaccessible when it faces the solid support. Consequently, only those proteins discovered in the topography scan which exposed the binding site of the antibody were also detected in the recognition scan, thus providing information about the orientation of every single protein. Complementary, by mapping the proteins with adenosine triphosphate tethered to the AFM tip the orientation was also unravelled. However, in this case all proteins were detected in the recognition scan because the adenosine triphosphate binding site is located inside the interior of the channel of uncoupling protein 1. But since the binding site is located closer to the one end of the channel than to the other, the size of the recognition spot represented the orientation of the protein, due to the longer free length of the linker between the antibody and the tip in the case when the short distance to the binding site is facing upwards. By a simple calculation they were furthermore able to determine the location of the binding site within the channel.[100]

In the same year, Li *et al.* investigated cells from lymphoma cancer patients.[102] By treating the cells with a fluorescent antibody against a tumour marker they were able to selectively measure on non-cultured human cancer B-cells. With the antibody rituximab linked to the AFM tip the distribution of the cell surface protein CD20 was mapped specifically by force maps. The study indicated that CD20 is organised in a non-random way on the cell surface. As healthy B-cells express CD20 as well, healthy red blood cells were investigated as negative control. Nonetheless, this study might be valuable for future investigations of this type of cancer, since CD20 is the target protein of tumour therapy by rituximab.[102]

In 2018 Danzberger *et al.* described MR-AFM imaging by the TREC mode on the *stratum corneum* of the human skin.[110] An antibody and wheat germ agglutinate was utilised to unravel the distribution of surface glycans in this tissue. The researchers discovered a heterogeneous distribution of the molecules of interest present on elevated regions of the *stratum corneum*. Furthermore, the density of glycans was drastically smaller in upper layers of the *stratum corneum*, pointing to a successive degrading process of glycans throughout the aging process of corneocytes, thereby being related to a looser contact between

corneocytes.[110] This discovery of a non-homogeneous distribution of glycans is of particular interest, since the identification of heterogeneous organisations of cell surface glycans by fluorescence microscopic approaches is highly debated.

So, these three studies provide a fascinating insight into the opportunities MR-AFM offers.

2.6 Synaptic Vesicles and their Protein Synaptophysin

2.6.1 Synaptic vesicles

As described in section 2.3, synaptic vesicles contain neurotransmitters which are released into the synaptic cleft upon arrival of a neuronal signal.[4] These tiny organelles with a mean diameter of about 40 nm are made up of a large amount of proteins. Indicatively, there are approximately 600 transmembrane domains on average inside the membrane of a synaptic vesicle, which accounts for 20 % coverage of the vesicle's surface. For comparison, the estimated number of phospholipids is only roughly ten times the number of transmembrane domains. Among these proteins, at least 13 SNARE proteins were found on synaptic vesicles, telling that these organelles are also endowed with proteins which do not have a known role in exocytosis but in other fusion steps, suggesting that synaptic vesicles might fuse with endosomes after endocytosis (see description of the synaptic vesicle cycle in section 2.3 and Figure 2.4).[111] To enable continuous signal transduction, these vesicles are reassembled repetitively[4,49] and the uptake of about 1800 transmitter molecules on average has to take place.[4,111] However, the exact mechanism of the uptake is still under debate.[51]

2.6.2 Synaptophysin

With a relative amount of 10 % of the mass of all vesicular membrane proteins, synaptophysin is the second most abundant protein in synaptic vesicle membranes, which corresponds to 32 copies per vesicle on average.[111] Synaptophysin was discovered and isolated for the first time by Jahn *et al.* in 1985.[112] The protein has a molecular weight of 38 kDa and consists of four transmembrane domains. Both termini are oriented to the cytoplasm and the transmembrane domains are connected by two long loops which are

located in the lumen of the vesicle and a short polar linker couples the second to the third transmembrane domain on the cytoplasmic side.[113] Each loop is circularised by a disulfide bond.[114]

The integrity of all of these four transmembrane domains is necessary for the translocation of the protein from the endoplasmic reticulum to the synaptic vesicles, as revealed by exchange of single or multiple transmembrane domains with those of connexin32. However, the native cytoplasmic regions are not essential for synaptophysin to leave the endoplasmic reticulum.[115] This might implicate an intrinsic curvature sensing of the transmembrane domains of synaptophysin.[18] Oligomerisation of synaptophysin molecules was reported in studies based on cross-linking experiments in combination with gel electrophoresis[114] and electron microscopy[113], which gave rise to the suggestion of the formation of non-covalent complexes up to tetramers and hexamers, respectively.

The physiological function of synaptophysin is not yet known. It is not essential to sustain life, as synaptophysin knockout mice were shown to have an unaltered chance of survival and to be fertile.[17] Exemplarily, it was suggested that synaptophysin oligomers serve as channels which might play a role in opening of the fusion pore,[113] it was described to control endocytosis[18] and to influence synaptic plasticity.[17] By investigating the latter, interestingly, neither a single knockout of synaptophysin, nor of synaptogyrin lead to a significant decrease in long term potentiation, only the simultaneous knockout of both proteins reduced long term potentiation considerably.[17] This again indicates that synaptophysin plays only a minor role or that its function can be substituted by other constituents.

3 Materials and Methods

3.1 Materials

3.1.1 Cells

Within the present thesis, molecular recognition atomic force microscopic experiments were primarily performed with PC12 cells. Primary neurons were only used for a concluding experiment.

3.1.1.1 PC12 cells

The PC12 cell line is derived from cells isolated from a phaeochromocytoma of the adrenal medulla of a rat in 1976. Due to their neuroendocrine nature, PC12 cells are endowed with vesicles containing transmitters, which can be released upon depolarisation.[116] PC12 cells are frequently employed as model systems for neuronal cells,[116] since the cell culture conditions for neuronal cells are much more time consuming.[117] For the present study three types of PC12 cells were used:[2]

1. wild type PC12 (PC12-WT-1) cells
2. a further sub-cell line of wild type PC12 (PC12-WT-2) cells
3. syntaxin-1 knockdown PC12 (PC12-Syx-KD) cells, derived from PC12-WT-2 cells

---

[2] PC12-WT-1 cells were kindly provided by Dr. Angela Gomez and Prof. Silvio O. Rizzoli (University Medical Center Göttingen). PC12-WT-2 and PC12-Syx-KD cells were originally produced[118] by and used with kind permission of Prof. Shuzo Sugita (University of Toronto) and were a donation of Sofia Elizarova and Prof. Nils Brose (Max-Planck-Institute of Experimental Medicine, Göttingen).

In PC12-Syx-KD cells syntaxin-1A und syntaxin-1B have been knocked down simultaneously. The cells were transfected with a vector containing, among others, a puromycin resistance gene.[118]

3.1.1.2 Primary neurons

Hippocampal neurons from embryonic day 18 rats were grown in coculture with astroglia cells according to an elaborated protocol suggested by Kaech and Banker.[117] The cell culture was performed by and the membrane sheets were, according to a similar procedure as for PC12 cells (see section 3.2.2), produced by the department of Prof. Silvio O. Rizzoli (University Medical Center Göttingen).

3.1.2 Cantilevers

Molecular recognition atomic force microscopy (MR-AFM) was performed with four different types of cantilevers: To couple conventional IgG antibodies to silicon nitride cantilevers, MLCT cantilevers (Bruker France, Wissembourg, France) with nominal force constants of $0.01 \, \text{N·m}^{-1}$ and $0.03 \, \text{N·m}^{-1}$ and a nominal tip radius of 20 nm were used. For nanobody coupling three types of cantilevers were employed: gold coated OBL-10 cantilevers (Bruker France, Wissembourg, France) with nominal force constants of $0.006 \, \text{N·m}^{-1}$ and $0.03 \, \text{N·m}^{-1}$ and a nominal tip radius of 30 nm, aminated cantilevers (ST-PNP-NH2, NanoAndMore, Wetzlar, Germany) with a nominal force constant of $0.08 \, \text{N·m}^{-1}$ and a tip radius of less than 40 nm and MLCT cantilevers which were, linked by a polyethylene glycol (PEG) chain ($M \approx 3400 \, \text{g·mol}^{-1}$), maleimide terminated by the manufacturer (CT.PEG.MAL, Novascan Technologies Inc., Ames, IA). For imaging purposes, non-modified MLCT cantilevers were used as well.

3.1.3 Bifunctional linkers for cantilever functionalisation

The following bifunctional polyethylene glycol linkers (Figure 2.1) were purchased from Johannes Kepler University (Linz, Austria) and used to couple antibodies (Acetal-PEG-NHS) or nanobodies (Maleimide-PEG-NHS) to cantilevers (see section 3.2.5 and Figure 3.4 and Figure 3.5 therein).
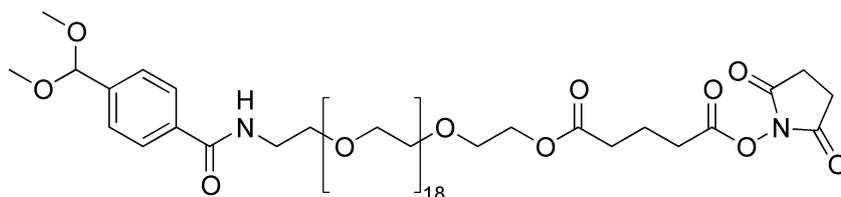
Acetal-PEG-NHS
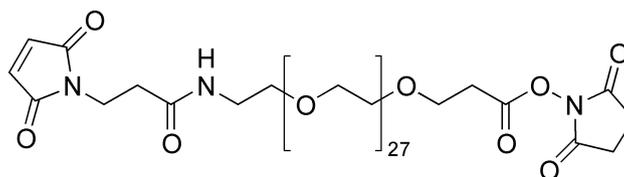
Maleimide-PEG-NHS

Figure 3.1: Structures of bifunctional polyethylene glycol linkers utilised to functionalise cantilevers with antibodies and nanobodies.

Aliquots of 1 mg were stored at −20 °C until use.

3.1.4 Nanobodies

Besides conventional IgG antibodies, camelids also express heavy-chain antibodies, which possess a short linker instead of the CH1 domain and lack the light-chains completely, as shown in Figure 3.2. Therefore, binding of the epitope is fulfilled by the single constant domain, the VHH domain, alone.[119,120] In the final stage, the VHH domain can be produced recombinantly, for example in bacteria.[119] These recombinantly produced VHH domains are called nanobodies (NBs). The main advantage of nanobodies is their small size with a molecular weight of about 15 kDa, which enables them to also recognise concave epitopes.[119,120] Furthermore, nanobodies are well soluble and show high stability.[119]
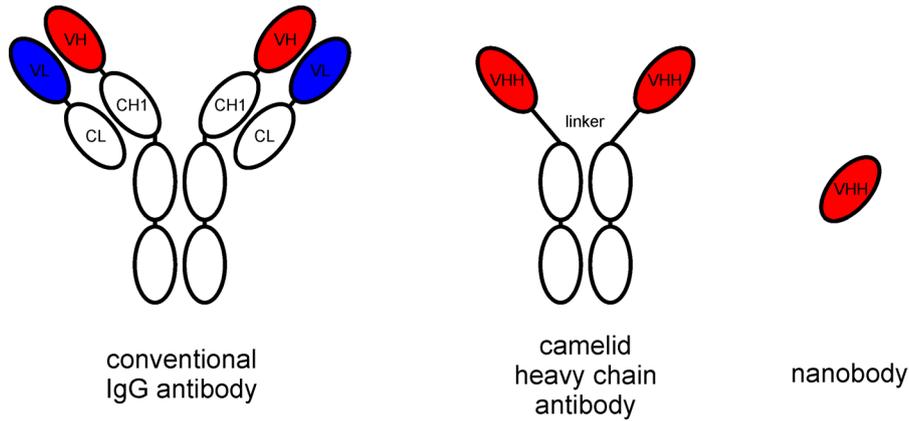
Figure 3.2: Schematic of the domain structure of conventional IgG antibodies, heavy-chain antibodies and nanobodies. Camelid heavy-chain antibodies consist of two truncated heavy chains. V stands for a variable, C for a constant domain, H denotes domains of the heavy and L domains of the light chain. Their variable VHH domain alone represents a nanobody.

For the present study nanobodies raised against rat syntaxin-1A and against mCherry were used.[3]

3.1.5 Micropipettes

For micropipette aspiration experiments, custom made glass pipettes with a nominal inner diameter of 3 µm, a bending angle of 40°, a length of 600 µm from the pointed end to the bend and an overall length of 5 cm (BioMedical Instruments, Zöllnitz, Germany) were used.

3.1.6 Ultrapure water

Except for some cleaning purposes, water was used in ultrapure quality only. Home-made ultrapure water with a electrical resistivity of 18.2 MΩ·cm at 25 °C was produced by Elix® Reference 5 (Merck, Darmstadt, Germany), Milli-Q® Advantage A10 (Merck, Darmstadt, Germany) and a 0.22 µm membrane filter (Millipak® Express 40, Merck, Darmstadt, Germany).

---

[3] The nanobodies were produced and kindly provided by Dr. Manuel Maidorn, Dr. L. Felipe Opazo Davila and Prof. Silvio O. Rizzoli (University Medical Center Göttingen).

3.1.7 Buffers and solutions

The following buffers and solutions were used for preparation and experiments. For all buffers ultrapure water was used as solvent. After the adjustment of the pH, buffers were filtered by a cellulose acetate filter of 0.2 µm pore size (Sartorius Stedim Biotech, Göttingen, Germany) and degassed under reduced air pressure thereafter.

Phosphate buffered saline (PBS)

The buffer contained 9.55 g·l^{-1} PBS Dulbecco (Biochrom, Berlin, Germany) corresponding to 137 mM sodium chloride, 2.68 mM potassium chloride, 8.10 mM sodium hydrogen phosphate and 1.47 mM potassium dihydrogen phosphate. The pH was adjusted to 7.4.

Sonication buffer

Sonication buffer was made up of 120 mM glutamic acid potassium salt (Sigma-Aldrich, Taufkirchen, Germany), 20 mM potassium acetate (AppliChem, Darmstadt, Germany), 20 mM 4-(2-hydroxyethyl)-1-piperazineethanesulfonic acid (HEPES) (Sigma-Aldrich, Taufkirchen, Germany) and 2 mM ethylene glycol-bis(β-aminoethyl ether)-*N,N,N',N'*-tetraacetic acid (EGTA) (Sigma-Aldrich, Taufkirchen, Germany). The pH was adjusted to 7.2 by a 1 M solution of potassium hydroxide in ultrapure water (Grüssing, Filsum, Germany). After filtration and degassing, the buffer was aliquoted and stored at −20 °C until use.

Buffered glucose solution

The buffer was prepared from a solution of 200 mM α-D(+)-glucose (Carl Roth, Karlsruhe, Germany), 5 mM HEPES (Sigma-Aldrich, Taufkirchen, Germany) and 0.2 mM magnesium chloride (Honeywell Specialty Chemicals Seelze, Seelze, Germany). Controlled by freezing point osmometry (Osmomat 3000, Gonotec, Berlin, Germany), the osmolarity was adjusted to (212 ± 3) mosmol·kg^{-1} by adding α-D(+)-glucose. The pH was set to 7.2. After filtration, the buffer was aliquoted and stored at −20 °C until use.

Tris buffered saline with Tween® 20 (TBS-T)

TBS-T was made up of 10 mM tris(hydroxymethyl)aminomethane (Carl Roth, Karlsruhe, Germany),150 mM sodium chloride (Carl Roth, Karlsruhe, Germany) and 0.2 % Tween® 20 (Carl Roth, Karlsruhe, Germany). The pH was adjusted to 7.4.

Further buffers and solutions which were only used in a single step of preparation or in a single type of experiment are described in section 3.2 and section 3.3, respectively.

3.2 Preparative Methods

3.2.1 Cell culture[4]

PC12-WT-1 cells were cultured in Dulbeccos Modified Eagle Medium (DMEM) containing 4.5 g·l^{-1} D-glucose and 4 mM L-glutamine additionally (Thermo Fisher Scientific, Waltham, MA), supplemented with fetal bovine serum (5 % v/v) (Biowest, Nuaillé, France) and heat inactivated donor horse serum (10 % v/v) (Biowest, Nuaillé, France) in a cell culture flask (TPP, Trasadingen, Switzerland) in a humidified cell culture incubator set to 37 °C at 7.5 % CO_2. To pass the cells, the medium was removed and 2-3 ml 0.05 %/0.02 % Trypsin/EDTA (Biochrom, Berlin, Germany) in PBS was added and incubated for 1-2 min at 37 °C. Next, the cells were resuspended in a mixture of 2-3 ml fetal bovine serum and 2 ml of the aforementioned culture medium. After centrifugation (4 min, 190 g), the supernatant was removed and the cells were resuspended in 1 ml of the above mentioned cell culture medium. Finally, the cells were seeded in a new cell culture flask. PC12-Syx-KD and PC12-WT-2 cells were treated accordingly using DMEM containing 4.5 g·l^{-1} D-glucose and L-glutamine additionally (GE Healthcare, Chalfont St Giles, United Kingdom), supplemented with fetal bovine serum (5 % v/v) and heat inactivated donor horse serum (5 % v/v). For PC12-Syx-KD 2.5 µg·ml^{-1} puromycine (Sigma-Aldrich, Taufkirchen, Germany) was added additionally.

Glass cover slips (22×22×0.13-0.16 mm^3) (MARIENFELD, Laude-Königshafen, Germany) were sterilised by incubation in ethanol *p.a.* (70 % v/v) (Sigma-Aldrich, Taufkirchen, Germany) for at least 30 min and subsequent treatment with a burner flame. After washing with ultrapure water, the glass cover slips were incubated with poly-L-lysine-hydrobromide (0.1 mg·ml^{-1}) (Sigma-Aldrich, Taufkirchen, Germany) in nuclease-free water (Thermo Fisher Scientific, Waltham, MA) for 1 h at r.t.. Afterwards, the solution was removed, the glass cover slips were dried for 1 h, washed with the appropriate cell culture medium (1×2 ml) and 2 ml of the cell suspension containing approximately 7.5·10^5 cells was added and grown for 1 d as

---

[4] Cell culture was performed by Angela Rübeling, Dr. Bastian Rouven Brückner and Dr. Tabea Oswald.

described above. For comparative syntaxin-1 immunostaining experiments (see section 4.1.6.3) two removable two-well culture inserts (ibidi, Martinsried, Germany) were placed onto PLL-coated glass cover slips and approximately $1.7 \cdot 10^4$ PC12 cells of each type were seeded in distinct wells in their appropriate medium and grown for 1 d.

For subsequent cell lysis the cells were grown for 2 d on tissue culture test plates (TPP, Trasadingen, Switzerland) in the appropriate medium.

3.2.2   Preparation of membrane sheets

Cell plasma membrane sheets were prepared to render the inner leaflet of the plasma membrane accessible to functionalised AFM cantilevers. After 1 d of cell growth, the glass coverslips were washed with 1-2 ml puromycine-free cell culture medium and transferred onto the bottom of a baker containing a filling level of about 2.5 cm ice-cold sonication buffer. Afterwards, to detach the upper part of the cells, a 0.1 s lasting ultrasonic pulse ($P \approx 50$-65 W) was applied by a tip sonicator (Sonoplus HD 2070, Bandelin, Berlin, Germany) at a distance of approximately 0.75 cm between the glass coverslip and the tip. Next, the proteins were fixed by addition of 1 ml of 4 % paraformaldehyde (Honeywell Specialty Chemicals Seelze, Seelze, Germany) and 0.2 % glutaraldehyde (Thermo Fisher Scientific, Waltham, MA) in PBS for 10 minutes on ice and additionally for 30-60 min at r.t.. The fixation agent was removed and the remains were quenched by 1 ml of a solution of glycine (0.1 M in PBS) (Sigma-Aldrich, Taufkirchen, Germany) for 15 min. Afterwards, the glass coverslips were washed with PBS (3×5 min, 2 ml each), the membrane was stained fluorescently by octadecyl rhodamine B chloride (1 µg·ml^{-1} in PBS) (Thermo Fisher Scientific, Waltham, MA) for 10 min and finally the solution was replaced by PBS. This procedure is shown schematically in Figure 3.3 and is adapted from Rizzoli and coworkers.[81]
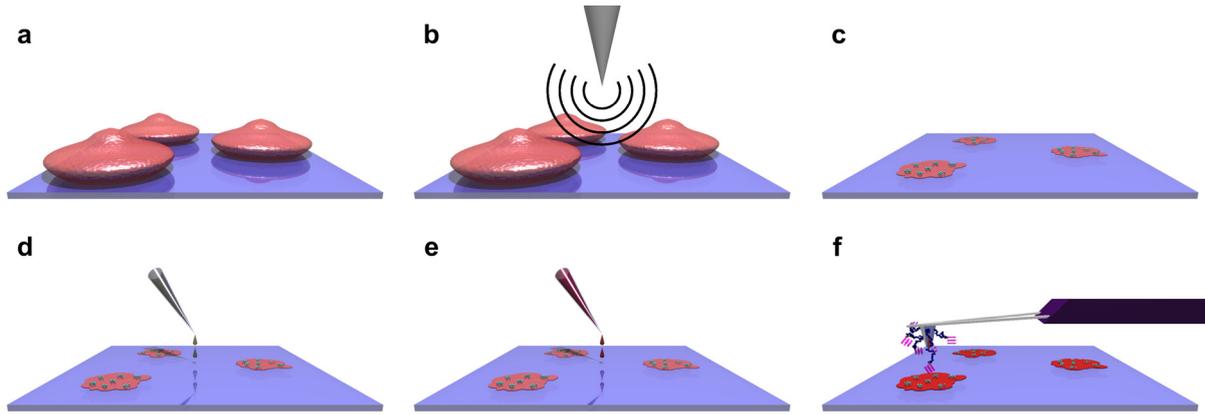
Figure 3.3: Production and treatment of membrane sheets. The cells were seeded on a PLL coated glass cover slip (**a**), membrane sheets were produced by an ultrasonic pulse (**b** and **c**), fixed by paraformaldehyde and glutaraldehyde (**d**), the membrane was stained by octadecyl rhodamine B (**e**) and afterwards an AFM measurement could be performed (**f**).

For AFM measurements, the membrane sheets were stained for actin by Alexa-Fluor®-488-phalloidin (165 nM in PBS) (Thermo Fisher Scientific, Waltham, MA) for 45 min subsequently and washed with PBS (3×5 min, 2 ml each).

3.2.3   Immunostaining of membrane sheets

Two different approaches for immunostaining were utilised.

For the evaluation of the efficiencies of distinct clones of antibodies in binding their target, the membrane sheets, where appropriate pre-stained with Alexa-Fluor®-647-phalloidin (Thermo Fisher Scientific, Waltham, MA) as described in section 3.2.2, were incubated with the respective monoclonal mouse-anti-rat-IgG antibody recognising syntaxin-1 (clone STX01 (HPC-1), abcam, Cambridge, United Kingdom or clone 78.2, Synaptic Systems, Göttingen, Germany) at a concentration of 12.5 µg·ml^{-1} in PBS containing 3 % w/v IgG-free bovine serum albumin (BSA) (Carl Roth, Karlsruhe, Germany), with at least 2.5 µg in total. After 1 h, the samples were washed with PBS (3×10 min) and the secondary antibody (Alexa-Fluor®-488-goat-anti-mouse-IgG (Thermo Fisher Scientific, Waltham, MA), 5 µg·ml^{-1} in PBS containing 3 % w/v IgG-free BSA (Carl Roth, Karlsruhe, Germany)) was coupled to the primary one for 1 h. Finally, the cover slips were washed with PBS (3×5 min).

To compare the amounts of syntaxin-1 in membrane sheets of distinct types of PC12 cells, membrane sheets were passivated with a solution of IgG-free BSA (1 % w/v) (Carl Roth,

Karlsruhe, Germany), normal goat serum (10 % v/v) (Thermo Fisher Scientific, Waltham, MA), glycine (0.3 M) (Sigma-Aldrich, Taufkirchen, Germany) and Tween® 20 (0.1 % w/v) (VWR International, Darmstadt, Germany) in PBS for 1 h. After washing with PBS (3×10 min), the samples were incubated with a mouse-anti-rat-IgG antibody against syntaxin-1 (5 µg·ml^{-1} in PBS supplemented with 1.5 % BSA) (clone STX01 (HPC-1), abcam, Cambridge, United Kingdom). The rest of the staining procedure was performed as described above.

3.2.4   Pre-use treatment of nanobodies

Nanobodies were stored at concentrations of 120 to 130 mM at −20 °C until use. A solution of tris-(2-carboxyethyl)-phosphine hydrochloride (TCEP) (10 µl, 10 mM, 50 equivalents) (Carl Roth, Karlsruhe, Germany) was added to the solution of nanobodies and incubated for 1 h on ice. Next, PBS was added to a final volume of 100 µl and the mixture was subject to size-exclusion chromatography by an Illustra™ NAP™-25 Sephadex G-25 column (GE Healthcare, Chalfont St Giles, United Kingdom), afterwards, to remove the TCEP. The loaded material was eluted with PBS: After the addition of 2.5-3.0 ml buffer, the nanobody fraction was eluted by adding further 500-800 µl PBS. Subsequently, the concentration of nanobodies was determined by ultraviolet-visible (UV-Vis) spectroscopy. The purified nanobodies were coupled to an AFM-tip (see section 3.2.5) within 4 h.

3.2.5   Functionalisation of cantilevers

To couple antibodies or nanobodies to cantilevers, different strategies of functionalisation were utilised, depending on the molecule to be bound and on the type of cantilever to be modified according to protocols adapted from the manufacturer of the bifunctional linkers described in section 3.1.3.[121]
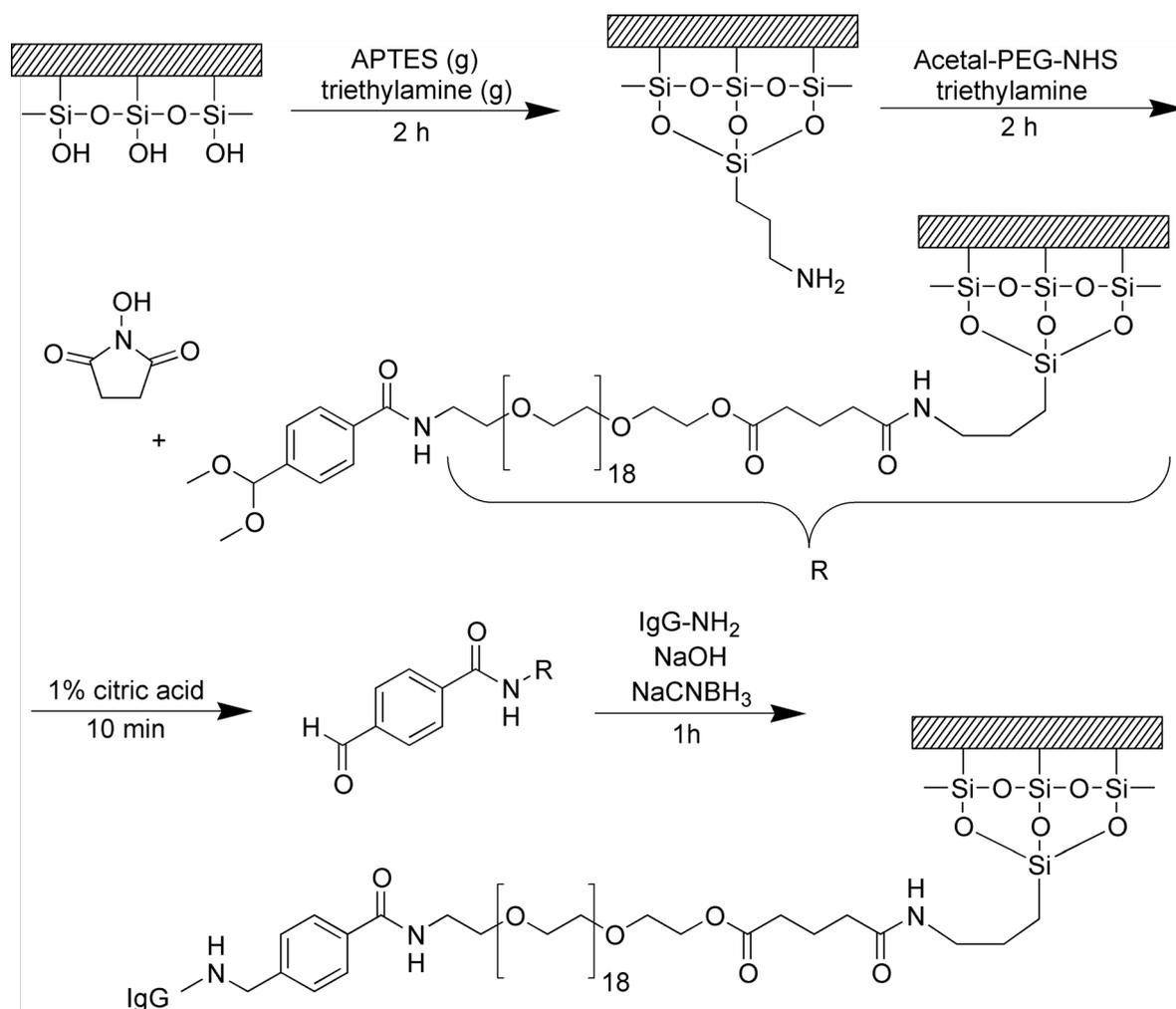
Figure 3.4: Reaction scheme of the functionalisation of silicon nitride cantilevers with IgG antibodies.

In order to bind IgG-antibodies to silicon nitride MLCT-cantilevers the probes were washed with chloroform (VWR International, Darmstadt, Germany) (3×5 min), dried in a stream of argon gas and silanised for 2 h by placing the cantilevers in a ground glass container filled with argon gas and adding 30 µl (3-amminopropyl)triethoxysilane (APTES) (abcr, Karlsruhe, Germany) and 10 µl triethylamine (Grüssing, Filsum, Germany) next to the probes. After removing the silane and the triethylamine from the glass container, the silanised cantilevers were cured for at least 2 d and not more than 7 d in an argon atmosphere. Next, Acetal-PEG-NHS (1 mg) was dissolved in chloroform (0.5 ml), supplemented with triethylamine (30 µl) and the cantilevers were deposited into the mixture. After 2 h, the cantilevers were washed with chloroform (3×10 min) and dried in a stream of argon gas. Immediately before the coupling of the antibody, the cantilevers were treated for 10 min with an aqueous solution of citric acid (1 %) (AppliChem, Darmstadt, Germany) to deprotect the aldehyde, washed with ultrapure water (3×5 min) and dried in a stream of argon gas. For the final coupling step, a solution of a monoclonal mouse-anti-rat-IgG antibody recognising

syntaxin-1 (20 µg in 100 µl PBS) (clone 78.2, Synaptic Systems, Göttingen, Germany) was pipetted onto the cantilevers and 2 µl of a freshly produced solution of 1 M sodium cyanoborohydride (Sigma-Aldrich, Taufkirchen, Germany) and 20 mM sodium hydroxide (Scharlau, Barcelona, Spain) in ultrapure water was added. After 1 h, 5 µl of a solution of ethanolamine hydrochloride (1 M, pH 8.0) (Sigma-Aldrich, Taufkirchen, Germany) in ultrapure water was added and incubated for additional 10 min. Finally, the cantilevers were washed with phosphate buffer (50 mM sodium hydrogen phosphate (AppliChem, Darmstadt, Germany) in ultrapure water, adjusted to pH 6.8) (3×5 min) and stored in PBS at 4 °C for not more than four days. The corresponding reaction scheme is shown in Figure 3.4.

To functionalise cantilevers with nanobodies, gold coated OBL-10 cantilevers were incubated with a 9:1 or in few cases with a 3:1 (v/v) mixture (when the latter mixture was used, it is noted for the corresponding experiments in chapter 4 explicitly) of 2 mM cysteamine hydrochloride (Carl Roth, Karlsruhe, Germany) and 2 mM 11-amino-1-undecanethiol hydrochloride (AUT) (Sigma-Aldrich, Taufkirchen, Germany) in ultrapure water for 2-3 d. The longer alkyl chain was used to provide conformational freedom for further functionalisation, but to prevent molecular crowding the short chain thiol cysteamine was added. Next, the cantilevers were washed with ultrapure water (3×5 min) and dried with a stream of argon gas. Afterwards, the cantilevers were coupled with a mixture of Maleimide-PEG-NHS (1 mg) and triethylamine (30 µl) in 0.5 ml chloroform inside a tightly closed ground glass container for 2 h. The probes were washed with chloroform (3×10 min) and dried with a stream of argon gas. 200 µl of the nanobody solution (0.1-3 µM, usually about 1 µM) obtained from size exclusion chromatography (see section 3.2.4) was supplemented successively with 4 µl of ethylendiaminetetraacetic acid disodium salt dihydrate (EDTA) (100 mM, pH 7.5) (Sigma-Aldrich, Taufkirchen, Germany), 10 µl HEPES (1 M, pH 7.5), 4 µl TCEP (100 mM) and 4 µl HEPES (1 M, pH 9.6) solutions in ultrapure water, strictly in the aforementioned order and by mixing thoroughly after the addition of each compound. Stocks of the four added solutions were aliquoted, frozen and stored at −20 °C and thawed individually for use. The mixture was added to the cantilevers and incubated for 3-4 h, to obtain the functionalised cantilever. After washing with PBS (3×5 min), the cantilevers were stored in PBS at 4 °C and used within three days. The reaction scheme for this functionalisation strategy is shown in Figure 3.5.
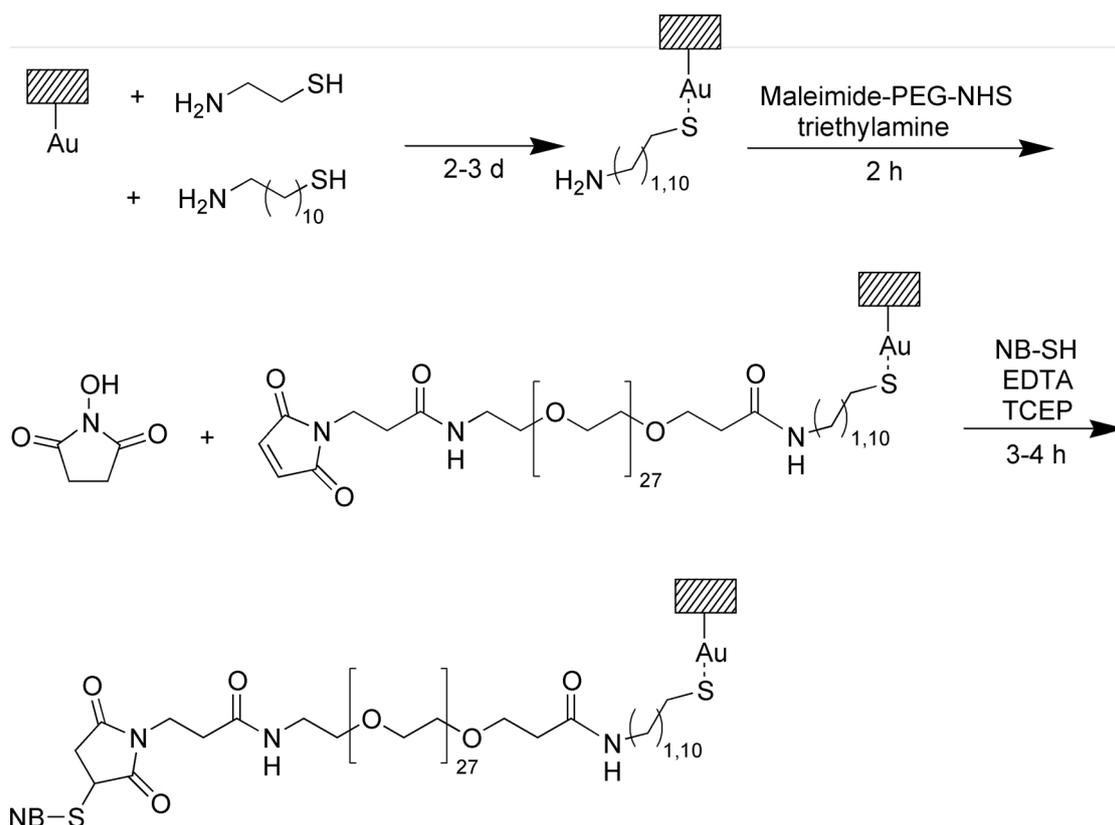
Figure 3.5: Reaction scheme of the functionalisation of gold coated cantilevers with nanobodies.

Amino-functionalised ST-PNP-NH2 cantilevers were rinsed with ethanol *p.a.* (Sigma-Aldrich, Taufkirchen, Germany) and afterwards exposed to the solution of Maleimide-PEG-NHS. Maleimide-functionalised CT.PEG.MAL cantilevers were treated with the solution of nanobodies directly as described above. All subsequent steps were performed according to the protocol for OBL-10 cantilevers.

3.2.6 Treatment of membrane sheets with proteases

Proteins present on membrane sheets were digested by adding a solution of pronase from *Streptomyces griseus* (2 mg·ml^{-1} in PBS) (Roche Diagnostics, Mannheim Germany) to the buffer above the membrane sheets (2 ml PBS), yielding a final concentration of approximately 0.67 mg·ml^{-1}. For a control experiment the same final concentration of BSA (albumin fraction V, Carl Roth, Karlsruhe, Germany) was used. Subsequent AFM imaging was performed in presence of the proteins, 20 min to 1.5 h after their addition. For MR-AFM measurements the membrane sheets were incubated for 30 min with the proteases

(approximately 0.67 mg·ml^{-1} in PBS) and afterwards the sample was washed five times with PBS.

3.2.7   Preparation of giant unilamellar vesicles

To produce giant unilamellar vesicles (GUVs) for control measurements of MR-AFM experiments and for test purposes of the setup for micropipette aspiration, 6 µl of a lipid solution of the appropriate mixture (1 mg·ml^{-1} in chloroform) (see Table 3.1) was pipetted onto the conducting sides of two indium tin oxide (ITO) glass slide (Präzisions Glas & Optik, Iserlohn, Germany) each. After evaporation of the solvent, the lipid material was mechanically distributed over an area of about 1.2×1.2 cm^2 to fit into the opening of a silicone spacer which was placed onto the ITO slides to set-up the electroformation chamber later. For the evaporation of remaining solvent, the ITO slides were placed into a drying cabinet set to 35 °C at reduced pressure for at least 2 h. Afterwards, conducting copper tapes were glued onto one end of the ITO slide opposed to their polytetrafluoroethylene (PTFE) spacers (see Figure 3.6 a). A silicone spacer was added with its opening fitting on the region covered with the lipid film of the one ITO slide. The second was laid onto the first one to obtain an enclosed chamber with two lipid films opposing each other at a distance of 2 mm, as shown in Figure 3.6 b. The electroformation chamber was fixed with three paper foldback clips (for clarity not shown in Figure 3.6 b).
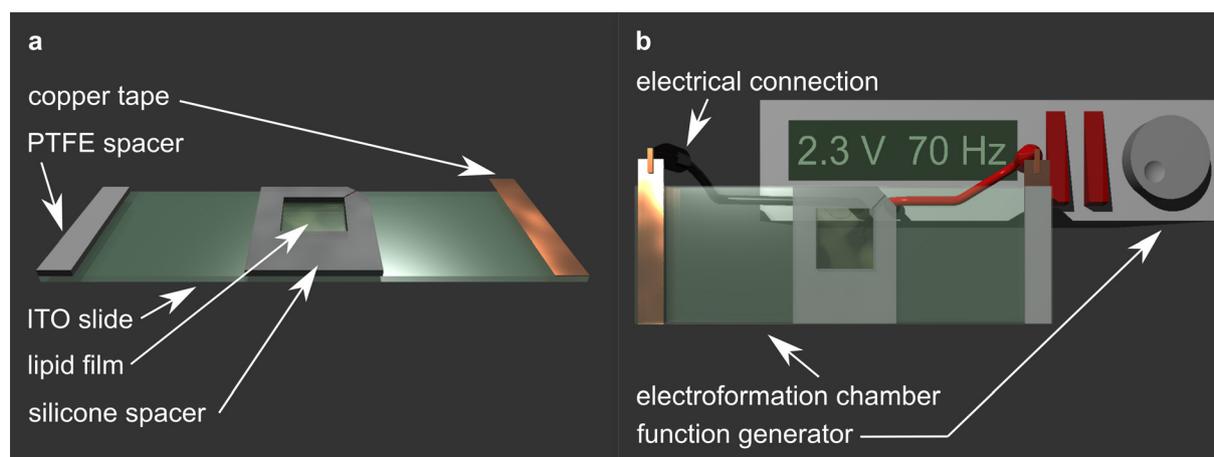
Figure 3.6: Setup of the electroformation chamber for preparation of GUVs. In **a** an ITO slide is shown with a PTFE spacer, adhesive copper tape and a silicone spacer. Inside the quadratic opening of the silicone spacer the lipid film is situated on the ITO slide. **b** depicts the assembled electroformation chamber which is electrically connected to a function generator.

The opening of the silicon spacer was filled with a solution of D(+)-sucrose (160 mM) (VWR International, Darmstadt, Germany) supplemented with 0.2 mM magnesium chloride (Honeywell Specialty Chemicals Seelze, Seelze, Germany) resulting in a final osmolarity of approximately 165 mosmol·kg^{-1}, measured by freezing point osmometry (Osmomat 3000, Gonotec, Berlin, Germany). Afterwards, the final preparation of GUVs was performed by electroformation based on its first description by Angelova *et al.*.[41] To this end, the electroformation chamber was subjected to a current of a peak-to-peak voltage of 2.3 V and a frequency of 70 Hz using a function generator (33220A, Keysight Technologies, Santa Rosa, CA) for 3-4 h. Next, the GUV dispersion was removed from the electroformation chamber and stored at 4 °C until use. In case of pure lipids vesicles, the experiments were not performed later than four days after preparation of the GUVs. Before being reused, the ITO slides and silicone spacers were cleaned with ethanol and water, sonicated for 15 min at 40 °C in an aqueous solution of Hellmanex® III (Hellma Analytics, Mühlheim, Germany), followed by three further sonication steps with ultrapure water and finally washed with ethanol *p.a.* (Sigma-Aldrich, Taufkirchen, Germany) and dried in a stream of nitrogen gas.

Table 3.1: Compositions of lipid films utilised for the production of GUVs.

Purpose	Constituents	Ratio (by moles)
preparation of GUV patches for MR-AFM	1,2-dioleoyl-*sn*-glycero-3-phosphocholine (DOPC) (Avanti Polar Lipids, Alabaster, AL) 1,2-dioleoyl-*sn*-glycero-3-phosphoethanolamine (Avanti Polar Lipids, Alabaster, AL) (DOPE) Texas Red™ 1,2-dihexadecanoyl-*sn*-glycero-3-phosphoethanolamine (TR-DHPE) (Thermo Fisher Scientific, Waltham, MA)	69:30:1
mechanical measurements by AFM[5]	DOPC 1,2-dioleoyl-*sn*-glycero-3-phospho-L-serine cholesterol 1,2-dioleoyl-*sn*-glycero-3-phosphoethanolamine-N-(cap biotinyl) TR-DHPE	63:10:25:1:1
test of micropipette aspiration	DOPC TR-DHPE	99:1
protein mechanic measurements by micropipette aspiration[5]	DOPC 1,2-dioleoyl-*sn*-glycero-3-phosphoethanolamine-N-(cap biotinyl) TR-DHPE	98:1:1

---

[5] Provided by Dr. Julia Preobraschenski (department of Prof. Reinhard Jahn, Max Planck Institute for Biophysical Chemistry, Göttingen).

GUVs used for the investigation of the influence of proteins on mechanics were prepared and provided by Dr. Julia Preobraschenski (department of Prof. Reinhard Jahn, Max Planck Institute for Biophysical Chemistry, Göttingen). Briefly, lipid films of the respective mixtures for AFM and for micropipette aspiration measurements (see Table 3.1) were swollen in a solution of the desired protein in detergent-containing buffer (sodium cholate, approximately 2 % w/v) with a protein to lipid ratio of 1:533 for synaptophysin (synaptophysin-1) and 1:133 for synaptobrevin (synaptobrevin-2). The different ratios for both proteins were used to account for the respective number of transmembrane domains and thereby obtaining the same lipid to transmembrane domain ratio in both cases. Small vesicles were prepared by the detergent removal method as described elsewhere.[122] The small vesicles were dried on platinum electrodes which were subject to electroformation thereafter to produce GUVs as published previously.[123] The electroformation was performed in solutions of D(+)-sucrose (200 mM). Proteoliposomes were used for experiments not later than one day after preparation.

3.2.8 Preparation of GUV membrane patches

To produce bilayer patches from GUVs, hereafter called GUV membrane patches (GUV-MPs), glass cover slips (22×22×0.13-0.16 mm^3) (MARIENFELD, Laude-Königshafen, Germany) were first washed with ultrapure water and cleaned by a mixture of ultrapure water, 25 % ammonium hydroxide solution (Thermo Fisher Scientific, Waltham, MA) and 35 % hydrogen peroxide (Thermo Fisher Scientific, Waltham, MA) (5:1:1 by volume) at 75 °C for 20 min. After completion, the glass cover slips were washed with ultrapure water and stored in ultrapure water until use. The GUVs were spread on the glass cover slips by incubation of 50 µl of a dispersion of GUVs with the composition described in Table 3.1 in 500 µl PBS for 50 min. Remaining GUVs were removed by buffer exchange (five times with PBS).

3.2.9 Cell lysis

PC12 cells grown for 2 d on tissue culture test plates (see section 3.2.1) were washed with PBS (2×5 ml) and lysed with 500 µl of a mixture of radioimmunoprecipitation assay buffer

(Sigma-Aldrich, Taufkirchen, Germany) and protease inhibitor (cOmplete[TM] mini EDTA free, Roche Diagnostics, Mannheim, Germany) (one tablet dissolved in 10 ml buffer) on ice for 5 min. The cells were scraped from the tissue plate and the resulting dispersion was removed and centrifuged (4000 g, 4 °C, 10 min). Afterwards, the supernatant was used as cell lysate. The overall protein concentration was determined using Pierce[TM] BCA Protein Assay Kit (Thermo Fisher Scientific, Waltham, MA) by comparison with a BSA standard according to the instructions of the manufacturer. Cell lysates were stored at −80 °C until use.

3.3 Instrumentation and Measurements

3.3.1 Western blots[6]

Cell lysates containing a protein mass of 2.5 or 5 µg were mixed with an equal volume of 2× sample buffer (175 mM tris(hydroxymethyl)aminomethane (Carl Roth, Karlsruhe, Germany), 2 % w/v sodium dodecyl sulfate (AppliChem, Darmstadt, Germany), 15 % w/v glycerine (Grüssing, Filsum, Germany), 0.3 M dithiothreitol (Carl Roth, Karlsruhe, Germany) and 0.02 % bromophenol blue (Carl Roth, Karlsruhe, Germany), pH 6.8) and the proteins were denatured at 85 °C for 5 min. These mixtures and a protein ladder (PageRuler[TM] Plus Prestained, Thermo Fisher Scientific, Waltham, MA) were loaded on sodium dodecyl sulfate polyacrylamide gels (Schägger gel, 10 % acrylamide (Carl Roth, Karlsruhe, Germany)). The electrophoresis was conducted by applying a voltage of 100-200 V (direct current) to the gel in electrophoresis buffer (100 mM tris(hydroxymethyl)aminomethane (Carl Roth, Karlsruhe, Germany), 100 mM tricine (Carl Roth, Karlsruhe, Germany) and 0.1 % w/v sodium dodecyl sulfate (AppliChem, Darmstadt, Germany)). After sufficient separation, the proteins were transferred to a nitrocellulose membrane (Bio-Rad, Hercules, CA) in blotting buffer (20 mM tris(hydroxymethyl)aminomethane (Carl Roth, Karlsruhe, Germany), 150 mM glycine (Grüssing, Filsum, Germany), 0.05 % sodium dodecyl sulfate (AppliChem, Darmstadt, Germany) and 20 % methanol (Sigma-Aldrich, Taufkirchen, Germany)) by applying a voltage of 15 V (direct current) for 1 h. The membrane was passivated by incubation with 5 % low fat dry milk (Carl Roth, Karlsruhe, Germany) in TBS-T (1 h). Afterwards, a mouse-anti-rat-IgG

---

[6] Parts of the gel electrophoresis, western blotting and luminescent staining of the blots were performed by Jonas Schäfer (department of Prof. Claudia Steinem, Institute of Organic and Biomolecular Chemistry, University of Göttingen).

antibody against syntaxin-1 (clone STX01 (HPC-1), abcam, Cambridge, United Kingdom or clone 78.2, Synaptic Systems, Göttingen, Germany) was added to 5 % low fat dry milk in TBS-T at a concentration of 0.5 µg·ml^{-1} and incubated overnight at 4 °C while gently shaking. After washing with TBS-T (3×10 min), the membrane was treated with a 1:1000 solution of a secondary goat-anti-mouse-IgG antibody comprising a horseradish peroxidase (Santa Cruz Biotechnology, Dallas, Tx) in 5 % low fat dry milk in TBS-T. After washing with TBS-T (3×20 min), luminescent staining was performed using WesternBright^{TM} Quantum (advansta, San Jose, CA) and luminescent signals were finally recorded by a chemiluminescent imaging system (Azure c300, azure biosystems, Dublin, CA).

3.3.2 UV-Vis spectroscopy

Ultraviolet-visible-spectroscopy (UV-Vis-spectroscopy) was utilised to evaluate the concentrations of nanobodies throughout the course of size exclusion chromatography, to determine the fraction with the largest amount of nanobodies and to determine the final concentration of nanobodies. A background signal of pure PBS was recorded for each series of measurements, since the sample was always dissolved in PBS. The absorbance was calculated by relating the recorded transmission signal of the sample to that of the background. For the present study a V-650 and a V-670 (Jasco, Pfungstadt, Germany) were used.

3.3.3 Fluorescence microscopic techniques

Fluorescence microscopy is frequently utilised in life sciences to image structures in tasks which cannot be fulfilled by conventional bright field light microscopy. To this end, the molecules or structures of interest are labelled with a fluorescent dye and can therefore be imaged specifically.

3.3.3.1 Epifluorescence microscopy

A standard epifluorescence microscope is equipped with a filter cube which enables transmission of a bandwidth of the initially polychromatic light containing the wavelength required for the excitation of the fluorophore and its reflection to the sample by an excitation filter and a dichroic mirror, respectively. The emitted light, which is shifted towards larger wavelengths due to the Stokes shift, is transmitted by the dichroic mirror and finally by the emission filter, leading to the detection of emitted light only.[124] A schematic of the optical path is shown in Figure 3.7.
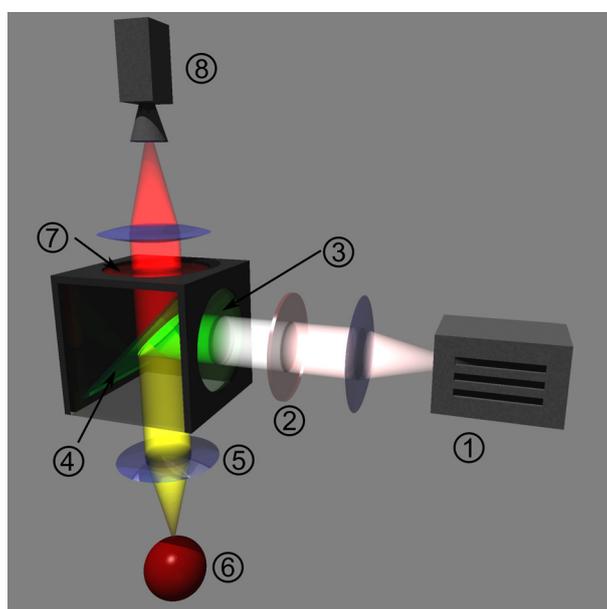
Figure 3.7: Schematic of the optical path in epifluorescence microscopy. The excitation light originating from the light source (1) is transmitted by an IR-filter (2) and an excitation filter (3) selectively before it is reflected by a dichroic mirror (4) and is focussed by an objective (5). The fluorescence light emitted by the sample (6) is transmitted by the dichroic mirror and the emission filter (7) selectively, to finally reach the camera (8).

Epifluorescence microscopy was used in conjunction with other techniques as detailed in sections 3.3.4.3 and 3.3.5.3.

3.3.3.2 Confocal laser scanning microscopy

Besides the described standard setup, another type of fluorescence microscopy is confocal laser scanning microscopy (CLSM). Here, a laser is scanned across the sample and the emission light is finally projected on a detector. Due to a pinhole located in front of the detector, light which does not originate from the focal plane does not reach the detector since it is blocked by the pinhole. Thus, only light from the focal plane is observed. The excitation light and the pinhole are focussed on the same point of the focal plane as described by the name confocal. This principle is illustrated in Figure 3.8. As a further advantage over conventional epifluorescence microscopy, CLSM is capable of reaching even a slightly higher lateral resolution.[125]
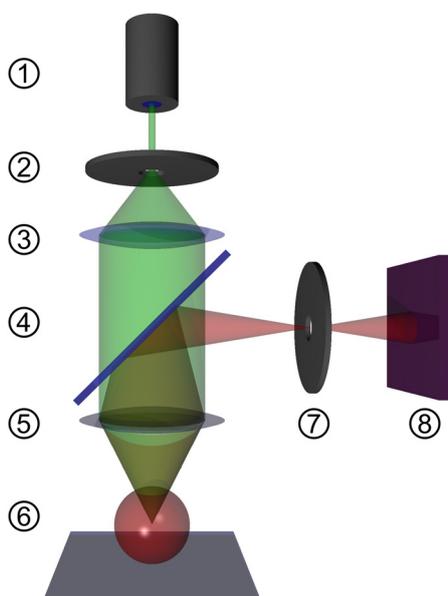
Figure 3.8: Schematic illustration of the optical path in a CLSM. The excitation light (green) originating from a laser source (1) passes through a pinhole (2), a lens (3) and a dichroic mirror (4) and is focussed by an objective lens (5) on the sample (6). The emitted light (red) is reflected by the dichroic mirror. Light from the focal plane exclusively passes through the pinhole (7) and finally reaches the detector (8). Note that by the confocal alignment the excitation light and the pinhole are focussed in the same plane of the sample.

Within the scope of this thesis an inverted and an upright CLSM were used for the investigation of binding of distinct antibodies against syntaxin-1 and for comparison of wild type and knockdown PC12 cells, respectively. For both types a FLUOVIEW FV 1200 (Olympus, Tokyo, Japan) was used, in case of the inverted one equipped with a 100× oil immersion objective (UPLFLN100XO2PH, Olympus, Tokyo, Japan), a 561 nm laser (85-YCA-020-230, Melles Griot, Bensheim, Germany), a 488 nm laser (Olympus, Tokyo, Japan)

and a microscope automation controller (ProScan™ III, Prior Scientific Instruments, Jena, Germany). The upright CLSM was equipped with a 60× water immersion objective (LUMFLN60XW, Olympus, Tokyo, Japan), a 561 nm laser (85-YCA-020-230, Melles Griot, Bensheim, Germany) and a 488 nm laser (85-BDD-020-003, Melles Griot, Bensheim, Germany).

3.3.3.3 Stimulated emission depletion microscopy

A convenient way to circumvent the diffraction limit of resolution in optical microscopy is stimulated emission depletion (STED) microscopy.
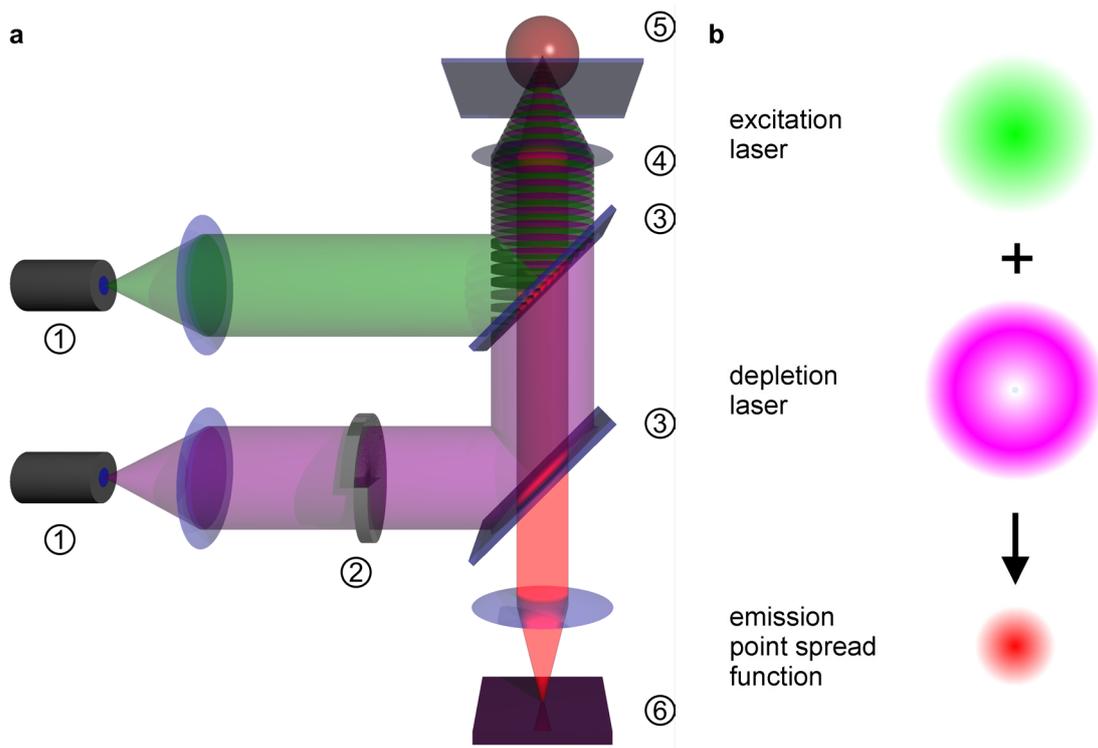
Figure 3.9: Schematic setup of a STED microscope and modulation of the point spread function. In **a** the schematic setup is shown. The excitation light (green) and the depletion light (magenta) are emitted by their respective laser sources (1). The STED laser is phase modulated by a phase plate (2). By being reflected on dichroic mirrors (3) both lasers are superimposed and focussed by an objective (4) on the sample (5). The emitted light (red) passes through the dichroic mirrors and is finally focussed on the detector (6). In **b** the overlay of the excitation (green) and the depletion (magenta) laser spot and the resulting effective emission point spread function (red) are illustrated schematically.

First described by Hell and Wichmann in 1994,[126] it uses stimulated emission by a STED laser which is partially superimposed with the illumination spot of the excitation laser in the focal plane to reduce the resulting effective point spread function. Consequently, the resolution is determined by the emerging point spread function and is therefore severalfold larger than in conventional fluorescence microscopy.[126] In contemporary setups the depletion is realised by a toroidal STED laser, which causes depletion in a radially symmetric way.[10] Figure 3.9 depicts a schematic STED microscopy setup and an illustration of the reduction of the point spread function.

For the present study a STEDYCON (Abberior Instruments, Göttingen, Germany) equipped with a 594 nm and a 640 nm excitation laser and a 775 nm STED laser was used. The STED system was used in conjunction with an inverted microscope (IX 81, Olympus, Tokyo, Japan) equipped with a 100× oil immersion objective (UPLSAPO100XO, Olympus, Tokyo, Japan).[7]

To compare STED images with atomic force microscopy, the sample was transferred to the JPK NanoWizard® 4 setup (see section 3.3.4.3) afterwards.

3.3.4   Atomic force microscopy

During the last decades atomic force microscopy (AFM) has become a multifunctional analytical tool in biophysics. Invented in the mid-1980s by Binnig, Quate and Gerber[127] and applied to record surface line profiles of a sample, it was soon used for imaging the topography of the specimen.[128,129] Later, first single molecule measurements were performed contemporaneously by Gaub and coworkers[130] who measured the force of the interaction between avidin present on the tip of the cantilever and biotin on the substrate and Colton and coworkers[131] who performed similar experiments with streptavidin on the substrate and biotin on a glass sphere attached to the cantilever. Among the diverse applications of AFM are the investigation of cellular mechanics and adhesion, imaging of single molecules, cantilevers serving as sensors for binding of biomolecules and nanolithography.[128]

---

[7] The STED microscope was kindly provided for test purposes by Abberior Instruments, Göttingen.

3.3.4.1 Working principle of the AFM

The physical principle of this technique is based on a tens of microns sized cantilever, usually equipped with a sharp tip on its bottom side, which deflects in contact with a sample. This deflection can be measured by the optical lever technique: A laser beam originating from a laser diode is reflected off the top surface of the cantilever and finally pointed on a segmented photodiode, a position sensitive detector (PSD) (see Figure 3.10).[129]
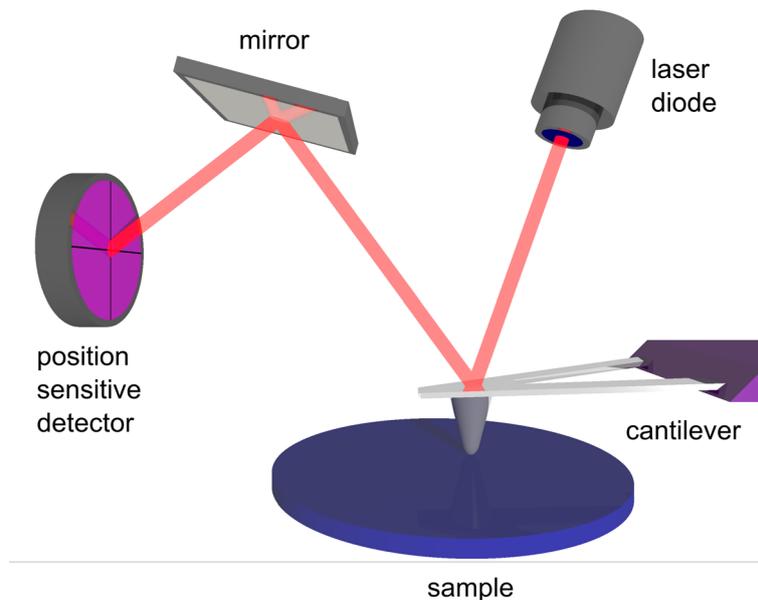
Figure 3.10: Schematic of the AFM setup. The laser beam originating from a laser diode is reflected off the upper side of the cantilever and finally pointed on a PSD. In AFMs of JPK Instruments, which were used for this thesis, the laser beam is reflected by a mirror before reaching the PSD.

To perform a force measurement, the cantilever is moved vertically towards the sample by the extension of a piezoelectric element, the so-called *z*-piezo, upon application of a voltage. When the tip of the cantilever gets in contact with a surface, the cantilever bends and as a consequence the laser beam is reflected in another angle and thus finally reaches the PSD at another location. As the PSD is a segmented photodiode, the amount of light which reaches the different segments, and therefore the current induced in the different segments, is altered. From the difference in the currents of the upper and lower segments of the PSD, the relative position of the laser spot on the detector can be inferred (see also Figure 3.10). Given that the movement of the cantilever is known by the extension of the piezoelectric element the change in current of the PSD can be related to the movement of the cantilever. Provided that the substrate is incompressible, the extension of the *z*-piezo corresponds to

the deflection of the cantilever. By relating that quantity to the readout of the PSD, the sensitivity of the setup including the cantilever can be determined. The tip-sample separation D, briefly called distance, is the sum of the extension of the piezoelectric element Z_p and the deflection of the cantilever Z_c:

$$D = Z_p + Z_c \qquad (3.1)$$

With the force constant of the cantilever k_c, the force acting on the cantilever can be calculated according to Hooke's law:

$$F = k_c \cdot Z_c . \qquad (3.2)$$

Plotting the force against the distance D yields a force-distance-curve or briefly called force curve. If a soft sample is indented, the deflection of the cantilever will change by a lower value than the z-piezo is extended, which leads to a negative distance according to the definition of equation (3.1).[132] A schematic force versus z-piezo displacement curve together with the assignment of some characteristic points, which are referred to in this thesis, is shown in Figure 3.11.
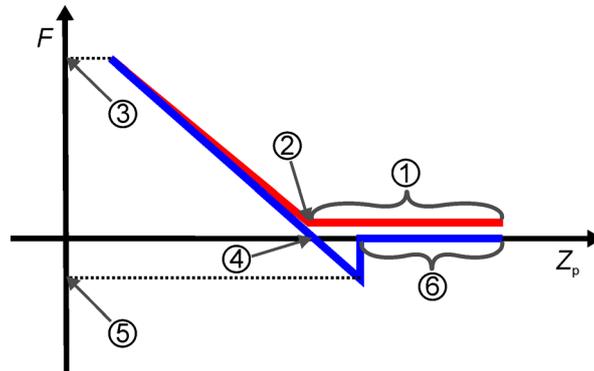
Figure 3.11: Schematic force versus z-piezo displacement curve. The approach curve is shown in red and the retraction curve in blue. The assigned points and ranges correspond to: 1: non-contact regime or baseline of the approach curve, 2: contact point, 3: maximum load force, 4: zero-force point when regarding the retraction curve, 5: maximum interaction force (except from force curves defined as a positive quantity) at the corresponding rupture distance, 6: non-contact regime or baseline of the retraction curve. Note the force discrepancy of the non-contact regimes which is due to hydrodynamic drag.

Images can be recorded by AFM upon scanning the surface of interest by two additional piezoelectric elements, one for each direction. In contact mode the tip of the cantilever stays in contact with the sample and either the force is held constant and the extension of the z-piezo necessary to maintain this force is measured or the other way around. The dynamic mode, also called tapping or intermittent contact mode, exploits the reduction of the

oscillation amplitude of a cantilever oscillating at a frequency close to the resonance frequency upon interaction with the sample. Unlike the contact mode, in this method the cantilever stays only for a very short part of the oscillation cycle in physical contact with the sample.[128] A more recently developed method is fast force-distance-curve based atomic force microscopy (FD-AFM), such as the quantitative imaging (QI[TM]) mode of JPK Instruments. Here, a force curve is recorded on every pixel of a two-dimensional grid. The advantage of the QI[TM] mode is that it combines a newly developed fast cantilever movement algorithm with a lateral rest of the cantilever at every single pixel, which enables measuring of the force distance curve at a constant speed. From these force curves the topography and multiple mechanical parameters can be extracted simultaneously.[128]

3.3.4.2 Calibration of the cantilever

The nominal force constant of a cantilever is calculated by geometric parameters and material properties. In order to obtain a more accurate measure of the force constant, the cantilever has to be calibrated. To this end, an approach-retract cycle of the cantilever is performed on a hard substrate. Thus, the extension of the piezoelectric element corresponds to the deflection of the cantilever and the sensitivity can be obtained as the slope of a plot of the extension against the voltage of the PSD.[132] Afterwards, a spectrum of the thermally induced deflection is recorded at a certain distance from the surface of the substrate. A Lorentzian curve is fitted to the peak of the power spectral density corresponding to the first mode of the resonant frequency. The integral of this curve equals the mean square displacement of the cantilever deflection. According to the equipartition theorem the following equality holds:[133]

$$\left\langle \frac{1}{2} k_c q^2 \right\rangle = \frac{1}{2} k_B T \, , \tag{3.3}$$

where q is the deflection of the cantilever, k_B the Boltzmann constant ($k_B = 1.381 \cdot 10^{-23}$ J·K^{-1}) and T the thermodynamic temperature. Thus, the force constant reads[133]

$$k_c = \frac{k_B T}{\left\langle q^2 \right\rangle} \, . \tag{3.4}$$

As the mean-square-displacement $\left\langle q^2 \right\rangle$ is known by the aforementioned integral, the force constant can be measured experimentally.

3.3.4.3 Experimental procedures

The glass cover slips containing the membrane sheets were mounted in a home-built sample chamber, which is shown schematically in Figure 3.12. This chamber comprised a lower and an upper part each containing a hole, through which the glass cover slip was accessible by the objective of an inverted epifluorescence microscope and by an AFM cantilever operated by a JPK AFM, respectively.
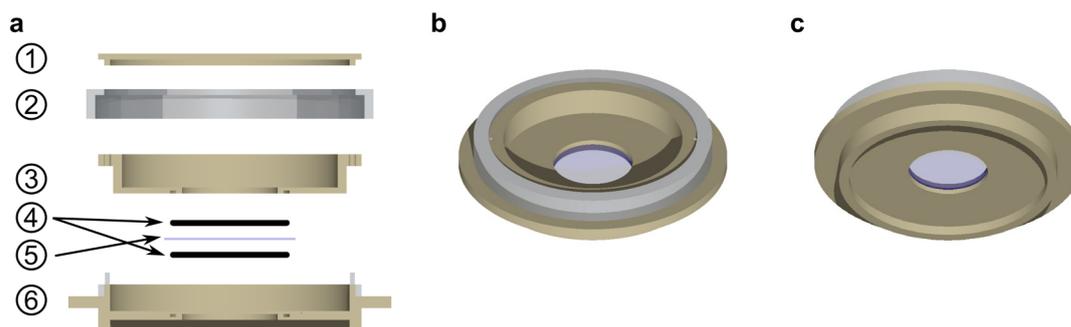

Figure 3.12: Schematic drawing of the sample chamber used for AFM measurements on membrane sheets. In **a** a cross section of the parts of the sample chamber is shown. 1: lid, 2: ring with thread for tightening, 3: upper part of the chamber, 4: O-rings for sealing, 5: glass cover slip, 6: lower part of the chamber. **b** shows a top view of the assembled chamber with a basin for buffer, accessible by the cantilever and **c** shows a bottom view of the same, demonstrating the accessibility by an objective.

Prior to use, the cantilevers were calibrated by the thermal noise method as described in section 3.3.4.2. To this end, five force curves were recorded on the stiff substrate at a maximum load force of a few nanonewton, the largest and the smallest obtained sensitivities were discarded as outliers and the mean value of the remaining three sensitivities was used for further calibration. The measured thermal noise at a distance of about 200 nm from the substrate was integrated over a few seconds and the force constant was obtained as detailed above.

A membrane sheet for the AFM measurement was chosen which shows a rather homogeneous structure in the fluorescence channel of the membrane dye and exhibits a low amount of actin (for an example see Figure 4.2 a, and d in section 4.1.1), as observed in the corresponding fluorescence channel (*vide infra*). On membrane sheets showing a region of brighter fluorescence at their edge (see Figure 4.2 a for an example), the measurement was performed in the centre of the sheet. For very large membrane sheets the right localisation of the cantilever tip was acknowledged visually by combining epifluorescence and bright field microscopy, however in most case a force map of an array of 16×16 force curves was

recorded to find an appropriate location for the following measurement in the height image. This procedure was commonly assisted by position calibration of the cantilever relative to a recorded fluorescence micrograph by the DirectOverlay™ feature provided by JPK Instruments (Berlin, Germany). For MR-AFM measurements, force-distance-curves were recorded on a 64×64 grid in a squared area of 0.25 to 5 μm edge length. Usually 1 μm edge length was used. The maximum load force was usually set to 0.2 nN. As far as not indicated otherwise, a dwell time of 0.5 s with constant height setting was applied at the point closest to the surface. Two combinations of approach and retraction speeds were used. In the first case both speeds were set to 1 μm·s⁻¹, for later experiments, in order to accelerate the measurement and to reduce lateral drift, an approach speed of 25 μm·s⁻¹ and a retraction speed of 5 μm·s⁻¹ were used. For maps recorded with a conventional IgG antibody linked to the cantilever the first combination and for ST-PNP-NH2 and CT.PEG.MAL cantilevers the second one was applied exclusively. For direct comparison of quantitative data, the same velocities were used for all categories which are compared. While recording the force curve, the cantilever was retracted 1 μm from the point of the maximum load force, as a compromise between an accurate detection of as many rupture events as possible and a fast completion of the measurement. A schematic of AFM measurements performed to detect the syntaxin-1 distribution in PC12 cell membrane sheets with nanobodies coupled to the cantilever is depicted in Figure 3.13.
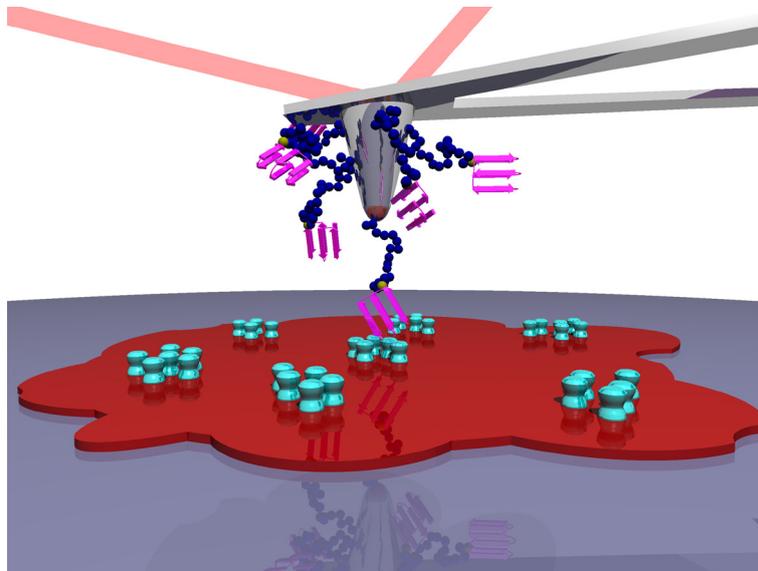
Figure 3.13: Illustration of the experimental approach of mapping protein distributions by AFM. Nanobodies (magenta) are attached to the cantilever (grey) by a polyethylene glycol linker (blue) to map the distribution of proteins (cyan) in a membrane sheet (red). The aim of these experiments is to infer the location of proteins by rupture events observed in the retraction part of the force curve. By recording force curves inside an array structure, the spatial organisation of these events is to be analysed.

Force-distance-based imaging by QI™ mode of JPK Instruments was occasionally performed with the functionalised cantilevers used for MR-AFM to evaluate the quality of the membrane sheet and the precise localisation of the recorded force map on the membrane sheet, immediately after the measurement of a force map. Those cantilevers were not used for force-distance-curve measurements afterwards. In all other cases, non-functionalised MLCT-cantilevers were used for FD-AFM imaging. For imaging purposes, a maximum load force setpoint of 0.1 nN, a cantilever retraction distance of at least 70 nm and a duration of at least 16 ms per pixel were commonly utilised in FD-AFM imaging by QI™ mode. For contact mode imaging, a maximum load setpoint of 0.1 nN and a line rate of 0.3 Hz was used.

To visualise the topography of PC12 cells, contact mode measurements were conducted with a force setpoint of 100 pN and a line rate of 0.3 Hz.

For the evaluation of mechanics of GUVs, force curves were recorded with MLCT cantilevers with a nominal force constant of $0.01 \, N \cdot m^{-1}$. 400 µl of the dispersion of GUVs (see section 3.2.7) were mixed with 400 µl of a buffer containing 150 mM sodium chloride, 20 mM HEPES and 1 mM magnesium chloride on a glass bottom Petri dish, functionalised with neutravidin as described elsewhere,[122] incubated for 20 min and filled to a final volume of 2 ml with the same buffer. For each force curve measurement the cantilever was placed above the vesicle so that the tip got in contact with the centre of the GUV during the approach. The maximum load force was set to 4 nN and the speed of both approach and retraction was $1 \, \mu m \cdot s^{-1}$. The experimental principle is shown schematically in Figure 3.14.
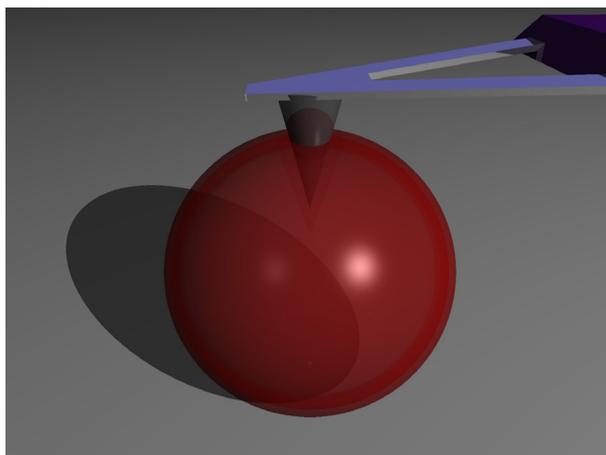
Figure 3.14: Schematic of a GUV indentation experiment. The cantilever indents the GUV in a central region to infer mechanical properties of its membrane.

For these measurements, a CellHesion® 200 AFM (JPK Instruments, Berlin, Germany) was utilised. The AFM head was mounted on an inverted microscope (IX 81, Olympus, Tokyo,

Japan) which was equipped with a 10× (UPLFLN10X2PH, Olympus, Tokyo, Japan) and a 40× (LUCPLFLN40XPH, Olympus, Tokyo, Japan) objective, a mercury-vapour lamp (U-HGLGPS, Olympus, Tokyo, Japan), a camera (XM10, Olympus, Tokyo, Japan) and a filter cube for excitation light of the wavelengths $\lambda \approx 542\text{-}578$ nm and emission light of the wavelengths $\lambda \approx 594\text{-}664$ nm (U-F49008, Olympus, Tokyo, Japan). The microscope was mounted on an active vibration isolation system (halcyonics_i4, Accurion, Göttingen, Germany) inside a home-built acoustic enclosure. For all other measurements, a NanoWizard® 4 (JPK Instruments, Berlin, Germany), mounted on an inverted microscope (IX 81, Olympus, Tokyo, Japan) which was equipped with a 10× (UPLFLN10XPH, Olympus, Tokyo, Japan) and a 40× (LUCPLFLN40XPH, Olympus, Tokyo, Japan) objective, a mercury-vapour lamp (X-Cite® SERIES 120 PC, Excelitas Technologies, Waltham, MA), a camera (XM10, Olympus, Tokyo, Japan) and filter cubes for excitation light of the wavelengths $\lambda \approx 538\text{-}582$ nm and emission light of the wavelengths $\lambda \approx 610\text{-}678$ nm (U-N41004, Olympus, Tokyo, Japan) and for excitation light of the wavelengths $\lambda \approx 460\text{-}498$ nm and emission light of the wavelengths $\lambda \approx 514\text{-}558$ nm (U-N41001, Olympus, Tokyo, Japan) was used. The microscope was placed on an active vibration isolation system (Micro 40, Accurion, Göttingen, Germany) inside a home-built acoustic enclosure.

3.3.5 Micropipette aspiration

Micropipette aspiration is a powerful technique to study the mechanical behaviour of lipid membranes from cells and artificial vesicles. Since the general setup of the system is built with standard and commercially available parts, it can be implemented in laboratories in home-built devices. The first report of micropipette aspiration of a cell by Mitchison and Swann dates back to 1954.[134] Since the early 1980s, Evans and coworkers performed pioneering work on its application to vesicles.[135,136] Throughout the following decades many studies have been published by different groups, focussing primarily on influences of different lipids and their mixtures,[22,137,138] but also new analytical procedures were described[139] and recently asymmetric membranes were investigated.[140] In general, the setup consists of a glass capillary with a micron-sized pointed end which is connected to a device capable of producing a reduced pressure, on the other end. By the reduced pressure inside the micropipette, the object of interest can be aspired. The process of aspiration is commonly observed by a microscope. Details of the setup used in the present study are presented in section 3.3.5.2.

3.3.5.1 Theory of micropipette aspiration of GUVs

If not swollen in a hypoosmotic solution, the membrane of a GUV is flaccid, exhibiting thermal undulations on length scales below the optical resolution limit. Upon aspiration, at low pressures, in the so-called low-pressure regime, these undulations are smoothed out. The entropic cost for this process is compensated by the work applied by the reduced pressure in the micropipette. When the membrane reservoirs stored in the undulations are largely depleted, further dilation of the vesicle's surface area is mainly provided by stretching the membrane, which is accompanied by an increase in the mean area per lipid molecule. In this high-pressure regime, the tension is not strictly of entropic nature any more, but mainly determined by an elastic stretch of the membrane like a two-dimensional spring. Both types of extension lead to a detectable increase of the projected membrane area inside the micropipette. In principle both effects can be investigated independently in their respective pressure regime. However, it has to be kept in mind that in a more realistic view both regimes are intermixed and that, to some extent, contributions from flattening of thermal undulations contribute to the observed increase in the projected area in the high-pressure regime.[32,139,141]

Using the Young-Laplace equation, Evans, Needham and Rawicz described the membrane tension τ of the aspired vesicle as[32,136]

$$\tau = \frac{\Delta p R_{\mathrm{P}}}{2\left(1 - \dfrac{R_{\mathrm{P}}}{R_{\mathrm{V}}}\right)},\tag{3.5}$$

where Δp is the applied pressure difference (aspiration pressure), R_{P} is the radius of the pipette and R_{V} the radius of the vesicle (see also Figure 3.15). In this model, the tension is assumed to possess a constant value over the whole surface of the vesicle,

The apparent area strain of the aspired GUVs is determined by[32]

$$\alpha_{\mathrm{app}} = \frac{A - A_0}{A_0} = \frac{\Delta L \cdot \left(\left(\dfrac{R_{\mathrm{P}}}{R_{\mathrm{V}}}\right)^2 - \left(\dfrac{R_{\mathrm{P}}}{R_{\mathrm{V}}}\right)^3\right)}{2 R_{\mathrm{P}}}.\tag{3.6}$$

Here, A is the current surface area of the vesicle, A_0 the initial area of the spherical vesicle and ΔL the length of the tubular part of the vesicle inside the micropipette.
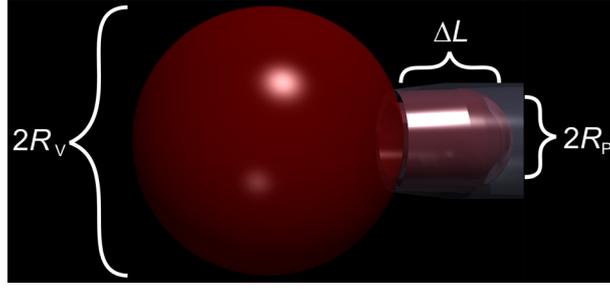
Figure 3.15: Schematic of an aspired GUV with assignment of geometric parameters. The GUV shown in red is aspired by a micropipette on the right side. R_V denotes the radius of the vesicle, R_P the radius of the pipette and ΔL is the length of the aspired membrane tube.

In the low-pressure regime, the membrane tension scales exponentially with the area dilation according to

$$\ln\left(\frac{\tau}{\tau_b}\right) = \frac{8\pi\kappa}{k_B T}\alpha_{app}, \tag{3.7}$$

where τ_b is the initial tension at $\alpha_{app} = 0$, κ is the bending modulus and $k_B T$ is the thermal energy. Thus, from a plot of the logarithm of the tension *versus* the apparent area strain in the low-pressure regime, one can deduce the bending modulus.[32]

In the high-pressure regime, the tension scales linearly with the apparent area strain

$$\tau = K_{app} \cdot \alpha_{app}, \tag{3.8}$$

where the apparent area compressibility modulus K_{app} can thus be determined from a linear fit of the tension as a function of the apparent area strain.[32]

To correct for the influence of smoothed thermal undulations on the determined area strain in the high-pressure regime, Evans and coworkers introduced a procedure by which each area strain value α_{app} is corrected by a logarithmic contribution of the corresponding tension τ.[141]

$$\alpha_{dir} = \alpha_{app} - \frac{k_B T}{8\pi\kappa}\ln\left(\frac{\tau}{\tau(1)}\right) \tag{3.9}$$

Here, $\tau(1)$ is the first tension value in the high-pressure regime and α_{dir} is referred to as direct area strain.

By that notion, the direct area compressibility modulus K_{dir} can be calculated similarly to eq. (3.8):

$$\tau = K_{dir} \cdot \alpha_{dir} \tag{3.10}$$

3.3.5.2 Setup of the micropipette aspiration device

For the present study, a micropipette aspiration device was assembled from purchased and home-built parts.
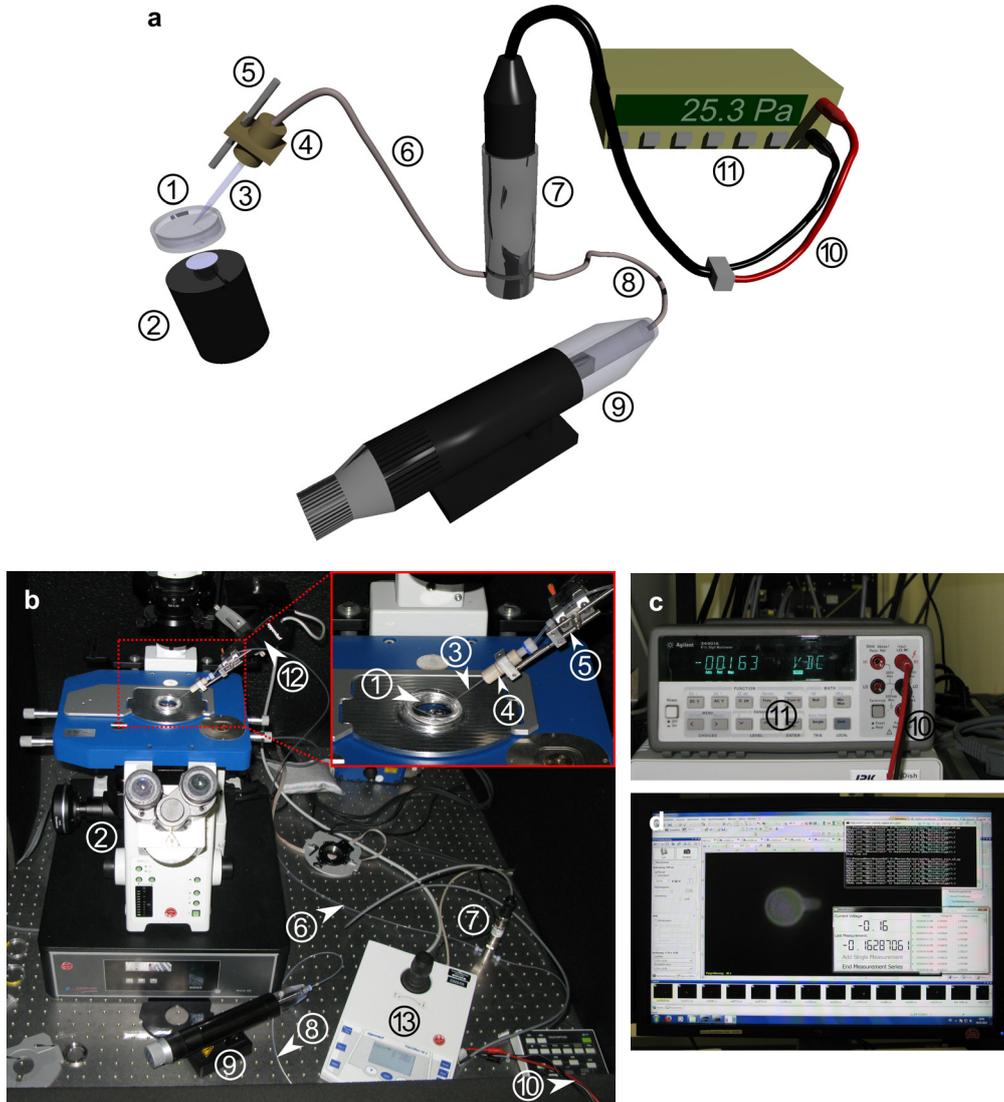
Figure 3.16: Setup of the micropipette aspiration device. a depicts a schematic of the setup, **b-d** show photographs of the self-assembled system. The inset in **b** is a detailed photograph of the region indicated by the red dashed box in the main figure. The sample (1) is observed by a fluorescence microscopic system (2). The micropipette (3) is connected to an adapter (4) which is fixed by a connection (5) which mechanically connects the micropipette to the micromanipulator (12, only shown in **b**). An air-filled tube (6) connects the micropipette to the pressure transducer (7). By a partially oil-filled second tube (8), the latter is connected to a microinjector (9) which is used to generate the reduced pressure. The voltage of the pressure transducer is transferred by an electrical connection (10) to a voltmeter (11 in **c**) which is finally read out by a computer (**d**). Like the micromanipulator itself, its controller (13) is only shown in **b**.

To produce a suction pressure, a hydraulic, manual microinjector (CellTram® vario, Eppendorf, Hamburg, Germany) was used (Figure 3.16 (9)). By a fitting tube (Eppendorf, Hamburg, Germany) (Figure 3.16 (8)) the suction pressure was transferred to a pressure transducer (PMX459-350HV(10V), OMEGA Engineering, Deckenpfronn, Germany) (Figure 3.16 (7)) and by a second tube (Figure 3.16 (6)) to a home-build adapter (Figure 3.16 (4)), which was capable of fixing the glass pipettes (Figure 3.16 (3)) (see section 3.1.5) and thereby finally transferring the aspiration pressure to the sample (Figure 3.16 (1)). To move the glass micropipette, a micromanipulator (InjectMan NI 2, Eppendorf, Hamburg, Germany) was utilised (Figure 3.16 (12) and (13)). The output voltage of the pressure transducer was detected by a multimeter (34401A, Keysight Technologies, Santa Rosa, CA) (Figure 3.16 (11)) and the data was transferred to a computer and saved as delimited text file by a program written in Python 2.7 (Python Software Foundation, Beaverton, OR) by Filip Savić (Institute of Physical Chemistry, University of Göttingen). Figure 3.16 depicts the described setup by photographs and by a schematic drawing. The setup was mounted on the same microscope used for AFM measurements of membrane sheets (see section 3.3.4.3).

3.3.5.3 Experimental procedure

To prevent adhesion to the inner wall of the micropipette and spreading of the GUVs, micropipettes were incubated in a solution of BSA (0.1 mM in glucose solution according to that used for the respective measurement) (albumin fraction V, Carl Roth, Karlsruhe, Germany) over night. Prior to the measurement, the micropipettes were placed in BSA-free glucose solution for at least 3 h to remove BSA from the solution inside the micropipettes.

3 ml of buffered or pure isoosmolar glucose solution in a cell culture Petri dish (TPP, Trasadingen, Switzerland) was placed onto the microscope stage in a home-built stage insert inducing a 7° or 9° tilt of the Petri dish to prevent a contact of any part of the micropipette except of its tip with the bottom of the Petri dish. 80-100 µl of the GUV dispersion was added. Controlled by bright field microscopy, the micropipette was approached to an appropriate GUV. Next, a slight suction pressure was applied to the micropipette and the pressure values were started to be recorded continuously. As soon as a vesicle was aspired, fluorescent micrographs showing the fluorescence of the GUV membrane were recorded at a rate of 0.5 Hz and commonly with 100 ms exposure time through the 40× objective. To determine mechanical moduli, the pressure difference was increased successively and held constant for at least 10 s to record not less than five images. This procedure was usually repeated

until the vesicle ruptured or until it was completely aspired. For constant pressure experiments, after the initial aspiration of a GUV a medium initial pressure was set and kept constant until lysis or complete aspiration of the vesicle occurred or up to 20 min.

3.4   Data Analysis

3.4.1   Analysis of western blots

For visualisation, images of western blots were processed using ImageJ 1.48v[142] (National Institutes of Health, Bethesda, MD). The image of the luminescent bands of the sample and the marker image were overlaid by a sum projection. Where appropriate, the resulting image was flipped horizontally and the lanes were moved and interchanged horizontally without changing the position of the bands in the direction of the mass-axis.

For comparison of the intensities of bands, a rectangular region of interest (ROI) around each band was chosen, each with the same size. Two regions of interest of the same size were chosen in the lane of the marker, therefore containing only noise in the luminescence channel. These data served as background signal. With Python 2.7 (Python Software Foundation, Beaverton, OR) the grey scale range of the ROIs was inverted, the intensity was integrated over the whole ROI, the obtained value was subtracted by the mean of the integrals of the inverted background ROIs and the ratio of the integrated and background corrected intensity of the band and the mean of the integrated and background corrected intensities of a reference sample was calculated.

3.4.2   Processing of fluorescence micrographs

Fluorescence micrographs were merely processed by adjusting the maximum and minimum values of the colour scale, converting the greyscale images to the green or magenta channel and overlaying them. These processes were performed using ImageJ 1.51f (National Institutes of Health, Bethesda, MD).

3.4.3 Fluorescence-based analysis of the syntaxin-1-level in membrane sheets

To analyse the data of comparative immunostaining of wild type and knockdown PC12 cell membrane sheets (see section 3.2.3), a self-written Python 2.7 (Python Software Foundation, Beaverton, OR) script was utilised. First, a region of interest containing a single membrane sheet was chosen in the channel of the fluorescence of the membrane dye. Only membrane sheets which might as well have been used for molecular recognition AFM studies were chosen for this analysis. Figure 4.3 depicts a representative example of a membrane sheet which was used for the analysis and another one which was discarded. The greyscale image of the membrane signal inside the ROI was binarised by the Otsu algorithm implemented in the Python package scikit-image[143], followed by a morphological closing and an opening algorithm of the same package. Calculating the sum of the white pixels gives a relative measure of the area of the membrane sheet. For the signal of the fluorescence excited by the 488 nm laser, corresponding to the fluorescence of the secondary antibody, a background correction was applied by subtracting the mean intensity of a second ROI from each pixel. This ROI was chosen at a region close to the corresponding membrane sheet which did not show any further fluorescence apart from noise. Integrating the background corrected signal over the whole area of the ROI yielded the overall amount of syntaxin-1. This signal was divided by the relative membrane area to obtain a normalised value accounting for the syntaxin-1 level per unit area of the membrane sheet.

3.4.4 Processing of AFM images

AFM images were processed by the software of the manufacturer of the AFM (JPK Data Processing 6.0, JPK Instruments, Berlin, Germany). For all images at least a background plane was subtracted from the raw image. If necessary, linear fits were subtracted from each line independently, first by regarding all values of the respective line and, if necessary, afterwards by only taking the lowest 70 % of the height values into account. Finally, up to four lines of the scan were replaced by the mean of the neighbouring lines to remove erroneous lines.

3.4.5   Analysis of force curves

First, the value of the z-piezo extension was corrected for the deflection of the cantilever by the data analysis software of the AFM manufacturer (JPK Data Processing 6.0, JPK Instruments, Berlin, Germany) to obtain values of the tip-sample-separation (see eq. (3.1)). Further analysis of force curves was performed in MATLAB R2014a (MathWorks, Natick, MA) by software written by Dr. Ingo Mey (Institute of Organic and Biomolecular Chemistry, University of Göttingen). With that software, first a baseline correction was performed by fitting a straight line to the data in the non-contact regime and subtracting the resulting function from all data points. The zero-distance-value was set to the data point of the retraction force curve which has the first absolute force value smaller than 0.5 times the standard deviation (SD) of the baseline fit. Peaks were detected if the difference of the forces of a local minimum and the closest local maximum exceeded a threshold value, which was usually set to 40 pN. Finally, the peak with the most negative force value was assigned as the maximum interaction force and as the rupture distance. The results of this automated analysis were checked for all force curves and, if necessary, corrected manually. Except from force curves themselves, the maximum interaction force is defined as a positive quantity in this thesis.

Whenever the presence of a binding event could not be determined from the force curve, the corresponding curve was discarded from further analysis and no interaction event was assigned to the map of spatial distribution of interaction events, which usually accounted for less than 2 % of all force curves. The same holds for other curves with shapes unlikely to represent a desired interaction event, namely for events with an extraordinary slow decline of the force to the baseline (Figure 3.17 a), for roundish courses of the force around the maximum interaction force (Figure 3.17 b) and for peaks located far within the contact regime ($F \approx 100$ pN or larger), as shown in Figure 3.17 c. The latter case might correspond to a desired interaction event. However, it can be explained by a binding molecule tethered at an elevated position of the tip of the cantilever such that the bond ruptures when the tip is still in contact with the sample. Therefore the corresponding binding partner is probably located farther away from the assigned position in the map and therefore leading to errors in location, if not discarded (see schematic drawing in Figure 3.17 f). Furthermore, only peaks with a magnitude distinct from the baseline level of force were regarded. Peak like events with a magnitude around baseline noise were discarded (Figure 3.17 d). Finally, force curves with bumps in the contact regime (Figure 3.17 e), which often appeared in subsequently recorded force curves, do not seem to represent a specific interaction and were therefore not used for

further analysis. All these evaluations were performed manually. In the following, the term events refers to the detected and not discarded rupture events.
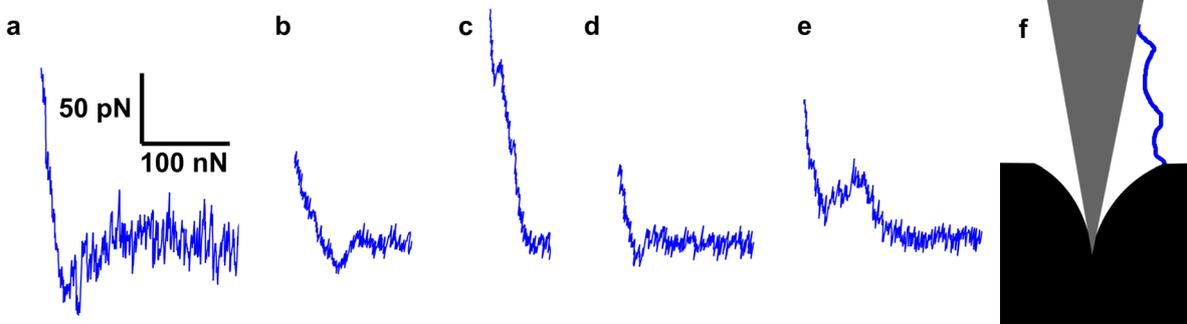
Figure 3.17: Exemplary discarded force curves according to different categories. The criterions to discard force curves were a slow decline of the interaction force to the baseline (**a**), a roundish shape of the force curve at the point where the cantilever tip loses contact with the sample (**b**), a peak far in the repulsive regime (**c**), a tiny peak with a magnitude close to baseline noise (**d**) and a bump in the contact regime (**e**). All these force curves are not likely to represent the desired interaction. **f** depicts a schematic of the interaction which might explain the situation causing an event as shown in **c**. The grey triangle represents the cantilever tip, the black part the sample and the blue line a tethered molecule. The scale shown in **a** holds for **b**-**e** as well.

To determine values of the persistence and the contour length from rupture events in MR-AFM, a function describing the behaviour of a wormlike chain (WLC)[91]

$$F = \frac{k_\mathrm{B}T}{L_\mathrm{p}} \left[\frac{1}{4}\left(1 - \frac{D}{L_\mathrm{c}}\right)^{-2} - \frac{1}{4} + \frac{D}{L_\mathrm{c}} \right] \tag{3.11}$$

was fitted to the data points between the origin and the maximum interaction force. Here, L_p denotes the persistence length, L_c the contour length and D the distance.

The quality of the fit was evaluated by the coefficient of determination according to

$$R^2 = 1 - \frac{\sum_i \left(F_i - \hat{F}_i\right)^2}{\sum_i \left(F_i - \bar{F}\right)^2} . \tag{3.12}$$

Here, F_i are the experimentally determined force values, $\hat{F}_i$ are the corresponding force values of the fit and $\bar{F}$ is the mean of the measured forces.

3.4.6 Cluster analysis by Ripley's *K*-function

Cluster analysis of data obtained from MR-AFM imaging was performed by an algorithm based on Ripley's *K*-function,[144] which is commonly used for cluster detection in super resolution fluorescence microscopy studies.[26,65] The basic analysis performed in the present thesis was adapted from Gaus and coworkers.[26] After the force curves were analysed for unbinding events as described in section 3.4.5, a two-dimensional binary grid was reconstructed, where a black pixel denotes a location corresponding to a force curve with a detected unbinding event. In Figure 3.18 the analytical procedure is visualised by an exemplary analysis of an artificially produced distribution of black pixels, which is shown in Figure 3.18 a. Such grids were subject to Ripley's *K*-function analysis which is described by the following equation:

$$K(r) = A_R \sum_{i=1}^{n} \sum_{\substack{j=1 \\ j \neq i}}^{n} \frac{I_{ij}}{n^2} \text{ where } I_{ij} = \begin{cases} 1 & d_{ij} < r \\ 0 & d_{ij} \geq r \end{cases} \tag{3.13}$$

K(*r*) accounts for the amount of clustering, A_R is the investigated area, *n* the overall number of events inside that area and d_{ij} denotes the Euclidian distance between two events *i* and *j*. *K*(*r*) is calculated as a discrete function of the parameter *r* which was usually performed in the range from zero to half the length of the investigated square at increments of 0.005 times that length. To reduce boundary effects, reflective boundary conditions were applied, which were favoured over periodic boundary conditions, since a cluster at the rim of the investigated area is likely to extend beyond the rim, which is better accounted for by reflective boundary conditions. Reflections of the regarded pixel itself were not accounted for (exclusion of self-counting). *K*(*r*) is in units of an area. To get to a distance representative of clustering it is converted to the *L*-function by

$$L(r) = \sqrt{\frac{K(r)}{\pi}} . \tag{3.14}$$

Finally, *r* is subtracted from *L*(*r*). The same analysis was performed for 100 homogeneous random distributions of events inside a grid of the same size with the same number of events *n* for every dataset which was analysed. For non-random data, a moving mean of *L*(*r*)−*r* was calculated within a window of nine values. An example of a plot of the resulting quantities is shown in Figure 3.18 b. Next, the *L*-value was calculated for every single pixel of the grid with a cut-off distance r_{max} corresponding to the maximum value of the moving mean of *L*(*r*)−*r*, regardless if the pixel corresponds to a force curve showing an event or not. Furthermore, the exclusion of self-counting described above was not applied in this step,

because it might lead to an artificial reduction of the $L(r_{max})-r_{max}$ value for a pixel with a present event compared with a neighbouring pixel not showing an event. Thus, the determined quantity can be described as

$$L_j\left(r_{max}\right) = \sqrt{\frac{A_R \sum_{i=1}^{n} \frac{I_{ij}}{n^2}}{\pi}} \; . \tag{3.15}$$

The resulting grid of $L_j(r_{max})-r_{max}$ values is referred to as Ripley density map (Figure 3.18 c). Again, the same procedure was executed for the 100 homogeneous random distributions. To binarise the Ripley density map in order to identify clusters, the mean and the standard deviation of the $L_j(r_{max})-r_{max}$ values of the random distributions were calculated. In that calculation, to avoid influences of boundary effects, only $L_j(r_{max})-r_{max}$ values with a distance larger than r_{max} from the boundary were regarded. The Ripley density map was binarised by a threshold value of the mean plus three standard deviations of the random $L_j(r_{max})-r_{max}$ values. A map of the areas of the Ripley density map with values larger than that threshold (cluster areas) is shown in Figure 3.18 d. Finally all events located within the cluster areas are identified (Figure 3.18 e) and referred to as clustered events. Figure 3.18 f shows an overlay of the Ripley density map and the clustered and non-clustered events, indicated by red and black coloured pixels, respectively. All locations inside the orange box in Figure 3.18 f are separated farther than r_{max} from the rim of the investigated area and therefore not influenced by boundary effects. For results in chapter 4, only representations like in Figure 3.18 b and f are shown.

The first four values in Figure 3.18 b are decreasing linearly with r and have a common value for all 100 homogeneous and the clustered distribution. These values correspond to r-values smaller than the width of one pixel and therefore $K(r)$ is zero and only the subtraction of r contributes to this decrease. Thus, such values were ignored in corresponding plots in chapter 4.
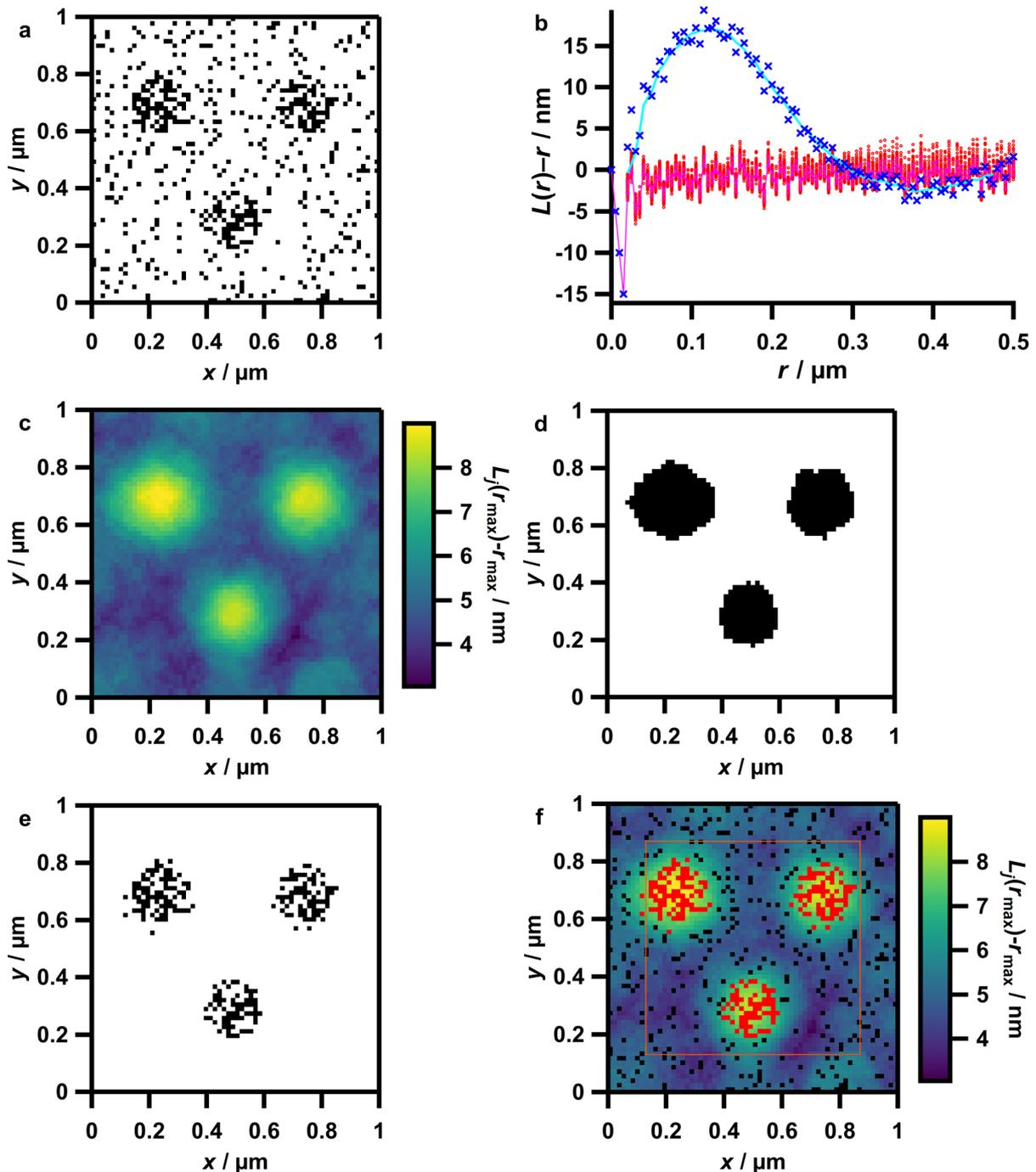
Figure 3.18: Illustration of the steps performed for cluster analysis. An artificial map of events (**a**) produced by overlaying three clusters with a radius of 0.1 µm and a probability of events of 0.5 with noise of a probability of occurrence of 0.1. In **b** the corresponding Ripley analysis is shown. The red circles correspond to 100 homogeneous random distributions of the same number of events as in **a**, the mean of these distributions is plotted in magenta, the error bars indicate the 95 % confidence interval (two times the standard deviation). Blue crosses show the $L(r)-r$ values for the map of events shown in **a**, the cyan curve is a moving mean of the blue crosses. The r-value corresponding to the maximum of the cyan curve is referred to as r_{max}. In **c** the Ripley density map at $r = r_{max}$ is shown. The black areas in **d** correspond to Ripley density values larger than a threshold value obtained from a statistical approach based on the 100 homogeneous distributions (clustered areas). **e** shows the clustered events situated inside the clustered area. The plot in **f** is an overlay of the Ripley density map, the clustered events (red) and all remaining non-clustered events (black). All pixels inside the orange square are separated farther than r_{max} from the boundary.

3.4.7 Analysis of combined AFM and STED measurements

AFM images were processed as described before (see section 3.4.4). The STED images of the membrane dye and the AFM images were overlaid manually in Inkscape 0.91 (Free Software Foundation, Boston, MA). Afterwards, the STED image of the membrane was replaced by that of the antibody fluorescence, whose pixel size was initially set to half of that of the AFM image, leading to a number of pixels four times of that of the AFM image. One or two quadratic ROIs were selected in each image and the corresponding AFM and STED data were extracted. A Gaussian filter with a standard deviation of 0.5 pixels was applied to the STED image and binarisation was performed by the Bradley adaptive threshold method, both implemented in MATLAB 2018a (MathWorks, Natick, MA). The binarised STED image was refined by a morphological opening algorithm with a diamond of an edge length of five pixels as structuring element by the package scikit-image in Python 2.7 (Python Software Foundation, Beaverton, OR) and the pixel number was reduced to that of the AFM ROI by Inkscape 0.91. This image was again binarised by setting all nonzero values to one. Finally, the measured height values of the AFM image were extracted at the positions which had a value of one in the binarised STED image. For control calculations, the binarised STED ROI was rotated one to three times by 90° and used to extract data from the AFM image as described before.

3.4.8 Analysis of GUV indentation experiments

GUV indentation force curves obtained with a conical indenter were analysed by using the tension model as described in a previous publication.[145] Briefly, the contour of the indented vesicle was parametrised as detailed in Figure 3.19.
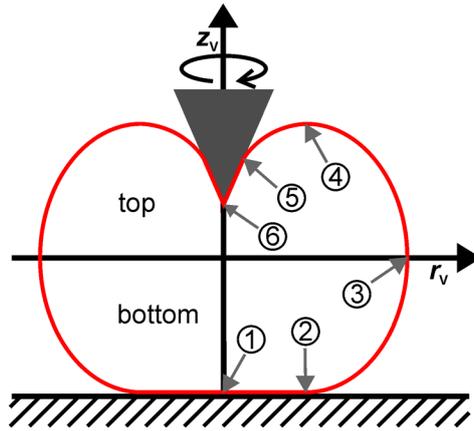
Figure 3.19: Parametrisation of a GUV indented by a conical AFM tip. The red line represents the cross sectional membrane of an indented GUV. The dark grey triangle indicates the tip of the cantilever. In the range from (1) to (2) the contour of the membrane is constrained by the substrate, between (2) und (5) the contour is free, reaching a maximum of the radius r_V at (3), which separates the bottom from the top part of the GUV. At (4) the maximal height is reached. Between (5) and (6) the contour is constrained by the tip, namely its half opening angle. The contour is rotated around the z_V-axis to describe the three dimensional body.

The surface of the corresponding solid of revolution is computed, enabling the description of the tension as

$$\tau = \tau_0 + K_A \cdot \frac{A_{ind} - A_{V,0}}{A_{V,0}} , \tag{3.16}$$

where τ_0 is the pre-stress, K_A is the area compressibility modulus, A_{ind} the surface of the indented vesicle and $A_{V,0}$ the surface of the corresponding unindented vesicle of the same volume. This tension can be utilised to calculate the force applied by the GUV on the indenter, i.e. the force equilibrium in the upper part of the indented GUV, and the force equilibrium in the lower part of the GUV. Under the constraints of conserved volume and negligible bending stiffness, the contour of the indented GUV can be computed for every single force value, enabling the subsequent calculation of the indentation depth. For experimental data a script for MATLAB R2014a (MathWorks, Natick, MA) written by Prof. Andreas Janshoff (Institute of Physical Chemistry, University of Göttingen) was utilised, which solves the corresponding equations based on a Levenberg-Marquardt minimisation. To accelerate the analysis, the number of data points of the force curve was reduced by regarding only every 200th data point of a moving mean of the raw data, calculated with a window size of 10 points.

Force curves exhibiting sudden declines of the force in the contact regime, which might stem from sliding GUVs or breakthrough events, were not analysed. For the final results fits with a

coefficient of determination smaller than 0.99 were discarded. An opening angle of the tip of 17.5° was assumed.

3.4.9   Analysis of micropipette aspiration experiments

For the extraction of geometric parameters from images of GUVs aspired by a micropipette and the further analysis of data obtained from micropipette aspiration, a self-written Python 2.7 (Python Software Foundation, Beaverton, OR) program was used.

To binarise the images, first a local Otsu algorithm implemented in the Python package scikit-image was applied inside circular regions of a radius of 15 pixels, followed by a morphological opening algorithm with a diamond of an edge length of five pixels as structuring element and a closing algorithm with a diamond of seven pixels edge length. The detection of the radius of the aspired membrane tube (R_P) was performed with the last recorded and analysed image for each vesicle, commonly corresponding to the longest tube observed. An example of a binarised image is presented in Figure 3.20 a. Using the binarised image, two straight lines were fitted to the edges of the tube inside a manually selected region (red lines in Figure 3.20 b). The mean distance of the two lines inside the selected region was assigned to the diameter of the tube. In more detail, this quantity was extracted by drawing two orthogonal lines (blue lines in Figure 3.20 b) to the upper fitted straight line through its first and its last point inside the selected region (cyan crosses in Figure 3.20 b), calculating the intersection point with the extrapolated lower straight line (magenta crosses in Figure 3.20 b) and determining the mean of the two lengths between the intersection points with both previously fitted lines (i.e. the mean length of the two blue lines in Figure 3.20 b). For the next steps, all detected, isolated regions in the binary images which were smaller than the projected area of the GUV of interest, stemming from smaller vesicles or lipid aggregates, were removed automatically. To infer the radius of the spherical part of the aspired vesicle, a region in an unprocessed image was selected manually in a way that the tube is excluded from the selection in all images but a large fraction of the spherical part of the GUV is included. Next, a Laplacian filter, implemented in the Python package SciPy, was applied to the binary image. By extracting the coordinates of pixels with negative values of the Laplace-filtered image inside the selected region, points of the borderline of the spherical part of the GUV were readily obtained (blue crosses in Figure 3.20 c).

To determine the radius R_V of the spherical part of the GUV introduced earlier, the function

$$\chi^2 = \frac{1}{N_{dp}} \sum_{i=1}^{N_{dp}} \left[\left(x_m - x_i \right)^2 + \left(y_m - y_i \right)^2 - R_V^2 \right]^2 \tag{3.17}$$

was minimised by a least-square fit provided by the Python package SciPy. In eq. (3.17) N_{dp} is the overall number of data points, x_m and y_m are the coordinates of the centre of the fitted circle and x_i and y_i are the coordinates of the detected borderline points. In Figure 3.20 c, the fitted circle is depicted by the red line and its centre by the green dot. For the determination of the length of the tube, first the end point of the tube was detected. This was accomplished by extracting profiles of the binarised image orthogonal to the mean slope of the two straight lines fitted to the boundaries of the tube. The profile furthest away from the neck between the tube and the spherical part of the GUV which still contained values of one, corresponding to parts of the vesicle, yielded the end point of the tube, which was extracted from that profile as the central point of the plateau of values of one (red dot in Figure 3.20 d, see figure caption for further details). To account for drifts of the vesicle and the micropipette inside the image plane, the straight lines fitted to the boundary of the tube were shifted according to the vector connecting the end points of the tube of the image used to fit the tube boundaries and the currently regarded image. Next, the intersection points between the two shifted straight lines and the fitted circle were calculated (magenta crosses in Figure 3.20 d). The centre of the line connecting the intersection points was assigned to the second end of the tube (blue dot in Figure 3.20 d) and the distance between the determined ends yielded the length of the tube ΔL (cyan line in Figure 3.20 d).

In the second step, all images of the aspired GUV along with the detected radius of the spherical part of the GUV (as in Figure 3.20 c) and the end points of the tube (as in Figure 3.20 d) were checked manually to exclude erroneous values. Whenever one of the quantities of interest was not detected correctly, all data corresponding to that time point were discarded. Next, the plateaus of the applied suction pressure and, correspondingly, of the aspired tube length were selected manually. If the first values of the tube length after the increase in suction pressure (see Figure 4.39 a) were substantially smaller than the following plateau values, these values were excluded to ensure that only values of an equilibrated system were regarded. For each plateau, the mean and the standard deviation of the tube lengths, of the radii of the spherical part of the GUV and of the pressure were calculated.
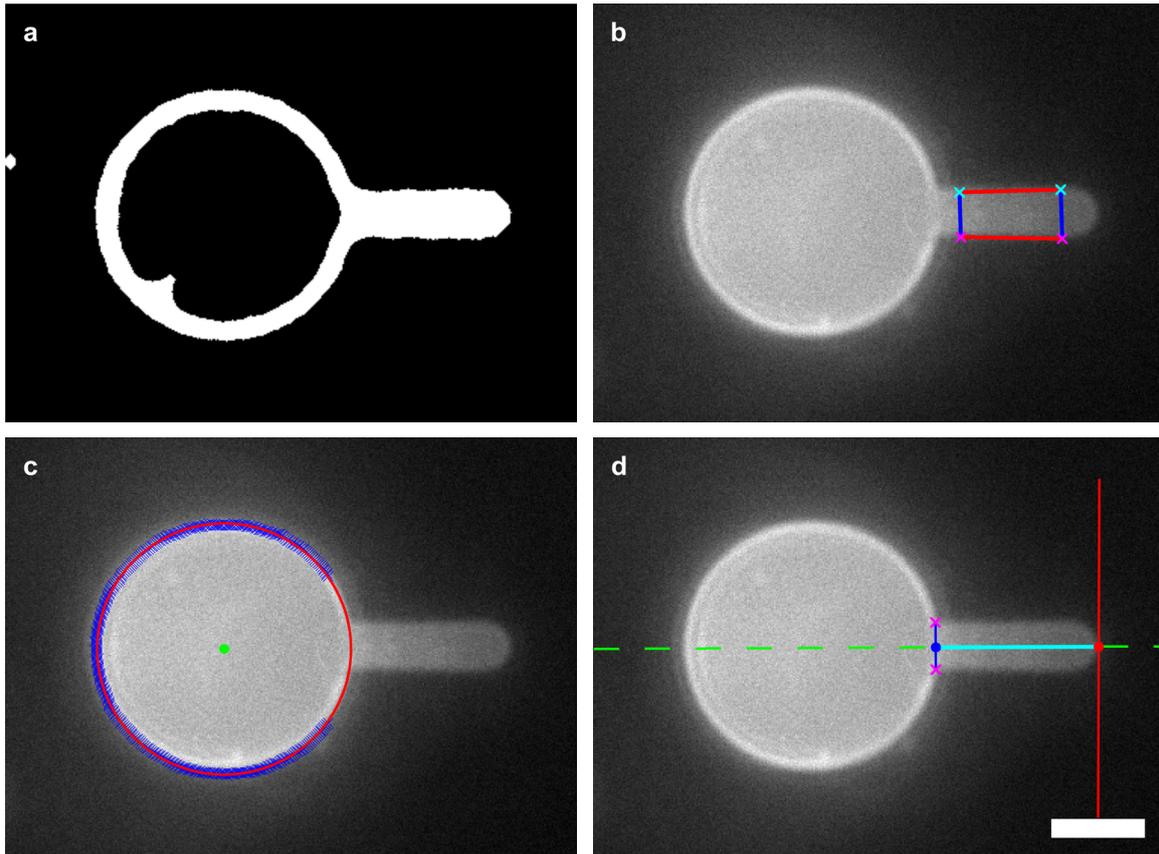
Figure 3.20: Elucidation of the algorithm used for the detection of geometric parameters based on an example of an aspired vesicle. a depicts a binarised image of an aspired GUV in the equatorial plane. **b** shows the same vesicle with two straight lines fitted to the boundary of the aspired tube (red) and two lines which are orthogonal to the upper fitted line (blue) through the first and last point of the fitted line (cyan crosses). The intersection with the extrapolated second line is indicated by magenta crosses. The mean length of the blue lines corresponds to the diameter of the tube. In **c** the detected boundary points of the spherical part of the GUV are assigned by blue crosses, the fitted circle is indicated by the red line and its centre by the green dot. In **d** the detection of the length of the tube is illustrated. The red line is moved from the right end of the image along the dashed green orthogonal line, whose slope is the mean of the slopes of the two fitted straight lines in **b**, towards the GUV. As it crosses white pixels in the binarised image (**a**) for the first time, the central white pixel along the red line is assigned to the origin of the tube (red dot). The intersection of the extrapolated straight lines in **b** with the red circle in **c** corresponds to the neck between the tube and the spherical part of the GUV (magenta crosses). The distance between the central point of the connecting blue line (blue dot) and the first origin of the tube (red dot) is assigned to the length of the tube ΔL (cyan line). Scale bar: 10 μm.

The last step was commenced by calculating the tensions and apparent area expansions from the mean values extracted from the plateaus by eqs. (3.5) and (3.6), respectively. In a plot of $\ln(\tau/\text{N·m}^{-1})$ *versus* α_{app}, the low- and high-pressure regimes were selected manually based on an apparent decrease of the slope at around $\tau \approx 0.5\,\text{mN·m}^{-1}$. According to equation (3.7), a linear function with a variable intercept was fitted to the values of $\ln(\tau/\text{N·m}^{-1})$ as a function of α_{app}.

The bending modulus κ can be deduced from the obtained fit as

$$\kappa = \frac{k_B T}{8\pi} \cdot \frac{\mathrm{d}\ln(\tau / \mathrm{N} \cdot \mathrm{m}^{-1})}{\mathrm{d}\alpha_{app}}$$ (3.18)

and the intercept corresponds to $\ln(\tau_b)$. In the high-pressure regime, a fit of a linear function with variable intercept yields the apparent area compressibility modulus K_{app} as the slope of the fitted function, according to eq. (3.8). The intercept accounts for influences at low area expansion which cannot be described by in-plane dilation of the membrane. Applying the formalism introduced by eqs. (3.9) and (3.10) finally yielded the direct area compressibility modulus K_{dir}. To this end, the mean bending modulus obtained from all values of measurements with a comparable type of sample was used. $\tau(1)$ was calculated from the fit of $\tau(\alpha_{app})$ at the lowest value of α_{app} assigned to the high-pressure regime.

The volume of the vesicle was calculated from the extracted geometric parameters as the sum of the volumes of a sphere with the radius R_V, a cylinder with the radius R_P and the length of the tube subtracted by R_P and a half sphere with the radius R_P, subtracted by the volume of a spherical cap of the main radius R_V and the radius of the base R_P as

$$V = \frac{4}{3}\pi R_V^3 + \pi R_P^2 (\Delta L - R_P) + \frac{2}{3}\pi R_P^3 - \frac{\pi\left(R_V - \sqrt{R_V^2 - R_P^2}\right)}{6} \cdot \left(3R_p^2 + \left(R_V - \sqrt{R_V^2 - R_P^2}\right)^2\right).$$ (3.19)

The absolute surface of the aspired vesicle was calculated accordingly, obviously only by subtracting the curved surface of the spherical cap:

$$A = 2\pi R_V \left(R_V + \sqrt{R_V^2 - R_P^2}\right) + 2\pi R_P (\Delta L - R_P) + 2\pi R_P^2.$$ (3.20)

To assign a value of the tension to a single image, the average of the pressure in a time window of 2 s centred at the time point when the image had been taken was used.

Besides the discarded data points in case of an inaccurate detection of the geometric parameters from fluorescence images (*vide supra*) whole measurements of single vesicles were rejected if only very few data points were detected due to a fast rupture of the vesicle so that the quantities of interest could not be determined accurately. Furthermore, fits of the tension as a function of the area strain were only included if at least three data points could be used for the fit. In this exclusion step, the fits of the low- and high-pressure regime along with the correspondingly obtained quantities were regarded and discarded independently of each other. For the determination of mechanic moduli all data points after the fission of a small vesicle inside the micropipette were discarded.

Due to the uncertainty in the determination of the borders of the GUV in the fluorescence micrographs an error of five pixels was assumed for the radius of the tube. The calculated standard deviations of the radii of the spherical part of the GUV, of the lengths of the tube and of the pressures were assigned to the errors of the corresponding quantity. The error of the temperature was set to 3 K. The error of the tension and that of the apparent area expansion were calculated by Gaussian error propagation with the aforementioned errors. For measurements on single GUVs, the errors of the mechanic moduli were calculated by Gaussian error propagation of the uncertainties of the fit parameters used to fit the tension as a function of the area expansion (*vide supra*). To calculate the error of the direct area compressibility modulus the standard deviation of the bending modulus obtained from all measurements of the same type of sample was used.

3.5   Software

In this section software used to analyse and present data and to produce plots and other figures is noted, which is partially already described in section 3.4.

The initial analysis of force curves and the processing of images obtained from atomic force microscopy was performed by the data analysis software of the manufacturer of the AFM (JPK Data Processing 6.0, JPK Instruments, Berlin, Germany).

MATLAB R2014a (MathWorks, Natick, MA) and software written therein was used for all further data analysis of AFM force curves, for cluster analysis of data obtained from MR-AFM experiments and for the analysis of GUV indentation experiments. Finally MATLAB R2014a was also used for final data collection and some final analyses of data stemming from micropipette aspiration experiments, which are not explicitly described in section 3.4.9.

Self-written Python 2.7 (Python Software Foundation, Beaverton, OR) programs were utilised to analyse confocal images to compare the amount of syntaxin-1 in PC12 cell membrane sheets and to analyse data obtained from micropipette aspiration experiments. Furthermore, Python 2.7 was used to compare the intensities of bands in western blots.

Confocal and epifluorescence images were processed in ImageJ (National Institutes of Health, Bethesda, MD).

All plots shown in this thesis were generated by Igor Pro 6 and Igor Pro 7 (WaveMetrics, Lake Oswego, OR).

Inkscape 0.91 (Free Software Foundation, Boston, MA) was used to produce vector graphics and to perform final modifications (error bars, added texts, numbers and letters) of images and plots.

Vector graphics were additionally produced by CorelDRAW® ESSENTIALS 3 (Corel, Ottawa, Canada).

Rendered schematic illustrations and visualisations of measured data were produced by the raytracing software POV-Ray 3.7 (Persistence of Vision Raytracer, Williamstown, Australia).

This thesis was written in Microsoft Word 2010 and Microsoft Word 2013 (Microsoft Corporation, Redmond, WA).

4 Results

4.1 Heterogeneity and Clustering in PC12 Membrane Sheets

As described in section 2.4 in detail, membrane proteins are described to be non-homogeneously distributed within cell membranes.[7,54,58,90] Most of the contemporary studies in this field are performed using fluorescence based methods.[74,75,81] However, these approaches are prone to intrinsic errors (see section 2.4.2).[25,83,85] To circumvent these problems, in this thesis membrane heterogeneity and protein clustering are investigated by a label free approach. The results of the corresponding experiments are described in this section.

After introductory experiments, MR-AFM measurements by using standard IgG-antibodies against syntaxin-1 coupled to the cantilever with their corresponding control experiments are presented. Afterwards, similar experiments performed with nanobodies are reported, followed by control experiments. Next, MR-AFM experiments with cantilevers that can be functionalised in a simpler way are described. Finally, the morphology of membrane sheets derived from PC12 cells is investigated in more detail.

4.1.1 Imaging of PC12 cells and membrane sheets

To obtain a basic insight into the morphology of PC12 cells, intact cells were imaged by atomic force, bright field and phase contrast microscopy. A representative image of a fixed wild type cell (PC12-WT-1) is shown in Figure 4.1. The topographical AFM height image in Figure 4.1 a indicates a cell diameter of about 14 μm and a height of about 3 μm. Some folds on the cap of the cell are already visible in the height image but they become even clearer in the error image, i.e. the deviation of the PSD voltage from the setpoint, in Figure 4.1 b. These structures, which might represent microvilli or sites of exocytosis, can also be

identified in the rendering of the height data in Figure 4.1 c. This representation indicates a rather flat shape of the cap of the cell. In Figure 4.1 d a phase contrast image is shown. Cells as shown in Figure 4.1 were subject to the sonication procedure described in section 3.2.2 to produce membrane sheets.
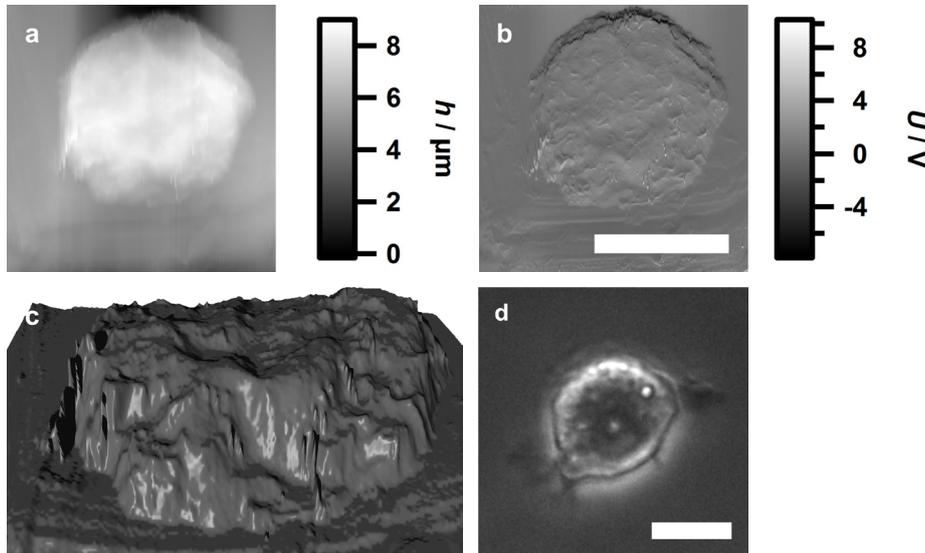
Figure 4.1: Morphological investigation of a fixed native PC12 cell. The cell was imaged by contact mode AFM. **a** shows the height image, **b** the corresponding error image. **c** shows a rendering of the height data presented in **a**. A phase contrast image of the cell is shown in **d**. Scale bars: 10 μm.

The epifluorescence micrographs of the membrane label (octadecyl rhodamine B chloride) of the obtained membrane sheets (Figure 4.2 a, b and c) are already distinct from fluorescence images of cells (not shown). When compared with PC12-WT-2 cells, PC12-WT-1 cells most times showed a more homogeneous surface, as indicated by Figure 4.2 b and Figure 4.2 a, respectively. However, in most PC12-WT-2 membrane sheets this heterogeneity was even more pronounced (data not shown). On the other hand, PC12-WT-1 membrane sheets more often possessed regions of brighter fluorescence at the rim of the sheets, as shown in Figure 4.2 a. These structures might correspond to overlapping membranes. Since the presence of such a structure indicates that the outer membrane leaflet might be facing upwards in these regions, care was taken that the MR-AFM measurement was performed in a central region of such a membrane sheet to avoid a measurement on the outer membrane leaflet, which does not contain accessible syntaxin-1 molecules. Figure 4.2 d-f show fluorescence micrographs of the actin label (Alexa-Fluor®-488-phalloidin) and Figure 4.2 g-i depict an overlay of the membrane and the actin image. In general, the sheets of PC12-WT-2 cells contain less actin than PC12-WT-1 sheets. The membrane sheet shown in Figure 4.2 c, f and i, stemming from a PC12-WT-1 cell, bears a huge amount of actin. Such a sheet was not used for further

measurements or analyses. Furthermore, actin was enriched in regions of brighter fluorescence in the membrane channel, as evident from Figure 4.2 g and i. That might be explained by actin wrapped with membrane which, therefore, could not be removed.
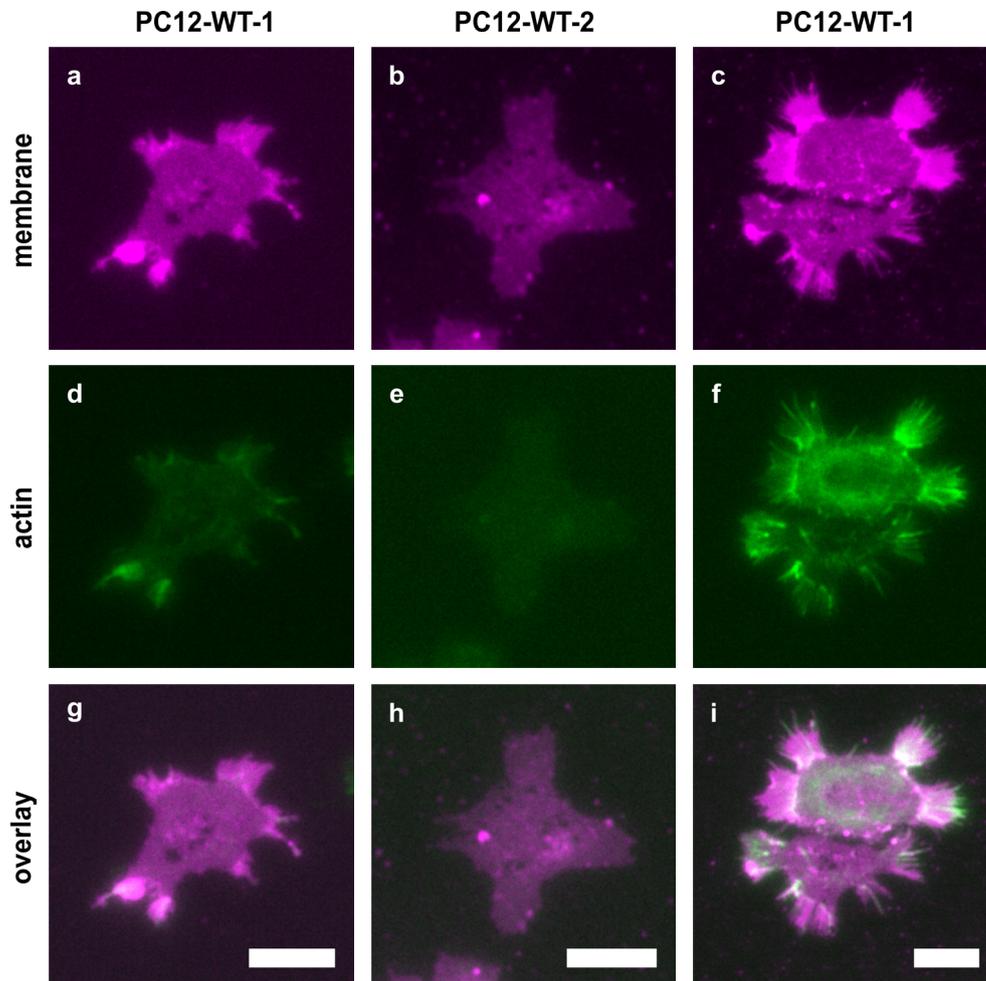
Figure 4.2: Fluorescence micrographs of PC12 membrane sheets obtained by epifluorescence microscopy. The magenta channel shows the fluorescence of the membrane label (**a**, **b** and **c**), the green one actin (**d**, **e** and **f**) and the last row is an overlay of both channels (**g**, **h** and **i**). The sheet shown in **a**, **d** and **g** is derived from a PC12-WT-1 cell, the one in **b**, **e** and **h** from a PC12-WT-2 cell and the one in **c**, **f** and **i** again stems from a PC12-WT-1 cell, but contains a much larger amount of actin. Scale bars: 10 μm.

To get a more detailed insight into the morphology of PC12 cell membrane sheets, CLSM and AFM imaging was employed. Figure 4.3 a and b shows confocal micrographs of PC12-WT-1 membrane sheets. The membrane image in Figure 4.3 a indicates some heterogeneous structures. Some membrane sheets exhibit larger accumulations of fluorescent material or regions depleted in the same (Figure 4.3 b). Due to low quality, such sheets were as well discarded from further analysis.

A more precise view of the morphology can be gained by AFM height imaging (Figure 4.3 d) of the membrane sheet shown in Figure 4.3 c. The borderline of the membrane sheet and the presence of holes within is generally confirmed by the AFM height image. The membrane sheet has a height plateau at about 20 nm as compared with the height of the substrate. Some small structures even reach heights above 100 nm. Nevertheless, a tremendous decrease of the height as compared with the native cell shown in Figure 4.1 is evident, confirming a successful production of a membrane sheet. Regions of brighter fluorescence signals in Figure 4.3 c do occasionally, but not entirely, colocalise with elevated regions in the AFM image. This shows that accumulations of membrane material play a role for the surface structure of the membrane sheets but also indicates that further structures might contribute as well, which is analysed in more detail in section 4.1.9 and discussed in section 5.1.1.
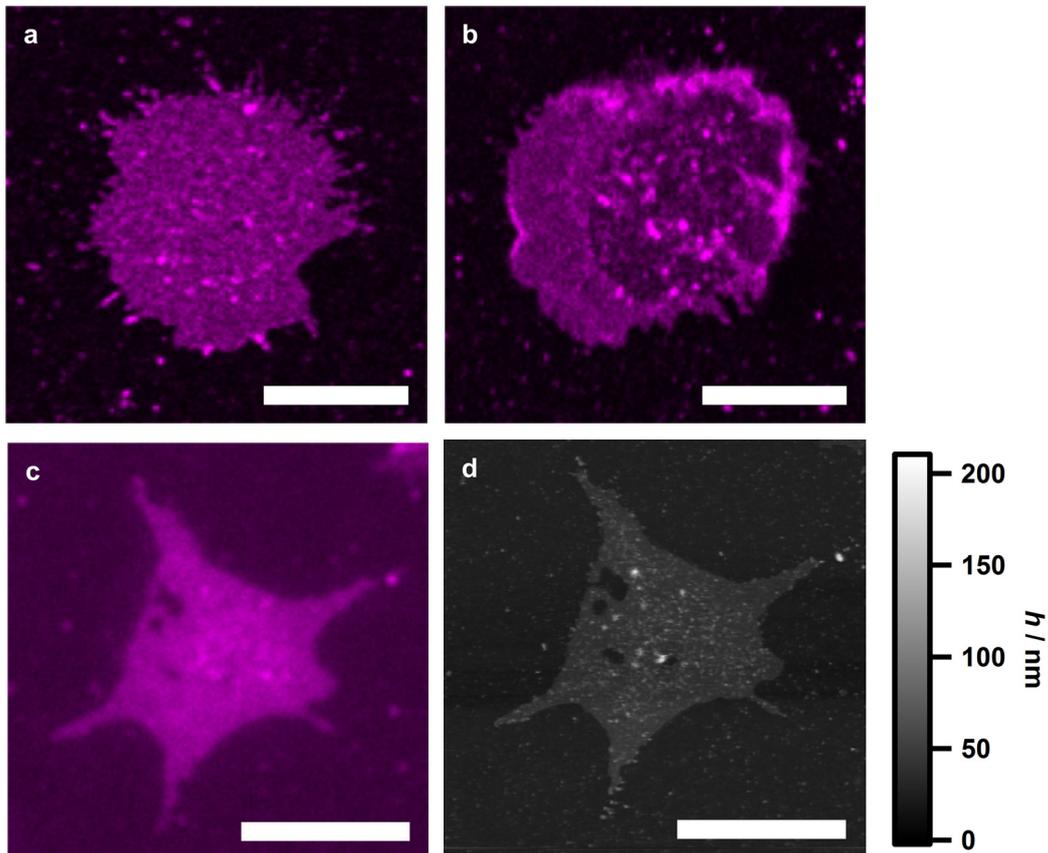
Figure 4.3: CLSM and AFM imaging of membrane sheets. In all cases sheets derived from PC12-WT-1 cells are shown. The confocal images depict a rather smooth homogeneous membrane sheet (**a**) and a more heterogeneous one (**b**), which would not have been used for further measurements. A further membrane sheet shown by an epifluorescence micrograph (**c**) was imaged in contact mode AFM to yield a height image (**d**). Scale bars: 10 μm.

To visualise the protein clusters to be investigated by MR-AFM, STED microscopy was performed employing immunofluorescence with an antibody directed against syntaxin-1. Figure 4.4 shows a representative example of a membrane sheet derived from a PC12-WT-2 cell (N = 9 membrane sheets from two glass cover slips of a single preparation). The green channel, corresponding to the immunofluorescence of the syntaxin-1 label (Alexa-Fluor®-488-goat-anti-mouse-IgG), shows a heterogeneous distribution with tiny regions of accumulated fluorescent probes. These structures are probably clusters of syntaxin-1 which are aimed to be investigated by MR-AFM in the present thesis.
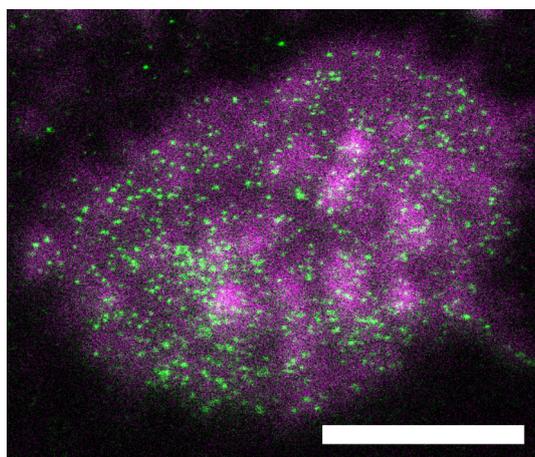
Figure 4.4: STED image of syntaxin-1 clusters in a membrane sheet. The fluorescence signal of the membrane marker is shown in magenta, the STED immunofluorescence signal of the syntaxin-1 marker in green. Note the tiny segregated regions of intense immunofluorescence. Scale bar: 5 μm.

4.1.2 Test of cluster analysis by artificially produced maps of events

The illustrative example in section 3.4.6 has already shown the general applicability of the cluster detection algorithm based on Ripley's K-function in a tiny grid of only 64×64 pixels. However, in order to test the algorithm on data more similar to those to be expected from the experiments performed for this thesis, random clusters were produced according to the properties of syntaxin-1 clusters published by Bar-On *et al.*.[90] That means inside a quadratic box corresponding to 1×1 μm², 14 non overlapping clusters with a mean diameter of 0.093 μm were produced randomly. The standard deviation of the diameter was set arbitrarily to 0.030 μm and the non-circularity described by Bar-On *et al.* was ignored, i.e. the clusters had a circular shape. The obtained clusters are shown in Figure 4.5.
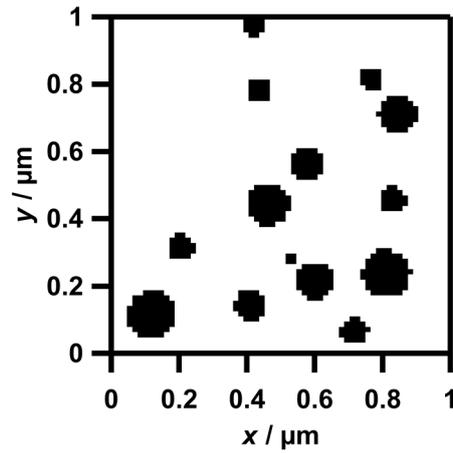
Figure 4.5: Artificially produced clusters for test purposes. The black regions represent clusters.
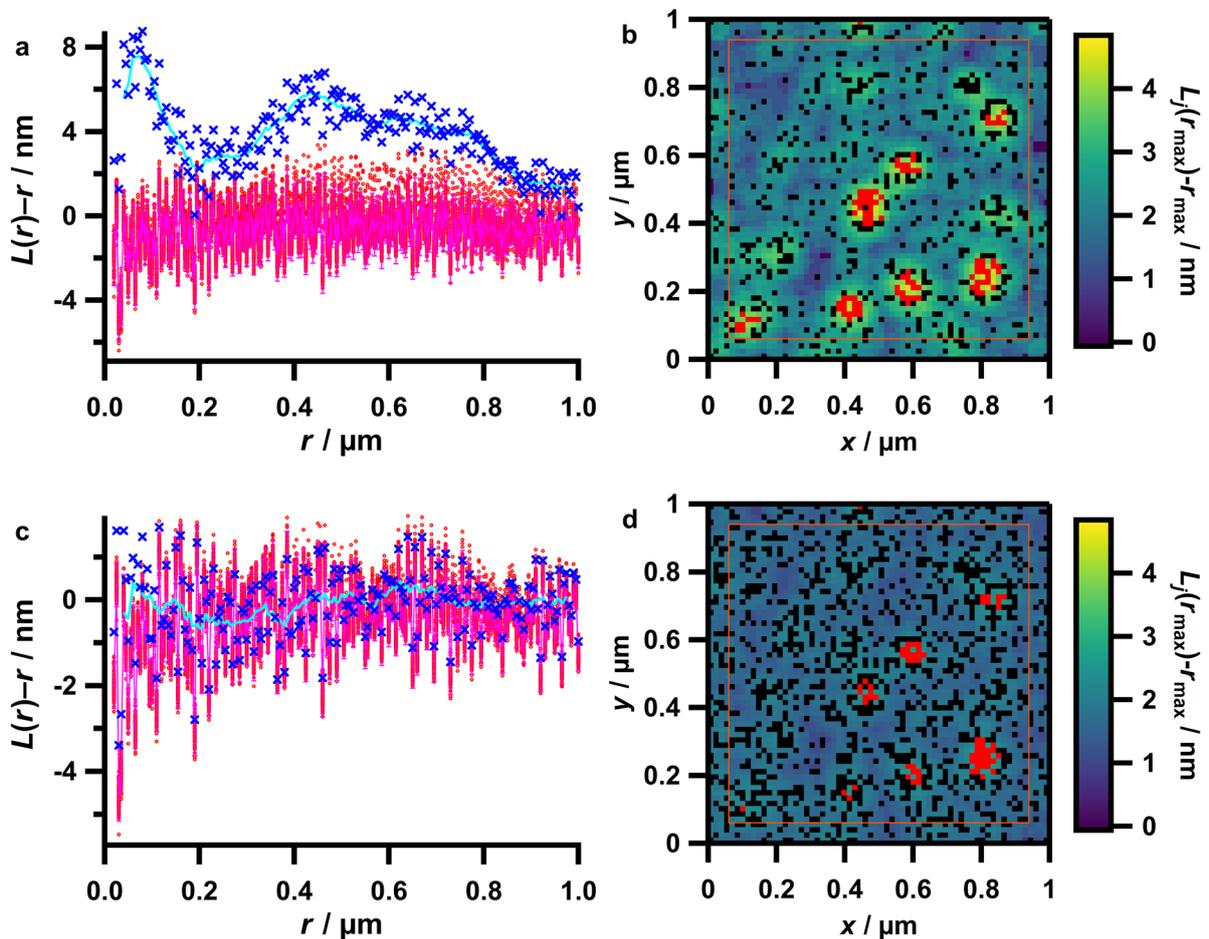
Figure 4.6: Cluster analysis based on Ripley's K-function of artificially produced clusters. In **a** and **b** the results for a noise-probability of 0.1 and in **c** and **d** those for a noise-probability of 0.25 are shown. **a** and **c** plot the $L(r)-r$ values for the artificial non-homogeneously distributed data (× and cyan line) and for homogeneous random data of the same number of events (○ and magenta line) as a function of r. In **b** and **d** the overlay of the Ripley density maps and the corresponding clustered events (red) and all other events (black) are shown. For details see caption of Figure 3.18.

Next, for each pixel inside a cluster the probability of occurrence of an event was set to 0.5. For all pixels, regardless if part of a cluster or not, a probability of occurrence of an event of 0.1, 0.25 or 0.5 was assumed additionally to account for unspecific events or specific events apart from clusters. This value is referred to as noise-probability in the following. The results for noise-probabilities of 0.1 and 0.25 are shown in Figure 4.6.

The global maximum of the cyan line in Figure 4.6 a, corresponding to the moving mean of the $L(r)−r$ values of the non-homogeneously distributed events, at $r = 0.06$ µm stems from the detection of single clusters since that value is in between the mean radius and the mean diameter. As the investigated local environment, indicated by r, gets larger, the mean density of events inside the local environment declines and therefore the value of $L(r)−r$ also does. The local maxima at $r \approx 0.45$ µm and $r \approx 0.6$ µm are caused by the inclusion of more than one cluster inside the local environment. When all events are included at $r \rightarrow 1$ µm the moving mean nearly declines to values of homogeneous distributions. The representation in Figure 4.6 b indicates that the seven largest clusters are recognised by the algorithm. Furthermore, a smaller cluster located close to the boundary is recognised by a single $L_j(r)–r$ value lying above the threshold. In other words, half of the clusters are identified. When having a considerably larger probability of noise events, corresponding to half the value caused by clusters, the Ripley analysis in Figure 4.6 c does hardly deviate from a homogeneous distribution, but still has its maximum at $r = 0.06$ µm. However, the spatially resolved cluster analysis (Figure 4.6 d) again recognises all the clusters identified at a noise-probability of 0.1 with at least one $L_j(r)–r$ value lying above the threshold. When generating an artificial map of events with a noise-probability of 0.5 (data not shown), the deviation from the confidence interval of the homogeneous distributions completely vanishes. Nevertheless, when the cluster analysis is performed at $r \approx 0.6$ µm, still five of the seven largest clusters are recognised and only two false positive clusters outside of the region which is not influenced by boundary effects (orange square in the Ripley maps) appear (data not shown). Thus, this analysis reveals that the applied algorithm should be capable of detecting a subset of the clusters of interest in the experimental data, provided that the clusters induce a high frequency of recognition events and that the frequency of events apart from clusters, caused by unspecific interactions and by non-clustered syntaxin-1 molecules, is not more than roughly half of that caused by specific interactions inside a cluster.

4.1.3 Molecular recognition AFM with conventional IgG antibodies[8]

As a first approach to map the distribution of syntaxin-1 molecules in membrane sheets derived from PC12-WT-1 cells (see section 3.2.2), mouse-anti-rat-IgG antibodies raised against syntaxin-1 (anti-Syx-AB) were coupled to AFM-cantilevers as described in section 3.2.5, and used to carry out MR-AFM experiments on membrane sheets as detailed in section 3.3.4.3. In initial experiments force maps of an array of 16×16 force curves (briefly called 16×16 force maps) were recorded to get a general overview over the interactions. These experiments yielded a relative frequency of the occurrence of an event of f_e = (33 ± 7) % (mean ± standard deviation (SD)) (N = 6 maps from three sheets and three independent preparations). A selection of force curves chosen arbitrarily from these maps is shown in Figure 4.7.
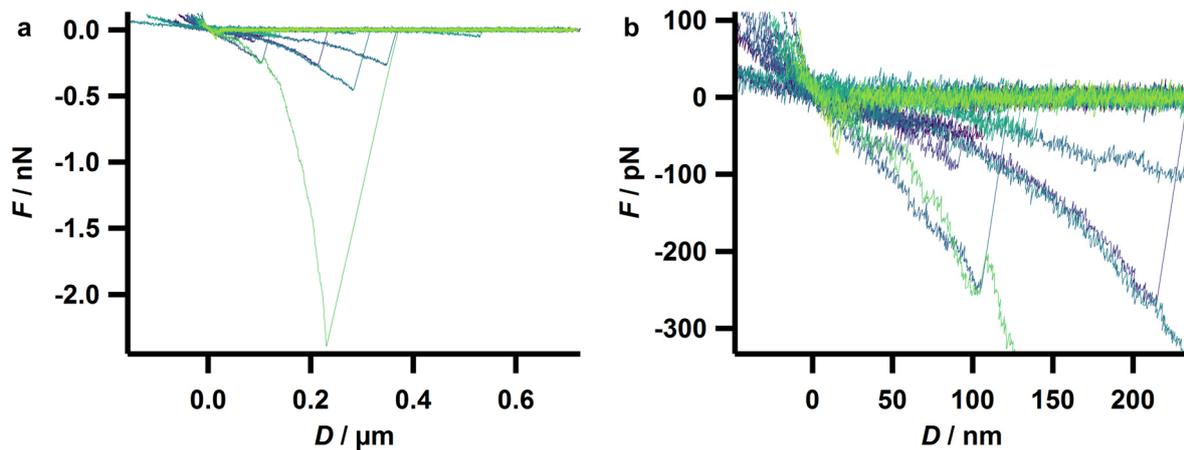
Figure 4.7: Arbitrarily chosen force curves obtained from MR-AFM experiments with conventional IgG antibodies against syntaxin-1 coupled to the cantilever on PC12-WT-1 membrane sheets. The force curves were recorded with a cantilever retraction speed of 1 µm·s⁻¹. In **a** five randomly picked force curves per force map, 30 in total, are shown. A magnification close to the zero-force point is plotted in **b**. The colours of the force curves are chosen arbitrarily to provide better distinguishability.

To obtain a basic insight into the spatial distribution of these events, an initial MR-AFM imaging experiment with exactly the functionalisation strategy described in section 3.2.5 was performed by measuring a single 64×64 force map. In Figure 4.8 the Ripley analysis of this experiment is presented.

---

[8] As the experiments described in this section are introductory ones, the reported results will, after the presentation of a selection of force curves, immediately be continued with observed binding efficiencies and clustering behaviour. For a more general introduction including a deeper explanation of the force curves and the presentation of a force map and force-distribution histograms, see the description of the main experiments in section 4.1.5.2.
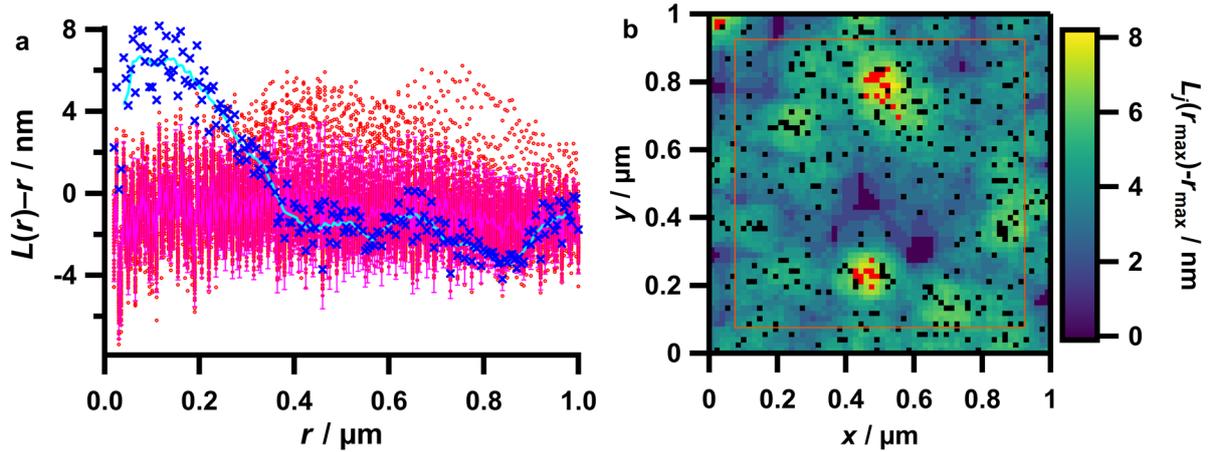
Figure 4.8: Ripley analysis of a MR-AFM experiment with a conventional IgG antibody. a plots the $L(r)-r$ values of the measured data (× and cyan line) and for homogeneous random data of the same number of events (○ and magenta line) as a function of r. In **b** the overlay of the Ripley density map, the corresponding clustered events (red) and all other events (black) is shown. For details see caption of Figure 3.18.

The Ripley analysis shows a non-homogeneous distribution of events at around 0.1 µm. By the subsequently performed spatial cluster analysis the presence of two segregated clusters in a central region of the investigated area and a tiny one close to the border was identified. The relative frequency of events is as low as $f_e = 8.0$ % in this map. In contrast to initial test experiments with smaller force maps which have not shown clear clusters (data not shown), this experiment implies the detection of clusters in PC12 membrane sheets. However, the specific nature of these events and the corresponding clusters has to be checked, additionally. To this end, some initial control experiments were performed which are described in the following sub-section.

4.1.3.1 Control experiments for MR-AFM by conventional IgG antibodies

First, to test whether the detected events are caused by the specific interaction of antibodies with syntaxin-1 molecules, a competition experiment was performed by the addition of 0.02 mg of the antibody to 2 ml measuring buffer and incubating for 1.5 h. Before and after the addition of the antibodies 16×16 force maps were recorded. This experiment showed, based on the comparison of the mean values and the corresponding standard deviations, no significant difference in the relative frequency of events ($f_e = (28 \pm 4)$ % (mean ± SD) ($N = 3$ maps from the same sheet as used for three maps before the addition of the antibody)), as compared with the previously described experiment without antibody competition (see

section 4.1.3). However, when compared with the data stemming from exactly the same membrane sheet recorded before the addition of the antibodies (f_e = (37 ± 4) % (mean ± SD) (N = 3 maps)), a significant difference is obtained (see Figure 4.9). Thus, comparing results from the same sheet the competition leads to a smaller amount of events. However, there are still many events left. These events might be caused by an incomplete competition or by unspecific interactions.
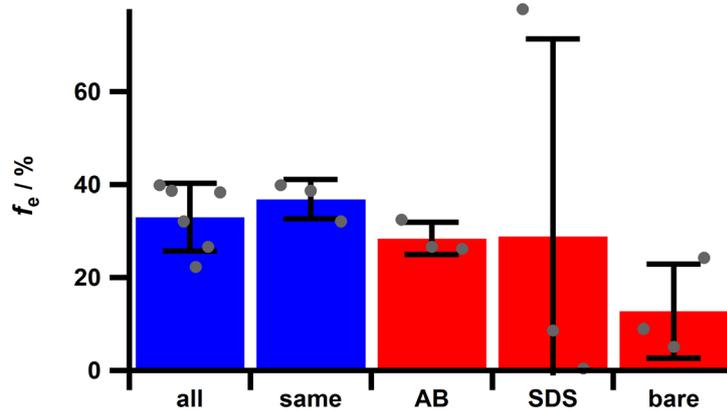
Figure 4.9: Relative frequency of events in MR-AFM with anti-Syx-ABs coupled to the cantilever on membrane sheets and related control experiments. Data of measurements with antibodies on the cantilever which are supposed to provide specific interactions are shown in blue, control experiments are shown in red. The caption of the bars denote: all: all six measurements supposed to show specific interactions with IgG-antibodies coupled to the cantilever, same: only those measurements supposed to show specific interactions which stem from the same membrane sheet used for the competition experiment with free antibodies, AB: free antibodies in solution, SDS: antibody denatured by sodium dodecyl sulfate, bare: non-functionalised bare silicon nitride cantilever. The bars show the mean values, the error bars correspond to the standard deviation and the grey circles show the values of individual force maps.

To shed more light on the latter hypothesis, measurements with non-functionalised cantilevers and denatured antibodies on the cantilever were performed. Due to the changed experimental approach of MR-AFM with nanobodies linked to the cantilever (see section 4.1.5) all experiments described in this section were only carried out a single time. First, a completely functionalised cantilever was subject to denaturation of the bound anti-Syx-ABs by incubation in 2 % sodium dodecyl sulfate in ultrapure water over night. Subsequent MR-AFM measurements of 16×16 force maps yielded a relative frequency of events of f_e = (29 ± 42) % (mean ± SD) (N = 3 maps on three membrane sheets from a single preparation). Note the large deviation of the relative frequency among individual maps (see also Figure 4.9). Furthermore, a bare silicon nitride cantilever was used to probe unspecific interactions. The corresponding measurements of 16×16 force maps show a mean relative

frequency of occurrence of an event of $f_e = (13 \pm 10)$ % (mean ± SD) ($N = 3$ maps on three membrane sheets from a single preparation). Despite the large variations among individual maps, the mean relative frequency of events in the case of the denatured antibody is close to that of the non-denatured. However, this statement is not quite robust since the mean value is largely increased by a single value at about 80 %. Furthermore, the measurements with the bare cantilever show that a subset of the events observed in MR-AFM experiments with a native antibody might stem from non-functionalised parts of the silicon nitride cantilever. A deeper discussion of possible non-specific interactions will be given in section 5.1.3.

4.1.3.2 MR-AFM experiments with unfixed membrane sheets

Since control experiments and measurements with antibodies supposed to be coupled to the cantilever yielded similar relative frequencies of events, the question arose whether fixation might render the epitopes inaccessible for the antibodies or alter in a way that specific interactions are inhibited. If that was the case, a larger binding probability would be expected in unfixed membrane sheets. Therefore, during preparation (see section 3.2.2) the fixation was left out but instead the sheets were washed directly with buffer and stained afterwards. In a single experiment 32×32 force maps were recorded whose analysis yielded a relative frequency of events of $f_e = (7 \pm 7)$ % (mean ± SD) ($N = 3$ maps on three membrane sheets from a single preparation) and, therefore, about four times smaller than in the case of fixed membrane sheets. Thus, this finding contradicts the above hypothesis. It might be that the non-fixed structures described in section 4.1.9 slipped upon approach of the cantilever which could lead to the significantly reduced value of f_e.

4.1.4 Control of antibody binding

The experiments presented in section 4.1.3 raised doubts that the observed binding events and the corresponding clusters are caused by specific interactions between syntaxin-1 molecules in the membrane sheets and their binding partner on the cantilever tip. In order to state on this issue, immunostaining experiments with the antibody used for the experiments described in the previous section (clone 78.2, Synaptic Systems, Göttingen, Germany) were performed on PC12-WT-1 membrane sheets. In four independent experiments ($N = 5$

experiments in total), no specific binding of syntaxin-1 could be observed, neither by CLSM nor by conventional epifluorescence microscopy. A typical image is shown in Figure 4.10 d. Only in a single additional experiment significant fluorescence intensity was present in the syntaxin-1 channel (see Figure 4.10 e).
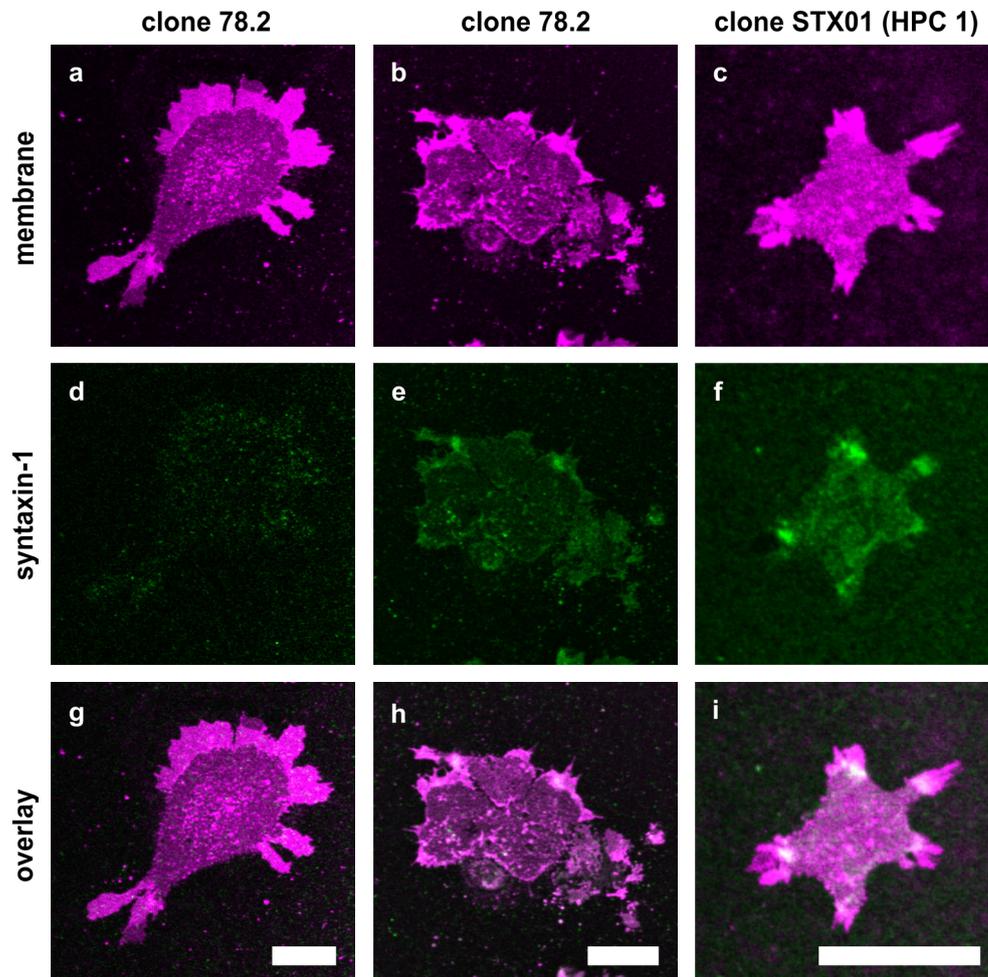
Figure 4.10: Immunostaining of PC12-WT-1 membrane sheets to evaluate binding efficiencies of distinct clones of anti-Syx-ABs visualised by CLSM. For staining of syntaxin-1 clone 78.2, (Synaptic Systems, Göttingen, Germany) (**a**, **b**, **d**, **e**, **g** and **h**) and clone STX01 (HPC 1) (abcam, Cambridge, United Kingdom) (**c**, **f** and **i**) were used. The magenta channel (**a**, **b** and **c**) shows the fluorescence of the membrane label, the green channel (**d**, **e** and **f**) that of the syntaxin-1 marker. An overlay is presented in the third row (**g**, **h**, **i**). The absolute intensities of different membrane sheets are not to be compared quantitatively. Scale bars: 10 μm.

However, a measurement during the incubation of anti-Syx-ABs already has shown slight but still well visible fluorescence in that channel. When regarding the overlay of the membrane and the syntaxin-1 antibody channel, a large colocalisation is apparent. These findings might indicate that the binding occurred in an unspecific way. Regardless of that single experiment, the other four have shown a poor binding efficiency of the antibodies. When staining was

performed by the anti-Syx-AB clone STX01 (HPC 1) (abcam, Cambridge, United Kingdom) in a single experiment a detection of structure on the membrane sheet was observed (see Figure 4.10 f). Further successful immunostainings with that clone are described in sections 4.1.1 and 4.1.6.3. When comparing the overlay images of the successful stainings of both clones of anti-Syx-ABs (Figure 4.10 h and i), in the case of clone STX01 (HPC 1) (Figure 4.10 i) the colocalisation of the fluorescence caused by the anti-Syx-AB with structures of the membrane channel (magenta) is less pronounced than in the case of clone 78.2 (Figure 4.10 h). Note especially the presence of dark magenta structures pointing to the absence of fluorescence from the syntaxin-1 label in Figure 4.10 i as compared with Figure 4.10 h. For the latter one also note the generally lighter colour in the overlay image compared with the channel of pure fluorescence of the membrane label (Figure 4.10 b), indicating the almost identical structure detected in both channels. Thus, it seems plausible that in the staining performed with clone 78.2 more unspecific binding with the membrane occurred than in the one with clone STX01 (HPC 1).

To test the antibody binding, a western blot by staining with clone 78.2 (Figure 4.11 a) and clone STX01 (HPC 1) (Figure 4.11 b) was performed by Jonas Schäfer (department of Prof. Claudia Steinem, Institute of Organic and Biomolecular Chemistry, University of Göttingen).
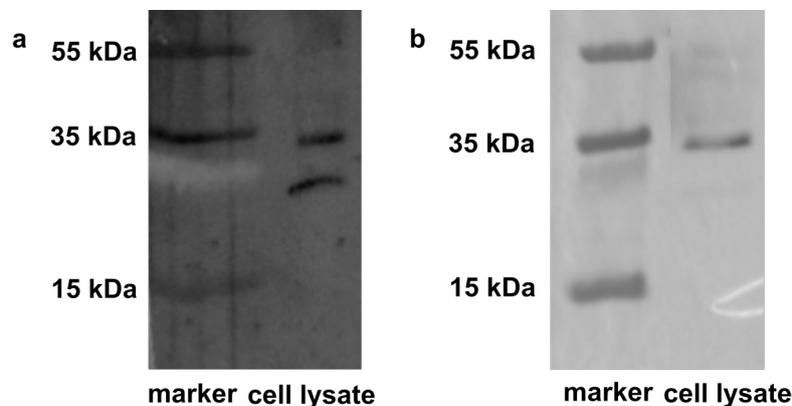
Figure 4.11: Western blots of lysates from PC12-WT-1 cells stained with distinct clones of antibodies. The detection of syntaxin-1 was performed by clone 78.2, (Synaptic Systems, Göttingen, Germany) (**a**) or by clone STX01 (HPC 1) (abcam, Cambridge, United Kingdom) (**b**). Both nitrocellulose membranes used for the detection by the distinct clones were derived from the same gel electrophoresis and western blot. Parts of the gel electrophoresis, western blotting and immunostaining were performed by Jonas Schäfer (department of Prof. Claudia Steinem, Institute of Organic and Biomolecular Chemistry, University of Göttingen).

In both cases a band at around 35 kDa is present. In the case of clone 78.2 a further band at less than 25 kDa (white band in the first lane of Figure 4.11 a) of unknown origin is visible which might be present in Figure 4.11 b with a very low intensity. At around 55 kDa dark

structures might represent a further recognition by both clones. The western blots show that clone 78.2 is capable of binding syntaxin-1, which has a mass of approximately 35 kDa,[146] but the absence of a further pronounced band in the case of clone STX01 (HPC 1) indicates a better suitability of the latter one.

Taken together, the investigation of both clones of anti-Syx-ABs indicates a successful detection of syntaxin-1 for both clones, at least in western blots, however, clone STX01 (HPC 1) shows less false positive bands in the western blot and performs better in immunofluorescence experiments. This might contribute to insufficient detection of syntaxin-1 in MR-AFM experiments. Furthermore, clone STX01 (HPC 1) was therefore used for following immunostaining experiments exclusively.

4.1.5 Molecular recognition AFM with nanobodies and PC12-WT-1 membrane sheets

The experiments described in sections 4.1.3 and 4.1.4 have revealed difficulties in detection of syntaxin-1 in MR-AFM as well as in immunostaining with the initially used anti-Syx-AB. Even though the second clone performed better, the use of nanobodies raised against syntaxin-1A (anti-Syx-NBs) seems to be more appropriate since nanobodies are described to show a better accessibility for the epitope and to possess a high stability.[119] Moreover, the nanobodies used for the present thesis[9] were modified at their C-terminus by adding a cysteine, so that the molecules could be bound regioselectively.

4.1.5.1 Purification of nanobodies after pre-use treatment

After the incubation of nanobodies with TCEP immediately before being coupled to the cantilever, the nanobodies were subject to size exclusion chromatography to remove TCEP. The fractions collected by chromatography were analysed by UV-Vis spectroscopy to confirm the presence of nanobodies and to identify the fraction with the largest concentration. Figure

---

[9] The nanobodies were produced and kindly provided by Dr. Manuel Maidorn, Dr. L. Felipe Opazo Davila and Prof. Silvio O. Rizzoli (University Medical Center Göttingen).

4.12 shows a representative set of UV-Vis spectra from a single experiment (out of $N = 6$ independent experiments).
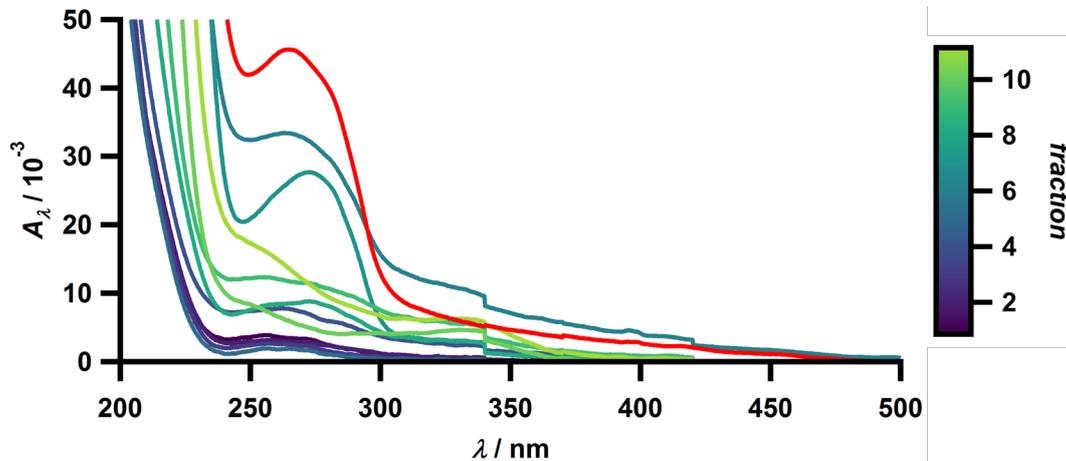
Figure 4.12: UV-Vis spectra of fractions obtained from size exclusion chromatography of anti-Syx-NBs. The absorbance (A_λ) is plotted against the wavelength λ. The spectra shown are cut at $\lambda = 500$ nm and $A_\lambda = 5 \cdot 10^{-2}$, since the peak used for analysis is located at around 270 nm. The assignment to the fractions of 500 µl is given by the colour scale on the right. The red curve corresponds to dissolved anti-Syx-NBs of a concentration of 1.3 µM, which were not treated with TCEP.

Each fraction corresponds to the further addition of 500 µl buffer. In this specific preparation, the fraction with the largest concentration of nanobodies was the sixth fraction, corresponding to an added volume reaching from 2.5 to 3.0 ml. In general, this peak concentration was found in the range from 2.5 to 3.5 ml. Comparison with a solution of anti-Syx-NBs of a concentration of 1.3 µM (red curve in Figure 4.12), which was not subject to TCEP treatment, yields a concentration of about 1.0 µM for the fraction with the largest amount of syntaxin-1. Usually, concentrations of about 1 µM were found. This analysis reveals that a sufficiently high concentration of nanobodies for coupling to the cantilever was obtained, according to suggestions of the manufacturer of the bifunctional linkers used for cantilever functionalisation.

4.1.5.2 Molecular recognition AFM experiments

In order to investigate the distribution of syntaxin-1 in PC12 membrane sheets by a label free approach, MR-AFM with nanobodies coupled to the AFM cantilever was carried out on membrane sheets derived from PC12-WT-1 cells. For most experiments ($N = 15$ maps on

twelve sheets from ten independent preparations with eleven cantilevers from eight independent functionalisations), a retraction speed of 1 µm·s⁻¹ was set. Amination of the gold coated cantilever was performed by incubation with a 9:1 molar ratio of cysteamine and 11-amino-1-undecanethiol (AUT).

In Figure 4.13 a force curves picked randomly but with equal amounts (five per force map) from the curves showing an event of the above mentioned force maps are overlaid. For a detailed view of the small force regime see the subset of force curves shown in Figure 4.13 b (two force curves per map). As the presented force curves possess different shapes, identifying one typical shape is not reasonable, however, the red curve represents a force curve with a quite often observed shape with a typical maximum interaction force. Moreover, the general shape of most curves is similar. The force curves with a large maximum interaction force often show multiple smaller peaks, as for example evident from the purple curve marked by the arrowhead in Figure 4.13 a. These minor peaks might stem from multiple rupture events. The force curves in the third quadrant of Figure 4.13 a are biased by the analysis, because they do not reach force values larger than zero in the contact regime. This is caused by a binding event in the preceding force curve where the bond was not pulled until unbinding took place. Nonetheless, the maximum interaction force can be identified correctly, just the distance of this subset of force measurements will be erroneous and negative.
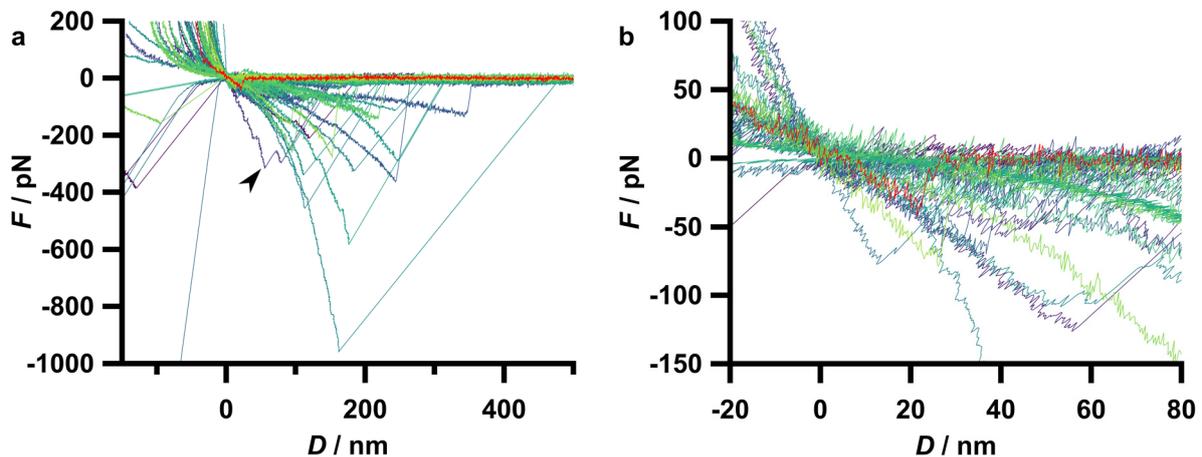
Figure 4.13: Arbitrarily chosen force curves obtained from MR-AFM experiments with nanobodies against syntaxin-1 coupled to the cantilever on PC12-WT-1 membrane sheets. The force curves were recorded with a cantilever retraction speed of 1 µm·s⁻¹. In **a** five randomly picked force curves per force map, 75 in total, are shown. The arrowhead marks a curve with multiple minor peaks. A magnification close to the zero-force point is plotted in **b**. For clarity, only two randomly picked force curves are presented per force map, i.e. 30 in total. The functionalisation was performed with a 9:1 molar ratio of cysteamine and AUT. The colours of the force curves are chosen arbitrarily to provide better distinguishability, except the additional red curve which exhibits a rather typical shape. Note that in **a** some curves are cut at negative distances for this representation.

For MR-AFM imaging spatial distributions of events are investigated. Thus, the focus is set on a single force map next. The distribution of detected maximum interaction forces of a single force map is shown by the red histogram in Figure 4.14 a. For comparison, the distribution of maximum interaction forces of all 13248 force curves from the 15 force maps described above is added to the plot by the blue histogram. Due to the pronounced positive skew of these distributions, median values and percentiles are regarded in the following instead of means and standard deviations. In this case, the median values are 77 pN and 50 pN, the 30th percentiles are 41 pN and 33 pN and the 70th percentiles are 153 pN and 93 pN for the selected force map and all force maps, respectively. This shows that a single force map reproduces the values of a larger set of measurements to some extent, however, small deviations are to be expected even when comparing individual measurements of the same system. Nevertheless, qualitative comparison of the shapes of the histograms shows a quite good correlation. For those force curves for which a positive rupture distance was detected, the Pearson correlation coefficient of $\rho = 0.32$ indicates a general increase of the maximum interaction force with the rupture distance, especially when considering the huge number of underlying data ($N = 12601$).

A possible spatial organisation of the maximum interaction force values might be inferred from the corresponding force map in Figure 4.14 b, where force values for pixels without a detected event in the force curve were set to zero.
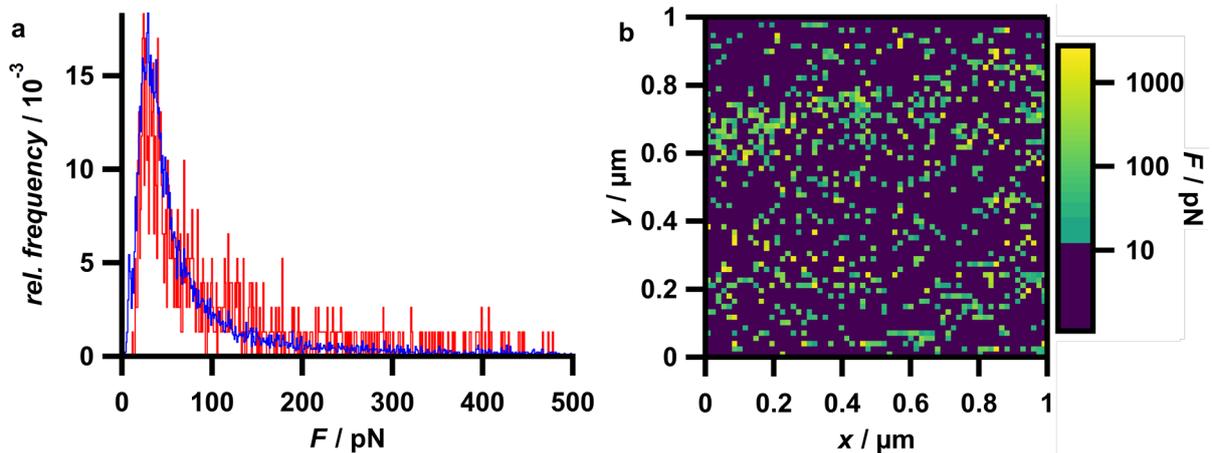
Figure 4.14: Force histogram and force map of a MR-AFM measurement with nanobodies coupled to the cantilever on a PC12-WT-1 membrane sheet. In **a** histograms are shown where the red one represents the histogram of a single map ($N = 765$) and the blue one that of all 15 maps of the same system ($N = 13248$). The histograms are cut at 0 pN (0.03 % of the values for the blue curve) and 500 pN (11.6 % for the red and 9.3 % for the blue curve). The histograms show the relative (rel.) frequency of force values within a bin size. The plot in **b** shows the spatial distribution of the maximum interaction forces plotted by the red histogram in **a**. Force values at locations without a detected event were set to zero.

This representation shows that, despite a heterogeneous distribution of the events regardless of the force values which is already evident without a quantitative analysis, forces of different magnitudes are localised almost equally to distinct regions. The cluster analysis corresponding to this map is shown in Figure 4.15 a and b.

To provide an overview of the obtained results from cluster analyses, Figure 4.15 presents two limiting cases of outcomes from Ripley's *K*-function cluster analysis. The one in Figure 4.15 a and b yields a few rather tiny clusters, among which two are situated inside the orange square and therefore not influenced by boundary effects. By comparison with the one shown in Figure 4.15 c and d, the latter one does not yield multiple small clusters but a larger accumulation of clustered events close to the boundary of the investigated area. Remarkably, the size of this accumulation seems to be larger than one micrometre. In Figure 4.15 b some events organised in a line along the *x*-axis can be found. As the *x*-axis is the fast scanning axis of the AFM, these pixels represent subsequently measured locations. However, this is a rather seldom observed phenomenon. When compared with Figure 4.14 b, no accumulation of predominantly larger or smaller forces can be identified within the clusters.

For all of the corresponding 15 force maps, the $L_j(r)-r$ values are, at least for a short range of distances r, distinct from the random values which most probably in all cases indicates a heterogeneous distribution of the detected events. A hard discrimination between both limiting cases presented in Figure 4.15 is not reasonable. The value of $L(r_{max})-r_{max}$ is in both cases about 6 nm and can consequently not serve as a criterion for discrimination. Furthermore, an identification of cluster sizes is irrational since many clusters and all larger accumulations are cut at the boundary of the investigated area or at least parts of the clusters are located closer than r_{max} to the boundary. Therefore, the description of the identified clusters has to be kept qualitative. To this end, it can be stated that at least half of the cluster analyses yielded pronounced clusters like those shown in Figure 4.15 b, which, however, might partially be caused by boundary effects. The relative frequency of events for 14 maps among these 15 ones which were recorded with a dwell time of 0.5 s (*vide infra*) is $f_e = (22 \pm 8)$ % (mean ± SD).
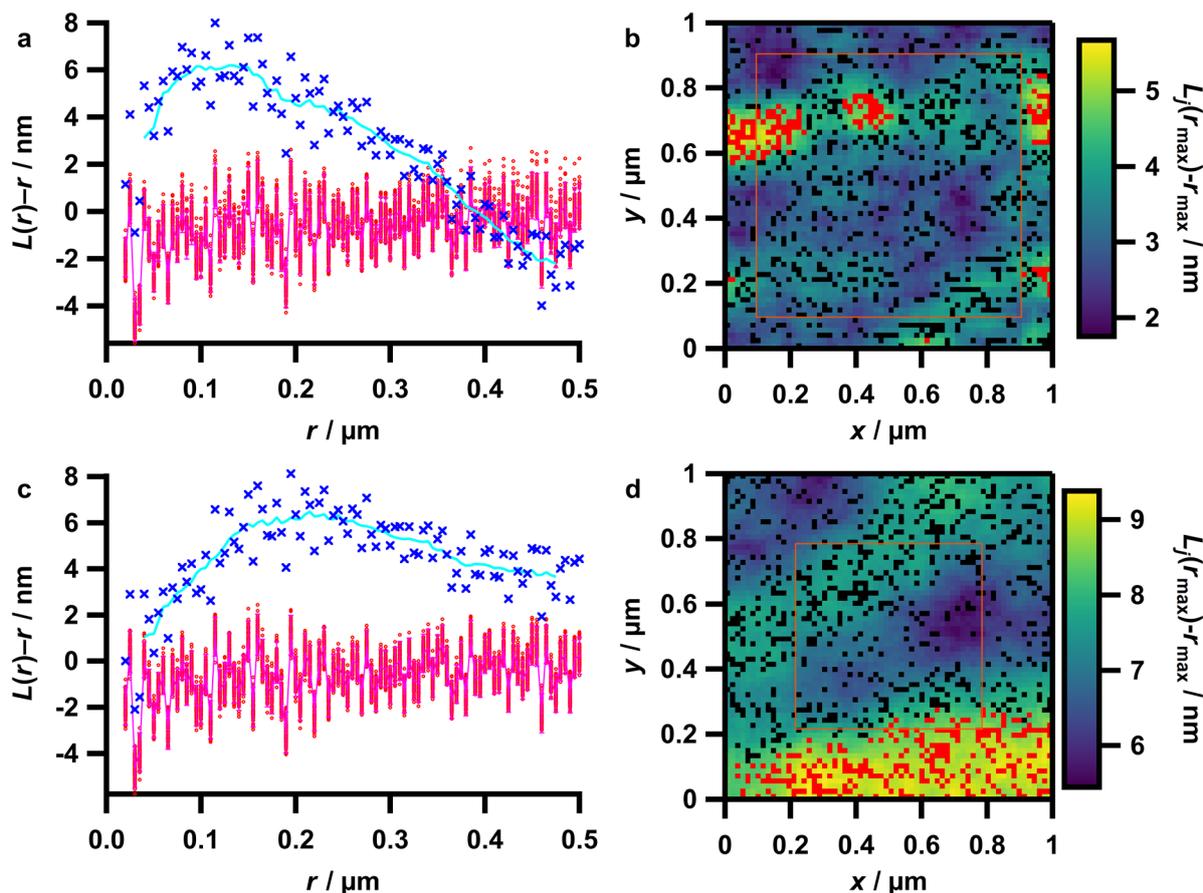
Figure 4.15: Examples of Ripley cluster analyses for MR-AFM experiments with nanobodies coupled to the cantilever on PC12-WT-1 membrane sheets. In **a** and **b** an example of a cluster analysis showing the presence of well defined, small sized clusters, some of them in the centre of the investigated area, is presented. In **c** and **d** a typical representative of an analysis uncovering a larger accumulation of clustered events at the rim of the investigated area is shown. **a** and **c** plot the $L(r){-}r$ values of the measured data (× and cyan line) and for homogeneous random data of the same number of events (○ and magenta line) as a function of r. In **b** and **d** the overlay of the Ripley density maps and the corresponding clustered events (red) and all other events (black) are shown. For details see caption of Figure 3.18.

Most of the 15 force maps measured by anti-Syx-NBs on PC12-WT-1 cell membrane sheets at a retraction speed of 1 µm·s^{-1} were recorded with an edge length of 1 µm. However, since large accumulations of clustered events were identified in these maps, the investigation of a larger area seems to be intuitive. By this means it might, moreover, be possible to identify more clusters as compared to the smaller maps, which might bare the risk of measuring in an area depleted of clusters. Furthermore, by measuring in a smaller area, one might identify tiny clusters which are too small to be uncovered by a map of 1×1 µm^2 in size. To this end, two maps with 5 µm, one with 3 µm and two with 0.25 µm edge length were measured among these 15 maps. However, in the larger maps even larger regions of clustered events, in one case similar to the situation shown in Figure 4.15 d, were detected. The analysis of the small-sized maps yielded in one case where the force curves were recorded with a dwell

time of only 0.05 s few small clusters of about 20 nm in diameter. Thus, the detection of regions of clustered events at the border of the investigated area is probably not just caused by the small size of the map. Generally, the organisation of clustered events within the maps is quite similar, regardless of the size of the investigated area.

A measurement of one of the aforementioned maps took almost three hours. Besides the time consumption, a further problem of such long measurements might be a lateral drift of the cantilever relative to the sample. In two independent experiments under the same conditions as used for the MR-AFM experiments described above lateral drifts of 1.3 µm and 0.6 µm were identified from two FD-AFM images recorded immediately before and after the measurement of the force map. To speed-up the measurement in order to decrease the lateral drift and to render the measurements less time consuming, an increase of the hydrodynamic drag and therefore a larger inaccuracy of the detected forces was accepted by increasing the approach speed to $25\,\mu m \cdot s^{-1}$ and the retraction speed to $5\,\mu m \cdot s^{-1}$. Additionally, the ratio of cysteamine to AUT was changed to 3:1 for increasing the amount of flexible linkers. In two corresponding MR-AFM measurements with an anti-Syx-NB-functionalisation of the cantilever on PC12-WT-1 membrane sheets inside an area of $0.5 \times 0.5\,\mu m^2$, again few small clusters were identified (see Supplementary Figure 1).

Taken together, the experiments described in this section have revealed the presence of spatially clustered interaction events in the recorded MR-AFM maps on PC12-WT-1 membrane sheets. However, as described in section 4.1.3 for measurements with IgG-antibodies coupled to the cantilever, it is not known whether these events are caused by specific interactions, and therefore show clustering of syntaxin-1, or other heterogeneously arranged structures cause unspecific interactions with the cantilever. To elucidate this question, a couple of control experiments were carried out, which are described in the following section.

4.1.6   Control experiments for MR-AFM investigations of syntaxin-1 clustering

4.1.6.1   Competition by free nanobodies in solution

To probe the specificity of the observed interactions between cantilevers modified by anti-Syx-NBs and PC12 membrane sheets, a first set of control experiments ($N = 2$ maps on two sheets from two independent preparations with two cantilevers from two independent

functionalisations) was performed by adding a solution of nanobodies (final concentrations of 0.02 and 0.10 µM), to the measuring buffer to compete for the epitopes on the syntaxin-1 molecules. The solution of nanobodies was identical to the solution used for the coupling procedure of the cantilevers utilised for the same experiment. The measurements were carried out at a retraction speed of 1 µm·s⁻¹ with cantilevers coupled by a 9:1-mixture of cysteamine and AUT. In independent measurements a dependency of the relative frequency of events on the dwell time was observed in the presence as well as in the absence of free nanobodies in solution (see Supplementary Figure 3). Therefore, for the second measurement the dwell time was decreased to 0.05 s and the edge length of the map to 0.25 µm. Prior to the addition of the nanobodies, a map to obtain data for the unbiased situation was recorded. Due to the small size of the measured maps and to the necessity to remove the cantilever for the addition of the nanobodies, the second map under presence of free nanobodies in solution could not be measured at exactly the same location. However, it was tried to record the map as close as possible to the first one. In the first measurement with a dwell time of 0.5 s the relative frequency of events was f_e = 36.6 % and f_e = 22.3 % and in the second experiment with a dwell time of 0.05 s the relative frequency of events was f_e = 19.6 % and f_e = 42.3 %, before and after the addition of the nanobodies, respectively. In the first experiment the relative frequency of events is smaller in the map recorded after the addition of the nanobodies, however, it almost perfectly matches the mean value of all the 14 maps, mentioned in section 4.1.5.2 which were recorded without free nanobodies in solution with the same dwell time.
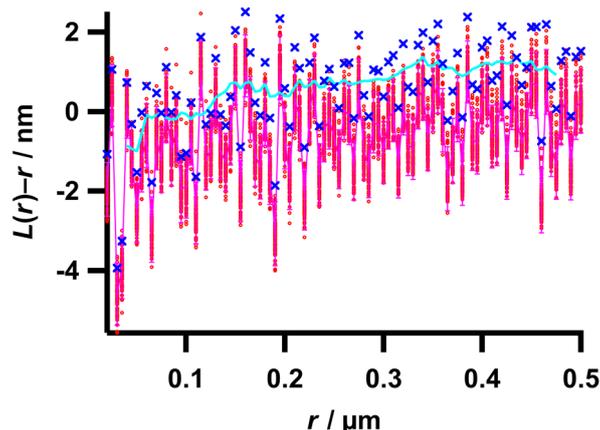
Figure 4.16: Ripley analysis of a close-to random distribution for a MR-AFM measurement under presence of free nanobodies in solution. The $L(r){-}r$ values of the measured data (× and cyan line) and for homogeneous random data of the same number of events (○ and magenta line) are plotted as a function of r. For details see caption of Figure 3.18.

For the second experiment the value of the relative frequency is even larger after the addition of the nanobodies. Nevertheless, it might be that clustering is altered. Indeed, for the first measurement the $L(r)-r$-values hardly deviate from the homogeneous random distribution (see Figure 4.16). However, in the second experiment clusters were observed with and without free nanobodies in solution (see Supplementary Figure 2).

This outcome might point to a predominate detection of unspecific interactions meaning that the identified clusters do not stem from syntaxin-1. On the other hand, possible explanations are that nanobodies from solution are somehow attached to the cantilever and induce further events or that the competition is not sufficient (see also discussion in section 5.1.2). Therefore, control experiments were to be carried out with a system that is not capable of showing specific interactions.

4.1.6.2 Control experiments with cantilevers modified by non-recognisable nanobodies

In order to perform experiments which exclude specific interactions, OBL-10 cantilevers were functionalised with a nanobody raised against mCherry, which is as a mutant protein derived from *Discosoma*, not present in mammalian cells.[147] In both experiments carried out with this functionalisation, a 3:1 mixture of cysteamine and AUT was used for the amination of the cantilever. Figure 4.17 shows a selection of force curves which were picked randomly from these maps. Here, the relative frequency of events was determined to be f_e = 23.3 % and f_e = 19.4 %, and thereby lying within the mean ± SD-interval of the corresponding maps with anti-Syx-NBs coupled to the cantilever. The events were in both cases distributed non-homogeneously and the maps showed two or three regions of clustered events (see Supplementary Figure 4).

Consequently, interactions between the cantilever and membrane sheets do also occur when specific interactions are prohibited by the use of a, with respect to the biological system which is investigated, non-functional nanobody. Moreover, even these unspecific interaction events organise into cluster-like regions.
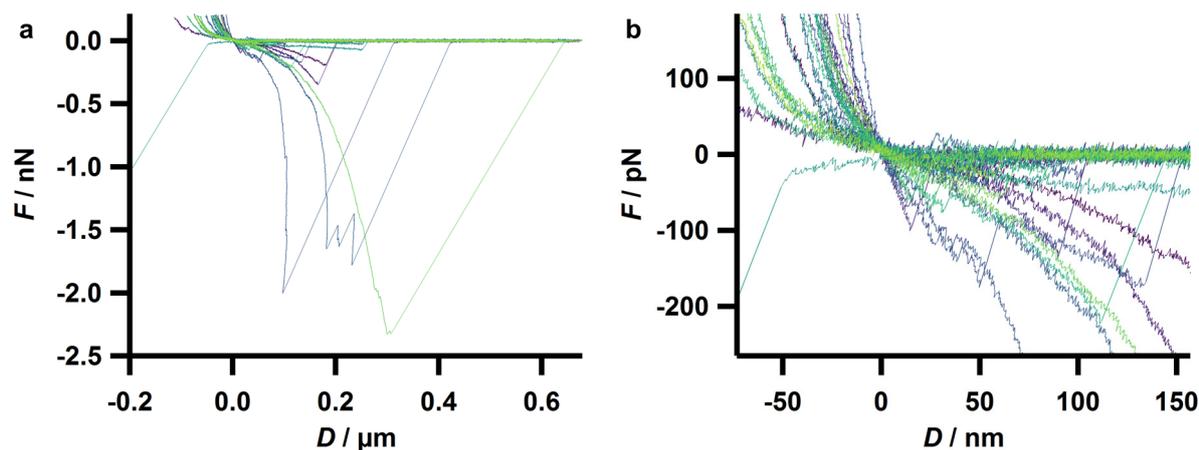
Figure 4.17: Arbitrarily chosen force curves obtained from MR-AFM experiments with nanobodies against mCherry coupled to the cantilever on PC12-WT-1 membrane sheets. The force curves were recorded with a cantilever retraction speed of 1 μm·s⁻¹. In **a** 15 randomly picked force curves per force map, 30 in total, are shown. A magnification close to the zero-force point is plotted in **b**. The functionalisation was performed with a 3:1 molar ratio of cysteamine and AUT. The colours of the force curves are chosen arbitrarily to provide better distinguishability. Note that in **a** one curve is cut at negative distances for this representation.

4.1.6.3 Control experiments with membrane sheets derived from syntaxin-1 knockdown PC12 cells

The results obtained in section 4.1.6.2 have revealed the occurrence of clusters caused by unspecific interactions. With the purpose of unravelling discrepancies in the relative frequency of events and possibly in the frequency of appearance and morphology of clusters, a flexible system which enables switching between enabled and disabled specific interactions was to be used. As doubts about the reliability of a competition experiment have been raised before (see section 4.1.6.1), membrane sheets derived from syntaxin-1A and syntaxin-1B double knockdown PC12 cells (PC12-Syx-KD) were utilised for further experiments.

To test the efficiency of the knockdown and to state on the remaining fraction of syntaxin-1, western blots of cell lysates from different types of PC12 cells were carried out first. Parts of the gel electrophoresis, the western blotting and luminescent staining were performed by Jonas Schäfer (department of Prof. Claudia Steinem, Institute of Organic and Biomolecular Chemistry, University of Göttingen) (PC12-WT-1 and PC12-Syx-KD: N = 4 lanes from two independent experiments, PC12-WT-2: N = 2 lanes from one experiment).
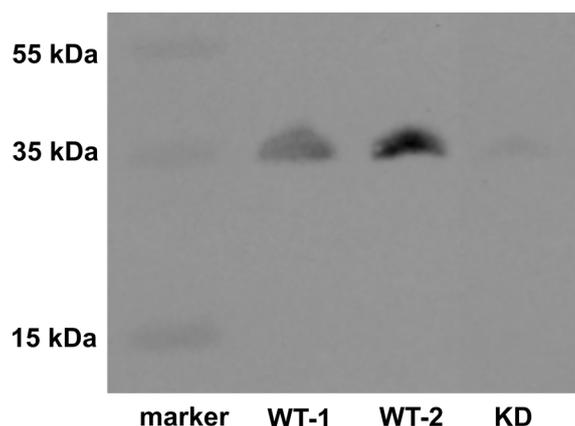
Figure 4.18: Representative western blot of cell lysates derived from different types of PC12 cells. For all lanes the same total mass of protein was applied to gel electrophoresis. The captions of the lanes denote: marker: protein ladder, WT-1: PC12-WT-1 cells, WT-2: PC12-WT-2 cells, KD: PC12-Syx-KD cells. Parts of the gel electrophoresis, western blotting and immunostaining were performed by Jonas Schäfer (department of Prof. Claudia Steinem, Institute of Organic and Biomolecular Chemistry, University of Göttingen).

The representative photograph of a western blot in Figure 4.18 indicates that the amount of syntaxin-1 is drastically decreased in PC12-Syx-KD cells as compared with both types of wild type cells. Nevertheless, still a small amount of syntaxin-1 is detected in the rightmost lane. By numbers, the integrated luminescence intensities of the bands of cell lysate from PC12-Syx-KD cells were 8 %, 9 %, 10 % and 10 % of that of the corresponding bands from PC12-WT-1 cells and 4 % and 5 % of that of PC12-WT-2 cells.

To further test the knockdown on membrane sheets and to evaluate whether syntaxin-1 is expressed in all cells to an equal level or whether a small subset of cells is not affected by the knockdown at all quantitative immunostaining experiments were performed. That issue may be of importance since in the second case a single measurement might accidentally be performed on a cell with wild type phenotype. Confocal fluorescence micrographs along with the quantitative analysis of the syntaxin-1 level are presented in Figure 4.19. From the fluorescence of the syntaxin-1 label of the PC12-Syx-KD membrane sheet (Figure 4.19 f) as compared with that of a PC12-WT-1 (Figure 4.19 d) and a PC12-WT-2 (Figure 4.19 e) membrane sheet, a considerably smaller level of syntaxin-1 in the membrane sheet of the knockdown cell is evident, consistent with the results of the western blot (Figure 4.18). A non-homogeneous distribution of syntaxin-1 on the membrane sheet can be assumed from images of the wild type membrane sheets (Figure 4.19 d and e).
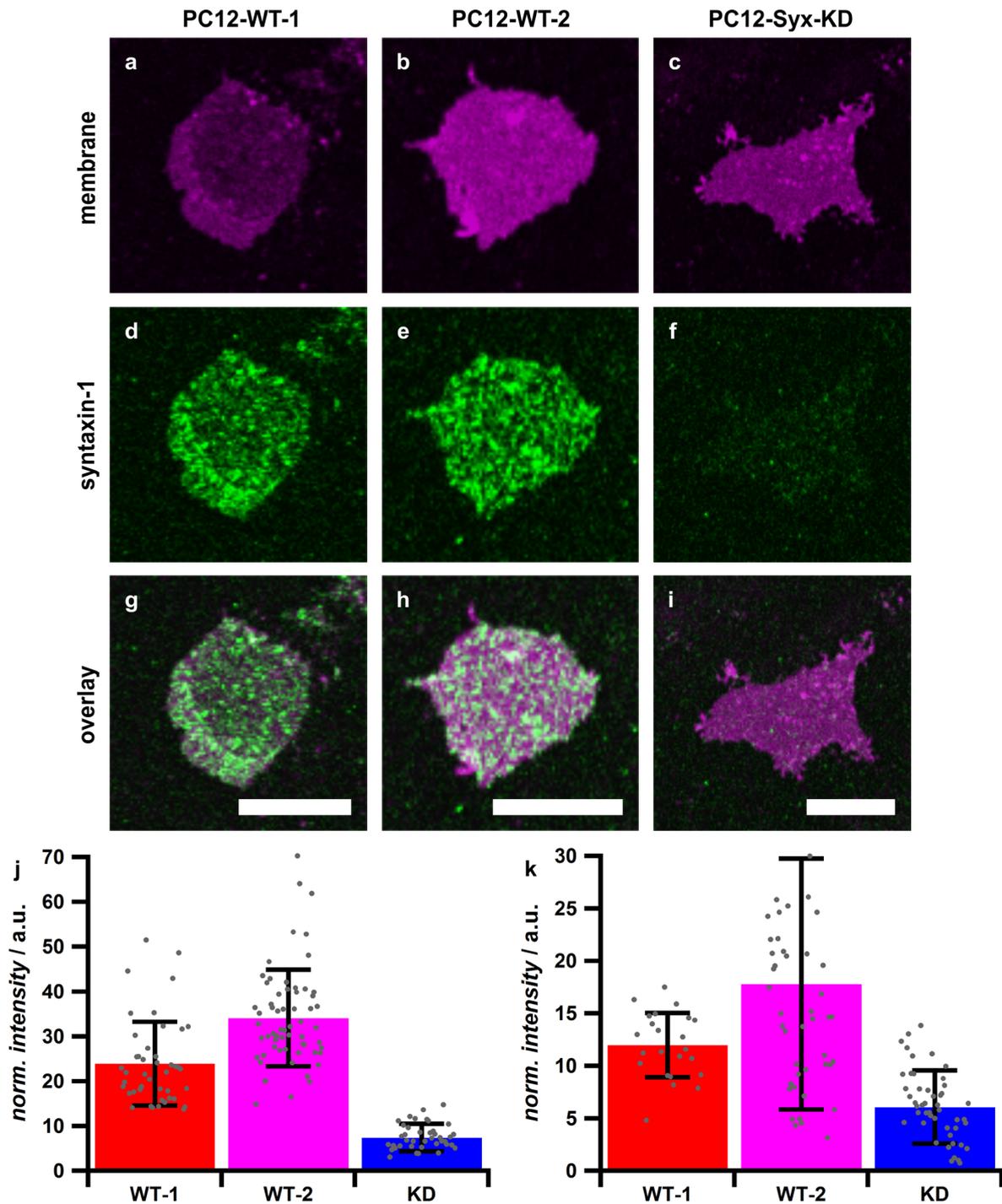
Figure 4.19: Test of the efficiency of the knockdown by CLSM. a-i show representative CLSM images of different types of PC12 cell membrane sheets, immunostained for syntaxin-1. The magenta channel (**a**, **b** and **c**) shows the fluorescence of the membrane marker, the green channel (**d**, **e** and **f**) that of the syntaxin-1 marker. In the third row (**g**, **h**, **i**) an overlay is presented. The sheet shown in **a**, **d** and **g** is derived from a PC12-WT-1, the one in **b**, **e** and **h** from a PC12-WT-2 and the one in **c**, **f** and **i** stems from a PC12-Syx-KD cell. Scale bars: 10 μm. In **j** and **k** the normalised intensities of the fluorescence of the syntaxin-1 marker of two independent experiments are plotted. The bars correspond to the mean values of the intensity of membrane sheets derived from PC12-WT-1 cells (WT-1, red), PC12-WT-2 cells (WT-2, magenta) and PC12-Syx-KD cells (KD, blue). Error bars indicate the standard deviations. The grey circles correspond to individual values from single membrane sheets. In the representation in **k**, four outliers of WT-2 above 30 a.u. and one of KD at negative values were left out.

In Figure 4.19 j and Figure 4.19 k the results of the quantitative analyses of the fluorescence of the syntaxin-1 label from two independent experiments are shown (PC12-WT-1: $N = 44$ and $N = 23$ sheets, PC12-WT-2: $N = 62$ and $N = 47$ sheets, PC12-Syx-KD: $N = 41$ and $N = 49$ sheets, for the two independent preparations, respectively). In both experiments a lower syntaxin-1 level is identified for the knockdown cells. In the first experiment (Figure 4.19 j) the difference between the knockdown and both wild type cells is significant, as the intervals of the mean ± SD do not overlap. In the second experiment (Figure 4.19 k) the difference is not as pronounced as in the first one, but still the mean value of the PC12-Syx-KD membrane sheets does not fall into the mean ± SD interval of the PC12-WT-1 cells and *vice versa*, and the mean value of the knockdown cell membrane sheets corresponds roughly to the mean $-$ SD value of the PC12-WT-2 cells. This quantitative analysis of a larger dataset reproduces the statements given for the CLSM images before.

In Figure 4.19 j there is not a single value for knockdown cells on a level determined for wild type cells, pointing to the hypothesis that all cells are affected by the knockdown. However, this does not hold for the second experiment. Here, the larger relative error for the knockdown and the PC12-WT-2 cells as compared with the corresponding relative errors of the first experiment might point to a better reliability of the first experiment.

Having shown that most probably all PC12-Syx-KD cells express a diminished amount of syntaxin-1, control experiments can be considered as trustable without major concerns to accidentally measure on cell membrane sheets containing a wild type level of syntaxin-1.

Measurements with anti-Syx-NB functionalised cantilevers on PC12-Syx-KD membrane sheets ($N = 5$ maps on four sheets from two independent preparations with four cantilevers from two independent functionalisations) were performed within an area of 0.5 µm edge length and with cantilevers functionalised with a 3:1 mixture of cysteamine and AUT (two maps with two different cantilevers) or with a 9:1 mixture (three maps with two different cantilevers). In the first case the retraction speed was set to 1 µm·s^{-1}, in the latter one to 5 µm·s^{-1}. For two maps recorded with the fast retraction speed the dwell time was decreased to 0.05 s. With that diversity of settings it was intended to identify parameters leading to a low amount of unspecific interactions. In Figure 4.20 a randomly chosen selection of force curves from the two maps recorded with a retraction speed of 1 µm·s^{-1} is shown.
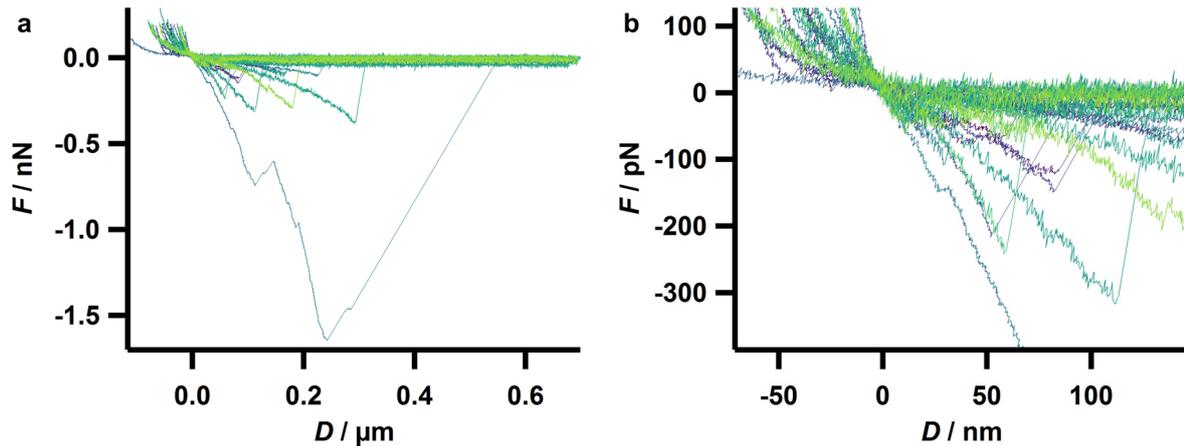
Figure 4.20: Arbitrarily chosen force curves obtained from MR-AFM experiments with nanobodies against syntaxin-1 coupled to the cantilever on PC12-Syx-KD membrane sheets. The force curves were recorded with a cantilever retraction speed of 1 µm·s⁻¹. In **a** 15 randomly picked force curves per force map, 30 in total, are shown. A magnification close to the zero-force point is plotted in **b**. The functionalisation was performed with a 3:1 molar ratio of cysteamine and AUT. The colours of the force curves are chosen arbitrarily to provide better distinguishability.

Essentially, these experiments show the same as the other control experiments and those supposed to identify the distribution of syntaxin-1 specifically. The maps recorded with the first cantilever functionalisation method mentioned above yielded smaller clusters, the latter one more or less larger accumulations of clustered events. For the measurements with a dwell time of 0.5 s the relative frequency of events was determined to be $f_e = (40 \pm 20)$ % (mean ± SD) ($N = 3$ maps on three sheets from two independent preparations with three cantilevers from two independent functionalisations), thereby even larger than that of the corresponding measurements on membrane sheets derived from wild type cells. Since a shorter dwell time leads to less interactions between sample and probe (see Supplementary Figure 3) only force maps recorded with the same dwell time as used for the measurements supposed to show specific interactions were taken into account. In essence, these measurements confirm the outcome of the other control experiments: Presumably unspecific interactions are abundant and group into clusters. A more detailed discussion will be given in section 5.1.2. A cumulative probability plot of the measured maximum interaction forces and rupture distances is given in Figure 4.22. Further experiments which directly compare maps recorded on knockdown and wild type membrane sheets with exactly the same cantilever are described in section 4.1.7.

4.1.6.4 Insight into the nature of the unspecific interactions

The results obtained in sections 4.1.6.1-4.1.6.3 indicate a frequent occurrence of unspecific interactions. To figure out whether these interactions are caused by the lipid membrane alone or by additional structures such as proteins residing on the membrane sheets, 16×16 force maps with anti-Syx-NB functionalised gold coated cantilevers were recorded inside a quadratic area of 2 µm edge length on membrane patches derived from pure lipid giant unilamellar vesicles (N = 36 maps on twelve GUV-MPs from two independent preparations with four cantilevers from two independent functionalisations). These experiments yielded a relative frequency of events of f_e = (28 ± 20) % (mean ± SD). For comparison, corresponding 16×16 maps inside a quadratic area of one time 10 µm and two times 20 µm edge length with anti-Syx-AB functionalised silicon nitride cantilevers showed relative frequencies of f_e = 12.1 %, 1.6 % and 3.9 % (N = 3 maps on three GUV-MPs from a single preparation with a single cantilever). These values indicate that the gold coated and NB-functionalised cantilever, presumably in contrast to the AB-functionalised silicon nitride cantilever, already interacts frequently with a lipid membrane on glass. It has to be noted that the values for the silicon nitride cantilever are just to be interpreted as a rough estimate due to insufficient number of data. To state whether the interactions observed with the gold coated and nanobody-functionalised cantilever when measuring on membrane sheets are indeed caused by the lipid membrane alone, a more detailed look at the force- and distance distributions is necessary. To this end, in Figure 4.21 histograms and plots of the cumulative probability (cum. probability) of the measured maximum interaction forces and rupture distances are presented. For comparison serve force maps recorded on PC12-WT-1 membrane sheets (N = 36 maps on twelve sheets from two independent preparations with four cantilevers from two independent functionalisations) with the same settings as applied for the GUV-MPs, including the retraction speed of 5 µm·s^{-1}. For these the relative frequency of events was determined as f_e = (45 ± 22) % (mean ± SD). This mean value is larger than that of the measurements on GUV-MPs, but not significantly when regarding the standard deviations.

The median forces are 73 pN and 33 pN, the 30th percentiles are 49 pN and 28 pN and the 70th percentiles are 129 pN and 38 pN for membrane sheets and for GUV-MPs, respectively. The median rupture distances are 54 nm and 5 nm, the 30th percentiles are 32 nm and 3 nm and the 70th percentiles are 80 nm and 7 nm for membrane sheets and for GUV-MPs, respectively.
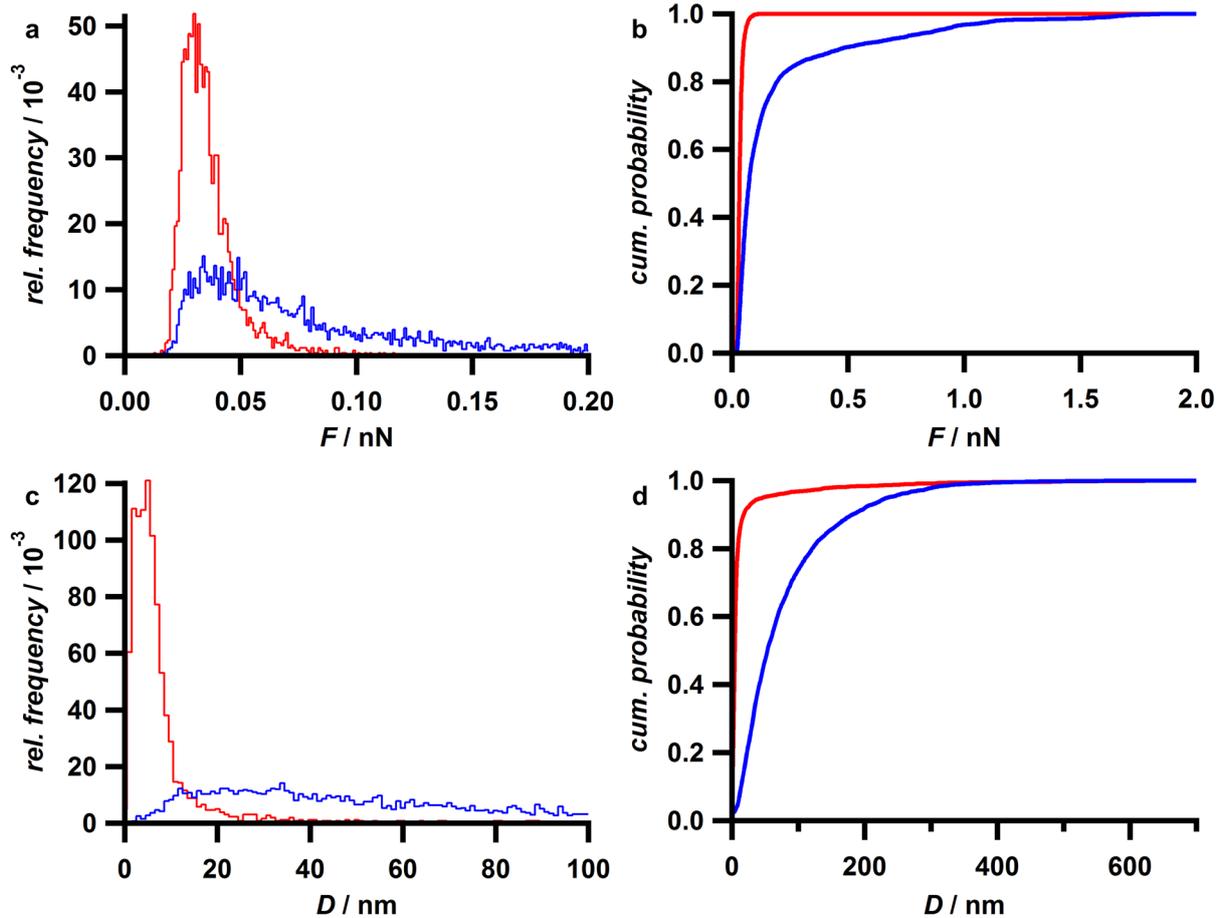
Figure 4.21: Force and distance distributions obtained by MR-AFM on membrane sheets and on GUV membrane patches. In **a** the histograms of the maximum interaction forces are shown, in **b** the cumulative probability plots of the forces, in **c** the histograms of the rupture distances and in **d** the cumulative probability plots of the rupture distances. Plots in blue denote data of membrane sheets ($N = 4101$), plots in red data of GUV-MPs ($N = 2604$). Note the different force and distances scales in the plots: The histograms show the small force or small distance regime, whereas the cumulative probability plots show the whole range of positive values. The plots of the distance are cut at $D = 0$. Thereby negative values, stemming from an inaccuracy in data recording, are omitted. These omitted values account for 2.0 % and 1.5 % of all data for membrane sheets and GUV-MPs, respectively.

Even though the most probable interaction force is quite similar for PC12 membrane sheets and artificial lipid bilayers (Figure 4.21 a), all other quantities differ. The distribution of the interaction forces with PC12 membrane sheets exhibits a pronounced positive skew, leading to a much larger median force. The distribution of the interaction forces with the artificial lipid membrane resembles a Gaussian like distribution which points to a simpler kind of interaction (for a more detailed discussion see section 5.1.3). More importantly, the distances at which the rupture takes place differ significantly. As the linker used in measurements on membrane sheets and on GUV-MPs is the same, the origin of the longer interaction in case of the PC12 derived membrane sheets has to lie in the structure of the sample. Therefore, it can be hypothesised that elongated structures, such as protein filaments, induce unspecific

interactions which unbind at long distances. This hypothesis will be further investigated in section 4.1.9.

4.1.6.5 Comparison of force and distance distributions

MR-AFM experiments performed with anti-Syx-NB functionalised cantilevers on PC12-WT-1 cells have revealed relative frequencies of events similar to the corresponding control experiments, except for the knockdown cells which show larger relative frequencies in two of three maps. For a more sophisticated analysis, the cumulative probabilities of the measured maximum interaction forces and of the rupture distances are plotted in Figure 4.22.
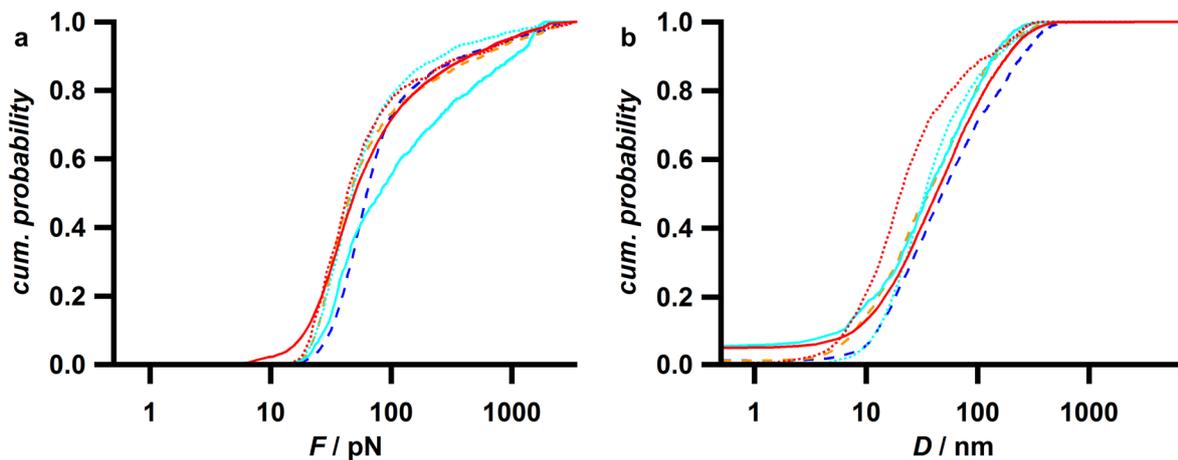
Figure 4.22: Force and distance distributions of MR-AFM experiments with anti-Syx-NB functionalised cantilevers on PC12-WT-1 membrane sheets and corresponding control experiments. The cumulative probability plots of the maximum interaction forces (**a**) and of the rupture distances (**b**) are shown. Data of experiments supposed to show specific interactions are plotted in red, data obtained by nanobody competition experiments in cyan, data measured with nanobodies raised against mCherry coupled to the cantilever in orange and those obtained from membrane sheets derived from PC12-Syx-KD cells in blue. Dotted lines correspond to experiments performed with a dwell time of 0.05 s, experiments corresponding to the dashed lines were performed with cantilevers which were aminated with a 3:1 mixture of cysteamine and AUT. In all other cases a dwell time of 0.5 s and a 9:1 mixture of aminoalkanethioles was used (experiments supposed to show specific interactions (0.5 s dwell time): $N = 12446$, experiments supposed to show specific interactions (0.05 s dwell time): $N = 802$, nanobody competition (0.5 s dwell time): $N = 914$, nanobody competition (0.05 s dwell time): $N = 1732$, nanobodies raised against mCherry: $N = 1748$, PC12-Syx-KD: $N = 2438$). Force curves of all data were measured with a retraction speed of 1 μm·s^{-1}. In **b** distances smaller than zero were omitted, accounting for up to 5.5 % (see offset at small values of D).

In these plots only measurements with a retraction speed of 1 µm·s^{-1} were used, thereby excluding one more measurement for PC12-Syx-KD membrane sheets. This is of importance since the Bell-Evans theory predicts an increase of the unbinding force with rising retraction speed.[148,149] The detailed statistics of the performed measurements can be found in sections 4.1.5.2 and 4.1.6.1-4.1.6.3.

In general the shapes of the curves are in both plots quite similar. However, some slight deviations can be seen: The force distribution of the nanobody competition experiment with a dwell time of 0.5 s (solid cyan line in Figure 4.22 a) is shifted towards larger forces, as well as the curve for the knockdown cells at medium force values (dashed blue line in Figure 4.22 a). More importantly, for MR-AFM experiments with PC12-WT-1 membrane sheets, anti-Syx-NBs coupled to the cantilever and a dwell time of 0.5 s (experiments supposed to show specific interactions, solid red line in Figure 4.22 a) a larger fraction of interaction forces is found at small forces below 25 pN. Small force values might correspond to specific interactions. However, this fraction only accounts for less than 20 % of all values measured and the corresponding forces are probably even too small (see discussion in section 5.1.2). Regarding the distribution of the distances all curves exhibit a similar shape, only that for the measurement with a PC12-WT-1 membrane sheet, anti-Syx-NBs coupled to the cantilever and a dwell time of 0.05 s (experiments supposed to show specific interactions, dotted red line in Figure 4.22 b) shows slightly smaller distances. However, these data just stem from a single measurement. Taken together, MR-AFM measurements on PC12-WT-1 membrane sheets with nanobodies against syntaxin-1 coupled to the cantilever and their corresponding control measurements show generally the same results. However, in some minor details the obtained results differ, which might point to a slight difference in the nature of the interaction events.

4.1.6.6 Evaluation of varying binding efficiencies

In order to obtain information about the variability of the probability of an event to occur, the data derived from MR-AFM measurements with anti-Syx-NB functionalised cantilevers on PC12-WT-1 membrane sheets with a retraction speed of 5 µm·s^{-1}, which were used for comparison in section 4.1.6.4, are plotted in Figure 4.23 in more detail. These data were used since they are the most systematic ones for comparing different cantilevers and different membrane sheets. The figure plots the relative frequencies of events, discriminated

by the individual membrane sheets and cantilevers. Force maps obtained from the same membrane sheet were recorded at different locations.
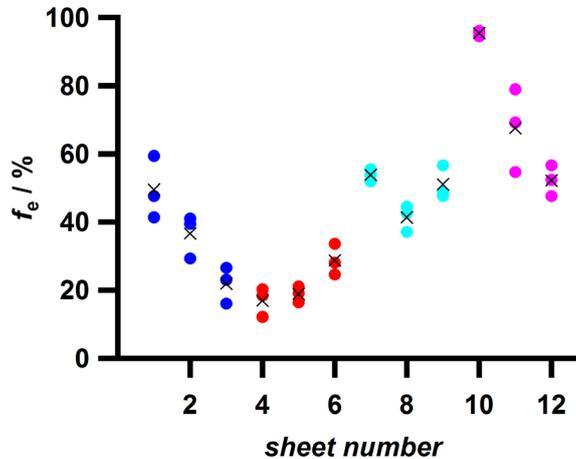
Figure 4.23: Relative frequencies of events of different membrane sheets and cantilevers. The plot shows the relative frequency of events for twelve PC12-WT-1 membrane sheets measured by four anti-Syx-NB-functionalised cantilevers. The circles indicate the values of individual maps, the crosses denote the mean values of the three maps recorded on the respective membrane sheet. The different colours indicate the four individual cantilevers used.

The data in Figure 4.23 show that the variability in f_e is rather small for maps recorded on a single membrane sheet, usually smaller than $\Delta f_e = 0.2$. When comparing values obtained from different membrane sheets but with the same cantilever (same colour of the circles in Figure 4.23), the variability is larger. Notably, the variability between values obtained with different cantilevers is even larger. Therefore, this analysis indicates that probably unknown properties of the membrane sheet and especially of the cantilever influence the determined relative frequency of events significantly. This is discussed in section 5.1.3.

4.1.7   Facilitated cantilever functionalisation

Sections 4.1.6 and 4.1.9 focus on unspecific interactions and possible reasons for their occurrence. Besides abundant unspecific interactions, a lack of specific ones might impede the detection of syntaxin-1 clusters as well. This might be caused by an insufficient or unsuccessful functionalisation of the cantilever. However, a chemical characterisation on a tiny surface such as an AFM cantilever or even on its curved tip is not straight forward. To circumvent the probably most critical steps of the cantilever functionalisation, namely the

amination of the gold surface and as a further step the amine - *N*-hydroxysuccinimide reaction, aminated and maleimide terminated cantilevers were utilised for further experiments (see Figure 3.5). Moreover, in these experiments exactly the same cantilever was used for subsequent measurements on membrane sheets from wild type and syntaxin-1 knockdown cells.

Two experiments using pre-aminated cantilevers functionalised with anti-Syx-NBs were performed. These experiments comprise one experiment comparing interactions on a PC12-Syx-KD membrane sheet (f_e = 35 %, *N* = 1 map) with those of a sheet of a PC12-WT-1 cell (f_e = 71 % and f_e = 53 %, *N* = 2 maps). In a second experiment first a force map was recorded on a membrane sheet derived from a PC12-WT-2 cell (f_e = 36 %, *N* = 1 map) and afterwards a second one on a PC12-Syx-KD sheet (f_e = 47 %, *N* = 1 map). Since no clear conclusion can be drawn from the relative frequencies of events, the corresponding cumulative probabilities of the measured forces and distances are plotted in Figure 4.24.
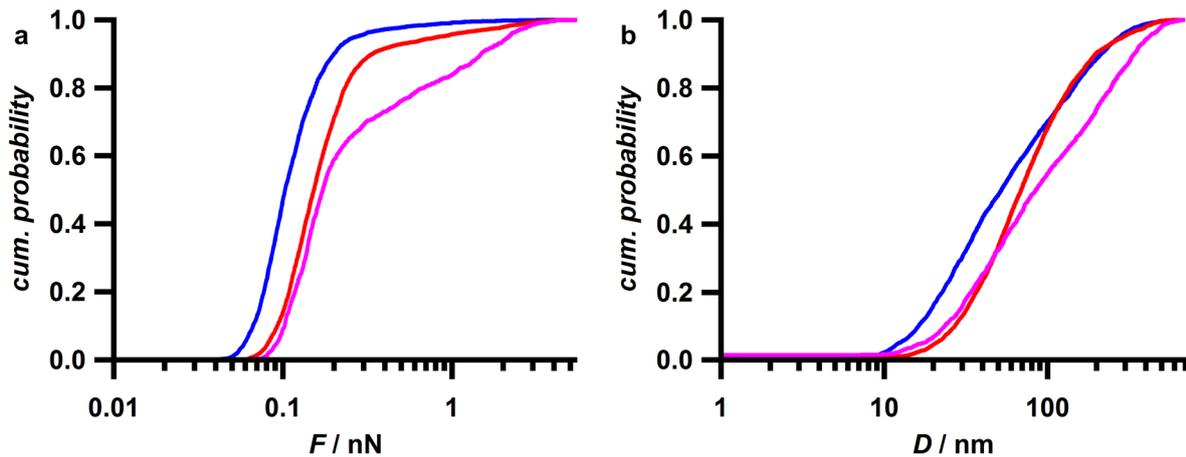
Figure 4.24: Force and distance distributions obtained by MR-AFM measurements with anti-Syx-NBs coupled to a cantilever aminated by the manufacturer on PC12 membrane sheets of different types. The cumulative probability of the measured forces is plotted in **a**, the corresponding distances are plotted in **b**. Data obtained from measurements on PC12-WT-1 membrane sheets are shown in red (*N* = 5069), those from PC12-WT-2 membrane sheets in magenta (*N* = 1458) and those from PC12-Syx-KD membrane sheets in blue (*N* = 3372). In **b** distances smaller than zero were omitted, accounting for 0.5 % of the data for PC12-WT-1, 1.6 % for PC12-WT-2 and for 0.2 % for PC12-Syx-KD membrane sheets.

The plot of the maximum interaction forces (Figure 4.24 a) indicates a discrepancy between the values measured on knockdown and on wild type cell membrane sheets. Below forces of approximately 200 pN and below distances of 50 nm, in the probably more relevant part for the interactions between the nanobody and syntaxin-1, both distance and force values of PC12-WT-1 cells are more similar to the other wild type than to the knockdown cells. Only at

large forces and distances, the distributions belonging to PC12-WT-1 membrane sheets rather resemble those of the values of knockdown membrane sheets. The statistical parameters of these distributions (Table 4.1 and Table 4.2) show the difference, especially regarding the maximum interaction forces.

Table 4.1: Statistical parameters of the maximum interaction force (F) distributions in MR-AFM experiments performed with cantilevers aminated by the manufacturer.

cell type	F (median) / pN	F (30th percentile) / pN	F (70th percentile) / pN
PC12-WT-1	153	122	198
PC12-WT-2	173	136	311
PC12-Syx-KD	103	86	130

Table 4.2: Statistical parameters of the rupture distance (D) distributions in MR-AFM experiments performed with cantilevers aminated by the manufacturer.

cell type	D (median) / nm	D (30th percentile) / nm	D (70th percentile) / nm
PC12-WT-1	69	47	105
PC12-WT-2	85	46	180
PC12-Syx-KD	52	30	100

These statistics might indicate the presence of other types of interactions in measurements on knockdown membrane sheets as compared to wild type membrane sheets. Note that the order of measurement on wild type and knockdown membrane sheets was interchanged between both experiments. However, the cluster analyses indicate a more pronounced clustering for membrane sheets derived from PC12-knockdown cells, as shown for the example of the preceding measurement on a PC12-WT-2 membrane sheet in Figure 4.25. Here, the $L(r){-}r$ values of the measurement on the knockdown sheet clearly shows clustering at distances between 0.1 and 0.4 µm (Figure 4.25 c), whereas for the wild type membrane sheet a broad plateau is observed (Figure 4.25 a).
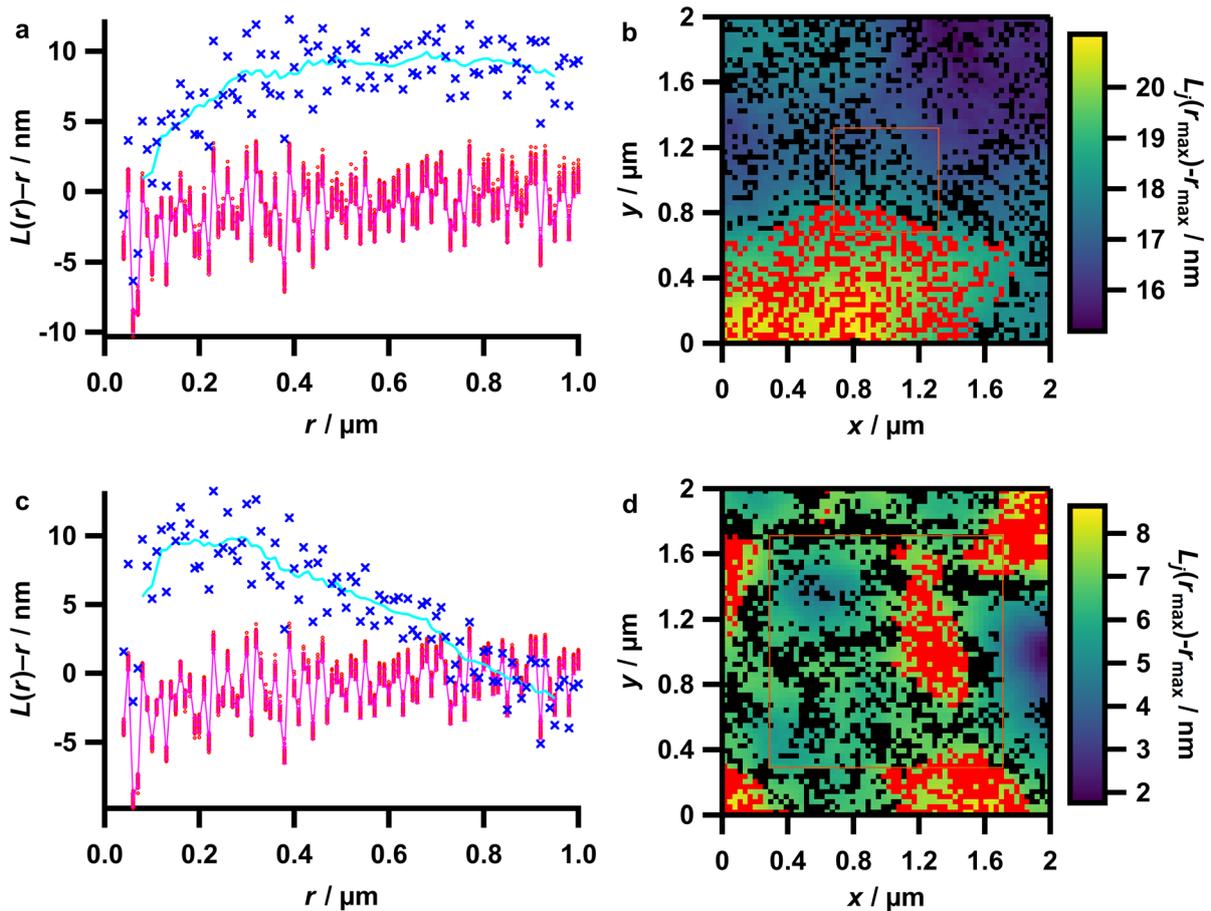
Figure 4.25: Ripley cluster analyses of MR-AFM experiments employing cantilevers aminated by the manufacturer. In **a** and **b** the cluster analysis of a MR-AFM force map measured on a membrane sheet derived from a PC12-WT-2 cell is shown, in **c** and **d** the analysis of a subsequent measurement on a membrane sheet derived from a PC12-Syx-KD cell. **a** and **c** plot the $L(r)−r$ values of the measured data (× and cyan line) and for homogeneous random data of the same number of events (○ and magenta line) as a function of r. In **b** and **d** the overlay of the Ripley density maps and the corresponding clustered events (red) and all other events (black) are shown. For details see caption of Figure 3.18.

This finding indicates that even though specific interactions might have been measured on membrane sheets derived from wild type cells, a detection of specific syntaxin-1 clusters is highly unlikely. For a deeper discussion see section 5.1.2.

To also circumvent the reaction step between the aminated surface and the *N*-hydroxysuccinimide on the bifunctional PEG-linker, cantilevers which were linked in that way by the manufacturer were used next. Furthermore, since membrane sheets of PC12-WT-1 and PC12-WT-2 cells show distinct morphological features in fluorescence images of membrane stainings (see Figure 4.2) and PC12-Syx-KD cells are derived from the latter, these cells were used for a final set of MR-AFM experiments with native membrane sheets. Another advantage might be that the discrepancy in the observed maximum interaction forces and rupture distances from knockdown membrane sheets is larger for

PC12-WT-2 than for PC12-WT-1 cells (*vide supra*). With anti-Syx-NBs coupled to the cantilevers mentioned above, experiments were carried out by measuring with exactly the same cantilever on wild type membrane sheets first and subsequently on knockdown membrane sheets and *vice versa* (N = 4 maps each on four sheets each from two independent preparations with four cantilevers from two independent functionalisations). The determined relative frequencies of events are f_e = (42 ± 12) % and f_e = (55 ± 25) % for MR-AFM measurements on membrane sheets derived from PC12-WT-1 cells and PC12-Syx-KD cells, respectively. These values might indicate a larger overall probability of interactions with knockdown membrane sheets. The mean value of the PC12-Syx-KD membrane sheets is, however, strongly influenced by a single map with f_e = 87 %. The cumulative probability of the maximum interaction forces and the rupture distances are plotted in Figure 4.26, the corresponding histograms can be found in Supplementary Figure 5.
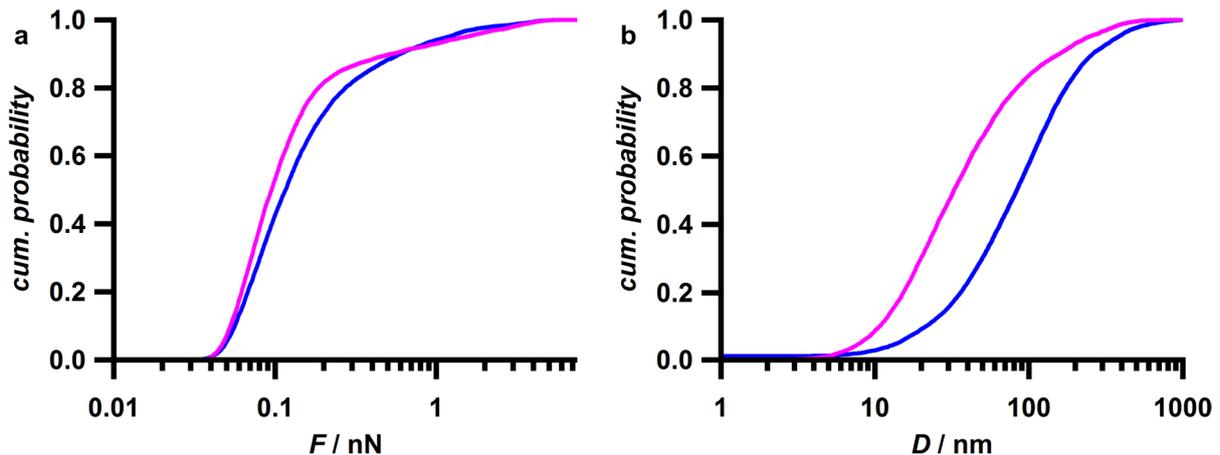
Figure 4.26: Force and distance distributions obtained by MR-AFM measurements with anti-Syx-NBs coupled to a cantilever maleimated by the manufacturer on membrane sheets from wild type and syntaxin-1 knockdown PC12 cells. The cumulative probability of the measured forces is plotted in **a**, that of the corresponding distances in **b**. Data obtained from measurements on PC12-WT-2 membrane sheets are shown in magenta (N = 6958) and those from PC12-Syx-KD membrane sheets in blue (N = 8960). In **b** distances smaller than zero were omitted, accounting for 0.3 % and 1.4 % of the data of membrane sheets derived from PC12-WT-2 and PC12-Syx-KD cells, respectively. For corresponding histograms see Supplementary Figure 5.

The median forces are 96 pN and 117 pN, the 30th percentiles are 72 pN and 81 pN and the 70th percentiles are 138 pN and 186 pN for PC12-WT-2 and for PC12-Syx-KD membrane sheets, respectively. The median rupture distances are 33 nm and 83 nm, the 30th percentiles are 20 nm and 50 nm and the 70th percentiles are 57 nm and 133 nm for PC12-WT-2 and for PC12-Syx-KD membrane sheets, respectively. A significant difference in the rupture distance between knockdown and wild type membrane sheets is evident from

Figure 4.26 b and is observed for all four cantilevers which were used for measurements on both types of membrane sheets successively (data not shown). The situation is not as clear for the maximum interaction forces. Here, the distribution of the forces is slightly shifted to larger values for the knockdown sample, but this difference does not seem to be significant, when comparing the statistical values. Furthermore, no clear tendency can be observed when regarding the cumulative probability plots for the individual cantilevers (data not shown). The discrepancy in the rupture distances is an indicator of distinct modes of interaction between the cantilever and either type of membrane sheet. However, since the interaction forces are similar in both cases and since the number of interaction events might be even slightly larger for membrane sheets derived from PC12-Syx-KD cells, specific interactions between the nanobody and syntaxin-1 seem to be unlikely to be the main contributor to this discrepancy (see section 5.1.2 for a discussion).

Moreover, a specific interaction is not supported by the cluster analysis. Among the four pairs of force maps, two were recorded inside an area of $1{\times}1$ µm^2 and one pair each inside an area of $0.5{\times}0.5$ µm^2 and $2{\times}2$ µm^2. Regardless of the size and of the cell type of origin of the membrane sheets, two types of spatial organisation were found. These types of organisations can be described as two or three larger accumulations of events almost exclusively spread to the border of the investigated area, and a gradient of the Ripley density map reaching from one border to the opposed one. For examples, see Supplementary Figure 6. However, no small clusters as described in the previous sections were detected.

4.1.8   Refinement and analytical controls of the cluster detection

By the analyses performed so far no clear evidence of the detection of specific syntaxin-1 clusters could be obtained. However, it might be that specific events are present but that their detection is cumbersome due to a heterogeneous lateral organisation of localisations with unspecific interaction events. To separate specific from unspecific interactions and to identify clusters, a subset of the force maps obtained in the present study were analysed in more detail as described in the following subsections.

4.1.8.1 Exclusion of colocalisation of events in the retraction force curve with the events in the approach force curve

Sudden declines in the contact regime of the approach force curve, possibly stemming from breakthrough events through structures on the membrane sheet, might by followed by a pronounced adhesion of material of the membrane sheet on the cantilever tip leading to interaction events in the retraction force curve. Two exemplary approach force curves with a breakthrough-like event are presented in Figure 4.27.
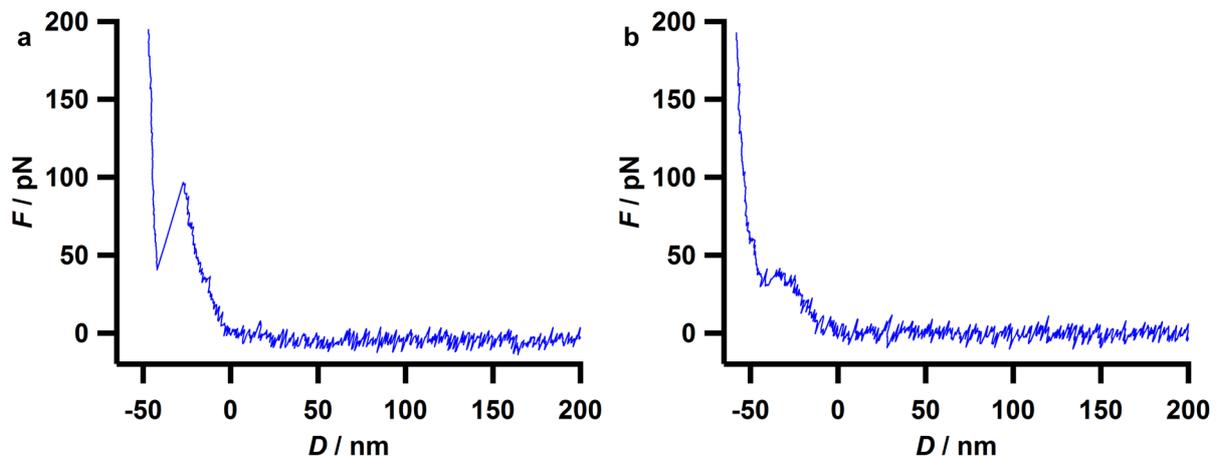
Figure 4.27: Approach force curves showing breakthrough-like events. In **a** an approach force curve with a sudden decline of the force in the contact regime and in **b** a force curve with a plateau in the contact regime is shown. Both curves are cut at a distance of D = 200 nm.

To exclude the possibility that such events account for the majority of the events observed in the retraction force curves and thus for the identified clusters, corresponding events in the approach curve were identified and compared with the respective map of events of the retraction force curves. For this purpose, three force maps obtained from MR-AFM measurements with anti-Syx-NB functionalised OBL-10 cantilevers on PC12-WT-1 membrane sheets were chosen arbitrarily. Table 4.3 shows the relative amount of events in the approach force map which colocalise with the localisation of events in the map of the retraction force curves. For comparison, the corresponding expectation value for the same number of events is added (calculated by the number of events in the approach force curve divided by the overall number of force curves inside the map).

Table 4.3: Number of colocalisations of the localisations of events between the map of events of the approach and retraction force curves and their corresponding expectation values, normalised by the number of retraction force curves showing an event for three exemplary force maps.

colocalisation	expectation value of colocalisation
7.97 %	7.67 %
13.2 %	14.1 %
13.2 %	9.61 %

The comparison of the colocalisations of events with their respective expectation values shows that the determined amount of colocalisation in two cases almost perfectly matches the expectation value. In one case the colocalisation is larger than to be expected, but still only about 1.4 times the expectation value. Thus, this analysis reveals that events observed in the retraction force curves probably do not stem from breakthrough-like or other events visible in the approach force curve.

4.1.8.2 Force and distance range selection

The analyses of MR-AFM measurements described in the present chapter have revealed broad distributions of maximum interaction forces and rupture distances. It is reasonable that, if present at all, only a small part of these ranges comprise specific interaction events. Therefore, it seems promising to perform cluster analyses only of events accounting for a limited range of the measured maximum interaction forces and rupture distances. To this end, in a first approach all events inside a range of about 30-40 pN around the most probable maximum interaction force were extracted from two MR-AFM maps showing small clusters and subject to Ripley's *K*-function cluster analysis. In one case the clusters seen before were detected more precisely, however, in the other case cluster detection became worse. Thus, in a more sophisticated analysis, an upper or a lower force or distance threshold was applied. This threshold was varied over a broad range of forces or distances until only few events were left. The whole range was divided into 100 steps. For all resulting threshold values a Ripley cluster analysis was performed and the moving mean of $L(r)-r$ was extracted. This analysis was performed for all eight maps measured using cantilevers which were already maleimated by the manufacturer and modified by anti-Syx-NBs.
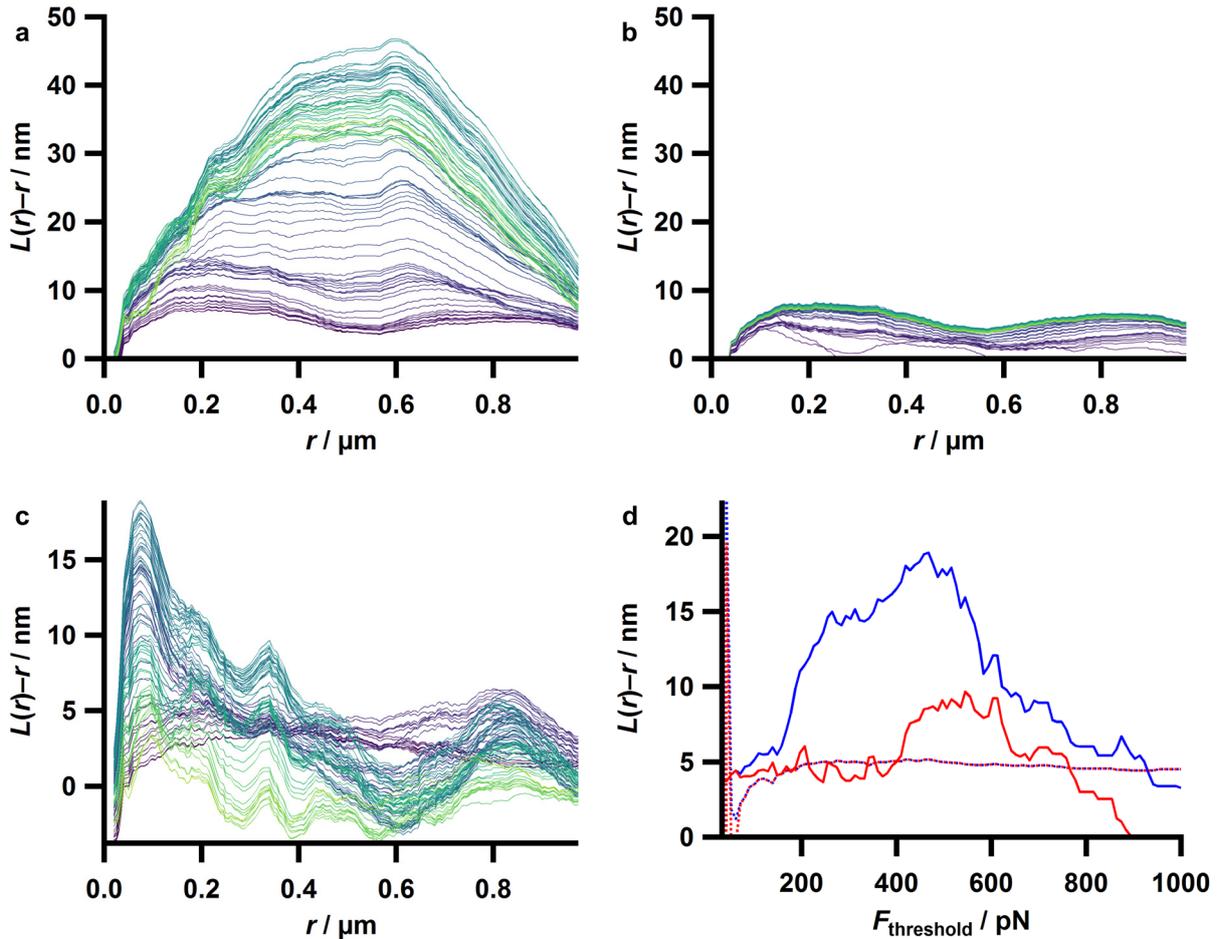
Figure 4.28: Ripley cluster analyses of selected force ranges. In **a-c** moving mean values of $L(r)$–r are plotted against r. The colour indicates the force threshold, where the darkest colour corresponds to the lowest and the lightest colour to the largest force threshold. **a** shows plots for which the lower force threshold was varied, **b** shows plots of the same map for which the upper threshold was varied. In **c** plots for another map are shown for which the lower force threshold was varied. Both maps were recorded on membrane sheets derived from PC12-WT-2 cells. Most corresponding plots are quite similar to **a** and **b**, however, for some a situation such as that in **c** was found. In **a** and **b** the lightest colour corresponds to a force threshold of 500 pN, the darkest colour in **a** corresponds to a force threshold of 30.2 pN. In **b** the five curves with the lowest force thresholds were omitted because they show irregular shapes due to an extremely low number of events, thus the darkest colour corresponds to a force threshold of 53.7 pN. In **c** the lightest colour corresponds to a lower force threshold of 1 nN and the darkest colour to a lower force threshold of 32.0 pN. In **d** single moving mean values of $L(r)$–r of the same dataset as used for **c** are plotted against the force threshold. The dotted curves correspond to the upper force threshold, the solid ones to the lower force threshold. The moving mean values of $L(r)$–r found at $r = r_{max}$ of an analysis in which the whole force range is used are shown in red, the maximum of the moving mean curve of the current force range is shown in blue.

In Figure 4.28 a and b typical results for the moving means of $L(r)$−r for the individual steps of increase of the lower and upper force threshold are shown. The presented examples were obtained from a measurement on a membrane sheet derived from a wild type PC12 cell. Curves for varying lower force threshold in Figure 4.28 a are shifted to larger $L(r)$−r values and the peak is shifted towards larger r with increasing threshold, only at very high threshold

values the maximum declines again. Almost the same holds for the lower force thresholds in Figure 4.28 b. A Ripley cluster analysis at r_{max} of the curve showing the largest values of $L(r)-r$ when increasing the lower force threshold yields a large accumulation in one corner of the map. The slight shifts of the curves indicate that no pronounced new structure, which might correspond to previously hidden clusters, is present in the map of events subject to force range selection.

In few cases, a previous local maximum evolves to a new global maximum when the threshold value is increased, as shown in Figure 4.28 c. When a Ripley cluster analysis is performed here in the same way as described before for the data shown in Figure 4.28 a, i.e. by using the lower force threshold corresponding to the maximum of the solid blue line in Figure 4.28 d, a small cluster is found which has not been identified before (see Supplementary Figure 7). However, the lower force threshold is large (F_{low} = 468 pN). Furthermore, a similar result is obtained from a measurement on a knockdown membrane sheet. In other cases as that shown in Figure 4.28 c a similar analysis yielded only a peak in the Ripley cluster analysis which was not distinguishable from the values of a homogeneous random distribution of the same number of events. For comparison, for homogeneous random data a reduction of the overall number of events leads to a gradual flattening of the moving mean curve reaching values of $L(r)–r$ close to zero which are predominantly caused by the constraints of the grid asymptotically (see Supplementary Figure 8). To construct these random data a threshold was applied to a 64×64 array of uniformly distributed random numbers. In general, the results are similar for the variation of the distance threshold.

Figure 4.28 d shows plots of the moving mean of $L(r)–r$ against the force threshold ($F_{threshold}$) for a constant r_{max} value, found for a Ripley analysis without applying a force threshold (red), and a value of r_{max} adapted to the maximum of the $L(r)–r$ curve by using the current force threshold (blue). The similarity between the curves of the upper force thresholds (dotted lines), which is representative for all analyses, also indicates that rather the $L(r)–r$ values of the whole curve are increased instead of the appearance of a new maximum at another r accompanied with a large increase of $L(r)–r$, which might indicate the identification of a new cluster. More importantly, among the regarded maps no systematic differences between membrane sheets derived from wild type and knockdown PC12 cells were evident from this analysis. Thus, as far as analysed, this approach does not lead to a more pronounced detection of previously hidden clusters in wild type membrane sheets as compared with knockdown sheets.

4.1.8.3   Wormlike chain analysis of force curves and cluster maps

When after successful binding between a nanobody and a syntaxin-1 molecule the cantilever is retracted, the PEG linker will be extended.[108] Since PEG chains have a defined persistence length and depending on the number of monomers also a defined contour length,[30,150] an extraction of specific interactions might be possible based on these parameters. To this end, a function corresponding to a wormlike chain model according to equation (3.11) was fitted to all force curves recorded with cantilevers maleimated by the manufacturer which exhibit an event in the retraction part (see section 4.1.7). Furthermore, the force curves recorded on GUV-MPs were fitted accordingly. Figure 4.29 shows a representative example of a force curve measured on a PC12-WT-2 membrane sheet and fitted with a high coefficient of determination ($R^2 > 0.95$) by the WLC model.
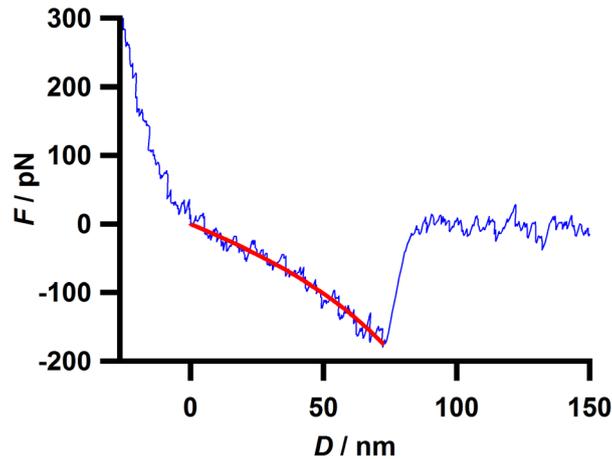
Figure 4.29: Force curve with a representative WLC-fit. The measurement was performed on a PC-WT-2 membrane sheet. Between the zero-force point and the point of the maximum interaction force, the force curve (blue) is fitted according to a WLC model (red). The obtained fit parameters are $L_c = 167$ nm and $L_p = 23$ pm. $R^2 = 0.959$.

Next, in Figure 4.30 the cumulative probability distributions of the contour length and the persistence length are plotted for measurements on membrane sheets derived from PC12-WT-2 cells, PC12-Syx-KD cells and GUV-MPs. For these plots and the following analysis only fits with $R^2 \geq 0.6$ were included.
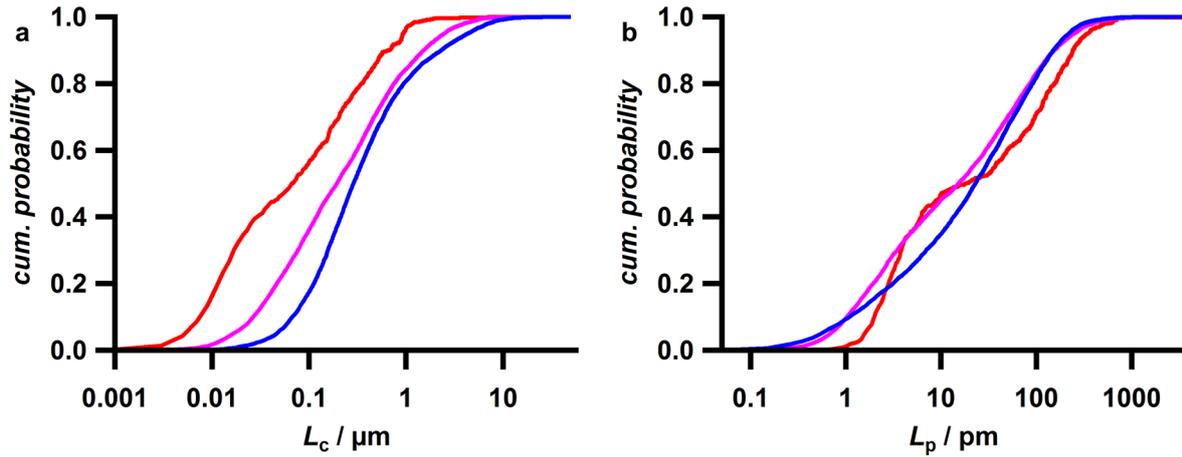
Figure 4.30: Distributions of the contour length and the persistence length. The cumulative probability of the contour length is plotted in **a** and that of the persistence length in **b**. Magenta lines indicated data obtained from measurements on PC12-WT-2 membrane sheets ($N = 5615$) and blue lines correspond to measurements on PC12-Syx-KD membrane sheets ($N = 6872$). For comparison data derived from fitting the force curves obtained from measurements on GUV-MPs ($N = 586$) are added by the red lines. For the plots only fits with $R^2 \geq 0.6$ were regarded.

The median, the 30th percentile and the 70th percentile of the contour length and of the persistence length are listed in Table 4.4 and Table 4.5, respectively.

Table 4.4: Statistical parameters of the contour length distributions in MR-AFM experiments performed with cantilevers maleimated by the manufacturer.

sample	L_c(median) / µm	L_c (30th percentile) / µm	L_c (70th percentile) / µm
PC12-WT-2	0.20	0.074	0.47
PC12-Syx-KD	0.29	0.16	0.58
GUV-MP	0.067	0.018	0.21

Table 4.5: Statistical parameters of the persistence length distributions in MR-AFM experiments performed with cantilevers maleimated by the manufacturer.

sample	L_p(median) / pm	L_p (30th percentile) / pm	L_p (70th percentile) / pm
PC12-WT-2	15	3.5	50
PC12-Syx-KD	23	7.1	57
GUV-MP	18	3.8	97

Compared to force curves from GUV-MPs, the contour lengths (Figure 4.30 a) obtained from measurements on knockdown membrane sheets are shifted about one order of magnitude to larger values. The distribution of the latter is also slightly shifted to larger contour length as

compared with the values of wild type cells. Note that for measurements on membrane sheets the PEG linker has about three times the length of that used for the experiments performed with GUV-MPs. The medians of the contour lengths for measurements on membrane sheets exceed the expected contour lengths by more than a factor of 10. This might indicate that longer linkers stemming from the membrane sheet might have adhered to the cantilever. The distribution functions of the persistence lengths (Figure 4.30 b) are much less shifted relative to each other. In all cases only a small amount of values can be found in the order of the persistence length of a PEG chain of L_p(PEG) = 0.38 nm,[150] most values are much smaller. This might be explained by the formation of multiple parallel bonds between the membrane sheet and the cantilever. In all three cases both quantities exhibit a broad distribution over about three orders of magnitudes. These findings do not point to the detection of specific interactions (see also discussion in section 5.1.3). Nevertheless, the fit with the wormlike chain model performs much better for the membrane sheets as compared to the fits of the data obtained from GUV-MPs, as indicated by the relative amount of force curves which are fitted by the WLC model with $R^2 \geq 0.6$. This quantity is 81 % and 77 % for membrane sheets of PC12-WT-2 and PC12-Syx-KD cells, respectively, but only 23 % for GUV-MPs (compare N values given in the caption of Figure 4.30 with those of Figure 4.26 and Figure 4.21).

To test the influence on cluster detection, a threshold variation procedure was performed for the contour and the persistence length similar to that for the maximum interaction force and the rupture distance in section 4.1.8.2. Again the eight maps recorded with cantilevers which were previously maleimated by the manufacturer were analysed. In essence, the results are quite similar to those described in section 4.1.8.2 for the variation of the force and the distance threshold. After applying thresholds of the contour and the persistence length, only the cluster already found by applying the lower force threshold for the analysis of a map recorded on a PC12-WT-2 membrane sheet described in section 4.1.8.2 was found again for the application of a large lower threshold of the contour length ($L_{c,low}$ = 2.94 μm). This length is not compatible with the polyethylene glycol chains used to couple the nanobodies (see discussion in section 5.1.3). However, it cannot be excluded that a more detailed analysis will yield the detection of further clusters. Exemplary plots can be found in Supplementary Figure 9. Again, no systematic difference between membrane sheets derived from wild type and knockdown cells were found.

4.1.9 Investigation of the topography of membrane sheets

As identified in section 4.1.6, the MR-AFM experiments performed on PC12 cell membrane sheets are perturbed by a huge number of unspecific interactions between the sample and the cantilever. With the purpose of unravelling details about the presumably large ratio between unspecific and specific interactions which might be related to the morphology of the membrane sheets, topographical images of membrane sheets were recorded by FD-AFM.

4.1.9.1 Detailed morphological investigations of membrane sheets by AFM height imaging

The introductory example in Figure 4.3 has already indicated that the membrane sheets display some elevated structures. To further investigate the morphology of membrane sheets and thereby possibly obtain more information about the reasons for unspecific interactions to occur in MR-AFM, PC12-WT-1 membrane sheets were stained for actin by fluorescent phalloidin and imaged in detail by FD-AFM. The representative example in Figure 4.31 a shows an epifluorescence micrograph of such a membrane sheet. The corresponding AFM height image in Figure 4.31 b again indicates the presence of elevated structures on the membrane sheet. Interestingly, an annular structure with a height of partially more than 300 nm can be seen which colocalises with the fluorescent signal of the actin label shown in Figure 4.31 a. Thus, even membrane sheets with a rather small amount of actin like the one in Figure 4.31 a possess large elevations caused by actin. The further magnified scan (Figure 4.31 c) inside the red square drawn in Figure 4.31 b, shows small globular structures with a size of up to a few hundreds of nanometres in lateral and axial direction, which are abundant in all membrane sheets measured. In Figure 4.31 d a further step of magnification is realised by a scan inside the cyan square in Figure 4.31 c.

These experiments reveal a heterogeneous organisation of the surface of the membrane sheets derived from PC12 cells. The observed structures might play a major role in force measurements performed on membrane sheets. Obviously, the question of the nature of these structures arises, which will be addressed in the next section.
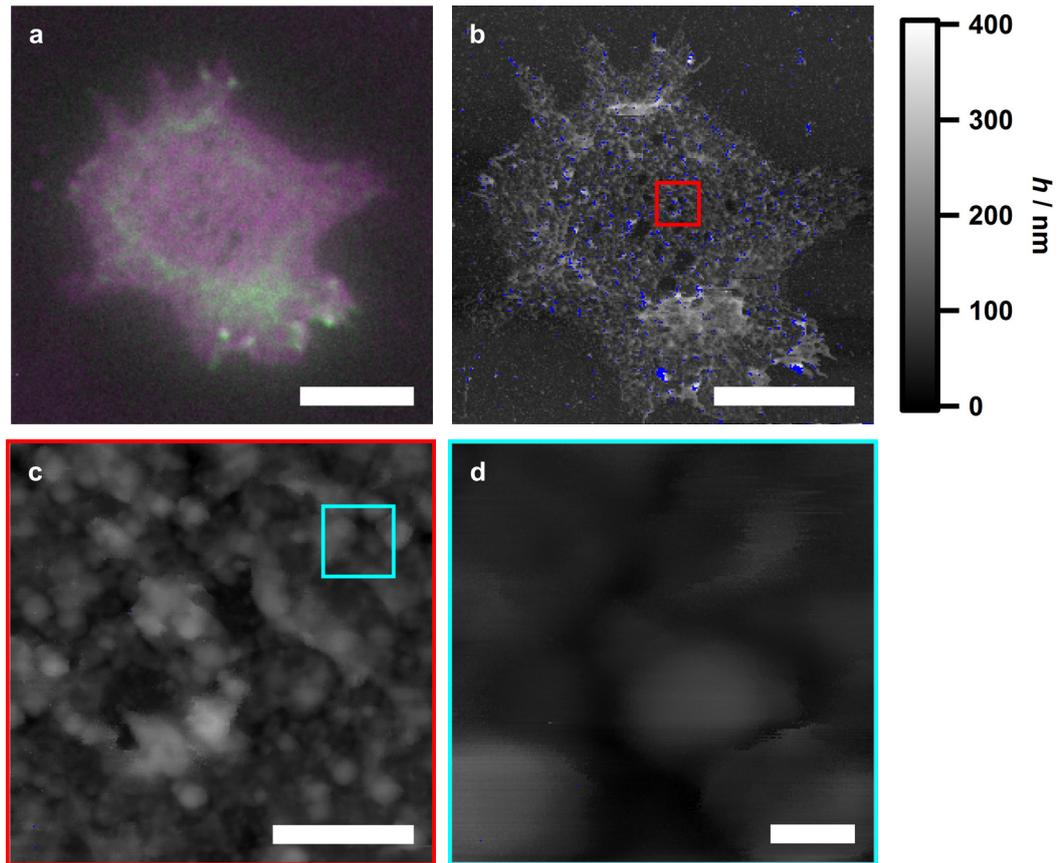
Figure 4.31: Topographical investigation of membrane sheets by AFM. The membrane sheets were derived from PC12-WT-1 cells. An immunofluorescence image of a selected membrane sheet is shown in **a**. The sheet was stained for the membrane (magenta) and for actin (green). AFM height images can be seen in **b-d**, where **c** shows a magnified recording of the region marked by the red square in **b** and **d** shows a magnified recording of the cyan square in **c**. The colour scale shown in **b** holds for **c** and **d** as well. Pixels marked in blue correspond to height values exceeding the colour scale or to missing values due to errors in the record. Scale bars: **a**: 10 μm, **b**: 10 μm, **c**: 1 μm, **d**: 100 nm.

4.1.9.2 Investigation of membrane sheets subject to protein digestion

To investigate a possible proteinaceous nature of the globular structures residing on PC12 cell membrane sheets, PC12-WT-1 membrane sheets were subject to a protein digestion by the addition of proteases (pronase from *Streptomyces griseus*). FD-AFM images were recorded before and after the addition of the proteases. Already 20 min after the addition, which was the smallest time span possible to investigate due to the experimental procedure, the structures observed before were diminished (N = 12 maps on eight different sheets from six digestions and four independent preparations of membrane sheets). Figure 4.32 shows representative AFM height images recorded before and about 1 h after the addition of

proteases. After protein digestion, most of the structure observed on untreated membrane sheets is gone (Figure 4.32 b). However, even after digestion smaller structures remain. These structures have a much smaller size of well below 100 nm, as evident from Figure 4.32 c. The histogram in Figure 4.32 d uncovers the decrease in height in more detail, showing that the most frequent height is decreased from approximately 30 nm to less than 10 nm. In a single control experiment, BSA was added at the same concentration as used for proteases. In two FD-AFM images on a single membrane sheet structures similar to those of untreated membrane sheets were observed (data not shown).
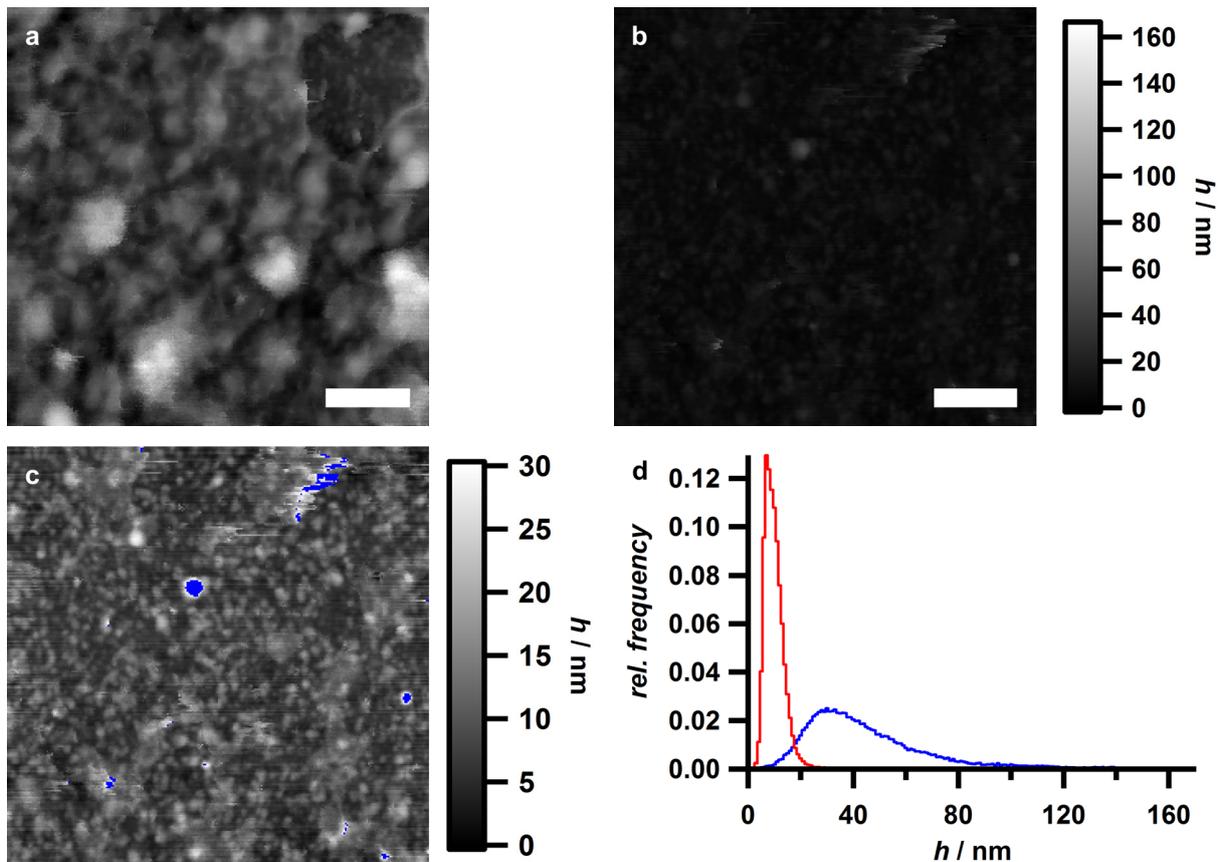
Figure 4.32: AFM images for the morphological investigation of membrane sheets of PC12-WT-1 cells treated with proteases. The image in **a** shows a selected region of a membrane sheet before the addition of proteases. In **b** a representative region of a membrane sheet after incubation with a solution of proteases for about 1 h is presented. The image was recorded on the same membrane sheet as the one shown in **a**, in a region nearby or partially overlapping with the region in **a**. The colour scale holds for **a** as well. **c** shows the same as **b**, but with an adapted colour scale to visualise smaller structures on the membrane sheet treated with proteases. Blue pixels represent values above the end of the colour scale ($h > 30$ nm). The histograms in **d** plot the relative frequency of height values of all pixels of the image before (blue) and after (red) the addition of proteases. Scale bars: 500 nm.

These experiments indicate that the heterogeneous structures observed on membrane sheets are either proteins themselves or at least structures which depend on the presence of certain proteins, such as vesicles.

To investigate whether the structure observed before the addition of the proteases is the only cause of unspecific interaction events with large maximum interaction forces, samples of PC12-WT-1 membrane sheets were washed after digestion (5× with PBS) and MR-AFM maps were recorded with anti-Syx-NB-functionalised cantilevers ($N = 36$ maps on twelve sheets from two independent preparations with three cantilevers from two independent functionalisations). The obtained relative frequency of events is $f_e = (19 \pm 14)$ % (mean ± SD), which is significantly smaller than the corresponding value of untreated membrane sheets (see section 4.1.6.4). Figure 4.33 plots cumulative probabilities of the measured maximum interaction forces and rupture distances. For comparison, corresponding data for MR-AFM measurements on untreated membrane sheets and on GUV-MPs, which are already shown in Figure 4.21, are added as well.
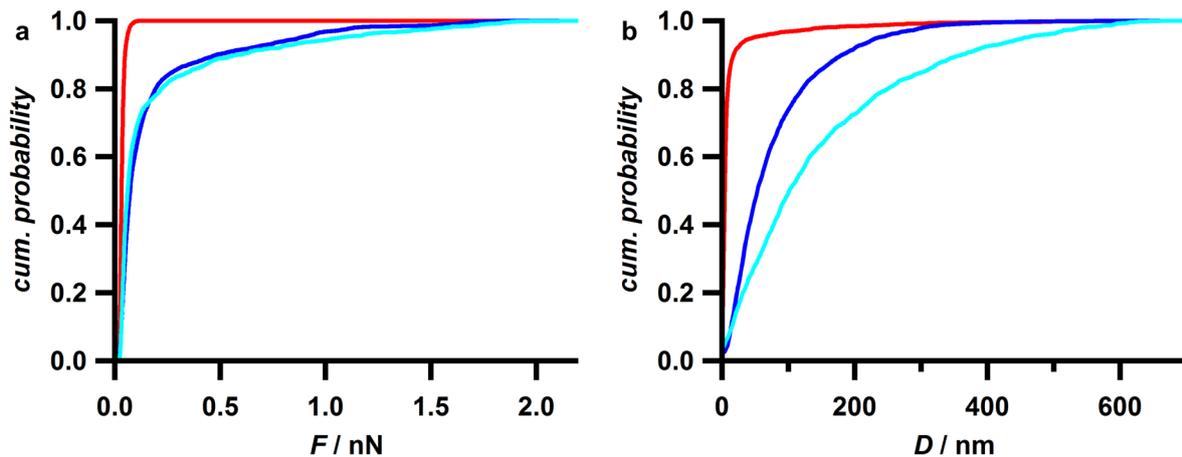
Figure 4.33: Force and distance distributions obtained from MR-AFM measurements on membrane sheets treated with proteases along with distributions from comparative measurements. The cumulative probabilities of the maximum interaction forces (**a**) and the rupture distances (**b**) are plotted. The cyan line represents the data obtained from MR-AFM measurements on PC12-WT-1 cells treated with proteases ($N = 1796$). For comparison, the data of untreated membrane sheets ($N = 4101$) and GUV-MPs ($N = 2604$), which are already shown in Figure 4.21, are plotted additionally by the blue and the red line, respectively. In **b** distances smaller than zero were omitted, accounting for 3.6 % of the data for PC12-WT-1 membrane sheets.

The determined median force for measurements on protease treated membrane sheets is 61 pN, the 30th percentile is 43 pN and the 70th percentile is 110 pN. The median rupture distance is 102 nm, the 30th percentile is 55 nm and the 70th percentile is 185 nm. For comparison with the values of untreated membrane sheets and GUV-MPs see section 4.1.6.4. Without the necessity to compare the numerical statistical values, directly

from the plots it is evident that the distribution of the forces is quite similar among protease treated and untreated membrane sheets. However, the distribution of the rupture distances is shifted towards larger distances for the protease treated as compared to the untreated membrane sheets. This experiment shows that interactions with the sample still occur after protein digestion, but possibly to a smaller extent. These interactions may be caused by the remaining structures, other binding partners which are not observed in the AFM height images or, even if unlikely, by remaining specific interactions. The similar distribution of forces of the protease treated and the untreated membrane sheets may point to the occurrence of the same interactions in both cases, which for the treated sheets for some reason take place at larger distances. In section 5.1.3 these results will be discussed in more detail.

4.1.9.3   Delayed fixation of membrane sheets

The observation that the globular structures observed on PC12 membrane sheets are proteins or protein dependent might offer the opportunity to decrease the amount of these structures, and especially of actin, when the fixation of the proteins is not performed immediately after the disruption of the cells, but instead after 25 min of storage in buffer. Two samples with PC12-WT-1 membrane sheets were treated according to this procedure. One sample was stored on ice during the delay time, the other one was kept at room temperature. However, for both samples a huge amount of actin was residing on the membrane sheets as identified by epifluorescence microscopy (data not shown). Furthermore, on the three membrane sheets of the sample stored at room temperature which were investigated by FD-AFM imaging the same structures as observed before when the fixation was performed immediately after the generation of the membrane sheets are found (data not shown). Therefore, this procedure has not been performed any longer.

4.1.10   Combination of topographic AFM imaging and STED measurements

The observed globular structures on the membrane sheets might hinder the interaction between the nanobodies on the cantilever and their binding partner on the membrane. The distribution of syntaxin-1 might, furthermore, be related to these structures. In that sense, a

hindrance of the interaction will be expected if the syntaxin-1 clusters observed in STED microscopy (Figure 4.4) colocalise with the elevations measured by AFM. To test this hypothesis, membrane sheets from PC12-WT-2 cells were stained for syntaxin-1, imaged with STED microscopy and subject to AFM height imaging afterwards (N = 3 sheets from a single preparation). Figure 4.34 shows an overlay of obtained AFM and STED images.
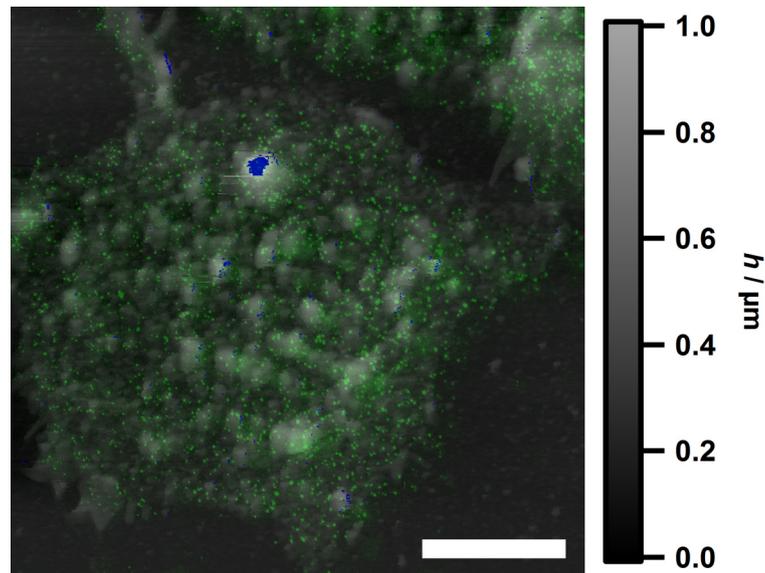
Figure 4.34: Overlay of an AFM height and a STED image of syntaxin-1 of a PC12 membrane sheet. The greyscale image shows the topography of a membrane sheet derived from a PC12-WT-2 cell. Blue pixels correspond to erroneous values or heights above 1 µm. The syntaxin-1 label measured by STED microscopy is shown in green. Scale bar: 5 µm.

For the membrane sheet shown in Figure 4.34 the correlation analysis between the height and the binarised fluorescence image of the syntaxin-1 label was performed inside a quadratic ROI of 9.6×9.6 µm^2 in a central region. In Figure 4.35 the cumulative probability of the height of all pixels inside that ROI (black), of the ones colocalising with syntaxin-1 in the binarised STED image (red) and for control purposes those obtained from rotating the STED image stepwise by 90° (cyan and blue, see caption of Figure 4.35) are shown. Generally, the distribution of height values of the regions which are, according to the STED image, occupied by syntaxin-1 (red line in Figure 4.35) resembles that of all pixels inside the ROI (black line in Figure 4.35). The slight deviation from control curves (blue and cyan lines in Figure 4.35) at around 0.4 µm is a unique feature of that membrane sheet and not found for the other two investigated membrane sheets. Consequently, the heights of the membrane sheets in regions with present signal from the syntaxin-1 label do not deviate from the overall height distribution. Thus, it can be concluded that the apparent distribution of syntaxin-1 is most probably not related to the topographical features of the membrane sheet.
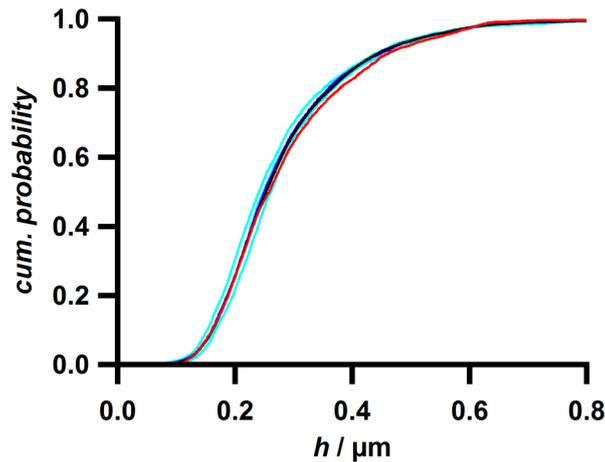
Figure 4.35: Quantification of the topography of regions of the membrane sheet occupied by syntaxin-1 compared with the whole ROI. The cumulative probability is plotted against the height of the membrane sheet measured by AFM. The back line corresponds to height values of all pixels inside a ROI on the membrane sheet shown in Figure 4.34. The red line represents height values of pixels inside the ROI which colocalise with syntaxin-1. For control purposes the cyan lines correspond to pixels detected by rotating the binary mask used to identify regions occupied by syntaxin-1 by 90°, 180° and 270°. The blue line is the cumulative probability of the height values of all three cyan control curves.

4.1.11 Topography of membrane sheets derived from primary neurons

PC12 cells have the advantage of relative time efficient procedures in cell culture. However, as pronounced elevations on membrane sheets derived from PC12 cells have been revealed by AFM height imaging as shown in section 4.1.9, it was sought for an alternative system for MR-AFM imaging of syntaxin-1 for future experiments. To this end, the topography of membrane sheets derived from primary rat hippocampal neurons was imaged by FD-AFM, as shown for a representative example in Figure 4.36 (*N* = 7 images from three sheets).

The image recorded at the border of the membrane sheet (Figure 4.36 a) shows the membrane sheet (middle grey) distinguishable from the substrate (dark grey) with present elevated structures (light grey). The image recorded closer to the centre (Figure 4.36 b) details the presence of structures which are quite similar to the ones found on PC12 cell membrane sheets.
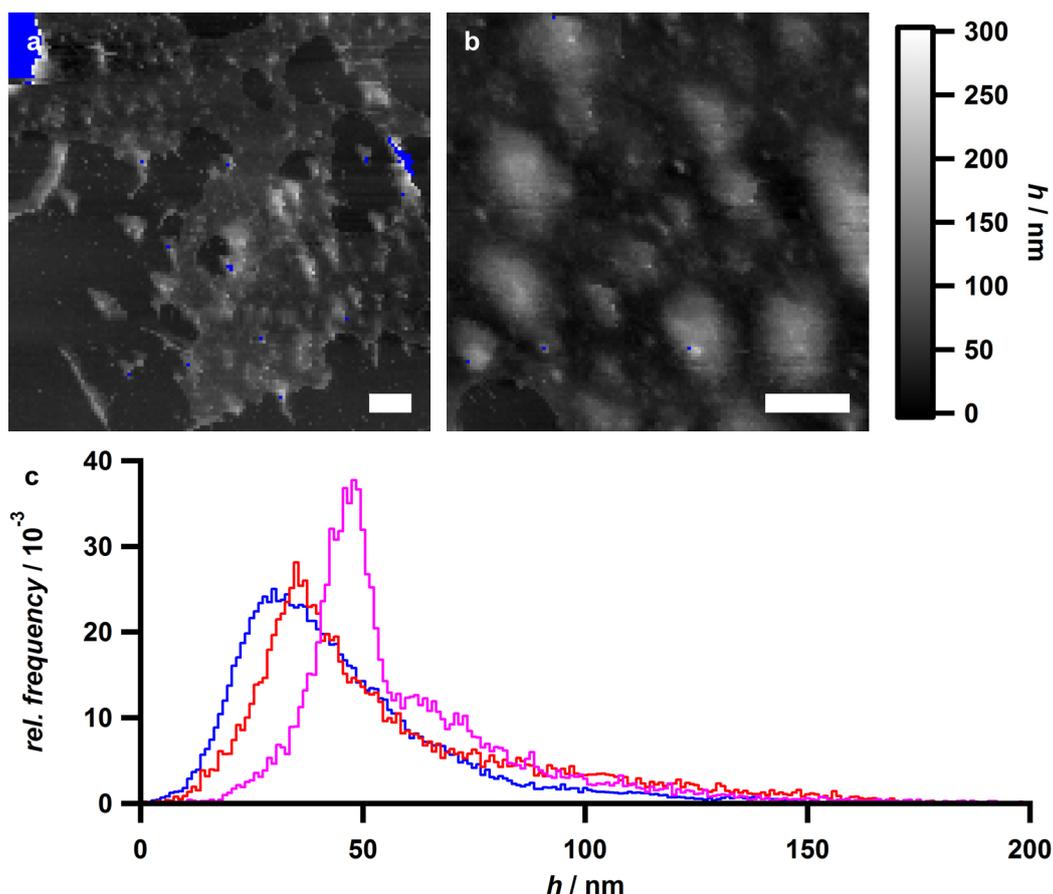
Figure 4.36: Topographical investigation of membrane sheets derived from primary neurons. In **a** a FD-AFM height image of a region at the border of a membrane sheet is shown, the one in **b** is recorded exclusively on the membrane of the same sheet. Blue pixels denote erroneous values and in **a** heights above 300 nm, additionally. The colour scale holds for both images. Scale bars: 1 µm. In **c** histograms of the height values are shown. The magenta coloured histogram corresponds to the image shown in **a** and the red one to that shown in **b**. For comparison, the histogram of the PC12-WT-1 membrane sheet already shown in Figure 4.32 is added in blue. The histograms are cut at $h = 200$ nm, thereby not showing height values accounting for 1.7 % and 0.06 % of all values for the histogram shown in magenta and red, respectively.

At first glance, these structures do not seem to be as dense as in PC12 cell membrane sheets, suggesting the possibility to perform MR-AFM measurements in between the elevations. However, a more detailed analysis of the distributions of height values shown in Figure 4.36 c indicates a good agreement in the distributions of heights in the images shown for primary neurons (red histogram) and for PC12-WT-1 cells (blue histogram). The larger offset in the magenta coloured histogram, which corresponds to the image measured at the border of the membrane sheet (Figure 4.36 a), is caused by the fact that the substrate is set to a height of zero instead of the lowest height on the membrane sheet, thereby shifting the height distribution about 10 nm towards larger height values as compared to the histogram shown in red. This shift can therefore serve as an estimate of a hypothetical flat membrane without the additional elevations.

4.2 Mechanics of GUVs Containing Synaptophysin

Synaptic vesicles are described to exhibit an increase in surface area by about 50 % or even more than 100 % upon uptake of neurotransmitters.[19,20] Jahn and coworkers observed this increase by dynamic light scattering experiments when synaptic vesicles took up glutamate.[20] However, due to limited tolerability to membrane tension such a large increase is not feasible by dilation of a lipid membrane alone which is only able to be dilated not more than about 4 %.[21,22] Thus, is was hypothesised that synaptophysin might be a key player in the facilitation of this process. To test that hypothesis, micromechanical experiments with giant unilamellar vesicles were performed. A special focus is set on the area compressibility modulus, since a decrease in that quantity leads to a larger maximum area expansion at constant rupture tension according to equation (3.10) and equation (3.16). The results of these experiments are described in the current section. This project was performed in collaboration with Dr. Julia Preobraschenski and Prof. Reinhard Jahn (Max Planck Institute for Biophysical Chemistry, Göttingen), who isolated synaptophysin, produced the GUVs and suggested the mentioned physiological role of synaptophysin. Most of the experiments and parts of the basic analyses were performed by Theresa Hune (Institute of Physical Chemistry, University of Göttingen) for her bachelor's thesis and in work performed thereafter.

4.2.1 Indentation experiments by atomic force microscopy

As an initial approach to probe the mechanics of GUVs which contain synaptophysin indentation experiments were performed by AFM (GUVs without synaptophysin: $N = 19$ ($N = 6$ remaining after data exclusion), GUVs with synaptophysin: $N = 25$ ($N = 8$ remaining after data exclusion), single experiment). A representative fitted force curve and the determined values of the area compressibility modulus and the pre-tension are shown in Figure 4.37.
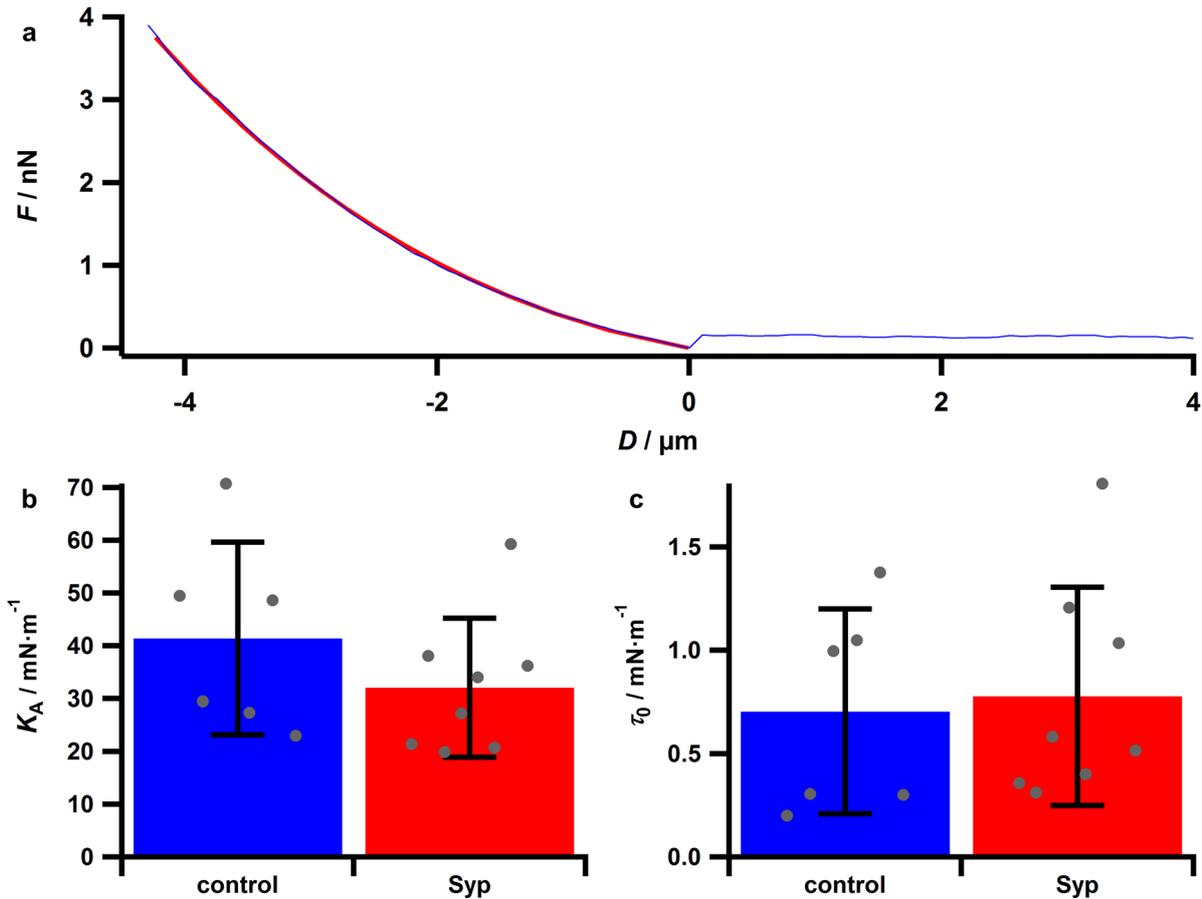
Figure 4.37: AFM indentation experiments to investigate the mechanics of GUVs containing synaptophysin. In **a** a representative force curve (blue) of the indentation of a GUV containing synaptophysin is shown along with the corresponding fit of the contact regime (red). The radius of the investigated vesicle was 9.9 µm. The resulting fit parameters are $K_A = 20$ mN·m^{-1} and $\tau_0 = 0.58$ mN·m^{-1} ($R^2 = 0.9996$). In **b** the area compressibility moduli are presented, in **c** the pre-stresses. The blue bars correspond to the respective mean values of vesicles without (control) and the red ones to that of vesicles with synaptophyin (Syp). Grey circles denote values from individual GUVs and the error bars indicate the standard deviations.

The fit shown in Figure 4.37 a indicates that the shape of the indentation curve is well described by the tension model (see section 3.4.8). Even though the mean area compressibility modulus of GUVs with synaptophysin is slightly lower than that for vesicles without synaptophysin, the fact that the mean values lie within the mean ± SD-interval of the other group (Figure 4.37 b) indicates a non-significant difference. For the values of the pre-stress there is hardly any difference between GUVs with and without synaptophysin (Figure 4.37 c). Thus, no clear evidence supporting the hypothesis that synaptophysin facilitated membrane dilation can be drawn from these AFM experiments. However, the throughput of this method is quite low because some preparations yielded hardly any adhered vesicles and vesicles ruptured or slipped away during indentation. Furthermore, the fluctuation of the

values of K_A in Figure 4.37 b is large. Therefore, another method was to be used to obtain more reliable results.

4.2.2   General results of micropipette aspiration experiments

To determine the area compressibility modulus of GUVs containing synaptophysin based on a larger number of vesicles and with higher accuracy than in section 4.2.1, a micropipette aspiration device was set up (see section 3.3.5.2) and the software necessary for the analysis of the obtained raw data was developed (see section 3.4.9). For test purposes GUVs composed of DOPC were aspired. A successful aspiration of such a GUV is shown in Figure 4.38 at different stages of aspiration.
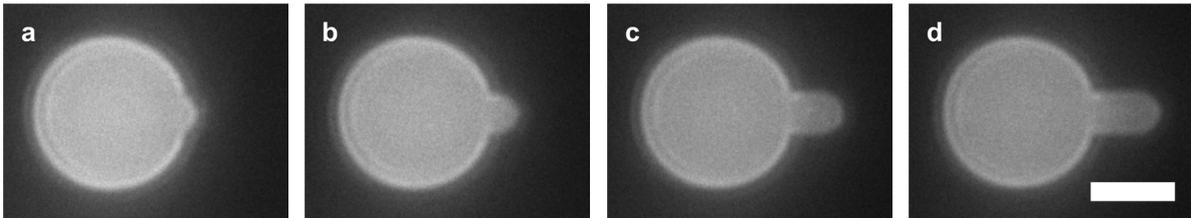
Figure 4.38: Fluorescence micrographs of the aspiration of a GUV composed of DOPC. The individual images show a GUV at different time-points of the aspiration: **a**: 0 s (Δp = 0 kPa, τ = 0 mN·m^{-1} (*per definitionem*)), **b**: 200 s (Δp = 0.49 kPa, τ = 0.85 mN·m^{-1}), **c**: 480 s (Δp = 2.5 kPa, τ = 4.9 mN·m^{-1}), **d**: 636 s (Δp = 3.9 kPa, τ = 6.8 mN·m^{-1}). The experiment was performed by Theresa Hune. Scale bar: 10 μm.

Plots like the one in Figure 4.39 a were used to identify individual steps of increase and plateaus of constant aspiration pressure (shown in blue) and corresponding increases of the tube length (shown in red). All plateaus which are especially visible in the plot of the pressure were selected manually. The logarithmic mean membrane tension values (equation (3.5)) obtained from each plateau are plotted in Figure 4.39 b against the corresponding mean apparent area strain (equation (3.6)). The assigned low- and high-pressure regimes are shown in green and cyan, respectively. A change in the course of the tension values, which was used as criterion for the separation of the regimes, is apparent from the plot (both regimes are separated by the magenta coloured circles). These distinct regimes were used to fit individual straight lines to the data points. The values of the mechanical parameters obtained from these fits according to equations (3.7), (3.8) and (3.10) are written in the caption of Figure 4.39.
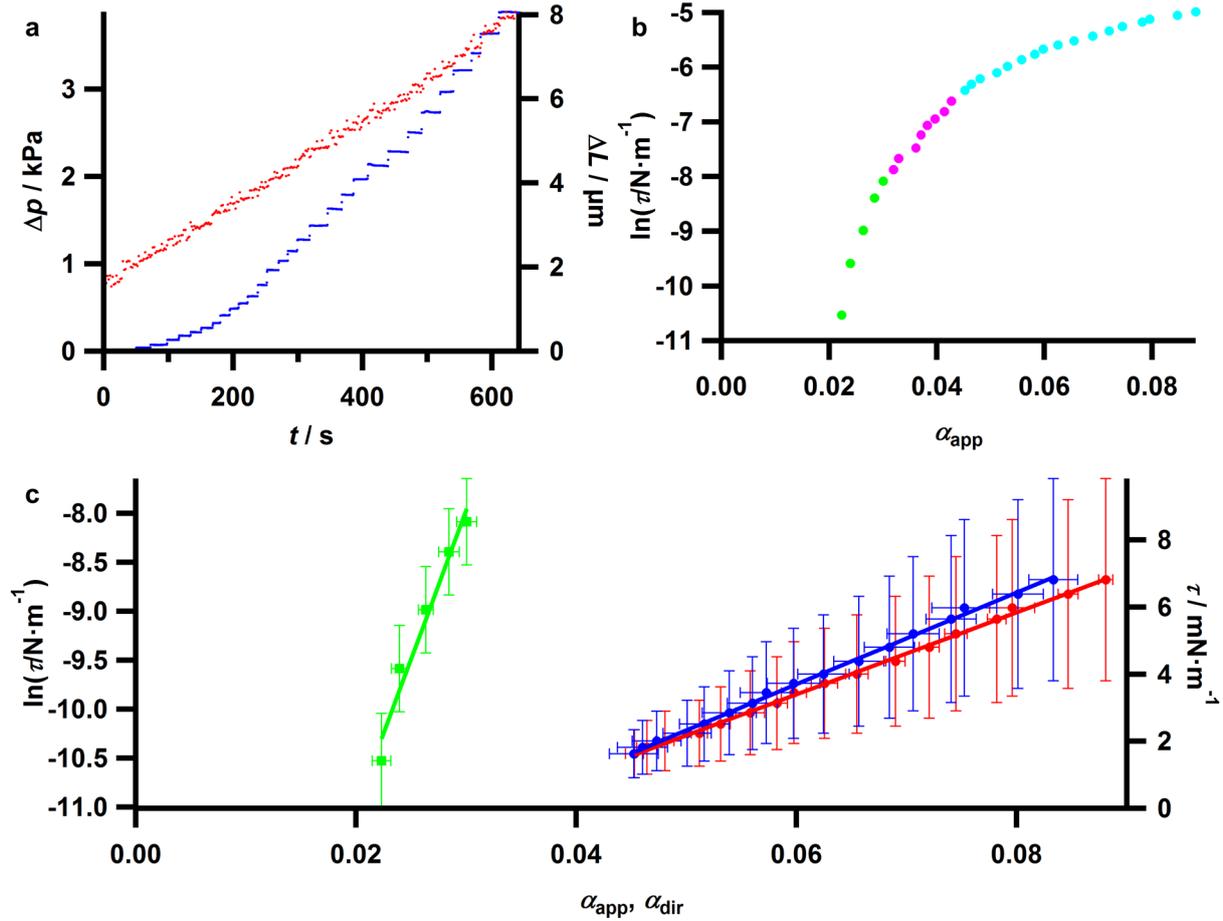
Figure 4.39: Analysis of an aspiration experiment of a GUV composed of DOPC. a plots the aspiration pressure Δp (blue dots, left ordinate) and the tube length ΔL (red dots, right ordinate) for the measurement of the vesicles shown in Figure 4.38 as a function of time since the beginning of the aspiration process. In **b** the logarithm of the membrane tension is plotted against the apparent area strain. The green circles denote the data points assigned to the low-pressure regime, the cyan circles were assigned to the high-pressure regime and the magenta coloured ones show the transition between both regimes and were excluded from further analysis. In **c** the data points assigned to the low- and the high-pressure regime in **b** are shown again with their calculated errors. Green squares denote the tension values in the low-pressure regime on a logarithmic scale (left ordinate) as a function of the apparent area strain. The red and the blue circles correspond to the tension values in the high-pressure regime on a linear scale (right ordinate) as a function of the apparent and the direct area strain, respectively. Error bars are obtained by Gaussian error propagation of the mean values obtained from **a** (see section 3.4.9). The linear fits of each of the three datasets are shown in the same colour. The analysis of these fits yielded $\kappa = (5.0 \pm 0.5) \cdot 10^{-20}$ J, $K_{app} = (122 \pm 1)$ mN·m^{-1} and $K_{dir} = (137 \pm 2)$ mN·m^{-1}. For the calculation of K_{dir} the individual value of κ obtained from this vesicle was used. The experiment was performed by Theresa Hune.

4.2.3   Test measurements with GUVs composed of DOPC

To test the magnitude of the mechanical parameters obtained with the micropipette aspiration setup a larger number of GUVs composed of DOPC, which are well described in literature,[140,141] were subject to micropipette aspiration (N = 27 GUVs from two independent preparations, N = 14 GUVs remaining after all steps of data exclusion). Figure 4.40 shows the determined bending modulus and the apparent and direct area compressibility moduli of GUVs composed of DOPC. For the plot of the direct area compressibility modulus and the determination of the corresponding statistic parameters four negative values of K_{dir} for single GUVs were excluded additionally (see description in section 4.2.5).
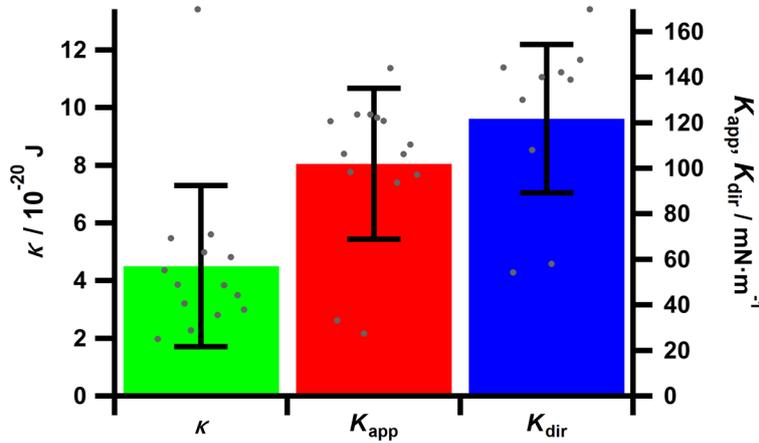
Figure 4.40: Mechanic moduli of GUVs composed of DOPC determined by micropipette aspiration. The mean value of the bending modulus (κ) is indicated by the green bar (left ordinate) and the mean values of the apparent (K_{app}) and the direct area compressibility modulus (K_{dir}) by the red and the blue bar, respectively (right ordinate). Error bars denote the standard deviations. The grey circles indicate the values measured by the aspiration of a single GUV. Note that for the direct area compressibility modulus data of four measurements resulting negative values are not shown. The experiments were performed by Theresa Hune.

The determined mechanical parameters are: κ = (4.5 ± 2.8)·10^{-20} J (mean ± SD), K_{app} = (102 ± 33) mN·m^{-1} (mean ± SD) and K_{dir} = (122 ± 33) mN·m^{-1} (mean ± SD). A discussion of the determined values and of possible errors will be given in section 5.2.1.

4.2.4   Behaviour of GUVs containing synaptophysin during aspiration

In aspiration experiments of GUVs prepared from small unilameller vesicles which were obtained by the detergent removal method (see section 3.2.7) a continuous flow of the vesicles into the pipette, i.e. a growth of the length of the membrane tube inside the pipette, without an intended increase in suction pressure was observed frequently (explicit numbers will be given in section 4.2.5). Figure 4.41 shows an example of the pressure and the corresponding tube length of an aspired GUV containing synaptophysin which exhibits a continuous aspiration during phases of constant pressure.
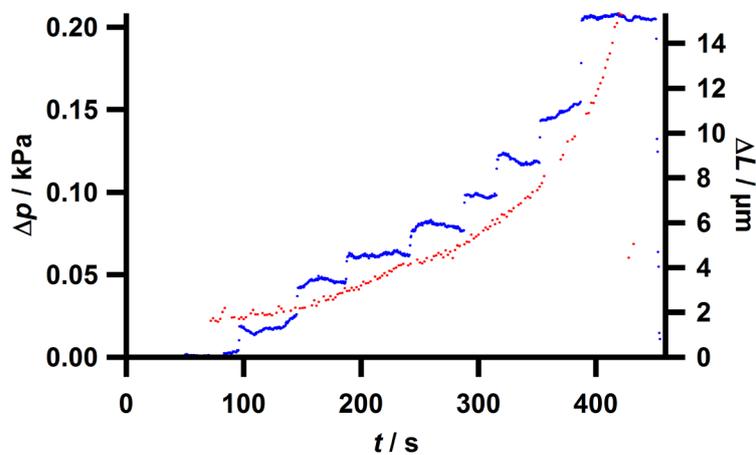
Figure 4.41: Flow of a GUV into the micropipette not related to the increase of aspiration pressure. A GUV containing synaptophysin was aspired by a micropipette. The aspiration pressure Δp is plotted by the blue dots (left ordinate) and the tube length ΔL by the red dots (right ordinate). The experiment was performed by Theresa Hune.

From this plot it is evident that the aspiration persists and is even accelerated when the pressure is kept constant for a while. Furthermore, a long tube length is reached at a relative low aspiration pressure, as compared to the example of the GUV in Figure 4.39 a which even has a radius two times as large as that of the vesicle containing synaptophysin. Since the vesicle keeps on being aspired during phases of constant aspiration pressure, there is probably no equilibrium reached between the aspiration pressure and the membrane tension of the vesicle. Therefore, the theory introduced in section 3.3.5.1 does not hold any more and the mechanical moduli cannot be determined accurately.

4.2.4.1 Aspiration of GUVs at constant set-pressure

To shed more light on the continuous aspiration during plateaus of constant pressure described before, aspiration experiments were carried out where the vesicles were aspired by an intermediate pressure and that pressure was kept constant while the progress of aspiration was monitored. Provided that the aspiration length reaches a constant value after a certain relaxation time, the data could be used to describe the kinetics of the underlying process.

During these experiments fission events of the aspired vesicles frequently occurred (69 % of the vesicles showing at least one fission event). In these events a neck is formed in the aspired tube, followed by complete fission, as shown exemplarily in Figure 4.42 b and c. Such events were observed in ordinary aspiration experiments with stepwise increase in aspiration pressure as well, however, less frequently (see section 4.2.5).
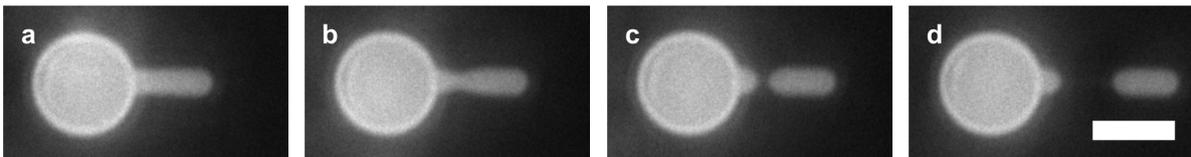
Figure 4.42: Fission of a vesicle during aspiration. A GUV containing synaptophysin was aspired at constant set-pressure. The fluorescence images were taken t = 680 s (**a**), t = 726 s (**b**), t = 728 s (**c**) and t = 740 s (**d**) after begin of the aspiration. The experiment was performed by Theresa Hune. Scale bar: 10 µm.

Importantly, a saturation of the aspiration length was never observed (N = 13 GUVs from three independent preparations). Therefore, the reason for this continuous aspiration was to be investigated, as it might be the case that in a slow process some kind of transition takes place by the action of synaptophysin which enables the large dilation of the membrane. To this end, the surface area of the curved side of the tube (second term in equation (3.20)), the volume of the aspired vesicle (equation (3.19)) and the aspiration pressure as a function of time were fitted with a straight line to obtain rates of the respective quantities. When fission events or other sudden changes in the rates occurred a further straight line was fitted. Non-linear increases of the tube length immediately before fission events were excluded from the fits. An exemplary plot of the fitted tube length and aspiration pressure is shown in Figure 4.43. Because of the fission events and other changes in the rates for most vesicles multiple rates were obtained for each quantity (blue circles in Figure 4.44). The mean value of the rates obtained from a single vesicle were calculated additionally (red circles in Figure 4.44).
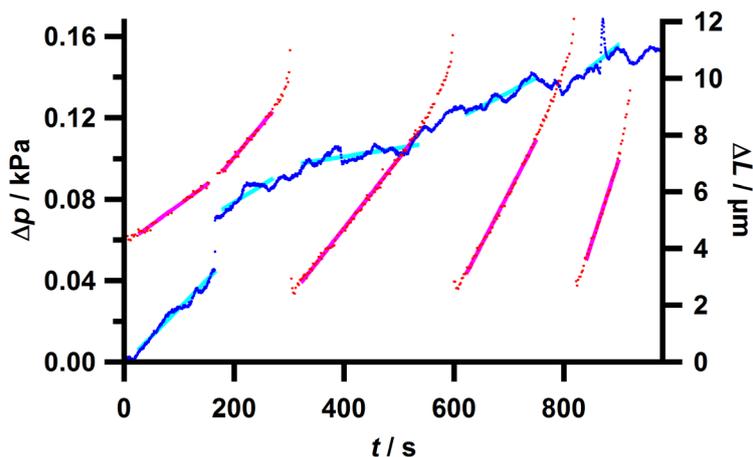
Figure 4.43: Aspiration of a GUV without intentional increase of the aspiration set-pressure. The aspiration pressure Δp is plotted by the blue dots and the corresponding fits by the cyan lines (left ordinate) and the tube length ΔL by the red dots and the corresponding fits by the magenta lines (right ordinate) against the time after beginning of the pressure measurement. The experiment was performed by Theresa Hune.

Then, possible correlations between the three rates were investigated by plotting the rates (Figure 4.44) and calculating Pearson correlation coefficients in order to state on possible reasons for the continuous aspiration like loss of volume or slightly increasing aspiration pressure.

Although the pressure was set to be constant, a slight increase in aspiration pressure was observed (0.08 Pa·s^{-1} on average, 0.23 Pa·s^{-1} at maximum, compared to 2.3 Pa·s^{-1} on average and at least 0.4 Pa·s^{-1} for experiments with intentional increase of the aspiration pressure with GUVs containing synaptophysin). However, the plot of the rate of tube area change against the pressure rate in Figure 4.44 a with Pearson correlation coefficients of $\rho = -0.15$ for all corresponding rates and $\rho = -0.10$ for the mean rates shows that this increase seems not to be the cause for the continuous aspiration.

On the other hand, the rate of volume change correlates negatively with the change of the aspired area (Figure 4.44 b), indicated by Pearson correlation coefficients of $\rho = -0.86$ for all rates and $\rho = -0.92$ for the mean rates.

Regarding the dependency of the loss in volume on the pressure change, the Pearson correlation coefficient of the mean values ($\rho = -0.27$) might indicate a correlation (data not shown). However, regarding the values of all individual fits ($\rho = 0.08$) there seems not to be a pronounced correlation. Such a correlation should, furthermore, lead to a dramatic loss of volume when the aspiration pressure is increased intentionally. Similar analyses were performed with regard to the rate of change of the tube length and of its volume. Since the radius of the tube is quasi the same for all pipettes used, this did not result in major changes

of the appearance of the plots. Here, the area of the tube was regarded because it is the most convenient quantity when talking about the aspiration of a defined quasi-constant surface.
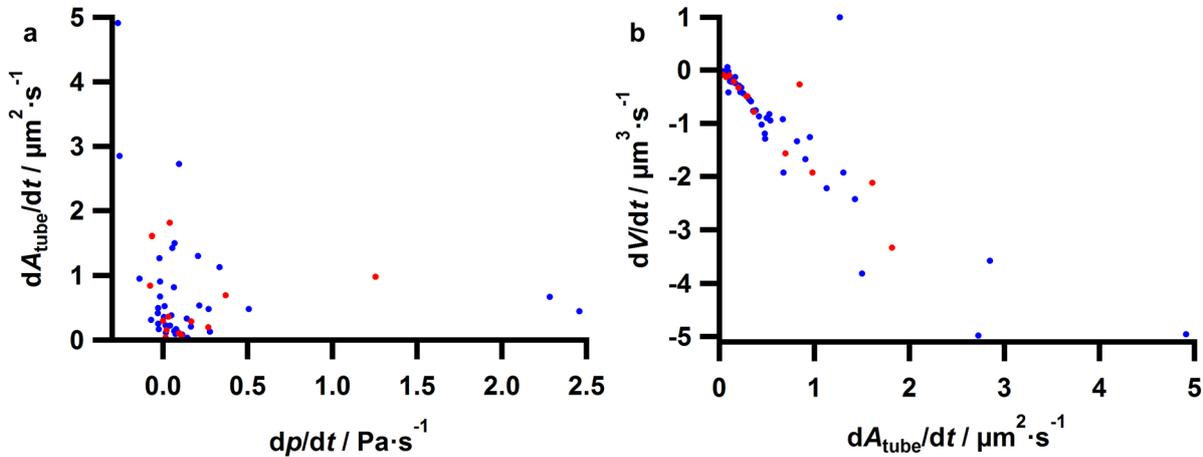
Figure 4.44: Relationships between the rate of pressure change, the rate of vesicle's surface area aspiration and the change of vesicle's volume. In **a** the rate of aspiration, described by the change in area of the aspired tube, is plotted against the rate of pressure change, in **b** the rate of the change of the vesicle's volume is plotted against the area change, which is plotted on the ordinate in **a**. Blue circles denote the values obtained from a single linear fit of the respective quantity, red circles denote the mean values of these slopes obtained from a single vesicle. The experiments were performed by Theresa Hune.

These data indicate that the continuous aspiration is probably caused by the loss of volume. However, for cells such a behaviour is well known to be caused by mechanic imbalance (for a discussion see section 5.2.3).[151,152] Alternatively, a loss of the vesicle's volume creates excess membrane leading to further aspiration even at constant pressure and possibly also constant membrane tension. Therefore, the data obtained from the experiments performed with constant set-pressure were analysed in more detail.

In Figure 4.45 a the normalised total volumes of the 13 investigated vesicles are shown. The quantity was normalised to the mean of the first 15 values. The colours denote the rate of increase of the surface area of the aspired tube (the darker the colour, the faster the aspiration rate). The plot shows a faster decrease of the volume for fast aspired GUVs. Sudden decreases in the volume are caused by fission events. This faster loss of volume is not exclusively attributed to fission but also the decrease of the volume is faster in between fission events for fast aspired vesicles (see sections 5.2.3 and 5.2.4 for a detailed discussion). A corresponding plot of the total surface areas is presented in Figure 4.45 b. This shows that vesicles which are faster aspired are more prone to fission. The plateaus in

between fission events indicate a faster and larger surface area increase for fast aspired vesicles (darker colours) than for the slowly aspired ones.
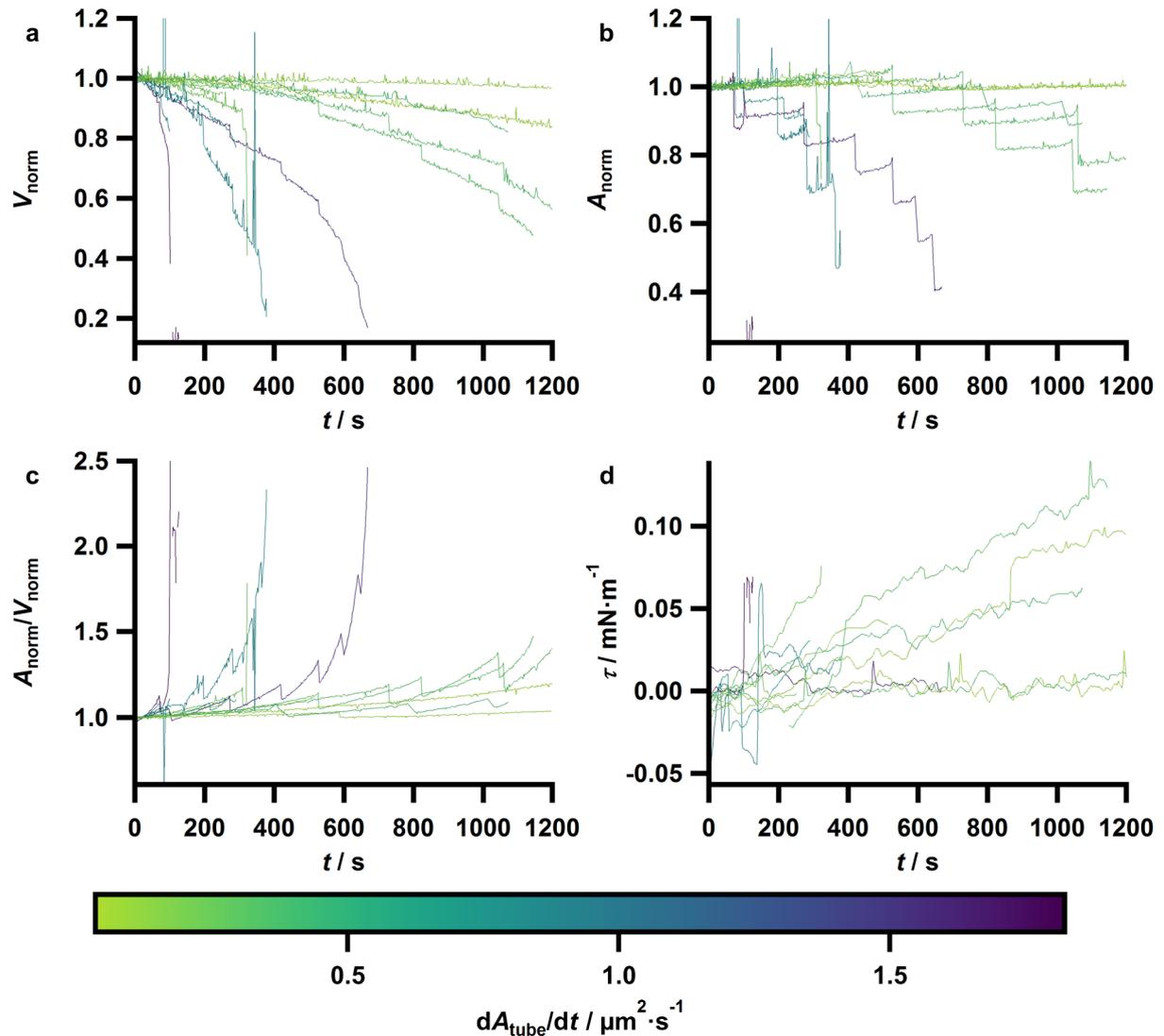
Figure 4.45: Time courses of different quantities during aspiration with constant set-pressure to investigate the continuous flow. The normalised total volumes of aspired vesicles are plotted in **a**, the normalised total surface areas of aspired vesicles are plotted in **b**, the normalised total surface areas divided by the normalised volumes of the vesicles are plotted in **c** and their membrane tensions in **d**. In all plots the colour represents the change of the aspired membrane surface with time, i.e. the change of the area of the curved side of the tube. The colour scale shown below **c** and **d** holds for all plots. Note that in **b** the diagram is cut at $A_{norm} = 1.2$, but two data points of a single curve exceed this value at about 100 s. The experiments were performed by Theresa Hune.

To get insight into the aspiration of excess area, the normalised total surface area divided by the normalised total volume (A_{norm}/V_{norm}) is plotted against time in Figure 4.45 c. By the normalisation one gets rid of the inverse radius dependency of the quotient of the area and the volume which is to be expected for a sphere. A larger GUV should show smaller values

of the total surface area divided by the total volume for the same tube length as compared with smaller GUVs. This influence is now removed by normalisation. The increase of A_{norm}/V_{norm} is much larger for fast aspired vesicles, as compared with slowly aspired ones, even though the first show frequent drops in A_{norm}/V_{norm} caused by fission. This quantity is a measure of the deviation from a spherical shape by extension of the tube. As such, a faster increase is somehow to be expected for GUVs exhibiting a high aspiration rate. Aspiration caused by a slight increase of the aspiration pressure should be accompanied by an increase of the membrane tension. On the other hand, liquid droplet-like objects are aspired without an increase in tension (see discussion in section 5.2.3).[152] Therefore, in Figure 4.45 d the membrane tension is plotted against time. This plot shows an increase of the membrane tension independent of the aspiration rate. Notably, the two GUVs exhibiting extraordinary large aspiration rates (purple curves in Figure 4.45) possess an almost constant membrane tension. However, there are also GUVs present which have a significant increase in tension (see discussion in section 5.2.3).

The fission described in this section was only observed inside the micropipette but not spontaneously without aspiration of the GUV. Most vesicles investigated in experiments with constant set-pressure show fission events. Numbers of the relative amount of GUVs exhibiting fission events are presented in the next section for vesicles containing synaptophysin or synaptobrevin and for control vesicles in measurements with intentionally increased suction pressure.

To summarise, faster aspired vesicles are more prone to fission, show a faster loss of volume not only caused by fission and provide excess surface area faster which is, notably, not caused by an increase in membrane tension. These findings taken together point again to the loss of volume as the cause of continuous aspiration.

4.2.5 Mechanical moduli of GUVs containing synaptophysin

In this section the mechanic moduli determined from measurements with stepwise increase of the aspiration pressure are presented. In the previous section a frequently occurring continuous aspiration of GUVs without further increase of the aspiration pressure was described. Since the loss of volume violates assumptions used in the theory utilised for the calculation of the mechanical moduli of aspired vesicles, such measurements have to be excluded from analysis. The most convenient way to account for such an influence would be to exclude data based on the rate of increase of the tube surface area or the rate of volume

loss during the plateau phases of constant pressure. However, an attempt to exclude vesicles based on the rate of tube area increase failed due to large fluctuations and few data points for each plateau, which is accompanied by large errors of the obtained rates. Therefore, plots such as shown in Figure 4.41 were checked manually to exclude data without apparent steps in the tube length which correlate with steps in pressure.

From all aspired vesicles (control: $N = 30$ from four independent preparations, synaptophysin: $N = 93$ from seven independent preparations, synaptobrevin: $N = 35$ from three independent preparations) only a minor fraction remained after all steps of exclusion (control: $N = 5$, synaptophysin: $N = 9$, synaptobrevin: $N = 3$) for the calculation of the area compressibility moduli. For comparison, from 27 aspired GUVs composed of DOPC 14 remained. Due to the data exclusion criterion that at least three data points have to lie in a single pressure regime to accept the data, the corresponding numbers for the bending modulus are even lower. By the final step of data exclusion due to continuous aspiration during plateaus of constant pressure 80 % and 77 % of the data present before were discarded for vesicles containing synaptophysin and synaptobrevin, respectively. Even 55 % of the data of control GUVs electroformed from small vesicles produced by the detergent removal method were removed in that step. For comparison, only 18 % of data from vesicles produced directly by electroformation of a lipid film of DOPC were discarded. This indicates that this continuous flow is probably more pronounced for GUVs containing proteins and possibly also for GUVs containing remains of detergents.
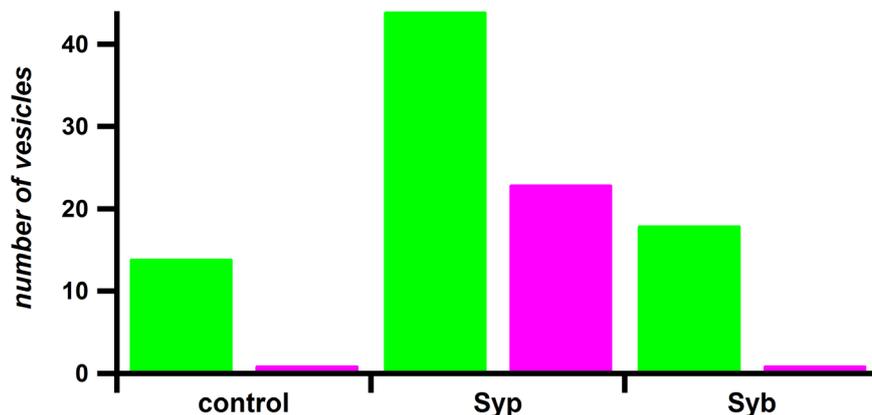
Figure 4.46: Fraction of vesicles showing fission events. The number of vesicles exhibiting fission events in experiments with intentional increase of the aspiration pressure are shown by magenta coloured bars, the number of vesicles not exhibiting fission events by green coloured bars for control vesicles (control), for vesicles containing synaptophysin (Syp) and vesicles containing synaptobrevin (Syb). The experiments were mostly performed by Theresa Hune.

An inspiring insight in a possible effect of synaptophysin can be gained from the number of vesicles which have shown fission events during these experiments (see Figure 4.46).

Among the GUVs which provided data capable of evaluating the occurrence of fission events, 7 % of the control vesicles, 34 % of vesicles containing synaptophysin and 5 % of vesicles containing synaptobrevin showed fission events (control: $N = 15$, synaptophysin: $N = 67$, synaptobrevin: $N = 19$). This finding indicates that GUVs containing synaptophysin might be more prone to fission. A possible influence of synaptophysin on the integrity of GUVs is discussed in section 5.2.4.
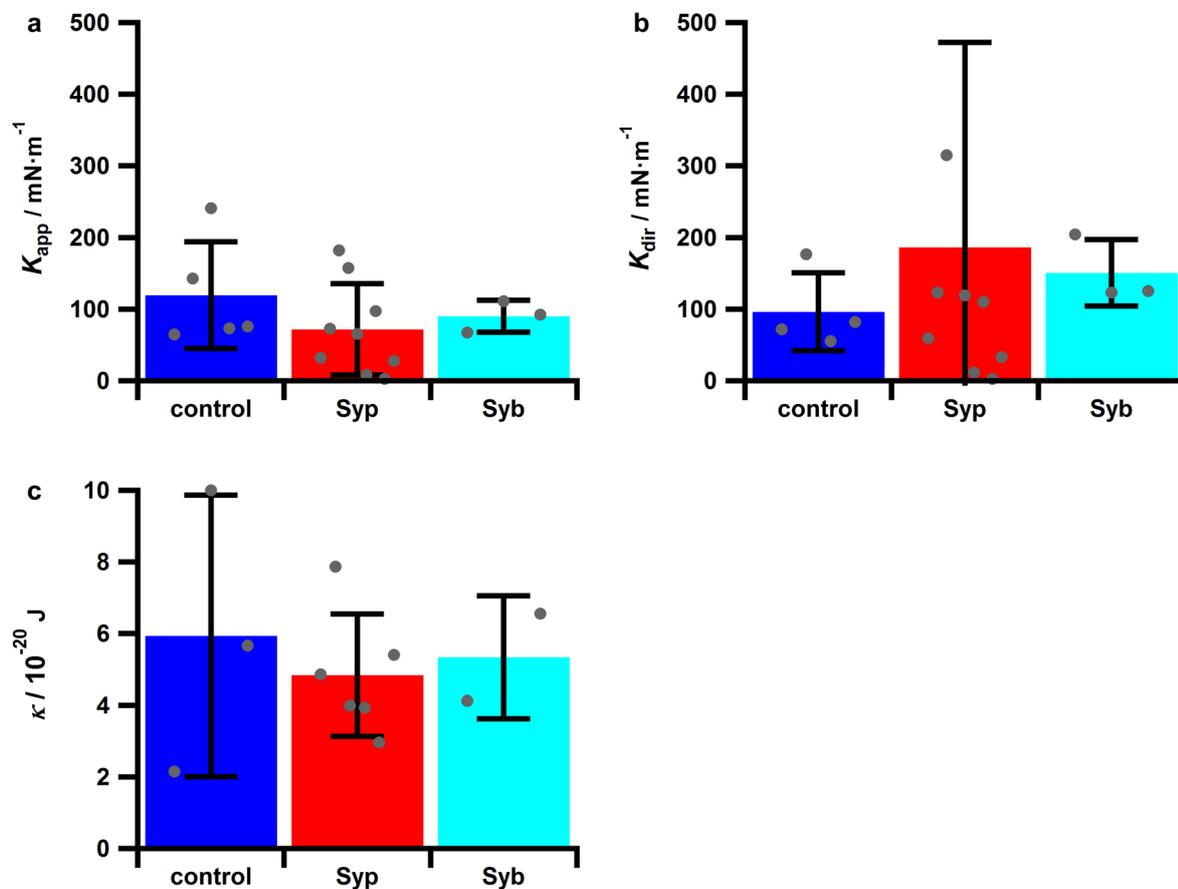
Figure 4.47: Mechanic moduli of GUVs containing synaptophysin or synaptobrevin compared to control vesicles without proteins. The diagram in **a** shows the apparent area compressibility moduli, the one in **b** the direct area compressibility moduli and that in **c** shows the bending moduli. The respective quantity of control vesicles (control) is shown by the blue coloured bar, that of vesicles containing synaptophysin (Syp) by the red and that of vesicles containing synaptobrevin (Syb) by the cyan coloured bar. The height of the bars indicate the mean value and the error bars correspond to the standard deviations. The grey circles show values of individual GUVs. For K_{dir} of GUVs containing synaptophysin one value lying above 500 mN·m^{-1} is not shown. The experiments were mostly performed by Theresa Hune.

Figure 4.47 shows the apparent and direct area compressibility moduli and the bending moduli for control vesicles and for those containing synaptophysin or synaptobrevin in their membranes.

The numerical values of the mean and the standard deviation plotted in Figure 4.47 can be found in Table 4.6.

Table 4.6: Apparent area compressibility moduli, direct area compressibility moduli and bending moduli of control vesicles, vesicles with synaptophysin and vesicles with synaptobrevin (mean ± SD).

sample (protein)	K_{app} / N·m^{-1}	K_{dir} / N·m^{-1}	κ / 10^{-20} J
control	0.119 ± 0.075	0.096 ± 0.055	5.9 ± 3.9
synaptophysin	0.072 ± 0.064	0.19 ± 0.29	4.8 ± 1.7
synaptobrevin	0.090 ± 0.022	0.151 ± 0.046	5.3 ± 1.7

The mean value of the apparent area compressibility modulus of control vesicles is the largest and that of the vesicles containing synaptophysin is the smallest (Figure 4.47 a). However, there is no significant difference in K_{app} when comparing vesicles containing synaptophysin with control vesicles nor with vesicles containing synaptobrevin. Especially the data of vesicles containing synaptobrevin have to be treated with care due to the small amount of values.

For vesicles containing proteins, the direct area compressibility modulus (Figure 4.47 b) is larger than the apparent one, as to be expected. However, for the control sample this value is smaller than the corresponding apparent area compressibility modulus. Here, one negative value of K_{dir} was excluded additionally before the calculation of the mechanical moduli. This negative value results from overcorrection for thermal undulations (see section 3.3.5.1), which leads to a negative slope of the fit of the tension versus the direct area strain. That results in the lower mean even when it is excluded because that individual value is the largest one of K_{app} measured (central data point for control vesicles in Figure 4.47 a). The order of the mean values of the direct area compressibility modulus among control, synaptophysin and synaptobrevin vesicles is inverted as compared with the apparent area compressibility modulus. The mean values of the bending modulus are even more similar to each other than the values of the area compressibility moduli. To conclude, no significant differences can be found for the mechanical moduli among control vesicles and vesicles containing synaptophysin or synaptobrevin. A discussion of the data can be found in section 5.2.2.

It has to be noted that the first five data points of vesicles containing synaptophysin in Figure 4.47 a originate from a single introductory experiment in an unbuffered glucose solution and the latter four points from measurements in buffered solutions. The mean value of the measurements of GUVs containing synaptophysin in the buffered solution lies below the mean $\pm$ SD interval of the measurements in the unbuffered solution (see Figure 4.48). However, one vesicle which loses volume during aspiration (see section 4.2.6) corresponds to the lowest value of K_{app} in Figure 4.47 a. When neglecting that vesicle, the mean value of the measurements performed in buffered glucose solution lies within the mean $\pm$ SD interval of the measurements in unbuffered solution. The mean value of the measurements performed in unbuffered glucose solution still exceeds the mean $\pm$ SD interval of the measurements performed in unbuffered solution. Moreover, the two values of control vesicles which were obtained from measurements in a buffered solution are also smaller than the ones from measurements in an unbuffered solution (see Figure 4.48). The former lie within the mean $\pm$ SD interval of the vesicles containing synaptophysin even when the value of the vesicle which loses volume (see section 4.2.6) is included.

Note that all measurements performed in unbuffered solutions stem from a single preparation and were measured on a single day.
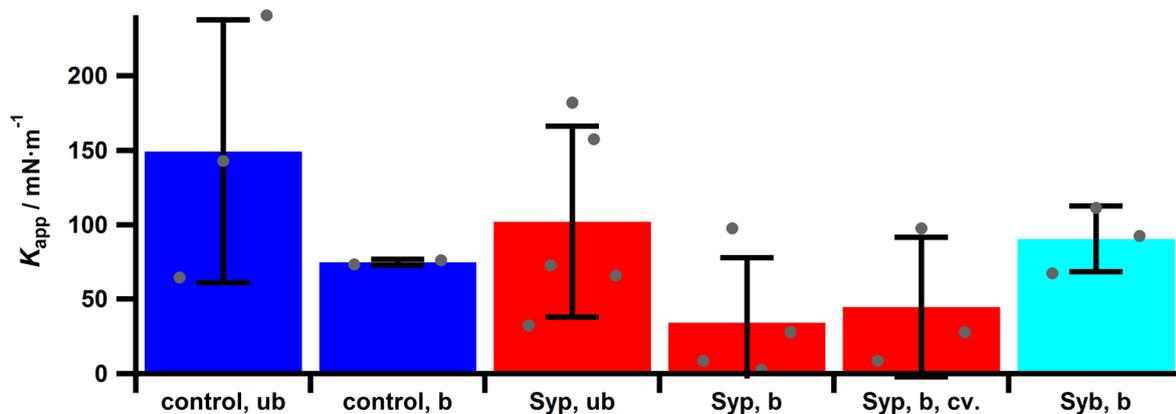
Figure 4.48: Apparent area compressibility modulus of GUVs containing synaptophysin or synaptobrevin and of control vesicles without proteins with regard to the solution used for the aspiration experiment. The mean values of control vesicles are shown by the blue coloured bars, that of vesicles containing synaptophysin (Syp) by the red ones and that of vesicles containing synaptobrevin (Syb) by the cyan coloured bar. Further abbreviations on the abscissa are: ub: unbuffered solution, b: buffered solution, cv: constant volume. The error bars correspond to the standard deviations. Grey circles show values of individual GUVs. The experiments were mostly performed by Theresa Hune.

Furthermore, the pH of the unbuffered glucose solution only deviated up to ΔpH = 0.4 from the pH of the buffered solution and the pH of the GUV dispersion was not more than ΔpH = 1 smaller than that of the glucose solution. When comparing the data of Figure 4.48 the poor statistics have to be considered. For these reasons values measured in unbuffered and values measured in buffered solution were merged for the main results in Figure 4.47 (see also discussion in section 5.2.2).

4.2.6   Time courses of the volume

In order to investigate whether the vesicles used for the determination of the mechanical moduli lost volume during aspiration, the time courses of an arbitrarily chosen subset of vesicle's volumes are regarded. From the plots shown in Figure 4.49, furthermore, constituents of the GUVs which might drive the loss of volume can be suggested.

The vesicles used for the determination of mechanical moduli generally show a constant volume (Figure 4.49 a and b), only a single GUV containing synaptophysin exhibits a steep decrease of the volume. This vesicle results in the lowest value of the apparent area compressibility modulus which is shown in Figure 4.47 a, as already noted above. This indicates that the data plotted in Figure 4.47 is reliable. If vesicles are included which were previously excluded due to continuous aspiration during plateaus of constant pressure (Figure 4.49 c and d) it can be found that only GUVs which lose a significant amount of volume during aspiration lead to the determination of values of the apparent area compressibility modulus below 10 mN·m^{-1} (Figure 4.49 d). Not for a single measurement which resulted in an apparent area compressibility modulus larger than 10 mN·m^{-1} (Figure 4.49 c) a significant loss of volume can be found.
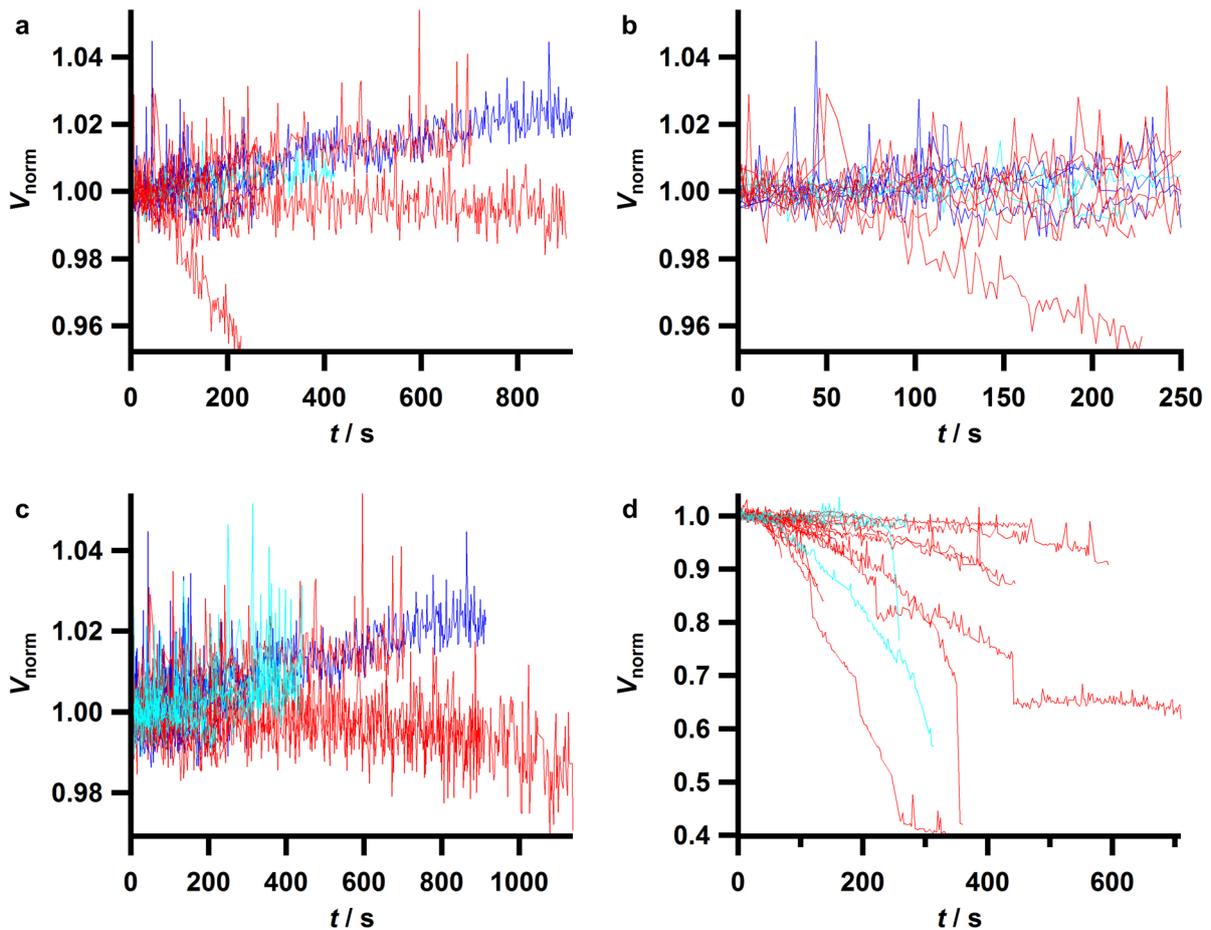
Figure 4.49: Time courses of vesicle's volumes during aspiration experiments capable of determining mechanical moduli. In **a** the volumes corresponding to data used for the determination of mechanical moduli, which are shown in Figure 4.47, are plotted against time. **b** shows a magnification of the data plotted in **a** at low times. In **c** and **d** data of measurements which were discarded because of fast aspiration during plateaus of constant pressure are included as well. **c** shows volume data of measurements with values of K_{app} which were calculated to be larger than 10 mN·m^{-1}, **d** shows a corresponding plot for values smaller than 10 mN·m^{-1}. Blue coloured curves show data of control vesicles, red coloured curves show data of vesicles containing synaptophysin and cyan coloured curves data of vesicles containing synaptobrevin. The experiments were mostly performed by Theresa Hune.

As already observed in section 4.2.4.1, vesicles which lose a large amount of their initial volume show a combination of a continuous decline of the volume and spontaneous events caused by fission. Regarding the different samples, pure lipid vesicles without proteins in their membranes do not show a pronounced reduction of the volume during aspiration. Various vesicles containing synaptophysin lose volume during aspiration. In numbers, among all vesicles whose volume course is plotted in Figure 4.49 c and d 18 of 38 GUVs containing synaptophysin (47 %), two of twelve GUVs containing synaptobrevin (17 %) and none of the control vesicles lose permanently volume below V_{norm} = 0.975 (see Figure 4.50).
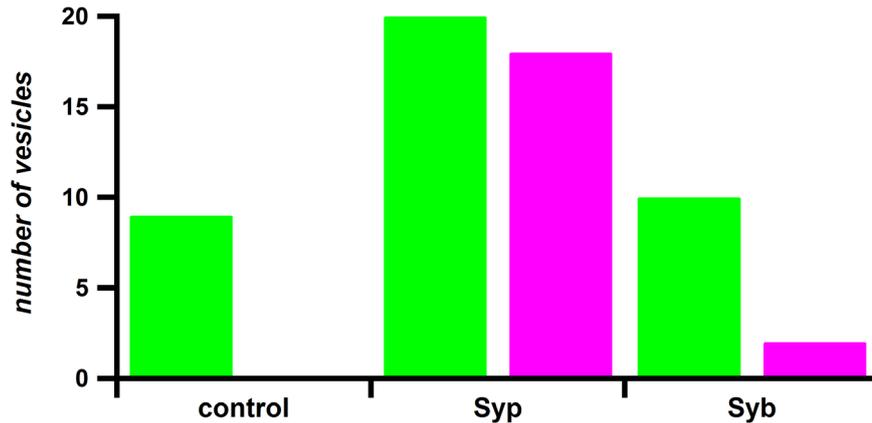
Figure 4.50: Fraction of vesicles which permanently lose volume below 97.5 % of its initial value. The number of vesicles losing considerable volume in experiments with intentional increase of the aspiration pressure are shown by magenta coloured bars, the number of vesicles not losing considerable volume by green coloured bars for control vesicles (control), for vesicles containing synaptophysin (Syp) and vesicles containing synaptobrevin (Syb). The experiments were mostly performed by Theresa Hune.

4.2.7 Maximum apparent area strain and maximum membrane tension

The results presented in section 4.2.5 do not provide significant evidence for the hypothesis that a reduction of the area compressibility modulus caused by synaptophysin enables a larger dilation of lipid membranes. However, even with an unchanged area compressibility modulus the maximum possible membrane dilation might be increased in membranes containing synaptophysin provided they withstand larger membrane tensions. To test this hypothesis, the maximum apparent area strains and the maximum membrane tensions were extracted from the experimental data described in section 4.2.5. These values were extracted from the last pressure plateau measured during aspiration. It has to be recognised that these values only provide a lower estimate, since some vesicles were completely aspired instead of being ruptured. A distinction between complete aspiration and rupture was for most vesicles not possible because at a frame rate of 0.5 Hz the majority of these events were not recorded by fluorescence images. However, the existence of both mechanisms could be shown exemplary for a subset of all measurements (see Supplementary Figure 10 for images of rupturing and completely aspired vesicles). Whenever a fission event was the cause for the decline of the measured tube length the corresponding measurement was discarded for the determination of the maximum membrane tension and the maximum apparent area strain. Among the data remaining after the last step of data exclusion for the determination of the mechanical moduli this accounts for one measurement of control and

vesicles containing synaptophysin, each. The obtained values of the maximum apparent area strains and the maximum membrane tensions for vesicles containing synaptophysin or synaptobrevin and for control vesicles are plotted in Figure 4.51.
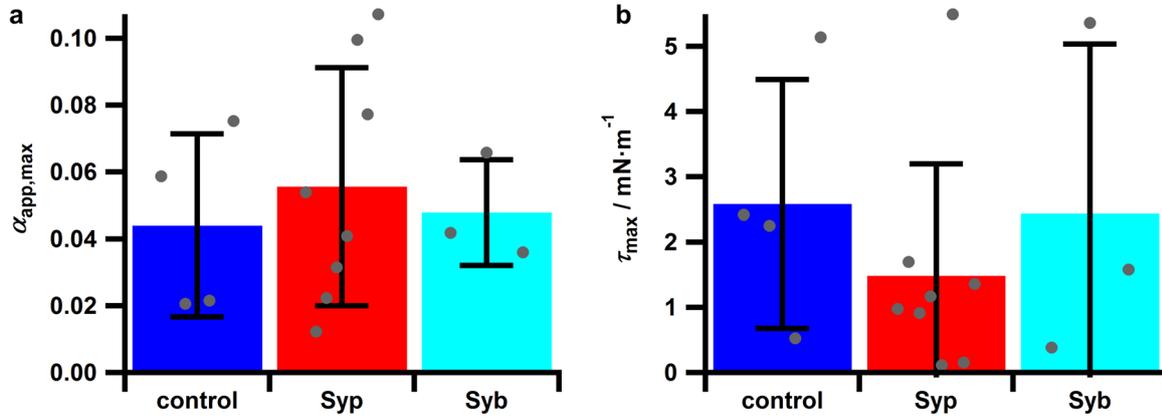
Figure 4.51: Maximum apparent area strains and maximum membrane tensions of GUVs containing synaptophysin or synaptobrevin and of control vesicles without proteins. The diagram in **a** shows the maximum apparent area strains and the one in **b** the maximum membrane tensions. By the blue coloured bars the respective quantity of control vesicles (control) is shown, by the red that of vesicles containing synaptophysin (Syp) and by the cyan coloured bars that of vesicles containing synaptobrevin (Syb). The height of the bars indicate the mean value and the error bars correspond to the standard deviations. Grey circles show values of individual GUVs. The experiments were mostly performed by Theresa Hune.

Table 4.7 lists the mean values and the standard deviations of the maximum apparent area strains and maximum membrane tensions plotted in Figure 4.51.

Table 4.7: Maximum apparent area strains and maximum membrane tensions of control vesicles, vesicles with synaptophysin and vesicles with synaptobrevin (mean ± SD).

sample (protein)	$\alpha_{app,max}$	τ_{max} / mN·m^{-1}
control	0.044 ± 0.027	2.6 ± 1.9
synaptophysin	0.056 ± 0.036	1.5 ± 1.7
synaptobrevin	0.048 ± 0.016	2.4 ± 2.6

The mean maximum apparent area strain of GUVs containing synaptophysin is slightly increased compared to control vesicles, however, this difference is not significant when regarding the standard deviations and the mean value of GUVs containing synaptobrevin is even closer to that of control vesicles. Regarding the maximum membrane tensions there is

no significant difference between the three samples, either. The maximum membrane tension of GUVs containing synaptophysin is on the same level as for the control and for GUVs containing synaptobrevin. There is no significant change of the maximum apparent area strain evident from Figure 4.51 which does therefore not support the hypothesis that synaptophysin facilitates membrane dilation. However, when regarding these values the low statistics have to be kept in mind.

Finally, in Figure 4.52 the values of the maximum apparent area strain are plotted again in the same way as done in Figure 4.48 for the apparent area compressibility modulus, i.e. the values of $\alpha_{app,max}$ are not only differentiated by the protein inside the GUV membrane but also with regard to the fact if the solution which was used for the measurement was buffered or not.
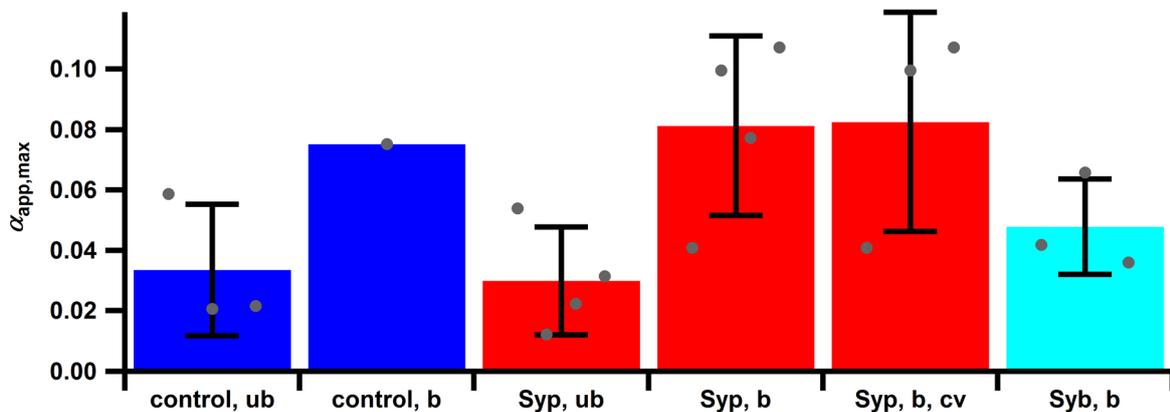
Figure 4.52: Maximum apparent area strain of GUVs containing synaptophysin or synaptobrevin and of control vesicles without proteins with regard to the solution used for the aspiration experiment. The mean values of control vesicles are shown by the blue coloured bars, that of vesicles containing synaptophysin (Syp) by the red ones and that of vesicles containing synaptobrevin (Syb) by the cyan coloured bar. Further abbreviations on the abscissa are: ub: unbuffered solution, b: buffered solution, cv: constant volume. The error bars correspond to the standard deviations. Grey circles show values of individual GUVs. Note that for buffered control vesicles only one value exists, therefore the height of the bar corresponds to this value and no error can be assigned. The experiments were mostly performed by Theresa Hune.

When measured in a buffered solution, the vesicles containing synaptophysin exhibit a significantly larger maximum apparent area strain as compared with those measured in an unbuffered solution. However, the single value for control vesicles measured in the buffered solution almost perfectly matches the mean value of buffered GUVs containing synaptophysin.

No clear conclusion can be drawn from this plot due to the low amount of data points for each category: The discrepancy between buffered vesicles containing synaptophysin and

unbuffered vesicles which contain synaptophysin or which do not may indicate an influence of the protein but the single value for buffered control vesicles may point to an influence of buffering rather than of the protein.

5 Discussion

5.1 Heterogeneity and Clustering in PC12 Membrane Sheets

5.1.1 PC12 cell membrane sheets show inhomogeneous organisation

An objective of the present thesis was to investigate the heterogeneous organisation of proteins on membrane sheets derived from PC12 cells. Membrane sheets were chosen to render the inner leaflet of the plasma membrane accessible. By FD-AFM imaging the presence of distinct globular structures on the surface of PC12 cell membrane sheets was uncovered (Figure 4.31). Upon protein digestion by proteases these structures were drastically diminished in size (Figure 4.32). This finding confirms a proteinaceous nature of these structures and possibly they are protein assemblies themselves.

Jahn and coworkers observed similar structures on PC12 membrane sheets by intermittent contact mode AFM.[153] A positive staining for secretory vesicles and their partial disappearance upon induction of fusion let them conclude that these structures represent docked vesicles. Since physiological docking of vesicles depends on proteins[5] a removement of vesicles upon protein digestion is reasonable. In that sense the results obtained in the present study are in agreement with the results of Jahn and coworkers. However, as a part of the structure was still present after stimulation of exocytosis in Jahn's study it might be possible that additional objects are present on PC12 membrane sheets. This is supported by the observation that not all structures found in the AFM height image are also visible by the fluorescent membrane staining (Figure 4.3).

Regarding the apparent size of a few hundreds of nanometres they might correspond to the general protein assemblies observed by Rizzoli and coworkers by STED imaging of stained proteins in membrane sheets derived from PC12 cells.[81] A broadening of the sizes of the structures by convolving the topography of the actually present structure with the geometry of the tip has only a minor influence on the observed lateral size since the tip radius of about 20 nm is considerably smaller. However, Rizzoli and coworkers reported an accumulation of

syntaxin-1 near the edge of the protein assemblies whereas in Figure 4.34 of the present study no correlation between the elevated structures in the AFM height images and the binarised fluorescence images of the syntaxin-1 label obtained by STED microscopy could be found. This finding contradicts the hypothesis that the structures observed by AFM are identical to those described by Rizzoli and coworkers. Furthermore, the height of some of the observed structures of more than 200 nm is not likely to represent a protein assembly.

Burgert *et al.* described that STORM imaging on three dimensional structures can lead to the detection of physically not present clusters.[83] If a protein imaged by STORM or PALM follows the elevations of the structures on PC12 cell membrane sheets observed in this thesis, it might give rise to the detection of false clusters as well.

MR-AFM experiments on PC12 cell membrane sheets yielded tiny clusters or at least larger heterogenic accumulations of clustered events even in control measurements which are not supposed to identify clusters of syntaxin-1 specifically. These measurements comprise those performed with free nanobodies in solution to compete for the epitopes of syntaxin-1 (section 4.1.6.1), force maps recorded with nanobodies against mCherry coupled to the cantilever (section 4.1.6.2) and MR-AFM experiments on syntaxin-1 knockdown membrane sheets (section 4.1.6.3 and Figure 4.25 c and d in section 4.1.7). For the knockdown sheets a significant decrease of the amount of syntaxin-1 was verified, which probably affects all cells (Figure 4.19). The recorded events most probably stem from unspecific interactions (see section 5.1.2). Therefore, these experiments reveal the presence of heterogeneously organised structures which cause unspecific interactions with the AFM cantilever.

In summary, the experiments recapitulated in this section show that there is a heterogeneous organisation present on membrane sheets derived from PC12 cells, which are partially revealed to be proteins or other protein dependent structures.

5.1.2   No evidence is found for the specific detection of clusters of syntaxin-1

In numerous force maps recorded in MR-AFM experiments clusters were identified. This holds for measurements with conventional IgG antibodies raised against syntaxin-1 coupled to the cantilever (Figure 4.8) and with coupled nanobodies against syntaxin-1 (section 4.1.5.2 and Figure 4.15 therein and section 4.1.7). When free IgG antibodies against syntaxin-1 were added to the measuring buffer a significant decrease in the frequency of events was observed as compared with a measurement on exactly the same membrane sheet before the

addition. This is the strongest evidence obtained that specific interactions might have been detected. However, still many events were present after the addition of the antibody. Such a finding is reasonable, especially at long dwell times since the local concentration of the nanobody on the cantilever is high and a substitution of the free antibody is favoured entropically. An even more pronounced non-effectiveness of the competition of antibodies when measured by conventional force mapping was described by Creasey *et al.* when they performed MR-AFM experiments on human lenses.[101] To solve this problem they suggested to use TREC mode imaging instead.

For antibody-antigen interactions most probable rupture forces of about 40-60 pN are reported.[28,99,101] In MR-AFM measurements from 15 maps of the present thesis recorded with anti-Syx-NBs coupled to gold coated cantilevers (Figure 4.14) this value is about 30 pN. For experiments with anti-Syx-NBs coupled to cantilevers which were maleimide functionalised by the manufacturer the most probable maximum interaction force is about 65 pN, irrespective of the type of membrane sheet used for the measurement (Supplementary Figure 5). The latter measurements were performed with a five times increased retraction speed, which might explain the larger forces. When compared with the values reported in literature, it has to be kept in mind that the cantilever retraction speed influences the unbinding force. Unfortunately, except for the study of Creasey *et al.*[101] who recorded their force curves with 400 nm·s^{-1}, no cantilever retraction speeds or loading rates are reported in the cited literature. Under these circumstances, the most probable forces observed might be compatible with the detection of specific interactions. However, when regarding the direct comparison between measurements on wild type and knockdown membrane sheets (Figure 4.24) the similarity in the force distributions does not point to a detection of specific interactions in the case of wild type sheets.

The median rupture distance obtained from MR-AFM measurements on PC12-WT-2 membrane sheets with cantilevers which were maleimated by the manufacturer (33 nm) is much closer to the contour length of the used PEG spacer ($M = 3.4$ kg·mol^{-1}) of almost 30 nm[30] than the median rupture distance observed on knockdown membrane sheets (83 nm) (Figure 4.26). As to be expected, the same tendency is observed for the contour lengths (Table 4.4) even if the absolute numbers are almost one order of magnitude larger than expected. A slightly longer rupture distance than the contour length of the PEG chain is reasonable since the size of the nanobody and that of the target protein contribute as well. The shorter rupture distances detected on wild type membrane sheets may indicate that the structures which induced the unspecific events depend on syntaxin-1. Alternatively, it might be explained by specific interactions with the PC12-WT-2 membrane sheets whereas for PC12-Syx-KD sheets, where presumably no specific interactions can occur, unspecific

interactions with filamentous or other elongated structures take place instead (see section 5.1.3), therefore giving rise to a larger rupture distance. However, such an effective competition for unspecific events is unlikely and can almost be excluded by other findings obtained in the present study (*vide infra*). Furthermore, this tendency is not observed when cantilevers which were just aminated by the manufacturer were used instead (Table 4.2). This might, however, be explained by a non-successful reaction between the aminated surface and the *N*-hydroxysuccinimide in the latter case. Alternatively, the genetic interference of the knockdown might have resulted in looser and more elongated structures which cause the unspecific events. Especially due to the loss of syntaxin-1, which can bind other proteins[73] and tether vesicles[5], a degeneration of the structures on the inner leaflet which leads to a looser organisation of the entire structure is reasonable. This hypothesis could be probed by performing MR-AFM measurements on membrane sheets derived from control PC12 cells which have been transfected with an empty vector corresponding to the one used for the knockdown but which does not induce a knockdown. Additionally, MR-AFM experiments with nanobodies raised against mCherry might also be performed on PC12-WT-2 and PC12-Syx-KD membrane sheets.

It has to be noted that the concentration of nanobodies used for the competition experiments was almost two orders of magnitudes smaller than suggested by Hinterdorfer.[154] However, in their first study Hinterdorfer *et al.* described a successful competition by using a concentration of antibodies which was only a factor of 1.5 larger than the concentration of nanobodies used for one competition experiment in the present study.[93] When in an initial experiment nanobodies, which had not been subject to treatment with TCEP, were added to the measuring buffer in a final concentration of 1 µM a large frequency of events with multiple peaks in the force curves was observed. Thus, the concentration was decreased and TCEP treated nanobodies were used for further experiments. Furthermore, this indicates that added nanobodies might be capable of inducing further interactions between the cantilever and the substrate on their own, as described in section 4.1.6.1.

A further source of cluster detection, even when only to a small extent, might be caused by the choice of the threshold value in the Ripley analysis: Due to the adaption of a threshold value of the mean plus three standard deviations of the $L_j(r)–r$ values from 100 homogeneous random distributions even for a homogeneous distribution of events six pixels with $L_j(r)–r$ values above the threshold are expected to be detected in a 64×64 grid.

It cannot completely be excluded that a cluster of remaining syntaxin-1 molecules in PC12-Syx-KD membrane sheets was detected, e.g. in Figure 4.25 d, since a minor amount of syntaxin-1 was still detected in PC12-Syx-KD sheets. However, the supposed distribution of syntaxin-1 in PC12 membrane sheets measured by super resolution microscopic methods

such as STED (see Figure 4.4) or direct STORM[90] revealed zones in membrane sheets depleted of syntaxin-1. Thus, there are also in membrane sheets derived from wild type cells regions with a sparse number of syntaxin-1 which might be comparable to that of knockdown cells. It is reasonable that some measurements on wild type membrane sheets were performed in such a region. This renders the above mentioned effect very unlikely. Furthermore, the frequency of events is not reduced in PC12-Syx-KD membrane sheets, in contrast to the expectation.

Strong evidence against the concerns that clusters detected by control experiments with antibody or nanobody competition or knockdown cells might be caused by remaining specific interactions can be gained from experiments performed with nanobodies raised against mCherry coupled to the cantilever. Here, in two independent experiments not only interaction events were observed but also identified to be segregated in clusters.

For most experiments it was attempted to compare frequencies of events between control measurements and those suggested to provide specific interactions. First, it has to be noted that for a few force curves the presence of an interaction event could not be evaluated and therefore the overall amount of events is slightly underestimated, because no event was assigned to the corresponding location. In most cases the determined frequencies were not significantly different or resulted only in slight differences and sometimes even indicated a larger frequency of events on syntaxin-1 knockdown membrane sheets as shown in section 4.1.7. The main contributor to the variation of f_e is probably the cantilever itself (Figure 4.23). This renders the obtained frequency of events kind of speculative, therefore direct comparisons can only be used for estimations, unless a larger number of membrane sheets or GUV-MPs and cantilevers were used for their determination. Nevertheless, the variations among different membrane sheets when using the same cantilever (Figure 4.23) indicate that membrane sheets of different quality are present which induces varying amounts of presumably unspecific events, which might be related to the structures residing on the membrane sheets.

Finally, by the threshold analyses described in sections 4.1.8.2 and 4.1.8.3 no differences between maps of events obtained from PC12-WT-2 and PC12-Syx-KD cells could be identified, either. For the only map of wild type membrane sheets yielding a cluster which was not identified without the threshold a large force threshold of F_{low} = 468 pN or a large lower threshold of the contour length of $L_{c,low}$ = 2.94 µm resulted in the maximum value of $L(r)–r$. Taking the expected maximum interaction force into account (*vide supra*) this value is unreasonably large. Thus, so far no additional clustering could be inferred in wild type membrane sheets which is not found in knockdown sheets similarly. However, the results of these analyses can only be regarded as preliminary, more intense analysis would be

necessary to certainly exclude a discrimination between membrane sheets derived from wild type and those from knockdown cells. Especially the large difference of the rupture distances between wild type and knockdown membrane sheets identified in Figure 4.26 b might be the most promising object of further analyses.

Taken together, only sparse evidence for a detection of specific events is found which are almost exclusively negated by other findings. Thus, it cannot be stated on the organisation of syntaxin-1 in PC12 membrane sheets.

5.1.3 Reasons for large ratio between unspecific and specific events remain uncertain

As stated in section 5.1.2 it is unlikely that specific events make up a large amount of the events observed in MR-AFM experiments. Thus, in this section possible reasons for the frequent occurrence of unspecific and, if present at all, low amount of specific events are considered.

Apart from the observation that the frequency of events is found to be smaller on the same membrane sheet after the addition of free IgG-antibodies in solution there is hardly any evidence for the detection of specific events when performing MR-AFM experiments with anti-Syx-ABs. By the non-regioselective binding of amine groups on IgG-antibodies the molecules might be bound in a way which does not promote interactions with the antigen, for example by tethering the antibody by its variable domains or by the antibody lying flat on the solid surface.[155] By changing to nanobodies which are coupled regioselectively to the cantilever by their C-terminal cysteine residue this problem should be excluded. Furthermore, immunostaining experiments (section 4.1.4) indicate that the antibody used for MR-AFM experiments might be less effective in recognising syntaxin-1 than another clone available, which might explain an insufficient detection of syntaxin-1 in MR-AFM force maps.

However, even the utilisation of nanobodies did not result in a discrimination between specific and unspecific interactions.

To exclude some expected reasons for a possible lack of specific interactions experimental precautions were taken. First, for almost all preparations a sufficient concentration of nanobodies was verified after size exclusion chromatography (section 4.1.5.1). Second, a hindrance of specific interactions by the fixation was tested and shown to be quite unlikely as for silicon nitride cantilevers with coupled anti-Syx-ABs the frequency of events was even

reduced in measurements on unfixed membrane sheets (section 4.1.3.2). Furthermore, this is also indicated by successful immunostaining experiments.

As already discussed in section 5.1.2 many elevations were discovered on membrane sheets (Figure 4.31), which were identified before to be, at least in parts, secretory vesicles.[153] Obviously these vesicles which dock to syntaxin-1 might hinder the interaction between the nanobodies on the cantilever and the target protein sterically. Even if parts of the structures stem from protein aggregates it is reasonable that larger proteins also block specific interactions and the detection of clusters in a similar way. However, the combination of AFM and STED imaging shown in Figure 4.34 indicates that syntaxin-1 is also abundant in regions of the membrane sheet which are not occupied by large elevations. Therefore, one might argue that in some regions of the membrane sheet steric blocking of specific interactions should be a less dominant phenomenon.

Not only plasma membrane proteins but also larger proteins on the secretory vesicles might be capable of inducing unspecific interactions on their own. Unspecific interactions of proteins and other biomolecules with cantilevers are well described in literature. For example, Oesterhelt *et al.* employed physisorption of bacteriorhodopsin on a silicon nitride cantilever to study the unfolding of the protein. In their experiments a dwell time of 1 s at a force of 1 nN resulted in a binding frequency of 15 % between the cantilever and the protein.[156] Dufrêne and coworkers observed a tremendously larger frequency of interactions of the cantilever with an extracellular matrix made up of polysaccharide intercellular adhesins compared with the cell surface of *Staphylococcus aureus*.[157] Moy and coworkers identified that upon interaction of a BSA-functionalised cantilever with a load force of 200 pN a dwell time of less than about 1-4 s is needed to keep the frequency of events below 17 % when interacting with a BSA-coated glass surface. When all other parameters were kept constant the dwell time could be increased to more than 10 s and to almost 50 s when the substrate was replaced by a PEG-coated glass and by an agarose bead, respectively.[158] These findings show that unspecific interactions are a quite common phenomenon in AFM measurements. When regarding the low probability of unspecific interactions on the agarose bead one can hypothesise a reason why so many unspecific interactions are observed in the present study: When taking the above mentioned results of Moy and coworkers into account,[158] the presence of glycolipids and glycoproteins on the outer leaflet of a cell membrane[33] may point to a larger risk of MR-AFM experiments being biased by unspecific interactions when measuring on the inner leaflet of a cell membrane as done in the present study. On the other hand, glycoproteins are also described to hinder specific interactions[154] or to induce adhesive interactions on their own.[157,159] Contamination of the cantilever by adsorption of molecules which might alter the interactions with the sample are described as

well.[160] By Creasey *et al.* it was noted that especially when employing standard force mapping one has to take care that only specific interactions are analysed.[101] This was implemented in the present thesis beginning with the manual check of every single force curve and exclusion of force curves that are very unlikely to represent specific interactions (see section 3.4.5). The most sophisticated approach was the fit of the force curves with a WLC model and the subsequently performed variation procedure of threshold values of the involved quantities in section 4.1.8.3. Interestingly, even structures remaining after protein digestion by proteases can induce strong unspecific interactions (Figure 4.33). This shows that unspecific interactions are a huge bias when performing MR-AFM experiments on membrane sheets. Notably, unspecific interactions were probably not caused by preceding interactions like breakthrough events or sliding away of vesicles visible in the approach force curve (section 4.1.8.1).

The protein dependent structures discussed in section 5.1.1 probably influence interaction events. It was observed that the frequency of events on membrane sheets treated with proteases differs significantly from that on untreated membrane sheets (sections 4.1.6.4 and 4.1.9.2). However, the distribution of maximum interaction forces is almost unchanged. It has already been noted in section 4.1.9.2 that this similarity points to the existence of the same kind of interactions in both cases. Since it is not expected that syntaxin-1 withstands this procedure, the finding mentioned before further supports the hypothesis that no or only very few specific interactions are detected in untreated membrane sheets. Notably, the rupture distance is significantly larger after protein digestion. It is unlikely that proteins are unfolded by proteases but the polypeptide chains withstand the treatment and thereby looser and unfolded filaments still interact with the cantilever in a similar way as before and thus causing the same maximum interaction force, but that due to the unfolded structure the rupture takes place at a larger distance. Instead, facilitation of lifting of the membrane in the altered membrane sheets might be a plausible explanation for the larger rupture distances. This is reasonable since the poly-L-lysine which tethers the membrane sheet to the glass cover slip should be affected by the protein digestion by the proteases as well and therefore the contact between the membrane sheet and the support should be weakened.

Evidence was found that structures residing on the membrane and not the lipid membrane itself causes the observed events. Interactions with pure lipid membranes take place at smaller maximum interaction forces and smaller rupture distances (Figure 4.33). On GUV-MPs the latter are much more similar to the length of the PEG chain than on membrane patches, supporting the notion that proteins on membrane sheets cause interactions with the cantilever. However, interactions with lipids present in membrane sheets but not in the GUV-MPs might also cause the observed differences. On the other hand, especially the long

rupture distances in the case of membrane sheets and complex shapes of some force curves (arrowhead in Figure 4.13 a) are in agreement with unfolding of proteins by AFM described in literature.[156,161] The quite symmetric distribution of maximum interaction forces found for measurements on GUV-MPs points to a simple kind of interactions like van-der-Waals forces between macroscopic bodies but not to multiple parallel bonds. Measurements on GUV-MPs with anti-Syx-NB functionalised gold coated cantilevers show a larger frequency of events as compared with anti-Syx-AB functionalised silicon nitride cantilevers. This might be explained by the five times larger Hamaker constant of an interaction between two gold surfaces in water compared with two silicon nitride surfaces.[162,163]

Unspecific interactions might also be induced by actin or other filaments present on the membrane sheets. The presence of actin on membrane sheets was revealed in several experiments (Figure 4.2 and Figure 4.31). Furthermore, the detection of quite heterogeneous structures in MR-AFM measurements on membrane sheets from knockdown cells might indicate adhesive interactions with filamentous structures (see elongated structures in Figure 4.25 d). On the other hand, it has to be noted that the amount of erroneous height values in the FD-AFM image in Figure 4.31 is quite low in regions of abundant actin. This points to only few very strong interactions with actin since extraordinary strong adhesive interactions might lead to errors in FD-AFM images. Furthermore, the small persistence length determined (*vide infra*) does not point to an interaction with actin when taking its large persistence length of about 17 μm into account.[164]

In Figure 4.22 cumulative probabilities from different experiments performed with varying cantilever functionalisation methods and experimental parameters are plotted. A varying mixture of aminoalkanethioles used for the functionalisation and different contact times can lead to varying numbers of parallel bonds. This has to be considered when comparing measurements performed with different conditions. The similarity of the distribution of the forces and the fact that most force curves only show a single peak do not point to the formation of different numbers of bonds or to multiple bonds at all. However, the observed tail towards large forces in the histograms points to the existence of multiple bonds for a subset of force curves. Next, in most experiments a large frequency of events was observed which renders the formation of multiple bonds very likely. Furthermore, the persistence lengths listed in Table 4.5 are significantly smaller than that of a PEG chain (L_p(PEG) = 0.38 nm).[150] Considering a parallel alignment of springs in equation (3.11), about 20 parallel bonds would be necessary to reduce the apparent persistence length to the values determined from the fits. However, such a situation does not fit to the rather small interaction forces determined. Thus, the WLC model does probably not accurately describe the interactions observed in the MR-AFM experiments. This is further indicated by the large

number of force curves with a small coefficient of determination. The obtained values of the persistence length and of the contour length are probably further biased by the finite and constant slope of the force curves at larger D (see Figure 4.13), which might stem from an additional elastic element like the lifted membrane.

Very likely experimental biases causing the lack of detection of syntaxin-1 in MR-AFM measurements on PC12 membrane sheets are illustrated schematically in Figure 5.1.
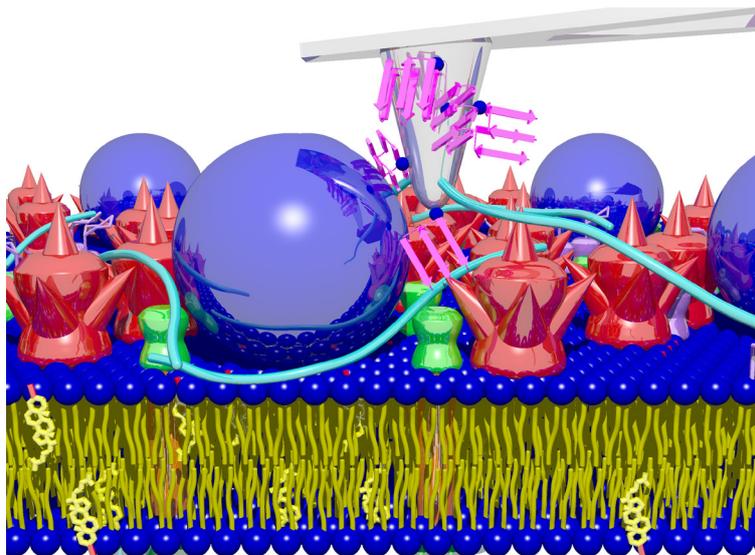
Figure 5.1: Schematic illustration of possible reasons for the large ratio between unspecific and specific interactions. The nanobody (magenta) on the cantilever is sterically hindered from the interaction with its binding partner syntaxin-1 (green) in the membrane, by synaptic vesicles (blue), other proteins (red) and filaments (cyan). Furthermore, proteins (shown for the cyan filaments) can bind to the cantilever and induce unspecific interactions. Adhesive interactions between the vesicles and the cantilever are likely as well. The different elements are not to scale.

A remaining concern is that the functionalisation of the cantilever might not have been intact or that the nanobodies do not bind their target any more when coupled to a surface, i.e. the tip. Varying frequencies of events among different cantilevers (Figure 4.23) do not necessarily point to more or less successful functionalisations of the cantilever but can also be caused by differences in the tip radius as a larger tip radius should lead to a larger probability of any kind of interaction. As already mentioned in section 4.1.7 a chemical characterisation on small surfaces such as AFM cantilevers and especially their curved tips is hard and often replaced by an indirect verification by observed interaction events and their successful competition.[27,28,101,110] For the sake of completeness it should be noted that for the present thesis in single experiments it was attempted to characterise functionalisations performed by the methods described in section 3.2.5 on oxidised silicon or gold coated

wafers (not described in previous chapters). By AFM imaging few tiny structures of a few nanometer in height and lateral size were found on an unfunctionalised gold coated wafer and on a wafer presumably functionalised with nanobodies. By a qualitative investigation the amount of these structures was not increased on the presumably functionalised wafer which might point to a non-successful functionalisation. However, since a discrimination between nanobodies and the structures on the unfunctionalised wafers might be difficult, this kind of experiment was not performed any longer. On the other hand, in an attempt to couple avidin to oxidised silicon wafers, measured contact angles increased or decreased with each step of functionalisation as it was to be expected. This might point to a successful functionalisation, but this measurement was not repeated and further experiments with avidin were not carried out. The amination of gold coated cantilevers by aminoalkanethioles was, in contrast to most reports, not performed in ethanol but in water. Due to less concerns about evaporation of the solvent, this method was adapted from Wirde *et al.* who revealed the coupling of cysteamine to gold surfaces in water to be as efficient as in ethanol.[165] Furthermore, *in situ* coupling of cysteine residues of a protein to gold coated cantilevers in aqueous buffer is also described.[166] Thus, in principle this reaction can be expected to be successful. Even if the first steps of cantilever functionalisation were not successful, they would be circumvented by the utilisation of cantilevers which had already been functionalised with a maleimide group by the manufacturer. However, since the experiments performed with those cantilevers did not lead to a detection of specific interactions either, the first steps of functionalisation were either not the cause of a lack of detection of specific events or there has to be another problem. Hinterdorfer and coworkers reported an average interaction force between a bare or a PEG-functionalised cantilever and a mica surface which was coated with chromatin of (118 ± 134) pN and (116 ± 63) pN,[28] respectively. For the corresponding antibody-antigen interaction they obtained an average force of (57 ± 20) pN.[28] In the 15 maps recorded with anti-Syx-NB functionalised cantilevers and a retraction speed of 1 µm·s^{-1} in the present study the determined maximum interaction force is (179 ± 375) pN (mean ± SD). This points to a non-successful functionalisation of the cantilever, however, for an accurate evaluation a cumulative probability plot of the data described by Hinterdorfer and coworkers would be beneficial, since the median force observed in the present study matches the average reported by Hinterdorfer and coworkers for the antibody-antigen interaction quite well.

Provided that the reaction between the maleimide and the nanobody is successful, a lack of specific interactions might still originate from non-functional nanobodies for example caused by denaturation of the nanobodies on the solid surface of the cantilever tip.

It has to be noted that some experiments suffer from few repetitions. Therefore, results of some kind of experiments can only be regarded as preliminary and more repetitions would be necessary to certainly state on the indications presented before. However, the vast amount of different indications obtained from varying kinds of experiments and approaches all pointing to the lack of specific and to abundant unspecific interactions together draw a clear picture.

5.1.4 Outlook

The lack of specific interactions and the huge amount of unspecific ones in MR-AFM measurements on membrane sheets derived from PC12 cells by different experimental approaches stress the need for changes in the experiment and for further characterisation of the functionalisation. Provided that the elevated structures on the membrane sheets cause these problems, a first investigation of membrane sheets derived from primary neurons (section 4.1.11) does not reveal this system to be a reasonable substitute since elevated structures are also present on these membrane sheets.

To probe the functionalisation of the cantilever a verification of proteins present on the cantilever is probably feasible by secondary ion mass spectrometry.[167] This, however, does not provide insight into the functionality of the coupled nanobodies. To check the functionality a technique could be utilised which uses the cantilever directly as a mass sensor by employing the dependency of the eigenfrequency of the cantilever on the bound mass or the deflection of the cantilever by compressive stress induced by bound molecules.[168,169] But this approach needs a sophisticated experimental setup. An indirect verification of the functionalisation in a much simpler system by successfully performing MR-AFM measurements on an artificial supported lipid membrane with reconstituted syntaxin-1 might be a feasible approach as well.

Even if the nanobodies were not functional in the present study and if in future functionalisations they are somehow bound in a way to the cantilever which provides functional nanobodies, most probably the large amount of unspecific interactions would still be a bias which would have to be circumvented.

Therefore, to reduce the amount of unspecific interactions in the present system there are several possible approaches. First, docked secretory vesicles could be removed by inducing fusion as reported by Jahn and coworkers.[153] This might, however, block syntaxin-1

because if not disassembled it is engaged in the fusion complex afterwards.[5] Another possibility might be to remove the vesicles mechanically, e.g. by hydrodynamic forces of a stream of buffer or by applying lateral forces by AFM imaging. Alternatively, PC12-Syx-KD membrane sheets, which should not be capable of docking vesicles which otherwise might hinder interactions with the proteins of interest in the membrane, could be used to detect specific interactions with other proteins. The synaptic protein bassoon might be a feasible candidate because of its large size, because it is suggested to contribute to vesicle recruitment[48] and also described to be organised heterogeneously.[81] A mild treatment with detergents could remove the structures which, however, also bears the risk of denaturing the protein of interest and destroying the membrane. To reduce the number of unspecific interactions, functionalised agarose beads could be used as a probe similar to the suggestion by Moy and coworkers to utilise agarose beads in single molecule force measurements as substrates.[158] This will, however, reduce the lateral accuracy of the localisation of events. Provided that unspecific interactions are significantly less probable with a lipid membrane than with functionalised cantilevers used in the present thesis, cantilever tips could be coated with a lipid membrane as done by Pera *et al.*.[170] Afterwards, nanobodies could be bound to functionalised lipids. This is probably the most promising approach.

5.2 Mechanics of GUVs Containing Synaptophysin

5.2.1 Home-built micropipette aspiration device was successfully implemented and applied for the aspiration of GUVs

For this project, a micropipette aspiration device was successfully implemented. The exemplary aspiration of a GUV presented in section 4.2.2 shows that the micropipette aspiration device constructed for the present thesis is capable of aspiring vesicles. By analysing the images recorded during the aspiration experiment and by using the simultaneously measured aspiration pressure, the software developed for this project yields parameters of the apparent and direct area compressibility moduli and of the bending modulus.

A few GUVs composed of DOPC were aspired and the mechanical moduli were determined. The obtained mean apparent area compressibility modulus of the DOPC membrane (K_{app} = (102 ± 33) mN·m^{-1}) is on the same order of magnitude but somewhat smaller than the ones obtained by other micropipette aspiration studies like reported by Lu *et al.* (K_{app} = (174 ± 20) mN·m^{-1})[140] and by Rawicz *et al.* (K_{app} = (237 ± 16) mN·m^{-1})[141]. However, the absolute difference between the values determined by Rawicz *et at.* and Lu *et al.* is almost identical to that between the values of Lu *et al.* and the one obtained in the present study. The resulting direct area compressibility modulus of the present study (K_{dir} = (122 ± 33) mN·m^{-1}) is also smaller than the literature values (K_{dir} = (210 ± 25) mN·m^{-1}[140] and K_{dir} = (265 ± 18) mN·m^{-1}[141]) determined by Lu *et al.* and Rawicz *et al.*, respectively. Like the apparent area compressibility modulus, the bending modulus (κ = (4.5 ± 2.8)·10^{-20} J) is also roughly half the values described in literature (κ = (9.1 ± 1.5)·10^{-20} J and κ = (8.5 ± 1.0)·10^{-20} J reported by Lu *et al.* and Rawicz *et al.*, respectively).[140,141] Regarding the standard deviations, the discrepancies seem unlikely to be explained by statistic variations. The representative fits in Figure 4.39 show that the data points are fitted well by a linear function. Thus, the deviation of individual values at different aspiration pressures from the linear correlation is rather low. On the other hand, the errors of the individual tension values are large. This is predominantly caused by the large error of five pixels estimated for the radius of the pipette and the error propagation of equation (3.5). When changing the threshold for the detection such that smaller values of the radius of the pipette are detected, K_{app} is even decreased. Changing the binarisation procedure such that larger radii of the pipette are detected is not appropriate when regarding the detected radius in Figure 3.20 b. However, if the contour of the projected vesicle is underestimated by not

setting the focal plane to the equatorial plane of the GUV, the radius of the pipette will be underestimated as well. Most micropipette aspiration studies use label free microscopy techniques instead of fluorescence microscopy.[32,137,140,141] This might give rise to a systematic error by the method used in the present study. A systematic error causing a constant factor of about one half for every single value of the tension could fully explain this discrepancy.

5.2.2 No significant influence of synaptophysin on the mechanical moduli is found

Next, the focus is set on possible contributions of synaptophysin on the behaviour of GUVs during aspiration. Micropipette aspiration experiments were carried out to test a possible influence of synaptophysin on the large membrane dilation observed in synaptic vesicles by Preobraschenski *et al.* during uptake of glutamate.[20] Such a behaviour was observed before by Budzinski *et al.* and was attributed to synaptic vesicle protein 2A.[19] To test whether synaptophysin can contribute to the observed increase in vesicle's surface of more than 100 %, which is not compatible with ordinary values of the maximum area strains,[21,22] the area compressibility modulus of lipid membranes containing synaptophysin was examined by micropipette aspiration. A smaller area compressibility modulus should lead to a larger possible area strain at unchanged rupture membrane tension.

Bassereau and coworkers developed a theory which describes a reduced bending modulus of membranes containing curvature inducing proteins.[171] When considering the proportionality between the bending and the apparent area compressibility modulus[141] and the possible curvature inducing effect of synaptophysin,[18,115] a reduction of the area compressibility modulus caused by synaptophysin seems to be plausible. However, the determined apparent area compressibility moduli are not significantly different between vesicles containing synaptophysin and those containing synaptobrevin or protein free control vesicles (Figure 4.47). The mean bending moduli are even more similar to each other. These slight decreases of the mean values of the bending moduli correspond to a factor of 0.8 and 0.9 for synaptophysin and synaptobrevin, respectively. Bassereau and coworkers found corresponding factors of 0.8[171] and 0.9[46] in micropipette aspiration experiments with GUVs containing the sarcoplasmic reticulum Ca^{2+}-ATPase in the absence of ATP. In the presence of ATP that ratio was found to be even smaller.[171] Along the same lines, Evans and Needham described a substantial decrease of the area compressibility modulus when

reconstituting artificial transmembrane peptides into GUVs as revealed by micropipette aspiration experiments.[172] Therefore, it cannot be excluded that the slightly lower mean values of the bending and area compressibility moduli of GUVs containing proteins observed in the present study, which are not significant based on the comparison of the standard deviations, are caused by a general protein effect. Regarding the maximum apparent area strains and maximum membrane tensions (section 4.2.7) significant differences cannot be found either. When comparing only measurements performed in buffered solutions the difference in the apparent area compressibility modulus between GUVs containing synaptophysin and control vesicles is more pronounced (Figure 4.48). A similar influence on the maximum apparent area strain cannot be found (Figure 4.52). However, the low amount of data points for each category renders any conclusion drawn from these results quite speculative. Thus, it seemed reasonable to merge data of measurements carried out in buffered and those carried out in unbuffered solution for the main results (Figure 4.47 and Figure 4.51). It should be noted that only a single experiment was performed in an unbuffered solution but most measurements which were not discarded stem from that experiment. This might point to a negative influence of the buffer on the quality of the measurement, since in the buffered solution more measurements had to be discarded. Furthermore, an influence of the buffer even on protein free control vesicles cannot be excluded when regarding the respective values of the apparent area compressibility modulus (Figure 4.48) and the maximum apparent area strain (Figure 4.52). Taken together, these findings do not support the above hypothesis.

Nevertheless, these results should not be interpreted as evidence against the hypothesis for several reasons. First, a lower mean value of the apparent area compressibility modulus of GUVs containing synaptophysin might indicate a tendency of an effect necessary for supporting the hypothesis. The mean value for vesicles containing synaptophysin is even lower than the one of vesicles containing synaptobrevin, which were investigated to exclude a general effect caused by transmembrane proteins. Note that except for the value of one vesicle containing synaptophysin which lost volume during aspiration the remaining values of K_{app} should be accurate since the vesicles were proved to maintain their volume (Figure 4.49). Second, the amount of synaptophysin reconstituted into GUVs might be smaller than present in synaptic vesicles. Third, the number of vesicles which provided reliable data for the determination of the mechanical moduli is quite low (nine vesicles for synaptophysin for the controls even lower). Regarding the large fluctuation of the individual values a larger number of data points would be necessary to draw a clear conclusion. Fourth, the results obtained by AFM (section 4.2.1) show the same, but also not significant, tendency. Fifth, the corrected direct area compressibility modulus, which should better be used for comparison,

is biased by even larger fluctuations and overcorrection for thermal undulations (see section 4.2.5) and is therefore not taken as reference in the present study. Finally, the model membrane in which 98 % of all lipid molecules are DOPC is a huge simplification of the complex lipid composition of synaptic vesicles.[111] This non-natural environment of the proteins might influence their functionality tremendously. Bassereau and coworkers reported that a ternary mixture of lipids has to be close to phase separation for lipid sorting caused by curvature to occur.[173] Therefore, when considering the above mentioned possible spontaneous curvature dependent effect of synaptophysin for the reduction of the area compressibility modulus the concern about the simplification of the lipid mixture of the membrane is reinforced.

5.2.3 Reason for continuous aspiration of vesicles at constant set-pressure is a loss of volume

In section 4.2.4 a continuous aspiration of GUVs at constant set-pressure was described. The increase in the aspired tube length is roughly linear with time as shown in Figure 4.43. Such a behaviour is described for micropipette aspiration of cells multiple times. For example, Guillou *et al.* attributed the continuous flow of T-lymphocytes into the micropipette at constant aspiration pressure accompanied with an increase in cell's surface area to the unfolding of membrane reservoirs like microvilli and folds of the membrane.[174] If synaptophysin somehow provided excess area in an artificial membrane, this would be a plausible explanation for the continuous flow of the vesicles into the micropipette described in this thesis. However, a significant increase of the area dilation was not observed either by comparison of the maximum apparent area strain between GUVs containing synaptophysin and control vesicles (Figure 4.51), nor did the aspiration at constant set-pressure lead to a substantial expansion of the total surface of GUVs containing synaptophysin (Figure 4.45).

Further reports attribute a continuous aspiration of cells without increase of their surface area to a liquid droplet-like behaviour.[151,152,175,176] Liquid droplets possess a constant surface tension. By rearranging equation (3.5) for Δp

$$\Delta p = 2\tau \left(\frac{1}{R_P} - \frac{1}{R_V} \right)$$ (5.1)

it becomes evident that as soon as the spherical cap inside the micropipette has formed ($\Delta L = R_P$), a further increase of the aspiration pressure, which is accompanied by a decrease

of R_V, without the possibility to increase the membrane tension leads to a mechanic imbalance.[152] Remarkably, in the present thesis the observed tube length as a function of time increases for the longest period of time linearly until, just before a fission event, it increases non-linearly (Figure 4.43). This might be caused by the beginning formation of the fission neck, nevertheless it resembles the shapes of corresponding plots for the aspiration of liquid-like cells obtained experimentally[176] and by finite element analyses[175]. As shown in Figure 4.44 a this gain in the tube length is not caused by the generally present slight increase of the suction pressure. However, for extendable lipid membranes like in GUVs which are described as elastic bodies,[32] the membrane dilation should render the membrane tension variable. On the other hand, if the vesicles reduce their volume while maintaining the surface area, they will gain excess area which can be aspired without the need to increase the tension. This will end up in a similar situation as for liquid droplet-like cells. Indeed some, especially two very fast aspired, vesicles maintain their tension during aspiration at constant set-pressure as shown in Figure 4.45 d. Nevertheless, some vesicles exhibit a modest increase in tension which might be attributed to the slight increase of the suction pressure. Pure kinetic or viscous effects are unlikely since no saturation of the aspired tube length was observed. A faster decrease of the volume for fast aspired vesicles is proved by Figure 4.44 b and Figure 4.45 a. The vesicles do not only lose their volume by fission of vesicles but also continuously in between fission events. For pure lipid vesicles the volume is described to be maintained within 0.1 % of its initial value.[32] In the present study no detectable loss of volume of control vesicles without proteins in their membrane could be found either (Figure 4.49). The further investigation of the time course of the normalised total surface area divided by the normalised volume for slower and faster aspired vesicles shows that the suggested provision of excess surface area is plausible (Figure 4.45 c).

To summarise, the loss of volume observed while aspiring GUVs most probably causes a continuous aspiration of the vesicles which is probably attributed to excess surface area resulting from the loss of volume while keeping the membrane tension at low values.

5.2.4 Synaptophysin possibly drives continuous loss of vesicle's volume and vesicle fission

The results discussed in section 5.2.2 have hardly shown any difference of the mechanical properties of GUVs containing synaptophysin and protein free GUVs or those containing synaptobrevin. Nevertheless, remarkable differences in the behaviour of GUVs containing

synaptophysin compared to the control samples were observed upon aspiration. First, the relative amount of vesicle fission was unexpectedly larger for vesicles containing synaptophysin (Figure 4.46). Furthermore, Figure 4.49 c and d indicate, that the loss of volume during aspiration, which was already discussed in section 5.2.3, is a feature of GUVs containing proteins. This is further quantified by numbers given in section 4.2.6 and Figure 4.50. Among the measurements performed this effect was predominantly found for vesicles containing synaptophysin. This might point to another specifically synaptophysin driven phenomenon.

Fission events, or also called fragmentation, during micropipette aspiration has been described before. Already in 1964, Rand described fragmentation of red blood cells and attributed it to insufficiently osmotically swollen cells which, therefore, possess a large amount of excess membrane area.[177] This is a reasonable explanation for GUVs containing synaptophysin which lose volume continuously already before and in between fission events as shown in Figure 4.45 a and Figure 4.49 b. The provision of excess area while keeping the membrane tension at low values was shown in Figure 4.45 c and d. Evans *et al.* explained this phenomenon by insufficient sealing between the aspired red blood cell and the pipette wall.[21] More importantly, Baumgart and coworkers observed fragmentation of phase separated vesicles when the suction pressure was applied to the liquid disordered phase.[178] Staining of GUVs containing synaptophysin from batches used for this thesis by fluorescent antibodies against synaptophysin (unpublished results of Preobraschenski and Jahn) indicate a heterogeneous, domain-like organisation of synaptophysin in the vesicle membrane. If present, aspiration of a synaptophysin rich domain could cause fragmentation of the vesicles similar to the description of Baumgart and coworkers.[178] However, the length of the transmembrane domains of synaptophysin of 18 amino acids[113] and a length of 0.15 nm[33] per amino acid in an α-helix results in a length of the transmembrane domain of 2.7 nm. This value perfectly matches the thickness of the hydrophobic core of a DOPC membrane.[141] Thus, a formation of synaptophysin domains by hydrophobic mismatch as observed for syntaxin-1[79] is not possible, at least at zero membrane dilation. Along the same lines, Emami *et al.* recently described spontaneous fission in phase separated GUVs of plant lipids without aspiration of the vesicles when subject to osmotic stress. These fission events occurred at the phase boundary.[179] Thus, in GUVs containing synaptophysin a possible domain boundary might nucleate fission events as well.

A function of synaptophysin in endocytosis is, however, only attributed to an indirect role for example by binding to dynamin-1,[180] which is the actual compound enabling vesicle fission, or only for increasing the number of simultaneously endocytosed vesicles, but not contributing to the fission efficiency of individual vesicles.[18] Nevertheless, this observation of

fission events is in accordance with a decreased bending modulus which would facilitate the large curvature just before the completion of fission. The reduction of the bending modulus again would be an indicator of a possibly also facilitated membrane dilation.

As noted before, besides losing membrane and volume via fission, GUVs containing synaptophysin also lose volume continuously. The larger frequency of fission events in vesicles containing synaptophysin as compared with those containing synaptobrevin points to an effect which is favoured by synaptophysin. This supports the hypothesis that synaptophysin molecules might form a channel which is permeable for water. As a suction pressure is applied, squeezing-out of water might be energetically favoured over aspiration as indicated by the aspiration experiments at constant set-pressure summarised in Figure 4.45. Indeed, a multimeric structure of synaptophysin that resembles mechanosensitive protein channels was observed by electron microscopy.[113] Especially the formation of mechanosensitive channels could explain the loss of water from the lumen of the GUV when subject to an aspiration pressure. Furthermore, a voltage-dependent and cation-selective channel activity of synaptophysin reconstituted into artificial lipid membranes was observed.[181] A channel structure might, furthermore, give rise to a boundary between domains which could initiate vesicle fission. Moreover, an increase of the pore opening diameter might be a further explanation for a possibility for synaptic vesicles to increase their membrane area as accordingly suggested by Budzinski *et al.*.[19] These hypotheses are illustrated in Figure 5.2. However, the fact that vesicles containing synaptobrevin also lose volume cannot be neglected.

An influence of remaining detergent is unlikely for several reasons. First, there is no significant difference in the apparent area compressibility modulus found between GUVs prepared directly from a lipid film (Figure 4.40) and those prepared via detergent removal (Figure 4.47), which both consist mainly of DOPC. Second, GUVs which were prepared by detergent removal and do not contain proteins do not lose volume (Figure 4.49). Third, the number of vesicles discarded due to continuous aspiration at constant set-pressure is smaller for control vesicles without proteins (section 4.2.5).
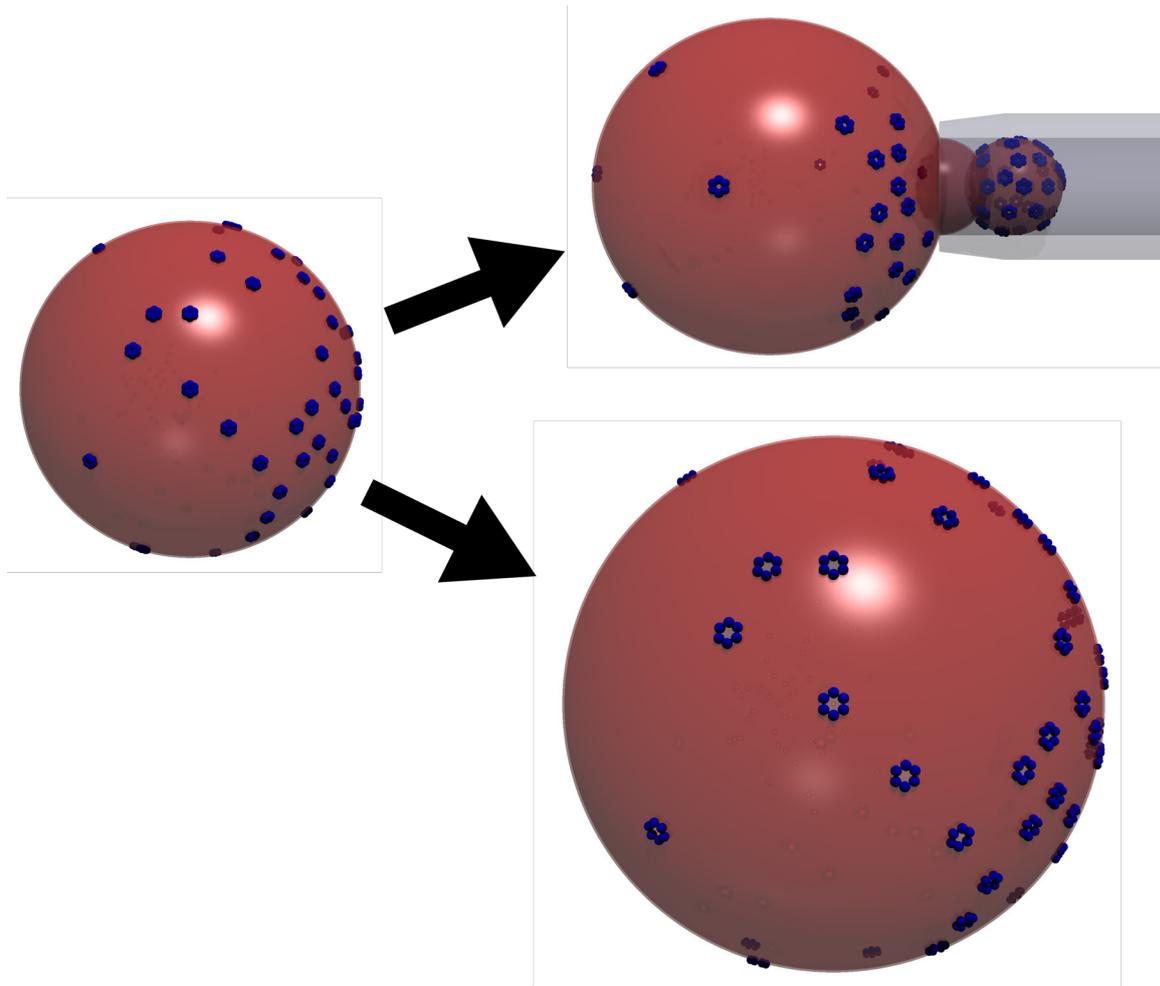
Figure 5.2: Hypothetical contributions of synaptophysin to the observations in micropipette aspiration experiments and to membrane dilation. Synaptophysin might form channels segregating into domains which are enriched in the protein (left). Upon micropipette aspiration mechanosensitive channels might be opened leading to the efflux of water and fission might be induced at the domain boundaries (upper right). Furthermore, wide opening of the channels might contribute to a possible membrane dilation (lower right).

Taken together, GUVs containing synaptophysin are more prone to fission and lose solvent from their interior which might be related to effects of synaptophysin. The formation of a channel, which has been described before, might possibly be the cause of this effect.

5.2.5 Outlook

The results discussed in the previous sections suffer from low amounts of reliable data. Therefore, all conclusions can only serve to indicate tendencies. Especially the determination of the mechanical moduli is only preliminary and more data are necessary. Due to the low throughput of the method (see section 4.2.5) the utilisation of a complementary method could be beneficial. Indirect evidence for a reduced area compressibility modulus in GUVs containing synaptophysin could be drawn from a method reported by Steinem and coworkers, who inferred a reduction of the area compressibility modulus upon binding of a protein domain from the shape of numerous adhered GUVs simultaneously by spinning disc confocal microscopy.[182] For the production of the GUVs, the utilisation of a multi compound lipid mixture which mimics the composition of synaptic vesicles might have several advantages: First, the physiological function of synaptophysin might depend on its native environment, which would better be respected with such a mixture. Furthermore, if the loss of solvent from the GUVs containing synaptophysin was an artefact, the addition of cholesterol might lower the permeability of water as observed by Rawicz *et al.*.[22]

The remarkable finding that possibly GUVs containing synaptophysin are more prone to a reduction of volume by fission and by a continuous loss of solvent as compared with GUVs containing synaptobrevin should be further investigated. To this end, more experiments with constant set-pressure should be performed which also include the investigation of GUVs containing synaptobrevin and of control vesicles lacking proteins.

Experiments to elucidate the mechanism of the fission events are desirable. Therefore, fluorescently labelled synaptophysin could be utilised. This could show if domains are formed and according to the hypothesis suggested in the previous section if fission is favoured when the GUVs are aspired at such a domain. Furthermore, provided that the loss of solvent from the lumen of the vesicles is indeed driven by synaptophysin, experiments to exclude a merely artificial effect could be performed. As a first step PC12 cells, which possess synaptophysin on their membranes,[81] could be aspired by micropipette aspiration and a specific effect could be tested by comparison with synaptophysin knockout PC12 cells.

6   Summary

The objective of this thesis was to investigate the lateral organisation and possible functions of selected neuronal proteins in the plasma membrane and to infer how they contribute to the structure and the mechanics of the respective system. To this end, atomic force microscopy and especially molecular recognition atomic force microscopy imaging was utilised to obtain insights into the heterogeneous structure of membrane sheets derived from PC12 cells and the assumed arrangement of syntaxin-1 in clusters. Furthermore, it was an aim to establish a micropipette aspiration device and to develop the corresponding analysis software to finally infer possible functions of synaptophysin and to state on the hypothesised mechanical influence of synaptophysin on the mechanics of lipid membranes.

By high resolution force distance based atomic force microscopy imaging details of the elevated structure of PC12 membrane sheets, which have already been described before, were visualised. Furthermore, the presence of actin on the membrane sheets was revealed by fluorescence staining and that structure was identified in AFM height images as well. Molecular recognition AFM imaging of syntaxin-1 was attempted by conventional IgG antibodies and by nanobodies coupled to the cantilever tip. Ripley's K-function cluster analyses of the obtained spatial distributions of recognition events revealed the significant segregation of these events into clusters or large accumulations. However, tests by nanobody competition, measurements performed with nanobodies incapable of binding any target on the membrane sheets specifically and the utilisation of membrane sheets derived from syntaxin-1 knockdown PC12 cells have shown that the vast majority if not all of these events stem from unspecific interactions. These interactions were mainly attributed to the adsorption of proteins residing on the membrane sheets to the cantilevers. Evidence for that hypothesis was found from the lower frequency of events in measurements on membrane sheets which have been treated with proteases. However, a lack of bound or a missing functionality of bound antibodies or nanobodies cannot be excluded. In any case the structures present on the membrane sheets are likely to block specific interactions sterically. Nevertheless, these experiments revealed a heterogeneous arrangement of the elements which cause the unspecific interactions.

The aims to set-up a micropipette aspiration device and to develop software to infer mechanical moduli of aspired vesicles were fulfilled. For the investigated GUVs composed of DOPC the area compressibility moduli and the bending modulus are on the same order of magnitude as those found in literature but somewhat smaller. No significant difference between the area compressibility moduli, the bending moduli, the maximum apparent area strains and the maximum membrane tensions of GUVs containing synaptophysin and those containing synaptobrevin or no protein at all could be found. These results, however, suffer from a low amount of measurements which were suitable to determine the desired quantities accurately. A larger amount of data optionally measured with a complementary method would be beneficial. Therefore, the hypothesis that synaptophysin enables a larger possible area dilation could not be tested reliably.

Two effects of GUVs containing synaptophysin were found. First, GUVs containing synaptophysin are more prone to fission when being aspired by a micropipette than those containing synaptobrevin or no protein. Second, many vesicles containing synaptophysin showed a considerable loss of volume which was attributed to squeezing-out of solvent from the vesicular lumen. This might point to the hypothesis that synaptophysin forms a multimeric channel, which has been described before. However, the corresponding loss of volume in GUVs containing synaptobrevin, even though to a smaller extent, stresses the necessity to perform a larger number of comparative measurements to finally state on the hypothesis of a synaptophysin induced loss of water and on the possible existence of a synaptophysin channel.

7   References

[1]   S. Herculano-Houzel, The remarkable, yet not extraordinary, human brain as a scaled-up primate brain and its associated cost, *Proc. Natl. Acad. Sci. USA* **2012**, *109*, 10661–10668.

[2]   D. A. Drachman, Do we have brain to spare?, *Neurology* **2005**, *64*, 2004–2005.

[3]   K. Senthilkumari, K. Umamaheswari, M. Bhaskaran, A study on median nerve conduction velocity in different age groups, *Int. J. Res. Med. Sci.* **2015**, 3313–3317.

[4]   T. C. Südhof, The Synaptic Vesicle Cycle, *Annu. Rev. Neurosci.* **2004**, *27*, 509–547.

[5]   J. Rizo, J. Xu, The Synaptic Vesicle Release Machinery, *Annu. Rev. Biophys.* **2015**, *44*, 339–367.

[6]   E. Merklinger, J.-G. Schloetel, P. Weber, H. Batoulis, S. Holz, N. Karnowski, J. Finke, T. Lang, The packing density of a supramolecular membrane protein cluster is controlled by cytoplasmic interactions, *eLife* **2017**, *6*, e20705.

[7]   T. Lang, D. Bruns, D. Wenzel, D. Riedel, P. Holroyd, C. Thiele, R. Jahn, SNAREs are concentrated in cholesterol-dependent clusters that define docking and fusion sites for exocytosis, *EMBO J.* **2001**, *20*, 2202–2213.

[8]   C. Rickman, F. A. Meunier, T. Binz, B. Davletov, High Affinity Interaction of Syntaxin and SNAP-25 on the Plasma Membrane is Abolished by Botulinum Toxin E, *J. Biol. Chem.* **2004**, *279*, 644–651.

[9]   A. Ullrich, M. A. Böhme, J. Schöneberg, H. Depner, S. J. Sigrist, F. Noé, Dynamical Organization of Syntaxin-1A at the Presynaptic Active Zone, *PLOS Comput. Biol.* **2015**, *11*, e1004407.

[10]   K. I. Willig, S. O. Rizzoli, V. Westphal, R. Jahn, S. W. Hell, STED microscopy reveals that synaptotagmin remains clustered after synaptic vesicle exocytosis, *Nature* **2006**, *440*, 935–939.

[11]   R. J. Kittel, C. Wichmann, T. M. Rasse, W. Fouquet, M. Schmidt, A. Schmid, D. A. Wagh, C. Pawlu, R. R. Kellner, K. I. Willig, S. W. Hell, E. Buchner, M. Heckmann, S. J. Sigrist, Bruchpilot Promotes Active Zone Assembly, Ca2+ Channel Clustering, and Vesicle Release, *Science* **2006**, *312*, 1051–1054.

[12]   N. D. Halemani, I. Bethani, S. O. Rizzoli, T. Lang, Structure and Dynamics of a Two-helix SNARE Complex in Live Cells, *Traffic* **2010**, *11*, 394–404.

[13]   T. Lang, S. O. Rizzoli, Membrane Protein Clusters at Nanoscale Resolution: More Than Pretty Pictures, *Physiology* **2010**, *25*, 116–124.

[14]   D. Choquet, A. Triller, The Dynamic Synapse, *Neuron* **2013**, *80*, 691–703.

[15]   T. J. Hausrat, M. Muhia, K. Gerrow, P. Thomas, W. Hirdes, S. Tsukita, F. F. Heisler, L. Herich, S. Dubroqua, P. Breiden, J. Feldon, J. R. Schwarz, B. K. Yee, T. G. Smart, A. Triller, M. Kneussel, Radixin regulates synaptic GABAA receptor density and is essential for reversal learning and short-term memory, *Nat. Commun.* **2015**, *6*, 6872.

[16]   B. Salavati, T. K. Rajji, R. Price, Y. Sun, A. Graff-Guerrero, Z. J. Daskalakis, Imaging-based neurochemistry in schizophrenia: a systematic review and implications for dysfunctional long-term potentiation, *Schizophr. Bull.* **2015**, *41*, 44–56.

[17]   R. Janz, T. C. Südhof, R. E. Hammer, V. Unni, S. A. Siegelbaum, V. Y. Bolshakov, Essential Roles in Synaptic Plasticity for Synaptogyrin I and Synaptophysin I, *Neuron* **1999**, *24*, 687–700.

[18]   S. E. Kwon, E. R. Chapman, Synaptophysin regulates the kinetics of synaptic vesicle endocytosis in central neurons, *Neuron* **2011**, *70*, 847–854.

[19]   K. L. Budzinski, R. W. Allen, B. S. Fujimoto, P. Kensel-Hammes, D. M. Belnap, S. M. Bajjalieh, D. T. Chiu, Large Structural Change in Isolated Synaptic Vesicles upon Loading with Neurotransmitter, *Biophys. J.* **2009**, *97*, 2577–2584.

[20]   J. Preobraschenski, R. Jahn, *in preparation*.

[21]   E. A. Evans, R. Waugh, L. Melnik, Elastic area compressibility modulus of red cell membrane, *Biophys. J.* **1976**, *16*, 585–595.

[22]   W. Rawicz, B. A. Smith, T. J. McIntosh, S. A. Simon, E. Evans, Elasticity, Strength, and Water Permeability of Bilayers that Contain Raft Microdomain-Forming Lipids, *Biophys. J.* **2008**, *94*, 4725–4736.

[23]   S. Letschert, A. Göhler, C. Franke, N. Bertleff-Zieschang, E. Memmel, S. Doose, J. Seibel, M. Sauer, Super-Resolution Imaging of Plasma Membrane Glycans, *Angew. Chem. Int. Ed.* **2014**, *53*, 10921–10924.

[24]   C. Rickman, C. N. Medine, A. R. Dun, D. J. Moulton, O. Mandula, N. D. Halemani, S. O. Rizzoli, L. H. Chamberlain, R. R. Duncan, t-SNARE Protein Conformations Patterned by the Lipid Microenvironment, *J. Biol. Chem.* **2010**, *285*, 13535–13541.

[25]   F. Baumgart, A. M. Arnold, K. Leskovar, K. Staszek, M. Fölser, J. Weghuber, H. Stockinger, G. J. Schütz, Varying label density allows artifact-free analysis of membrane-protein nanoclusters, *Nat. Methods* **2016**, *13*, 661–664.

[26]   A. Magenau, D. M. Owen, Y. Yamamoto, J. Tran, J. M. Kwiatek, R. G. Parton, K. Gaus, Discreet and distinct clustering of five model membrane proteins revealed by single molecule localization microscopy, *Mol. Membr. Biol.* **2015**, *32*, 11–18.

[27]   A. Raab, W. Han, D. Badt, S. J. Smith-Gill, S. M. Lindsay, H. Schindler, P. Hinterdorfer, Antibody recognition imaging by force microscopy, *Nat. Biotechnol.* **1999**, *17*, 902–905.

[28]   C. Stroh, H. Wang, R. Bash, B. Ashcroft, J. Nelson, H. Gruber, D. Lohr, S. M. Lindsay, P. Hinterdorfer, Single-molecule recognition imaging microscopy, *Proc. Natl. Acad. Sci. USA* **2004**, *101*, 12503–12507.

[29]   J. Zhang, L. A. Chtcheglova, R. Zhu, P. Hinterdorfer, B. Zhang, J. Tang, Nanoscale Organization of Human GnRH-R on Human Bladder Cancer Cells, *Anal. Chem.* **2014**, *86*, 2458–2464.

[30]   M. Pfreundschuh, D. Alsteens, R. Wieneke, C. Zhang, S. R. Coughlin, R. Tampé, B. K. Kobilka, D. J. Müller, Identifying and quantifying two ligand-binding sites while imaging native human membrane receptors by AFM, *Nat. Commun.* **2015**, *6*, 8857.

[31]   P. Hinterdorfer, Y. F. Dufrêne, Detection and localization of single molecular recognition events using atomic force microscopy, *Nat. Methods* **2006**, *3*, 347–355.

[32]   E. Evans, W. Rawicz, Entropy-driven Tension and Bending Elasticity in Condensed-Fluid Membranes, *Phys. Rev. Lett.* **1990**, *64*, 2094–2097.

[33]   B. Alberts, A. Johnson, J. Lewis, M. Raff, K. Roberts, P. Walter, *Molecular biology of the cell,* 5th ed., Garland Science Taylor & Francis, New York, **2008**.

[34]   J. Alcaraz, L. Buscemi, M. Grabulosa, X. Trepat, B. Fabry, R. Farré, D. Navajas, Microrheology of Human Lung Epithelial Cells Measured by Atomic Force Microscopy, *Biophys. J.* **2003**, *84*, 2071–2079.

[35]   C. Selhuber-Unkel, M. López-García, H. Kessler, J. P. Spatz, Cooperativity in Adhesion Cluster Formation during Initial Cell Adhesion, *Biophys. J.* **2008**, *95*, 5424–5431.

[36]   B. R. Brückner, A. Janshoff, Importance of integrity of cell-cell junctions for the mechanics of confluent MDCK II cells, *Sci. Rep.* **2018**, *8*, 14117.

[37]   A. D. Dupuy, D. M. Engelman, Protein area occupancy at the center of the red blood cell membrane, *Proc. Natl. Acad. Sci. USA* **2008**, *105*, 2848–2852.

[38]   J. N. Israelachvilli, *Intermolecular and Surface Forces,* 3rd ed., Academic Press, Burlington, San Diego, Oxford, London, Amsterdam, **2011**.

[39]   E. Sackmann, Supported Membranes: Scientific and Practical Applications, *Science* **1996**, *271*, 43–48.

[40]   R. P. Richter, R. Bérat, A. R. Brisson, Formation of Solid-Supported Lipid Bilayers: An Integrated View, *Langmuir* **2006**, *22*, 3497–3505.

[41] M. I. Angelova, D. S. Dimitrov, Liposome Electroformation, *Faraday Discuss. Chem. Soc.* **1986**, *81*, 303–311.

[42] S. F. Fenz, K. Sengupta, Giant vesicles as cell models, *Integr. Biol.* **2012**, *4*, 982–995.

[43] G. Rivas, S. K. Vogel, P. Schwille, Reconstitution of cytoskeletal protein assemblies for large-scale membrane transformation, *Curr. Opin. Chem. Biol.* **2014**, *22*, 18–26.

[44] E. Loiseau, J. A. M. Schneider, F. C. Keber, C. Pelzl, G. Massiera, G. Salbreux, A. R. Bausch, Shape remodeling and blebbing of active cytoskeletal vesicles, *Sci. adv.* **2016**, *2*, e1500465.

[45] E. Schäfer, T.-T. Kliesch, A. Janshoff, Mechanical Properties of Giant Liposomes Compressed between Two Parallel Plates: Impact of Artificial Actin Shells, *Langmuir* **2013**, *29*, 10463–10474.

[46] P. Girard, J. Pécréaux, G. Lenoir, P. Falson, J.-L. Rigaud, P. Bassereau, A New Method for the Reconstitution of Membrane Proteins into Giant Unilamellar Vesicles, *Biophys. J.* **2004**, *87*, 419–429.

[47] E. Sackmann, R. Merkel, *Lehrbuch der Biophysik,* 2nd ed., Wiley-VCH, Weinheim, **2012**.

[48] T. C. Südhof, The Presynaptic Active Zone, *Neuron* **2012**, *75*, 11–25.

[49] S. O. Rizzoli, W. J. Betz, Synaptic vesicle pools, *Nat. Rev. Neurosci.* **2005**, *6*, 57–69.

[50] R. Jahn, T. C. Südhof, Membrane Fusion and Exocytosis, *Annu. Rev. Biochem.* **1999**, *68*, 863–911.

[51] J. Preobraschenski, J.-F. Zander, T. Suzuki, G. Ahnert-Hilger, R. Jahn, Vesicular Glutamate Transporters Use Flexible Anion and Cation Binding Sites for Efficient Accumulation of Neurotransmitter, *Neuron* **2014**, *84*, 1287–1301.

[52] S. J. Singer, G. L. Nicolson, The Fluid Mosaic Model of the Structure of Cell Membranes, *Science* **1972**, *175*, 720–731.

[53] E. Sezgin, I. Levental, S. Mayor, C. Eggeling, The mystery of membrane organization: composition, regulation and roles of lipid rafts, *Nat. Rev. Mol. Cell Biol.* **2017**, *18*, 361–374.

[54] I. Levental, S. Veatch, The Continuing Mystery of Lipid Rafts, *J. Mol. Biol.* **2016**, *428*, 4749–4764.

[55] D. A. Brown, J. K. Rose, Sorting of GPI-Anchored Proteins to Glycolipid-Enriched Membrane Subdomains during Transport to the Apical Cell Sdreurface, *Cell* **1992**, *68*, 533–544.

[56] K. Simons, E. Ikonen, Functional rafts in cell membranes, *Nature* **1997**, *387*, 569–572.

[57] C. Zurzolo, G. van Meer, S. Mayor, The order of rafts. Conference on Microdomains, Lipid Rafts and Caveolae, *EMBO Rep.* **2003**, *4*, 1117–1121.

[58] A. Kusumi, T. K. Fujiwara, N. Morone, K. J. Yoshida, R. Chadda, M. Xie, R. S. Kasai, K. G. N. Suzuki, Membrane mechanisms for signal transduction: the coupling of the meso-scale raft domains to membrane-skeleton-induced compartments and dynamic protein complexes, *Semin. Cell Dev. Biol.* **2012**, *23*, 126–144.

[59] E. Sevcsik, M. Brameshuber, M. Fölser, J. Weghuber, A. Honigmann, G. J. Schütz, GPI-anchored proteins do not reside in ordered domains in the live cell plasma membrane, *Nat. Commun.* **2015**, *6*, 6969.

[60] J. Chen, J. Gao, J. Wu, M. Zhang, M. Cai, H. Xu, J. Jiang, Z. Tian, H. Wang, Revealing the carbohydrate pattern on a cell surface by super-resolution imaging, *Nanoscale* **2015**, *7*, 3373–3380.

[61] M. Maglione, S. J. Sigrist, Seeing the forest tree by tree: super-resolution light microscopy meets the neurosciences, *Nat. Neurosci.* **2013**, *16*, 790–797.

[62] J. Malinsky, M. Opekarová, G. Grossmann, W. Tanner, Membrane Microdomains, Rafts, and Detergent-Resistant Membranes in Plants and Fungi, *Annu. Rev. Plant Biol.* **2013**, *64*, 501–529.

[63] C. G. Specht, I. Izeddin, P. C. Rodriguez, M. El Beheiry, P. Rostaing, X. Darzacq, M. Dahan, A. Triller, Quantitative Nanoscopy of Inhibitory Synapses: Counting Gephyrin Molecules and Receptor Binding Sites, *Neuron* **2013**, *79*, 308–321.

[64] J. Gao, Y. Wang, M. Cai, Y. Pan, H. Xu, J. Jiang, H. Ji, H. Wang, Mechanistic insights into EGFR membrane clustering revealed by super-resolution imaging, *Nanoscale* **2015**, *7*, 2511–2519.

[65] J. Gao, J. Chen, H. Wang in *Membrane biophysics*. *New insights and methods* (Eds.: H. Wang, G. Li), Springer, Singapore, **2018**, 117–145.

[66] F. Fricke, S. Malkusch, G. Wangorsch, J. F. Greiner, B. Kaltschmidt, C. Kaltschmidt, D. Widera, T. Dandekar, M. Heilemann, Quantitative single-molecule localization microscopy combined with rule-based modeling reveals ligand-induced TNF-R1 reorganization toward higher-order oligomers, *Histochem. Cell Biol.* **2014**, *142*, 91–101.

[67] A. D. Douglass, R. D. Vale, Single-Molecule Microscopy Reveals Plasma Membrane Microdomains Created by Protein-Protein Networks that Exclude or Trap Signaling Molecules in T Cells, *Cell* **2005**, *121*, 937–950.

[68] D. J. Williamson, D. M. Owen, J. Rossy, A. Magenau, M. Wehrmann, J. J. Gooding, K. Gaus, Pre-existing clusters of the adaptor Lat do not participate in early T cell signaling events, *Nat. Immunol.* **2011**, *12*, 655–662.

[69]   D. M. Owen, D. J. Williamson, A. Magenau, K. Gaus, Sub-resolution lipid domains exist in the plasma membrane and regulate protein diffusion and distribution, *Nat. Commun.* **2012**, *3*, 1256.

[70]   A. Schreiber, S. Fischer, T. Lang, The Amyloid Precursor Protein Forms Plasmalemmal Clusters via Its Pathogenic Amyloid-β Domain, *Biophys. J.* **2012**, *102*, 1411–1417.

[71]   N. Ehmann, S. van de Linde, A. Alon, D. Ljaschenko, X. Z. Keung, T. Holm, A. Rings, A. DiAntonio, S. Hallermann, U. Ashery, M. Heckmann, M. Sauer, R. J. Kittel, Quantitative super-resolution imaging of Bruchpilot distinguishes active zone states, *Nat. Commun.* **2014**, *5*, 4650.

[72]   J. J. Sieber, K. I. Willig, R. Heintzmann, S. W. Hell, T. Lang, The SNARE Motif Is Essential for the Formation of Syntaxin Clusters in the Plasma Membrane, *Biophys. J.* **2006**, *90*, 2843–2851.

[73]   A. Pertsinidis, K. Mukherjee, M. Sharma, Z. P. Pang, S. R. Park, Y. Zhang, A. T. Brunger, T. C. Südhof, S. Chu, Ultrahigh-resolution imaging reveals formation of neuronal SNARE/Munc18 complexes in situ, *Proc. Natl. Acad. Sci. USA* **2013**, *110*, E2812-E2820.

[74]   A. T. Bademosi, J. Steeves, S. Karunanithi, O. H. Zalucki, R. S. Gormal, S. Liu, E. Lauwers, P. Verstreken, V. Anggono, F. A. Meunier, B. van Swinderen, Trapping of Syntaxin1a in Presynaptic Nanoclusters by a Clinically Relevant General Anesthetic, *Cell Rep.* **2018**, *22*, 427–440.

[75]   J. J. Sieber, K. I. Willig, C. Kutzner, C. Gerding-Reimers, B. Harke, G. Donnert, B. Rammner, C. Eggeling, S. W. Hell, H. Grubmüller, T. Lang, Anatomy and Dynamics of a Supramolecular Membrane Protein Cluster, *Science* **2007**, *317*, 1072–1076.

[76]   H. Koldsø, M. S. P. Sansom, Organization and Dynamics of Receptor Proteins in a Plasma Membrane, *J. Am. Chem. Soc.* **2015**, *137*, 14694–14704.

[77]   F. Y. H. Teng, Y. Wang, B. L. Tang, The syntaxins, *Genome Biol.* **2001**, *2*.

[78]   P. Recouvreux, P.-F. Lenne, Molecular clustering in the cell: from weak interactions to optimized functional architectures, *Curr. Opin. Cell Biol.* **2016**, *38*, 18–23.

[79]   D. Milovanovic, A. Honigmann, S. Koike, F. Göttfert, G. Pähler, M. Junius, S. Müllar, U. Diederichsen, A. Janshoff, H. Grubmüller, H. J. Risselada, C. Eggeling, S. W. Hell, G. van den Bogaart, R. Jahn, Hydrophobic mismatch sorts SNARE proteins into distinct membrane domains, *Nat. Commun.* **2015**, *6*, 5984.

[80]   J. Goyette, K. Gaus, Mechanisms of protein nanoscale clustering, *Curr. Opin. Cell Biol.* **2017**, *44*, 86–92.

[81]   S. K. Saka, A. Honigmann, C. Eggeling, S. W. Hell, T. Lang, S. O. Rizzoli, Multi-protein assemblies underlie the mesoscale organization of the plasma membrane, *Nat. Commun.* **2014**, *5*, 4509.

[82]   P. Sengupta, S. van Engelenburg, J. Lippincott-Schwartz, Visualizing Cell Structure and Function with Point-Localization Superresolution Imaging, *Dev. Cell* **2012**, *23*, 1092–1102.

[83]   A. Burgert, S. Letschert, S. Doose, M. Sauer, Artifacts in single-molecule localization microscopy, *Histochem. Cell Biol.* **2015**, *144*, 123–131.

[84]   B. L. Busse, L. Bezrukov, P. S. Blank, J. Zimmerberg, Resin embedded multicycle imaging (REMI): a tool to evaluate protein domains, *Sci. Rep.* **2016**, *6*, 30284.

[85]   C. Stadler, E. Rexhepaj, V. R. Singan, R. F. Murphy, R. Pepperkok, M. Uhlén, J. C. Simpson, E. Lundberg, Immunofluorescence and fluorescent-protein tagging show high correlation for protein localization in mammalian cells, *Nat. Methods* **2013**, *10*, 315–323.

[86]   A. T. Bademosi, E. Lauwers, P. Padmanabhan, L. Odierna, Y. J. Chai, A. Papadopulos, G. J. Goodhill, P. B. Verstreken, B. van Swinderen, F. A. Meunier, In vivo single-molecule imaging of syntaxin1A reveals polyphosphoinositide- and activity-dependent trapping in presynaptic nanoclusters, *Nat. Commun.* **2016**, *7*, 13660.

[87]   D. Alsteens, M. C. Garcia, P. N. Lipke, Y. F. Dufrêne, Force-induced formation and propagation of adhesion nanodomains in living fungal cells, *Proc. Natl. Acad. Sci. USA* **2010**, *107*, 20744–20749.

[88]   D. Alsteens, H. Trabelsi, P. Soumillion, Y. F. Dufrêne, Multiparametric atomic force microscopy imaging of single bacteriophages extruding from living bacteria, *Nat. Commun.* **2013**, *4*, 2926.

[89]   L. Janosi, Z. Li, J. F. Hancock, A. A. Gorfe, Organization, dynamics, and segregation of Ras nanoclusters in membrane domains, *Proc. Natl. Acad. Sci. USA* **2012**, *109*, 8097–8102.

[90]   D. Bar-On, S. Wolter, S. van de Linde, M. Heilemann, G. Nudelman, E. Nachliel, M. Gutman, M. Sauer, U. Ashery, Super-resolution Imaging Reveals the Internal Architecture of Nano-sized Syntaxin Clusters, *J. Biol. Chem.* **2012**, *287*, 27158–27167.

[91]   J. F. Marko, E. D. Siggia, Stretching DNA, *Macromolecules* **1995**, *28*, 8759–8770.

[92]   G. van den Bogaart, K. Meyenberg, H. J. Risselada, H. Amin, K. I. Willig, B. E. Hubrich, M. Dier, S. W. Hell, H. Grubmüller, U. Diederichsen, R. Jahn, Membrane protein sequestering by ionic protein-lipid interactions, *Nature* **2011**, *479*, 552–555.

[93] P. Hinterdorfer, W. Baumgartner, H. J. Gruber, K. Schilcher, H. Schindler, Detection and localization of individual antibody-antigen recognition events by atomic force microscopy, *Proc. Natl. Acad. Sci. USA* **1996**, *93*, 3477–3481.

[94] D. Alsteens, D. J. Müller, Y. F. Dufrêne, Multiparametric Atomic Force Microscopy Imaging of Biomolecular and Cellular Systems, *Acc. Chem. Res.* **2017**, *50*, 924–931.

[95] M. Li, D. Dang, L. Liu, N. Xi, Y. Wang, Imaging and Force Recognition of Single Molecular Behaviors Using Atomic Force Microscopy, *Sensors* **2017**, *17*, 200.

[96] K. T. Sapra, P. M. Spoerri, A. Engel, D. Alsteens, D. J. Müller, Seeing and sensing single G protein-coupled receptors by atomic force microscopy, *Curr. Opin. Cell Biol.* **2019**, *57*, 25–32.

[97] T. Haselgrübler, A. Amerstorfer, H. Schindler, H. J. Gruber, Synthesis and Applications of a New Poly(ethylene glycol) Derivative for the Crosslinking of Amines with Thiols, *Bioconjugate Chem.* **1995**, *6*, 242–248.

[98] A. Ebner, L. Wildling, A. S. M. Kamruzzahan, C. Rankl, J. Wruss, C. D. Hahn, M. Hölzl, R. Zhu, F. Kienberger, D. Blaas, P. Hinterdorfer, H. J. Gruber, A New, Simple Method for Linking of Antibodies to Atomic Force Microscopy Tips, *Bioconjugate Chem.* **2007**, *18*, 1176–1184.

[99] C. M. Stroh, A. Ebner, M. Geretschläger, G. Freudenthaler, F. Kienberger, A. S. M. Kamruzzahan, S. J. Smith-Gill, H. J. Gruber, P. Hinterdorfer, Simultaneous Topography and Recognition Imaging Using Force Microscopy, *Biophys. J.* **2004**, *87*, 1981–1990.

[100] R. Zhu, A. Rupprecht, A. Ebner, T. Haselgrübler, H. J. Gruber, P. Hinterdorfer, E. E. Pohl, Mapping the Nucleotide Binding Site of Uncoupling Protein 1 Using Atomic Force Microscopy, *J. Am. Chem. Soc.* **2013**, *135*, 3640–3646.

[101] R. Creasey, S. Sharma, C. T. Gibson, J. E. Craig, A. Ebner, T. Becker, P. Hinterdorfer, N. H. Voelcker, Atomic force microscopy-based antibody recognition imaging of proteins in the pathological deposits in Pseudoexfoliation Syndrome, *Ultramicroscopy* **2011**, *111*, 1055–1061.

[102] M. Li, X. Xiao, L. Liu, N. Xi, Y. Wang, Z. Dong, W. Zhang, Nanoscale mapping and organization analysis of target proteins on cancer cells from B-cell lymphoma patients, *Exp. Cell Res.* **2013**, *319*, 2812–2821.

[103] C. Formosa-Dague, Z.-H. Fu, C. Feuillie, S. Derclaye, T. J. Foster, J. A. Geoghegan, Y. F. Dufrêne, Forces between Staphylococcus aureus and human skin, *Nanoscale Horiz.* **2016**, *1*, 298–303.

[104] M. Li, L. Liu, N. Xi, Y. Wang, Z. Dong, X. Xiao, W. Zhang, Mapping CD20 molecules on the lymphoma cell surface using atomic force microscopy, *Chin. Sci. Bull.* **2013**, *58*, 1516–1519.

[105] A. C. Dumitru, L. Conrard, C. Lo Giudice, P. Henriet, M. Veiga-da-Cunha, S. Derclaye, D. Tyteca, D. Alsteens, High-resolution mapping and recognition of lipid domains using AFM with toxin-derivatized probes, *Chem. Commun.* **2018**, *54*, 6903–6906.

[106] D. J. Müller, Y. F. Dufrêne, Atomic force microscopy: a nanoscopic window on the cell surface, *Trends Cell Biol.* **2011**, *21*, 461–469.

[107] D. J. Müller, J. Helenius, D. Alsteens, Y. F. Dufrêne, Force probing surfaces of living cells to molecular resolution, *Nat. Chem. Biol.* **2009**, *5*, 383–390.

[108] D. Alsteens, M. Pfreundschuh, C. Zhang, P. M. Spoerri, S. R. Coughlin, B. K. Kobilka, D. J. Müller, Imaging G protein-coupled receptors while quantifying their ligand-binding free-energy landscape, *Nat. Methods* **2015**, *12*, 845–851.

[109] D. Alsteens, R. Newton, R. Schubert, D. Martinez-Martin, M. Delguste, B. Roska, D. J. Müller, Nanomechanical mapping of first binding steps of a virus to animal cells, *Nat. Nanotechnol.* **2017**, *12*, 177–183.

[110] J. Danzberger, M. Donovan, C. Rankl, R. Zhu, S. Vicic, C. Baltenneck, R. Enea, P. Hinterdorfer, G. S. Luengo, Glycan distribution and density in native skin's stratum corneum, *Skin Res. Technol.* **2018**, *24*, 450–458.

[111] S. Takamori, M. Holt, K. Stenius, E. A. Lemke, M. Grønborg, D. Riedel, H. Urlaub, S. Schenck, B. Brügger, P. Ringler, S. A. Müller, B. Rammner, F. Gräter, J. S. Hub, B. L. de Groot, G. Mieskes, Y. Moriyama, J. Klingauf, H. Grubmüller, J. Heuser, F. Wieland, R. Jahn, Molecular Anatomy of a Trafficking Organelle, *Cell* **2006**, *127*, 831–846.

[112] R. Jahn, W. Schiebler, C. Ouimet, P. Greengard, A 38,000-dalton membrane protein (p38) present in synaptic vesicles, *Proc. Natl. Acad. Sci. USA* **1985**, *82*, 4137–4141.

[113] C. P. Arthur, M. H. B. Stowell, Structure of Synaptophysin: A Hexameric MARVEL-Domain Channel Protein, *Structure* **2007**, *15*, 707–714.

[114] P. A. Johnston, T. C. Südhof, The Multisubunit Structure of Synaptophysin. Relationship between disulfide bonding and homo-oligomerization, *J. Biol. Chem.* **1990**, *265*, 8869–8873.

[115] R. E. Leube, The topogenic fate of the polytopic transmembrane proteins, synaptophysin and connexin, is determined by their membrane-spanning domains, *J. Cell Sci.* **1995**, *108*, 883–894.

[116] R. H. S. Westerink, A. G. Ewing, The PC12 cell as model for neurosecretion, *Acta physiol.* **2008**, *192*, 273–285.

[117] S. Kaech, G. Banker, Culturing hippocampal neurons, *Nat. Protoc.* **2006**, *1*, 2406–2415.

[118] S. Park, N.-R. Bin, R. M. M. Rajah, B. Kim, T.-C. Chou, S.-Y. A. Kang, K. Sugita, L. Parsaud, M. Smith, P. P. Monnier, M. Ikura, M. Zhen, S. Sugita, Conformational states of syntaxin-1 govern the necessity of N-peptide binding in exocytosis of PC12 cells and Caenorhabditis elegans, *Mol. Biol. Cell* **2016**, *27*, 669–685.

[119] T. de Meyer, S. Muyldermans, A. Depicker, Nanobody-based products as research and diagnostic tools, *Trends Biotechnol.* **2014**, *32*, 263–270.

[120] A. Desmyter, S. Spinelli, A. Roussel, C. Cambillau, Camelid nanobodies: killing two birds with one stone, *Curr. Opin. Struc. Biol.* **2015**, *32*, 1–8.

[121] Johannes Kepler Universität Linz, *Crosslinkers and Protocols for AFM Tip Functionalization,* https://www.jku.at/institut-fuer-biophysik/forschung/linker/, [accessed 11.09.2018].

[122] A. Witkowska, R. Jahn, Rapid SNARE-Mediated Fusion of Liposomes and Chromaffin Granules with Giant Unilamellar Vesicles, *Biophys. J.* **2017**, *113*, 1251–1259.

[123] A. Witkowska, L. Jablonski, R. Jahn, A convenient protocol for generating giant unilamellar vesicles containing SNARE proteins using electroformation, *Sci. Rep.* **2018**, *8*, 9422.

[124] J. W. Lichtman, J.-A. Conchello, Fluorescence microscopy, *Nat. Methods* **2005**, *2*, 910–919.

[125] W. B. Amos, J. G. White, How the Confocal Laser Scanning Microscope entered Biological Research, *Biol. Cell* **2003**, *95*, 335–342.

[126] S. W. Hell, J. Wichmann, Breaking the diffraction resolution limit by stimulated emission: stimulated-emission-depletion fluorescence microscopy, *Opt. Lett.* **1994**, *19*, 780–782.

[127] G. Binnig, C. F. Quate, C. Gerber, Atomic Force Microscope, *Phys. Rev. Lett.* **1986**, *56*, 930–933.

[128] D. Alsteens, H. E. Gaub, R. Newton, M. Pfreundschuh, C. Gerber, D. J. Müller, Atomic force microscopy-based characterization and design of biointerfaces, *Nat. Rev. Mater.* **2017**, *2*, 17008.

[129] G. Meyer, N. M. Amer, Erratum: Novel optical approach to atomic force microscopy [Appl. Phys. Lett. 53 , 1045 (1988)], *Appl. Phys. Lett.* **1988**, *53*, 2400–2402.

[130] E. Florin, V. Moy, H. Gaub, Adhesion Forces Between Individual Ligand-Receptor Pairs, *Science* **1994**, *264*, 415–417.

[131] G. U. Lee, D. A. Kidwell, R. J. Colton, Sensing Discrete Streptavidin-Biotin Interactions with Atomic Force Microscopy, *Langmuir* **1994**, *10*, 354–357.

[132] H.-J. Butt, B. Cappella, M. Kappl, Force measurements with the atomic force microscope: Technique, interpretation and applications, *Surf. Sci. Rep.* **2005**, *59*, 1–152.

[133] J. L. Hutter, J. Bechhoefer, Calibration of atomic-force microscope tips, *Rev. Sci. Instrum.* **1993**, *64*, 1868–1873.

[134] J. M. Mitchison, M. M. Swann, The Mechanical Properties of the Cell Surface, *J. Exp. Biol.* **1954**, *31*, 443–460.

[135] R. Kwok, E. Evans, Thermoelasticity of large lecithin bilayer vesicles, *Biophys. J.* **1981**, *35*, 637–652.

[136] E. Evans, D. Needham, Physical Properties of Surfactant Bilayer Membranes: Thermal Transitions, Elasticity, Rigidity, Cohesion and Colloidal Interactions, *J. Phys. Chem.* **1987**, *91*, 4219–4228.

[137] J. Henriksen, A. C. Rowat, E. Brief, Y. W. Hsueh, J. L. Thewalt, M. J. Zuckermann, J. H. Ipsen, Universal Behavior of Membranes with Sterols, *Biophys. J.* **2006**, *90*, 1639–1649.

[138] Z. Shi, T. Baumgart, Membrane tension and peripheral protein density mediate membrane shape transitions, *Nat. Commun.* **2015**, *6*, 5974.

[139] J. R. Henriksen, J. H. Ipsen, Measurement of membrane elasticity by micro-pipette aspiration, *Eur. Phys. J. E* **2004**, *14*, 149–167.

[140] L. Lu, W. J. Doak, J. W. Schertzer, P. R. Chiarot, Membrane mechanical properties of synthetic asymmetric phospholipid vesicles, *Soft matter* **2016**, *12*, 7521–7528.

[141] W. Rawicz, K. C. Olbrich, T. McIntosh, D. Needham, E. Evans, Effect of Chain Length and Unsaturation on Elasticity of Lipid Bilayers, *Biophys. J.* **2000**, *79*, 328–339.

[142] C. A. Schneider, W. S. Rasband, K. W. Eliceiri, NIH Image to ImageJ: 25 years of Image Analysis, *Nat. Methods* **2012**, *9*, 671–675.

[143] S. van der Walt, J. L. Schönberger, J. Nunez-Iglesias, F. Boulogne, J. D. Warner, N. Yager, E. Gouillart, T. Yu, scikit-image: image processing in Python, *PeerJ* **2014**, *2*, e453.

[144] B. D. Ripley, The second-order analysis of stationary point processes, *J. Appl. Probab.* **1976**, *13*, 255–266.

[145] E. Schäfer, M. Vache, T.-T. Kliesch, A. Janshoff, Mechanical response of adherent giant liposomes to indentation with a conical AFM-tip, *Soft matter* **2015**, *11*, 4487–4495.

[146] M. Tagaya, S. Toyonaga, M. Takahashi, A. Yamamoto, T. Fujiwara, K. Akagawa, Y. Moriyama, S. Mizushima, Syntaxin 1 (HPC-1) Is Associated with Chromaffin Granules, *J. Biol. Chem.* **1995**, *270*, 15930–15933.

[147] N. C. Shaner, R. E. Campbell, P. A. Steinbach, B. N. G. Giepmans, A. E. Palmer, R. Y. Tsien, Improved monomeric red, orange and yellow fluorescent proteins derived from Discosoma sp. red fluorescent protein, *Nat. Biotechnol.* **2004**, *22*, 1567–1572.

[148] G. Bell, Models for the Specific Adhesion of Cells to Cells, *Science* **1978**, *200*, 618–627.

[149] E. Evans, K. Ritchie, Dynamic Strength of Molecular Adhesion Bonds, *Biophys. J.* **1997**, *72*, 1541–1555.

[150] F. Kienberger, V. P. Pastushenko, G. Kada, H. J. Gruber, C. Riener, H. Schindler, P. Hinterdorfer, Static and Dynamical Properties of Single Poly(Ethylene Glycol) Molecules Investigated by Force Spectroscopy, *Single Mol.* **2000**, *1*, 123–128.

[151] E. Evans, A. Yeung, Apparent viscosity and cortical tension of blood granulocytes determined by micropipet aspiration, *Biophys. J.* **1989**, *56*, 151–160.

[152] R. M. Hochmuth, Micropipette aspiration of living cells, *J. Biomech.* **2000**, *33*, 15–22.

[153] J. Avery, D. J. Ellis, T. Lang, P. Holroyd, D. Riedel, R. M. Henderson, J. M. Edwardson, R. Jahn, A Cell-Free System for Regulated Exocytosis in PC12 Cells, *J. Cell Biol.* **2000**, *148*, 317–324.

[154] T. Puntheeranurak, I. Neundlinger, R. K. H. Kinne, P. Hinterdorfer, Single-molecule recognition force spectroscopy of transmembrane transporters on living cells, *Nat. Protoc.* **2011**, *6*, 1443–1452.

[155] A. K. Trilling, J. Beekwilder, H. Zuilhof, Antibody orientation on biosensor surfaces: a minireview, *Analyst* **2013**, *138*, 1619–1627.

[156] F. Oesterhelt, D. Oesterhelt, M. Pfeiffer, A. Engel, H. E. Gaub, D. J. Müller, Unfolding Pathways of Individual Bacteriorhodopsins, *Science* **2000**, *288*, 143–146.

[157] C. Formosa-Dague, C. Feuillie, A. Beaussart, S. Derclaye, S. Kucharíková, I. Lasa, P. van Dijck, Y. F. Dufrêne, Sticky Matrix: Adhesion Mechanism of the Staphylococcal Polysaccharide Intercellular Adhesin, *ACS Nano* **2016**, *10*, 3443–3452.

[158] E. Celik, V. T. Moy, Nonspecific interactions in AFM force spectroscopy measurements, *J. Mol. Recognit.* **2012**, *25*, 53–56.

[159] N. Kamprad, H. Witt, M. Schröder, C. T. Kreis, O. Bäumchen, A. Janshoff, M. Tarantola, Adhesion strategies of Dictyostelium discoideum - a force spectroscopy study, *Nanoscale* **2018**, *10*, 22504–22519.

[160] Y. F. Dufrêne, T. Ando, R. Garcia, D. Alsteens, D. Martinez-Martin, A. Engel, C. Gerber, D. J. Müller, Imaging modes of atomic force microscopy for application in molecular and cell biology, *Nat. Nanotechnol.* **2017**, *12*, 295–307.

[161] S. A. Contera, V. Lemaître, M. R. R. de Planque, A. Watts, J. F. Ryan, Unfolding and Extraction of a Transmembrane α-Helical Peptide: Dynamic Force Spectroscopy and Molecular Dynamics Simulations, *Biophys. J.* **2005**, *89*, 3129–3140.

[162] H. D. Ackler, R. H. French, Y.-M. Chiang, Comparisons of Hamaker Constants for Ceramic Systems with Intervening Vacuum or Water: From Force Laws and Physical Properties, *J. Colloid Interface Sci.* **1996**, *179*, 460–469.

[163] S. Biggs, P. Mulvaney, Measurement of the forces between gold surfaces in water by atomic force microscopy, *J. Chem. Phys.* **1994**, *100*, 8501–8505.

[164] A. Ott, M. Magnasco, A. Simon, A. Libchaber, Measurement of the persistence length of polymerized actin using fluorescence microscopy, *Phys. Rev. E* **1993**, *48*, R1642-R1645.

[165] M. Wirde, U. Gelius, L. Nyholm, Self-Assembled Monolayers of Cystamine and Cysteamine on Gold Studied by XPS and Voltammetry, *Langmuir* **1999**, *15*, 6370–6378.

[166] D. Seiwert, H. Witt, A. Janshoff, H. Paulsen, The non-bilayer lipid MGDG stabilizes the major light-harvesting complex (LHCII) against unfolding, *Sci. Rep.* **2017**, *7*, 5158.

[167] D. S. Mantus, B. D. Ratner, B. A. Carlson, J. F. Moulder, Static Secondary Ion Mass Spectrometry of Adsorbed Proteins, *Anal. Chem.* **1993**, *65*, 1431–1438.

[168] T. Braun, V. Barwich, M. K. Ghatkesar, A. H. Bredekamp, C. Gerber, M. Hegner, H. P. Lang, Micromechanical mass sensors for biomolecular detection in a physiological environment, *Phys. Rew. E* **2005**, *72*, 31907.

[169] F. Huber, M. Hegner, C. Gerber, H.-J. Güntherodt, H. P. Lang, Label free analysis of transcription factors using microcantilever arrays, *Biosens. Bioelectron.* **2006**, *21*, 1599–1605.

[170] I. Pera, R. Stark, M. Kappl, H.-J. Butt, F. Benfenati, Using the Atomic Force Microscope to Study the Interaction between Two Solid Supported Lipid Bilayers and the Influence of Synapsin I, *Biophys. J.* **2004**, *87*, 2446–2455.

[171] P. Girard, J. Prost, P. Bassereau, Passive or Active Fluctuations in Membranes Containing Proteins, *Phys. Rev. Lett.* **2005**, *94*, 88102.

[172] E. Evans, D. Needham, Giant Vesicle Bilayers composed of Mixtures of Lipids, Cholesterol and Polypeptides. Thermomechanical and (Mutual) Adherence Properties, *Faraday Discuss. Chem. Soc.* **1986**, 267–280.

[173] B. Sorre, A. Callan-Jones, J.-B. Manneville, P. Nassoy, J.-F. Joanny, J. Prost, B. Goud, P. Bassereau, Curvature-driven lipid sorting needs proximity to a demixing point and is aided by proteins, *Proc. Natl. Acad. Sci. USA* **2009**, *106*, 5622–5626.

[174] L. Guillou, A. Babataheri, M. Saitakis, A. Bohineust, S. Dogniaux, C. Hivroz, A. I. Barakat, J. Husson, T-lymphocyte passive deformation is controlled by unfolding of membrane surface reservoirs, *Mol. Biol. Cell* **2016**, *27*, 3574–3582.

[175] J. L. Drury, M. Dembo, Hydrodynamics of Micropipette Aspiration, *Biophys. J.* **1999**, *76*, 110–128.

[176] A. Mohammadalipour, M. M. Burdick, D. F. J. Tees, Deformability of breast cancer cells in correlation with surface markers and cell rolling, *FASEB J.* **2018**, *32*, 1806–1817.

[177]   R. P. Rand, Mechanical Properties of the Red Cell Membrane: II. Viscoelastic Breakdown of the Membrane, *Biophys. J.* **1964**, *4*, 303–316.

[178]   A. Tian, C. Johnson, W. Wang, T. Baumgart, Line Tension at Fluid Membrane Domain Boundaries Measured by Micropipette Aspiration, *Phys. Rev. Lett.* **2007**, *98*, 208102.

[179]   S. Emami, W.-C. Su, S. Purushothaman, V. N. Ngassam, A. N. Parikh, Permeability and Line-Tension-Dependent Response of Polyunsaturated Membranes to Osmotic Stresses, *Biophys. J.* **2018**, *115*, 1942–1955.

[180]   C. Daly, M. Sugimori, J. E. Moreira, E. B. Ziff, R. Llinás, Synaptophysin regulates clathrin-independent endocytosis of synaptic vesicles, *Proc. Natl. Acad. Sci. USA* **2000**, *97*, 6120–6125.

[181]   D. Gincel, V. Shoshan-Barmatz, The Synaptic Vesicle Protein Synaptophysin: Purification and Characterization of Its Channel Activity, *Biophys. J.* **2002**, *83*, 3223–3229.

[182]   M. Gleisner, B. Kroppen, C. Fricke, N. Teske, T.-T. Kliesch, A. Janshoff, M. Meinecke, C. Steinem, Epsin N-terminal Homology Domain (ENTH) Activity as a Function of Membrane Tension, *J. Biol. Chem.* **2016**, *291*, 19953–19961.

Appendices

Supplementary Figures
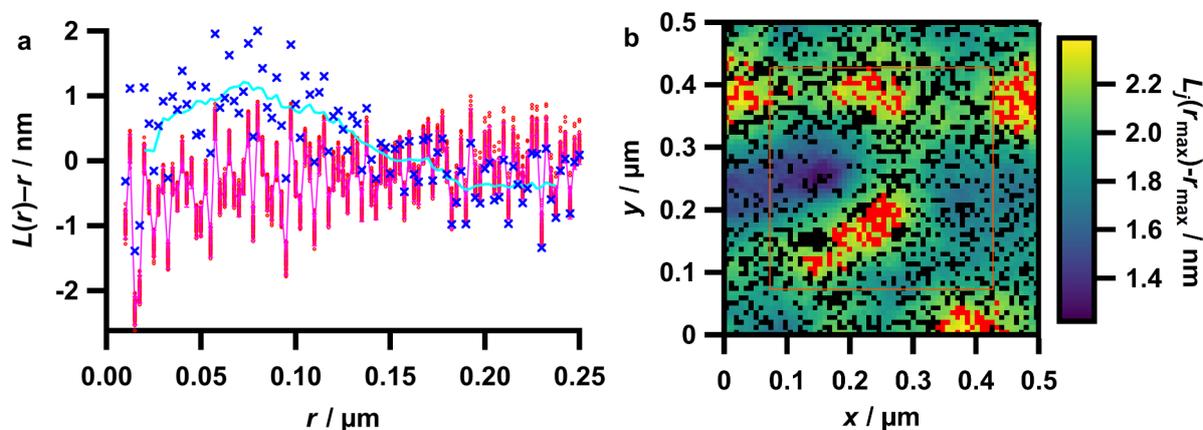
Supplementary Figure 1: Ripley analysis of a MR-AFM measurement with a retraction speed of 5 μm·s⁻¹ and with anti-Syx-NBs coupled to the cantilever with a 3:1 mixture of cysteamine and AUT. a plots the $L(r)-r$ values of the measured data (**×** and cyan line) and for homogeneous random data of the same number of events (○ and magenta line) as a function of r. In **b** the overlay of the Ripley density map and the corresponding clustered events (red) and all other events (black) is shown. For details see caption of Figure 3.18.
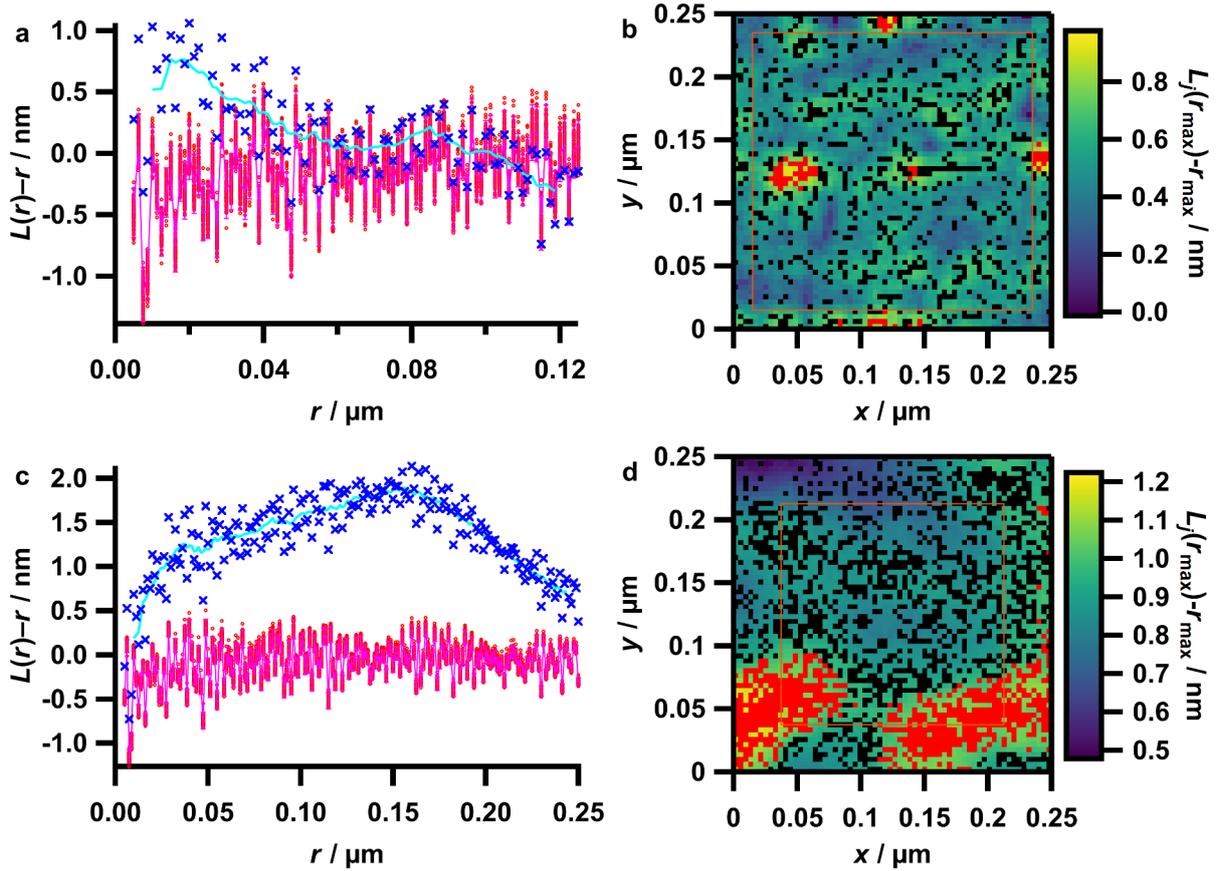
Supplementary Figure 2: Ripley cluster analyses of MR-AFM measurements before and after addition of free nanobodies in solution. In **a** and **b** the cluster analysis of a MR-AFM force map measured on a membrane sheet derived from a PC12-WT-1 cell before the addition of free nanobodies in solution is shown, in **c** and **d** the analysis of a subsequent measurement on the same membrane sheet under presence of 0.1 µM free nanobodies in solution. **a** and **c** plot the $L(r)-r$ values of the measured data (× and cyan line) and for homogeneous random data of the same number of events (○ and magenta line) as a function of r. In **b** and **d** the overlay of the Ripley density maps and the corresponding clustered events (red) and all other events (black) are shown. For details see caption of Figure 3.18.
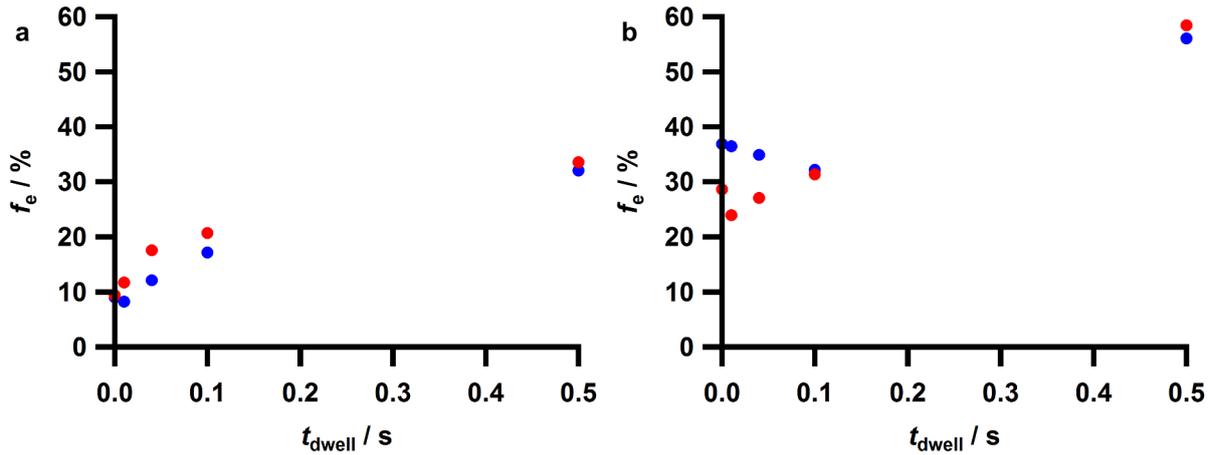
Supplementary Figure 3: Frequency of events as a function of the dwell time.
MR-AFM experiments were performed with anti-Syx-NBs coupled to the cantilever on
PC12-WT-1 cell membrane sheets without (**a**) and with (**b**) free nanobodies in solution
(0.1 µM). Blue circles correspond to the first series of measurements with a successive
increase of the dwell time, red circles correspond to the second series with a successive
decrease. Both measurements stem from different membrane sheets from independent
preparations. All data points of the same plot were measured at the same location of the
membrane sheet in a 16×16 force map.
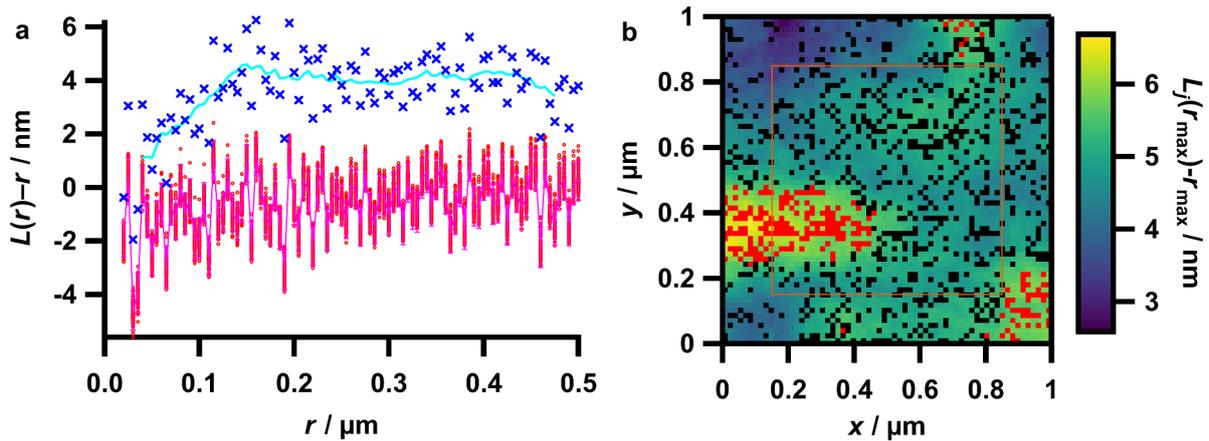
**Supplementary Figure 4: Ripley analysis of a MR-AFM measurement on a
PC12-WT-1 membrane sheets with nanobodies raised against mCherry coupled
with a 3:1 mixture of cysteamine and AUT to the cantilever. a** plots the $L(r)-r$ values
of the measured data (× and cyan line) and for homogeneous random data of the same
number of events (○ and magenta line) as a function of r. In **b** the overlay of the Ripley
density map and the corresponding clustered events (red) and all other events (black) is
shown. For details see caption of Figure 3.18.
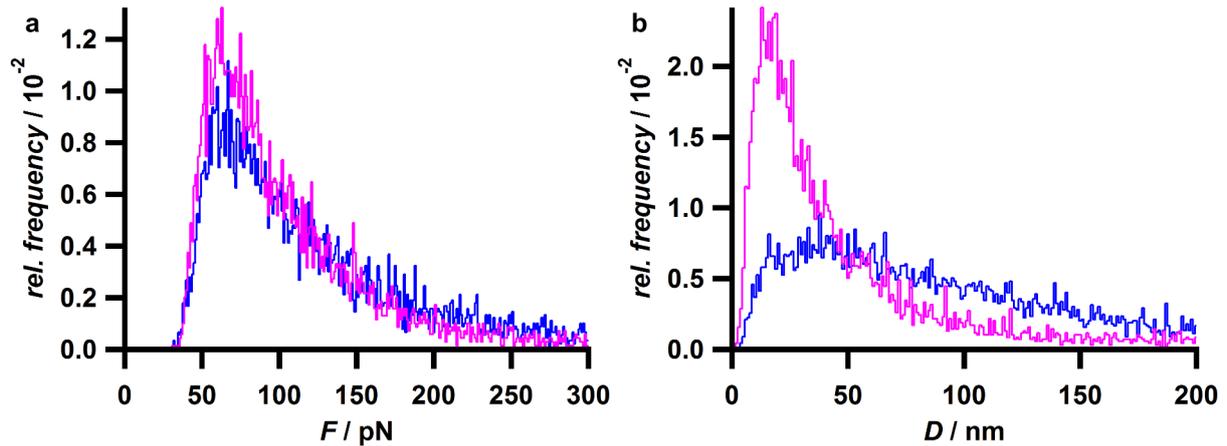
Supplementary Figure 5: Force and distance histograms of MR-AFM measurements with anti-Syx-NBs coupled to a cantilever maleimated by the manufacturer on membrane sheets derived from wild type and syntaxin-1 knockdown PC12 cells. In **a** the force and in **b** the distance histograms are shown, which plot the relative frequency of force and distance values within a bin size, respectively. The magenta coloured histograms correspond to measurements performed on membrane sheets derived from PC12-WT-2 cells ($N = 6958$) and the blue coloured histograms correspond to measurements performed on membrane sheets derived from PC12-Syx-KD cells ($N = 8960$). In Figure 4.26 the corresponding cumulative probability plots are shown. The force histogram is cut at 300 pN (13.6 % of the values of the magenta coloured and 18.5 % of the blue coloured histogram) and the distance histogram is cut at 0 nm (0.29 % of the values of the magenta coloured and 1.4 % of the blue coloured histogram) and at 200 nm (6.9 % of the values of the magenta coloured and 15.8 % of the blue coloured histogram).
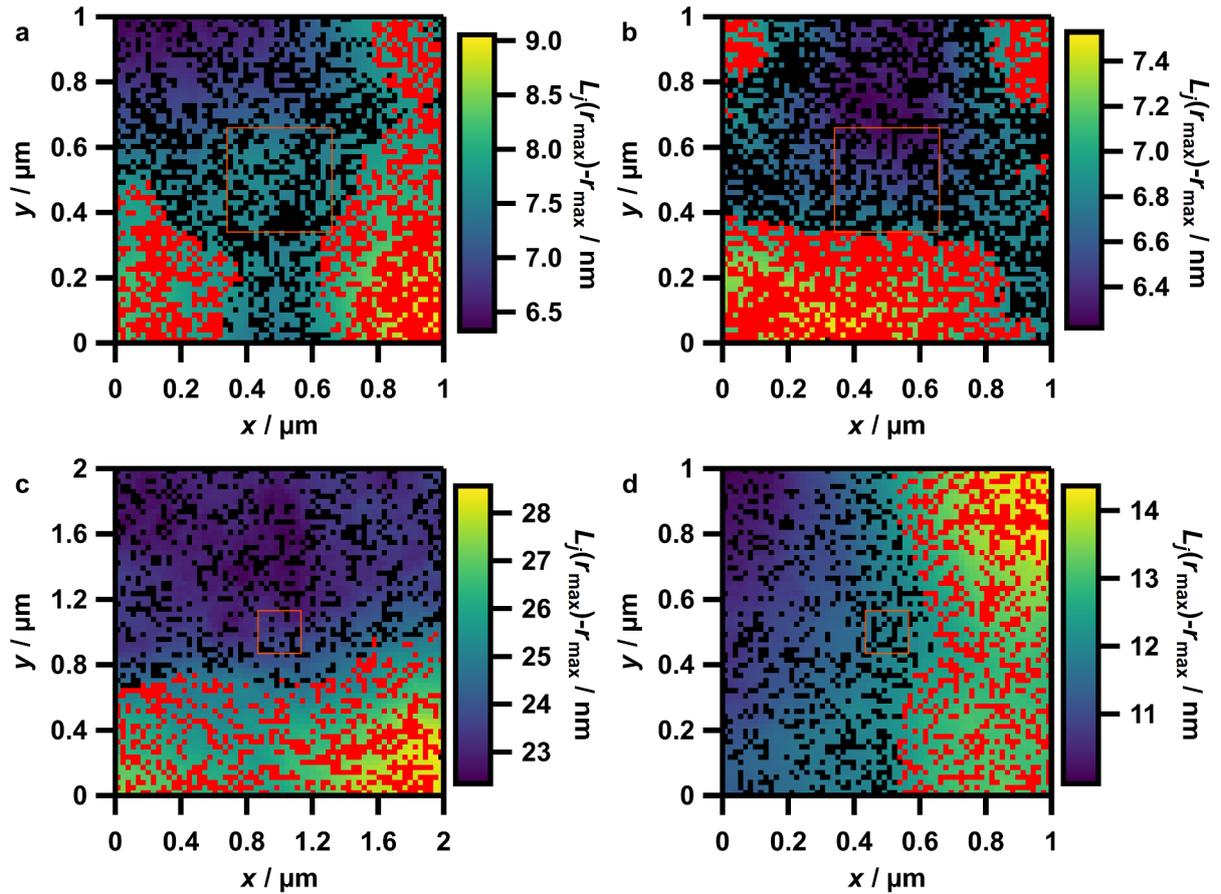
Supplementary Figure 6: Results of Ripley analyses of experiments performed with a cantilever which was maleimated by the manufacturer. In **a** and **b** examples for maps of events with two or three larger accumulations are shown. Both maps were recorded with exactly the same cantilever. In **c** and **d** two examples of maps with a gradient of the density of events are shown. The maps in **a** and **c** were recorded on membrane sheets derived from PC12-WT-2 cells and the ones in **b** and **d** on sheets derived from PC12-Syx-KD cells. All plots show the overlay of the Ripley density maps and the corresponding clustered events (red) and all other events (black). For details see caption of Figure 3.18. Force threshold analysis of the map in **a** yielded an additional cluster as shown in Supplementary Figure 7.
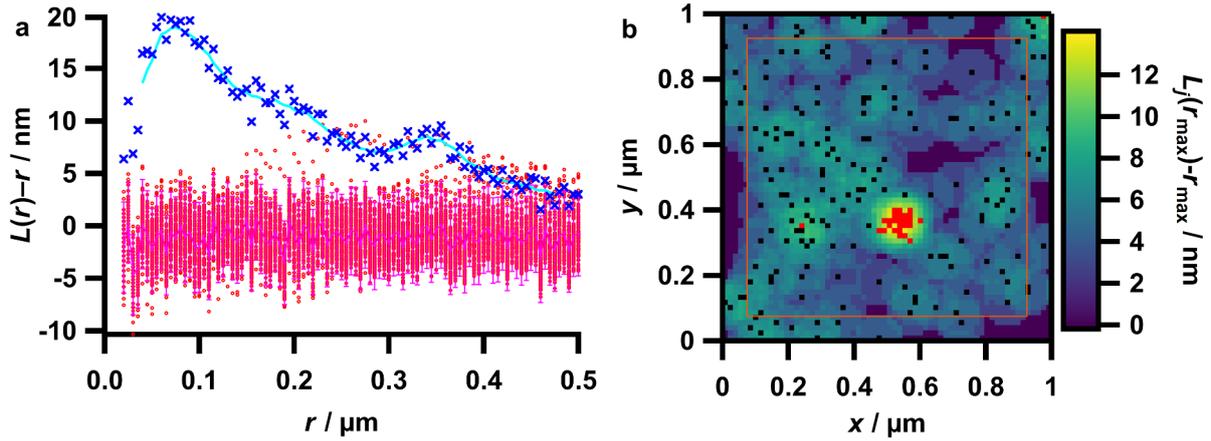
Supplementary Figure 7: Detection of a cluster when applying a lower force threshold of F_{low} = 468 pN. The map used for the analysis is the same as shown in Supplementary Figure 6 a. **a** plots the $L(r)-r$ values of the measured data (× and cyan line) and for homogeneous random data of the same number of events (○ and magenta line) as a function of r. In **b** the overlay of the Ripley density map and the corresponding clustered events (red) and all other events (black) is shown. For details see caption of Figure 3.18.
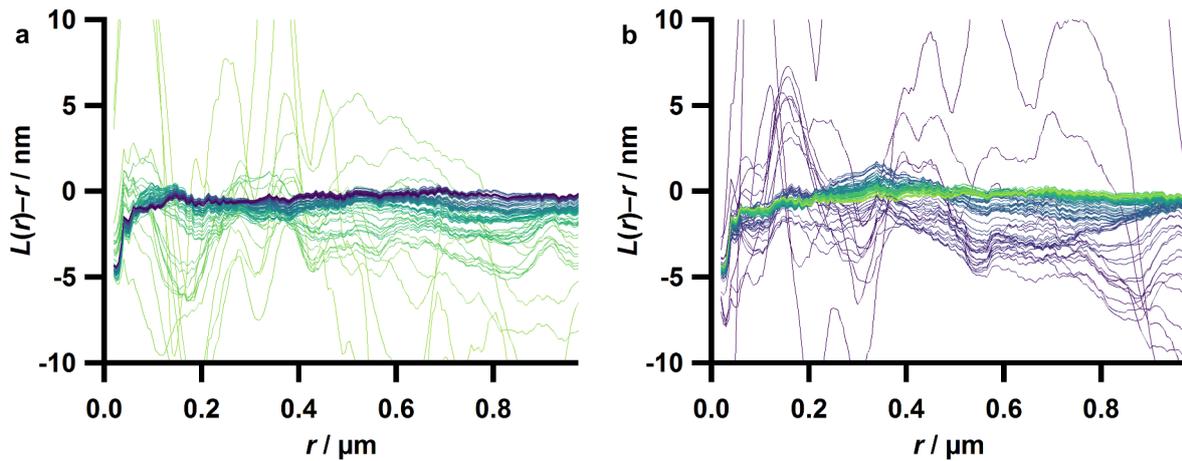
Supplementary Figure 8: Ripley cluster analyses of selected ranges of random numbers from a 64×64 array of uniformly distributed random numbers. The moving mean values of $L(r)–r$ are plotted against r. The colour indicates the threshold, where the darkest colour corresponds to the lowest and the lightest colour to the largest threshold. **a** shows plots for which the lower threshold was varied, **b** shows plots of the same map for which the upper threshold was varied. Note that in **a** a larger threshold leads to a smaller number of events whereas in **b** a larger threshold leads to a larger number of events. The ordinates are cut at ±10 nm.
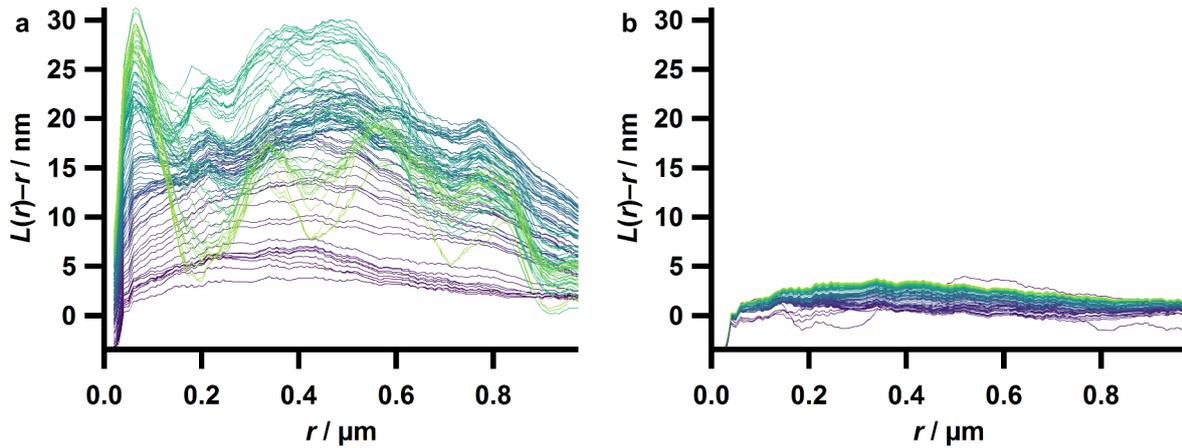
Supplementary Figure 9: Ripley cluster analyses of selected ranges of the contour length. Moving mean values of $L(r)$–r are plotted against r. The colour indicates the contour length threshold, where the darkest colour corresponds to the lowest and the lightest colour to the largest contour length threshold. **a** shows plots for which the lower contour length threshold was varied, **b** shows plots of the same map for which the upper threshold was varied. The corresponding map (the same as used for Figure 4.28 c and Supplementary Figure 7) was recorded on a membrane sheet derived from a PC12-WT-2 cell. The lightest colour corresponds to a contour length threshold of 3.5 µm, the darkest colour corresponds to a threshold of 0 µm.
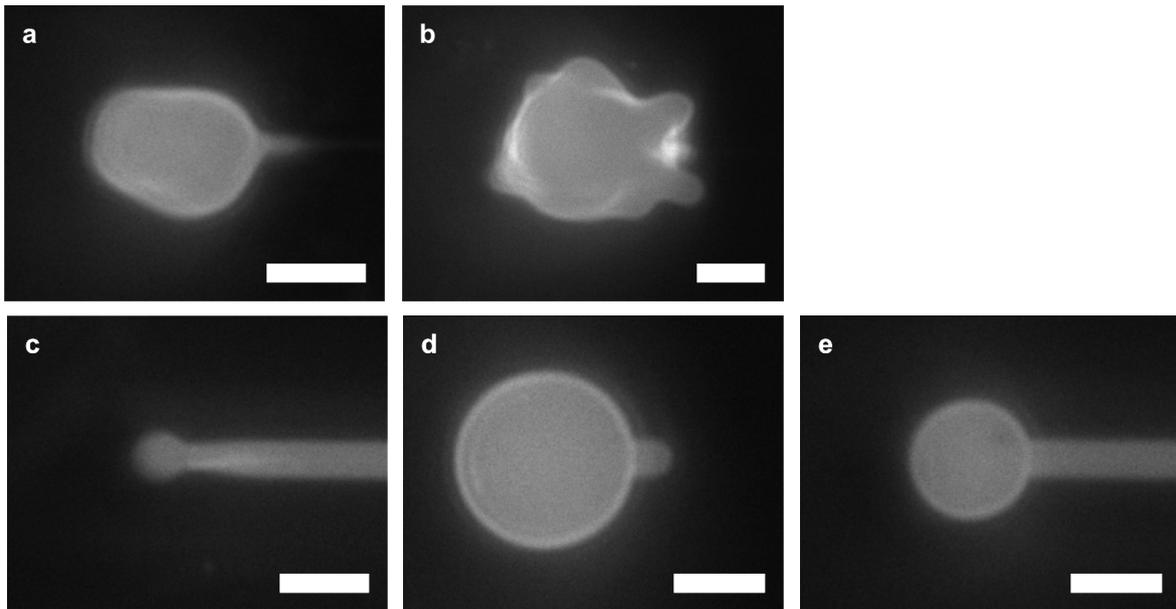
Supplementary Figure 10: Fluorescence micrographs of vesicles which ruptured during aspiration or which were completely aspired. In **a** and **b** two vesicles which presumably ruptured during aspiration are shown. **c** depicts a vesicle which was completely aspired instead of being ruptured. In **d** and **e** another vesicle which was aspired completely is shown. The time difference between both images is 2 s. In the images recorded 2 s after the ones shown in **a**, **b**, **c** and **e** the respective vesicle is not visible any more. Scale bars: 10 µm.

List of Figures

List of Tables

List of Abbreviations

a.u.	arbitrary units
AFM	atomic force microscopy
anti-Syx-AB	mouse-anti-rat-IgG antibody raised against syntaxin-1
anti-Syx-NB	nanobody raised against syntaxin-1A
APTES	(3-amminopropyl)triethoxysilane
AUT	11-amino-1-undecanethiol hydrochloride
BSA	bovine serum albumin
CLSM	confocal laser scanning microscopy
cum. probability	cumulative probability
DMEM	Dulbeccos Modified Eagle Medium
DOPC	1,2-dioleoyl-*sn*-glycero-3-phosphocholine
DOPE	1,2-dioleoyl-*sn*-glycero-3-phosphoethanolamine
e.g.	*exempli gratia* (Latin): for example
EDTA	ethylendiaminetetraacetic acid
eq.	equation
et al.	*et alii* (Latin): and others
FD-AFM	force-distance-curve based atomic force microscopy
GUV	giant unilamellar vesicle
GUV-MP	giant unilamellar vesicle membrane patch
HEPES	4-(2-hydroxyethyl)-1-piperazineethanesulfonic acid
i.e.	*id est* (Latin): that is
IgG	immunoglobulin G
ITO	indium tin oxide
MR-AFM	molecular recognition atomic force microscopy
NB	nanobody
norm. intensity	normalised intensity
NSF	N-ethylmaleimide sensitive factor
p.a.	*pro analysi* (Latin): for analysis
PALM	photo-activated localisation microscopy
PBS	phosphate buffered saline
PC12-Syx-KD	syntaxin-1A and B double knockdown PC12 cell
PC12-WT-1	wild type PC12 cell, first sub-cell line
PC12-WT-2	wild type PC12 cell, second sub-cell line

PEG	polyethylene glycol
PSD	position sensitive detector
PTFE	polytetrafluoroethylene
QI™	quantitative imaging mode of JPK Instruments
r.t.	room temperature
rel. frequency	relative frequency
ROI	region of interest
SD	standard deviation
SNARE	soluble N-ethylmaleimide sensitive factor attachment protein receptor
STED	stimulated emission depletion
STORM	stochastic optical reconstruction microscopy
TBS-T	tris buffered saline with Tween® 20
TCEP	tris-(2-carboxyethyl)-phosphine
TR-DHPE	Texas Red™ 1,2-dihexadecanoyl-*sn*-glycero-3-phosphoethanolamine
TREC	topography and recognition
UV-Vis	ultraviolet-visible
v/v	volume percentage with respect to volume of the entire solution
w/v	ratio between added matter in gram with respect to volume in millilitre or simply percentage by assuming a density of $1\ \mathrm{g \cdot ml^{-1}}$ for water or buffer
WLC	wormlike chain

List of Physical Quantities, Constants and Parameters

A	surface area of vesicle
A_0	initial surface area of spherical vesicle
A_{ind}	surface area of adhered and indented vesicle
A_{norm}	normalised surface area of vesicle
A_R	investigated area in Ripley analyses
$A_{V,0}$	surface area of adhered but unindented vesicle
A_λ	absorbance
D	tip-sample separation
d_{ij}	Euclidian distance between events corresponding to indices i and j
F	force
f_e	frequency of events
F_i	experimentally determined force value
$\hat{F}_i$	fitted force value
$\bar{F}$	mean of measured forces
F_{low}	lower force threshold
g	acceleration due to gravity of the earth
I_{ij}	$I_{ij} = 1$ if $d_{ij} < r$; $I_{ij} = 0$ if $d_{ij} \geq r$
κ	bending modulus
$K(r)$	Ripley's K-function
K_A	area compressibility modulus determined by GUV indentation experiments
K_{app}	apparent area compressibility modulus
k_B	Boltzmann constant ($k_B = 1.381 \cdot 10^{-23}$ J·K^{-1})
k_c	force constant of cantilever
K_{dir}	direct area compressibility modulus
$L(r)$	Ripley's L-function
L_c	contour length
$L_{c,low}$	lower threshold of contour length
$L_j(r)$	Ripley's L-function at the pixel corresponding to index j
L_p	persistence length
ΔL	length of tubular part of aspired vesicle inside pipette
M	molar mass
n	overall number of events inside investigated area
N	number of statistical repetitions (objects or measurements)

N_{dp}	number of data points of borderline of GUV
Δp	aspiration pressure
P	power
pH	negative common logarithm of proton concentration
q	deflection of cantilever
r	distance threshold in Ripley analyses
R^2	coefficient of determination
r_{max}	distance threshold which leads to maximum value of moving mean of $L(r)$–r
R_P	radius of aspiration pipette
r_V	radius coordinate of GUV in indentation experiments
R_V	radius of spherical part of aspired GUV
T	thermodynamic temperature
t	time
V	volume of vesicle
V_{norm}	normalised volume of vesicle
x_i	first coordinate of data points of borderline of GUV
x_m	fitted first coordinate of GUV centre
y_i	second coordinate of data points of borderline of GUV
y_m	fitted second coordinate of GUV centre
Z_c	deflection of cantilever
Z_p	extension of piezoelectric element
z_V	height coordinate of GUV in indentation experiments
α_{app}	apparent area strain
$\alpha_{app,max}$	maximum apparent area strain
α_{dir}	direct area strain
λ	wavelength
π	ratio between circumference and diameter of a circle ($\pi \approx 3.14159$)
ρ	Pearson correlation coefficient
τ	membrane tension
τ_{max}	maximum membrane tension
τ_0	pre-stress
τ_b	membrane tension at $\alpha_{app} = 0$
$\tau(1)$	fitted first tension value in high pressure regime

Curriculum Vitae

Personal Details

Date of birth	09.12.1989
Place of birth	Gronau (Leine)
Email	Marian.Vache@chemie.uni-goettingen.de
	Marian.Vache@gmx.de

Education

2015-2019	PhD thesis at the Institute of Physical Chemistry, University of Göttingen Thesis title: "*Structure and Mechanics of Neuronal Model Systems – Insights from Atomic Force Microscopy and Micropipette Aspiration*" under supervision of Prof. Dr. Andreas Janshoff
2012-2014	Master of Science studies in Chemistry, University of Göttingen Master's thesis: "*Modellierung der Zelladhäsion anhand von Riesenvesikeln*" under supervision of Prof. Dr. Andreas Janshoff final grade: very good (1.1), with distinction
2009-2012	Bachelor of Science studies in Chemistry, University of Göttingen Bachelor's thesis: "*Rheologie an Riesenliposomen*" under supervision of Prof. Dr. Andreas Janshoff final grade: very good (1.2), with distinction
2002-2009	Gymnasium Alfeld (Leine) Acquirement of the general qualification for university entrance

Publication

04/2015	Schäfer, E.; Vache, M.; Kliesch, T.-T.; Janshoff, A., Mechanical response of adherent giant liposomes to indentation with a conical AFM-tip, *Soft Matter* **2015**, *11*, 4487 – 4495.

Selected Talks

09/2018	*Molecular recognition imaging of biomembranes*
	SFB 1286 Retreat 2018, Teistungen, Germany
02/2016	*Mechanics and dynamics of biological adhesion*
	(together with Nadine Kamprad)
	International Symposium "Biological Dynamics from Microscopic to Mesoscopic Scales", Grimma, Germany

Selected Poster Presentations

07/2017	*Investigation of Protein Clusters by Atomic Force Microscopy*
	19th IUPAB congress and 11th EBSA congress, Edinburgh, United Kingdom
09/2016	*Mechanics of Giant Lipid Vesicles by indentation with a conical AFM-tip*
	Annual Meeting of the German Biophysical Society, Erlangen, Germany
07/2015	*Cell mimetic adhesion by giant vesicles*
	10th European Biophysics Congress, Dresden, Germany

Danksagung

Meinen Kooperationspartnern Jan Wehland und Prof. Dr. Ulf Diederichsen danke ich für die Synthese und Bereitstellung von Peptiden. Insbesondere gilt mein Dank meinen Kooperationspartnern Dr. Julia Preobraschenski und Prof. Dr. Reinhard Jahn für die regelmäßige Lieferung von synaptophysinhaltigen GUVs, deren Verwendung in der Mikropipettenaspiration immer noch die besten Resultate dieser Arbeit geliefert hat, sowie für die fachlichen Diskussionen.

Für die Erfahrungen die ich beim Betreuen ihrer Arbeiten im Arbeitskreis sammeln konnten und für ihre Beiträge zu meinen Ergebnissen danke ich meinen Abteilungspraktikantinnen und -praktikanten sowie Bachelorstudentinnen und -studenten Ljowa Mstojan, Rahel Ziemer und insbesondere Theresa Hune, deren umfangreiche Messungen mit der Mikropipettenaspiration einen Großteil der Daten für das zweite Projekt dieser Arbeit geliert haben, die ich in der zu dem Zeitpunkt verbliebenen Zeit in dem Umfang alleine nicht mehr hätte bewerkstelligen können. Die Zusammenarbeit mit ihr hat mir immer Freude bereitet.

Meinen Kolleginnen Susanne Karsch und Andrea Cordes danke ich zunächst für die intensive Zusammenarbeit in der Lehre über die letzten knapp vier Jahre. Auch wenn es nur kleine Schritte waren glaube ich doch dass wir ein paar kleine Verbesserungen für alle Seiten zustande bekommen haben. Die Arbeit daran war stets eine willkommene Abwechslung.

Darüber hinaus danke ich der neben mir ebenfalls neuen Doktorandin vom Februar 2015 Susanne Karsch für die insbesondere in der Anfangszeit, als ich endlich Messungen machen konnte, gegebenen Hilfestellungen und Hinweise am AFM, wenn mal wieder ein neuer für mich scheinbar unlösbarer Fehler aufgetreten ist, sowie für ihre Ratschläge was sie an meiner Stelle bei verschiedenen Angelegenheiten machen würde.

Filip Savić gilt mein Dank für die vielen Hilfestellungen bei allem was Computer und insbesondere Python betrifft, seit Beginn meiner Masterarbeit.

Sarah Verbeek danke ich für die netten Gespräche in Büro und Labor und für die gemeinsame Pflege des Peptidlabors – ich finde es ist in einem guten Zustand.

Für die Durchführung der Western Blots danke ich Jonas Schäfer.

Stefan Nehls und insbesondere Hannes Witt danke ich für die aufmerksame Durchsicht dieser Arbeit, für die darin investierte Zeit und die daraus resultierenden Verbesserungen.

Petra Lappe gilt mein Dank ich für die Organisation des Arbeitskreises und ihre Expertise mit der Bürokratie.

Allen übrigen ehemaligen und aktuellen Mitgliedern des Arbeitskreises Janshoff die ich seit 2012 kennenlernen und mit denen ich zusammenarbeiten durfte danke ich ebenfalls für ihre

Mithilfe, für die gemeinsamen Mensagänge, die Kaffeepausen, an denen ich viel zu selten teilgenommen habe, die Grill-, Film- und sonstigen Abende, die gemeinsam besuchten Konferenzen und die schöne gemeinsame Zeit. Ohne den Austausch mit meinen Mitdoktorandinnen und –doktorenden wäre ich an mancher Stelle verzweifelt.

Gleiches gilt für die Mitglieder des Arbeitskreises Kruss, deren große Vielfalt unseren Arbeitskreis bereichert hat.

Auch den Mitgliedern des Arbeitskreises Steinem gilt mein Dank für die gemeinsame Zeit und die weitere Unterstützung. Schade dass die enge Zusammenarbeit und die gemeinsamen Aktionen seit unserem Umzug in die PC immer mehr gelitten haben und wohl in Zukunft noch weiter leiden werden.

Meinem Bruder, meiner Familie und meinen Verwandten danke ich für die Abwechslung außerhalb der Uni, für die gemeinsamen Treffen und für die Erkenntnis, dass es auch noch ein Leben abgesehen von Uni, Studium und Promotion gibt.

Abschließend gilt mein besonderer Dank meinen Eltern ohne deren Unterstützung und Überzeugung mein Bildungsweg sicherlich lange vor dem Verfassen dieser Arbeit ein vorzeitiges Ende gefunden hätte.